Mechanical and Microstructural Behaviour of Tangled Metal Wire Devices

A Thesis submitted to the University of Sheffield

for the degree of Doctor of Philosophy in the Faculty of Engineering

by

Kartik Chandrasekhar

Department of Mechanical Engineering

University of Sheffield

December 2016

Abstract

As the push towards the use of lighter and more efficient materials continues, energy dissipation from vibrating structures made from such materials is growing in importance. Viscoelastic materials have most often been employed to tackle vibration problems. In several applications, such as in the space and defence fields, the operating conditions usually do not allow for such solutions to be utilised. Tangled metal wire (TMW) devices offer an alternative damping strategy. Since the microstructure of such devices is made of metallic materials, they operate resiliently over a wide range of environments. The microstructure of a typical TMW device is made of metal wires that have been woven and compressed into an entangled state. Although they possess favourable properties, the manufacturing process makes the microstructure very complex, and the mechanical behaviour, as a result, tends to be unpredictable.

The main theme of this thesis links the mechanical behaviour of TMW devices to their microstructural characteristics. A new algorithm is developed to study the microstructure of TMW devices from images obtained via microcomputed tomography (μ-CT) scanning. Following the application of compressive loads during the μ-CT scanning, it has been shown, for the first time, how the complex microstructural state evolves under different loading conditions. Parallel to this, displacement controlled experiments are performed on the TMW devices under quasi-static, low frequency, and high frequency loading conditions in an effort to ascertain the important phenomenological effects that dominate their response. Various analytical models are also explored and analysed with the aim of identifying an appropriate model for TMW devices. An analytical model, the frictional Zener model, is developed further to replicate the experimentally observed force-displacement hysteretic trends. The developed models, named the multi-chain frictional Zener models, include various additional terms to the basic model. Parameters are identified for the proposed models, and a model that gives acceptable accuracy with respect to experimentally observed hysteresis is found. This model is able to exhibit the spring-like nature of TMW devices, and it provides energy dissipation via classical Coulomb friction. The terms in the model are justified through analysis of the image processing results.

Previous researchers have thus far not been able to fully justify the reasons why TMW devices behave the way they do since the microstructure has not been completely understood. The benefit of studying both the microstructural and mechanical properties of TMW devices in the manner outlined above is that a more holistic reasoning for observed behaviour is attained. The relatively simple proposed analytical model can be used to predict dynamic response when TMW devices are applied to real structures. As the confidence levels in the understanding of the TMW device microstructure and modelling aspects increase, more applications can take advantage of the favourable mechanical properties (especially in terms of energy dissipation) TMW devices showcase.

ACKNOWLEDGEMENTS

One of the earliest adages I was taught as a child was the order of respect one must give: “Matha, Pitha, Guru, Deivam”, which translates to “Mother, Father, Teacher, God”.

I would like to thank, first and foremost, my parents, Mrs. Vidya Chandrasekhar and Dr. Chandrasekhar Srinivasan, for everything they have given me throughout my life. They instilled in me the pursuit of knowledge from a very early age, showed me what hard work and sacrifice was, taught me to be humble, caring, and most important of all, respectful of everyone and everything around me. I will eternally be thankful that I was lucky enough to be your son.

On an equal standing with my parents, I will forever be grateful to Dr. Jem Rongong and Dr. Elizabeth (Lizzy) Cross, my teachers and supervisors. The numerous amounts of times I entered Jem's office unannounced, whether to ask for advice, or share some of my small breakthroughs, were always greeted with a wide smile, and a kind and wise response. Please never change, Jem. Lizzy, thank you for all the help and the constant words of encouragement you've given me throughout my studies. A special mention should also go to Dr. Charles Lord, whom I have also troubled countless times, for countless reasons, from having casual chats about life, to seeking knowledge from his infinite wisdom. Last, but not least, on this list of teachers is Mr. Dave Webster, our in-house expert technician, who spent several hours with me while performing experiments, advising me on the designs of my test structures, and helping to accelerate the manufacturing processes.

Lastly, I would like to thank the big guy upstairs. Without His blessings, I would not have had the strength to carry out the journey that has brought me this far. I also believe that there is a God (and good) in everyone. I would specifically like to thank the following people (in no particular order): Daniela Tiboaca, Patrick Sawyer, Banafshe Tabdili, Haval Asker, Dharana Jayawardane, Shalini Weerasooriya, Alessio Datteo, Haichen Shi, Ning Tang, Suzhou Chen, Joaquin Zafra, Evangelos Papatheou, Niloufar Motazedi, Sam Gorji, Keith Worden, Nikolaos Dervilis, Sneha Kumar, Prithika Krishnan, and the numerous others who have accompanied, and supported, me in my journey. You have all become less friends, and more family, to me. Thank you.

I dedicate this work to Divya Chandrasekhar-Yashwanth (my sister), Yashwanth Sekhar (my brother-in-law), and Mihika Yashwanth (Michu, my beautiful niece).

"Cogito ergo sum - I think, therefore I am"

- René Descartes

LIST OF PUBLICATIONS

Conferences:

[1] K. Chandrasekhar, J.A. Rongong, and E.J. Cross. Frequency and amplitude dependent behaviour of tangled metal wire dampers. *ISMA - International Conference on Noise and Vibration Engineering*, Leuven, Belgium, 17 September 2014.

[2] K. Chandrasekhar, E.J. Cross, and J.A. Rongong. Mechanical and microstructural behaviour of tangled metal wire dampers. *11th International Conference on Advances in Experimental Mechanics*, Exeter, United Kingdom, 7 September 2016.

Table of Contents

LIST OF FIGURES

LIST OF TABLES

Chapter 1

INTRODUCTION

This chapter provides an introduction to various topics that are the subject of the work carried out for this thesis. It provides a brief introduction to mechanical vibrations, and why they are often undesired. The different types of damping are introduced, and some traditional damping technologies are discussed. Tangled metal wire (TMW) devices, the mechanics of which are the primary focus of this work, are also introduced. Finally, the motivations, aims and objectives of this work are stated, and the structure of this thesis is outlined.

1.1 Mechanical vibrations

A vibration is defined as any movement that repeats itself over a distinct time period. Mechanical vibrations occur in any structure that possesses mass and elasticity. They involve the transfer of energy from potential energy (which is provided by the elasticity of structures) to kinetic energy (which is facilitated through its mass).

Sometimes, vibrations are useful. The most obvious useful vibration allows the sense of hearing. They are also advantageous in medical ultrasonics, where the health of a baby may be monitored from an early stage, and in mechanical clocks, where the vibration of a physical resonator is used to keep track of time. Structural health monitoring (SHM) and condition monitoring (CM) use vibration traces of systems to monitor the health of various components.

High levels of vibrations are often undesired. They lead to noise pollution, fatigue, and loss in structural performance. When structures are freely excited, they tend to vibrate at their natural frequencies. If a structure is forcefully excited at its natural frequency, which can often happen in rotating machinery, the amplitudes of vibration become extremely large, and the structure resonates.

The vibration of real systems, which are continuous in nature, can be approximated using coordinates to describe their motion. The number of coordinates used in the approximation indicates the degrees of freedom of the system. Each degree of freedom consists of a natural frequency, and hence a potential resonant frequency to avoid.

As the push for improving structural efficiency continues, applications are tending towards lighter materials. Since lighter structures often have lower strength, reducing the impacts of mechanical vibrations is a necessity, and makes energy dissipation vital.

1.2 Damping

Damping provides a means to reduce high amplitudes of vibrations by dissipating kinetic energy present in a structure. Different damping techniques can be categorised into three general forms [1]:

- Viscous damping
- Friction damping
- Structural, or hysteretic damping

Viscous damping is arguably the most commonly used damping strategy. It utilises the viscosity of a material to provide resistance to motion. Examples of viscous materials include oil, water, and air. Viscoelastic materials are by far the most common damping materials. These are materials that possess properties of both viscous and elastic materials. Examples of such materials include natural rubbers, and other elastomers. Viscoelastic materials are relatively simple to produce, and the production can be manipulated to provide specific material performances. Intensive research on viscoelastic materials has been historically carried out by several researchers, and the performance of these materials is therefore well understood.

However, due to the inherent nature of viscoelastic and other viscous materials, the performance could degrade significantly due to external factors, such as extreme operating temperatures. In such cases, other damping strategies are sought.

One alternative strategy is the use of friction (or Coulombic) damping. Friction is often not thought of as an attractive feature, such as in high precision robotics [2], or in frictionless bearings. However, interfacial friction is an important source of energy dissipation. When two contacts have relative motion occurring between them, some of the energy of the motion is dissipated in the form of heat.

Structural damping is closely related to friction damping. It refers to the energy dissipation in the form of microscopic friction occurring within the grain boundaries of a structure when it is deformed. Typically, structural damping is not a sufficient method of dissipating vibrations since the damping levels are relatively low.

1.3 Examples of damping techniques

The three damping types discussed in the previous section are applied to real structures in various forms. Here, some of the most common techniques to suppress vibrations are discussed.

1.3.1 Constrained layer damping

Constrained layer damping (CLD) consists of a constrained layer, which is typically a viscoelastic polymer, and a constraining layer, typically a material with a high Young's modulus. Once attached to a host structure, mechanical strains are transmitted between the sandwiched structures into the constrained layer. These cause the constrained layer to shear, and result in damping. Once optimised, they are capable of damping broadband vibrations to a moderate level.

1.3.2 Tuned mass damping

Tuned mass dampers (TMDs) involve attaching a mass and a material that can store energy (i.e. an elastic material) to a host structure. They are used to tackle narrowband problems, i.e. for resonant frequencies that are of particular importance. They work by modifying the physical properties of the combined structure (host structure with the TMD), such that the natural (and hence resonant) frequency, shifts away from the old value, and will instead consist of two or more frequencies that are away from the frequency of interest. As an example, one can think of an engine whose optimised working regime occurs at a frequency, whose dominant harmonics coincide with the resonant frequency of the structure. Adding a TMD to the motor would allow the engine to operate at its optimised working regime without any resonance problems since the new natural frequency and its harmonics are now moved away from the optimised engine operating speed.

1.3.3 Particle damping

When particles are attached to vibrating structures, the kinetic energy of the vibrating structure is transmitted to the particles via the container housing them. The particles behave in three distinct phases: solid, liquid, and gaseous. In the solid phase, the particles appear stationary, and microslip at contact points dominates the energy dissipation. In the liquid phase, the particles roll against each other, and macroslip occurs. Finally, in the gaseous phase, the particles are unrestrained, and they move around vigorously. In this phase, inter-particle momentum exchange is quite significant. The onset of each phase depends on various factors, such as the amplitude of vibration, the shape of the particles, and the shape of the container housing the particles. They are highly nonlinear, but they can be tuned for particular vibration problems.

1.3.4 Other friction damping applications

Friction damping can be found in several applications. Underplatform dampers can be found in gas turbines, which rely on the centrifugal forces of the spinning turbine to restrict the vibration levels of the blade. In such a case, the mass of the damper plays a huge part in the effectiveness of energy dissipation [3]. Another example can be found in shrouded blades [4]. The shrouds not only limit the vibration amplitude and raise the natural frequencies of possible low frequency blades, but also dissipate energy via friction damping [5]. Wire rope isolators have proven useful in dealing with vibration as well as shock loading. Interfacial damping is the main component in these devices. When loaded, the strands of wire in the wire rope isolator move relative to each other leading to friction. The friction converts the kinetic energy to heat [6]. Tinker [6] indicated the benefit of the helical cable isolators over conventional dampers (e.g. polymeric dampers) as a use in the adverse space environments. They are stable over a wide range of temperatures, and are more resistant to wear.

1.3.5 Limitations

While the damping techniques that have been discussed so far have been successfully applied to solve vibration problems, each possesses some shortcomings.

- CLDs are heavily reliant the properties of the viscoelastic material it employs. At high temperatures, these can pose a problem, since the material will simply melt away, or even burn depending on the thermosetting process. At low temperatures, the viscoelastic material operates in its glass phase, where the material characteristically is brittle, and has low damping. Therefore, it is easy to de-optimise a system with a CLD. Depending on the material choice, material aging could also be another source of concern.
- TMDs are not suitable for broadband vibrations, since they are typically tuned for just one frequency region.
- PDs are highly nonlinear, and their properties may not always be predictable.

The limitations of current damping technologies formed the motivation and drive to study a different type of energy dissipating material, tangled metal wire devices.

1.4 Tangled metal wire devices

Tangled metal wire (TMW) devices are energy dissipating materials that are formed through a series of steps:

- Initially, a long chain of thin metal spiral wires are stretched and drawn.

- The stretched wires are randomly woven to form an amorphous shape.
- The amorphous tangled wires are compressed in a mold to produce a desired shape.

Figure 1.1 shows various shapes and sizes of manufactured TMW devices.

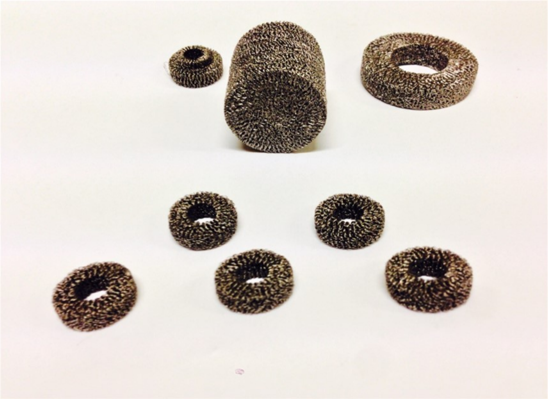

Figure 1.1: Various shapes and sizes of TMW devices

The material composition of the devices shown in Figure 1.1 is stainless steel. Other materials have also been used to create TMW devices, including aluminium, copper, titanium, and nickel based superalloys.

TMW devices have had a few aliases throughout their history. When they were first introduced to the research community in the 1960s, they were known as elastic metal mesh [7]. They have also been known as porous wire mesh, and more recently, metal rubber. The term ‘metal rubber’ was particularly used due to the similarity in mechanical properties of the devices to that of some rubbers and other synthetic elastomers. Some typical values are seen in Table 1.1.

Material	**Elastic modulus, MPa**	**Loss factor, η**
Butyl rubber	5.6-6.7	0.11-0.18
Nitrile rubber	9.9-11.5	0.11-0.18
Ethylene-vinyl acetate	10.1-11.9	0.09-0.18
ISD 112 viscoelastic polymer	0.1-10.0	1
TMW	1.3-11.6	0.15-0.60

Table 1.1: Typical elastic modulus and loss factor values for a few elastomers, and TMW devices

The name ‘metal rubber’ suggests a stacked/sandwiched structure comprised of metal and rubber, or even rubber infused with some form of metal. Since this can cause confusion with other applications (for example, see [8], or [9]), this thesis standardises all previously used names to tangled metal wire, or TMW for short.

As the mechanical properties are quite similar to elastomers, TMW devices offer an alternative option for damping and isolation in applications that elastomers cannot be used. This is especially true in space applications, where environmental conditions may be harsh. The primary energy dissipation mechanism of TMW devices is widely accepted as friction. Here, the interaction between wires in the microstructure convert the kinetic energy of oscillatory motion to heat. This mechanism can be analogously compared to the energy dissipation mechanism of viscoelastic elastomers. In viscoelastic elastomers, friction occurs between polymer chains at a much smaller scale. At higher temperatures, the polymer chains in viscoelastic elastomers decompose and melt, providing no useful mechanical properties. On the other hand, since the microstructure of TMW devices is made of metal, they can retain their properties over a wider range of temperatures, until the material melting point.

1.5 Motivation

As mentioned above, TMW devices have several appealing features that include high energy dissipation, and the ability to retain their mechanical properties over a wide working range [10]. They can be produced to have low relative densities, meaning that the weight penalty can be low. The devices also possess a relatively high elastic modulus, illustrating their ability to handle stresses that may act on them. They have found use in several applications including cryogenics [11], seals in motors, absorption of sound, vibration control, among others in several industries including the space, marine and automotive industries [12].

TMW devices have been subject to vigorous research over the years. There are several factors that influence observed behaviour. Reportedly, these have included effects of pre-compression, amplitude, wire thickness, orientation angle, frequency, lubrication, and temperature. It is easy to see that the interdependence of several of these conditions may play a part on the overall dynamics of the device. This has been a motivation for researchers to carry out experimental investigations to appreciate and understand the importance of these parameters.

However, thus far, there have been no definitive answers to why TMW devices behave the way they do. This is because the effects of the microstructure are not very well understood. The research carried out in this thesis was therefore performed to fill in the gap in the current state of the art, and provide better insight into the effects of the microstructure to the experimentally observed behaviour.

1.6 Aims and objectives

The main aim of this thesis is to understand the microstructural properties of tangled metal wire (TMW) devices that influence the observed mechanical behaviour. Therefore, the question the thesis is trying to answer is: what is the most important microstructural parameter that dominates the observed hysteretic behaviour of TMW devices?

To fulfil this aim, the objectives of the thesis can hence be stated as follows:

i Develop methods to study the microstructure.

ii Objectively study and explain quasi-static and low frequency behaviour.

iii Objectively study and explain high frequency behaviour.

iv Study and develop analytical models that can explain the observed hysteretic behaviour.

It must be emphasised here that the statistical variabilities between TMW devices are significant due to the nature of the manufacturing process, and the characteristics of the microstructure. The main objective of the thesis is not to quantify these variabilities, rather it is to understand the underlying physics that dominates the response behaviour. As a result, only a limited number of TMW devices are tested, and the results reported in this thesis must not be considered as a complete statistical representation of TMW device behaviour.

In order to study the microstructure in a static setting, a novel image processing algorithm is proposed. This algorithm identifies the “skeleton” of the TMW microstructure using wire centroid locations under different loading conditions. Quasi-static and low frequency tests are carried out on an industrial test system, and the observed behaviour is explained in terms of the microstructure. Research has mainly focused on quasi-static and low frequency behaviour in the past. Therefore, a new test rig is developed to test high frequency behaviour. Since TMW device behaviour have been known to be nonlinear, the test rig is incorporated with a PI controller. Finally, several analytical models are studied with an effort to replicate the observed experimental hysteretic trends. Finally, parameters are identified using the Metropolis-Hastings method for the proposed analytical models in an attempt to validate the models.

1.7 Thesis layout

Chapter 2 provides a literature review of the current state of the art of TMW devices. These include discussing the numerous experimental activities that have been carried out by researchers in the past, and the few models that have been reported. There is also a brief discussion on wire rope isolators, which are made of ordered metal spirals, and on the nonlinearity exhibited by fibrous materials.

Chapter 3 discusses a novel image processing algorithm that identifies the wires contained in the TMW device microstructure. Images for this algorithm are acquired from reconstructed micro-computed tomography (μ-CT) scan images at various static loading conditions. This is one key area that requires attention since no one has previously studied the microstructure of TMW devices in a quantitative manner, whilst it is appreciated that people have analysed μ-CT images in a qualitative manner. The microstructure is thus not well interpreted currently. The chapter discusses the development of the algorithm and its various functions, the experimental μ-CT scanning procedures, and the analysis of the results that stemmed from the algorithm.

Chapter 4 details the quasi-static and low frequency dynamic experiments performed. The methods used to calculate and analyse the dynamic behaviour are also explained. Prior to the experimental investigation, a number of hypotheses that predict the mechanical behaviour are proposed based on the material microstructure. The experimental results are thus analysed with respect to these hypotheses.

Chapter 5 provides a discussion of work carried out in understanding the high frequency behaviour of TMW devices. This is another key area lacking in literature, since previous work in this area is either unreported, or underreported. The chapter discusses a new test structure that is designed and manufactured for the high frequency work carried out, it is validated, and the results are also analysed with respect to the same hypotheses proposed in Chapter 4.

In Chapter 6, the analytical modelling aspects of TMW devices are reported. Since TMW devices provide energy dissipation via friction, a few experimentally observed friction phenomena and a number of models that aim to explain some of the phenomena are introduced. Next, a few pre-existing analytical models that consist of microelements are introduced, and their behaviours are interpreted. One of these models, the frictional Zener model, produces hysteresis loops with similar characteristics to that of the TMW devices. This is developed further to produce the "multi-chain frictional Zener model" in an effort to replicate experimentally observed trends. The proposed models are then fed into the Metropolis-Hastings algorithm to identify model parameters, and hence either reject the proposed models, or validate them.

Chapter 7 summarises the key findings emerging from this thesis. Some of the outcomes from the research carried out opens new possibilities for future analysis of entangled or fibrous materials. This is especially true regarding the novel image processing algorithm. Therefore, the chapter also details some key features that the proposed algorithm can be improved upon, and other areas where further work stemming from this research can be carried out.

The design and implementation of a PI controller on a National Instruments CompactRIO industrial controller is reported in Appendix A. The controller was designed to be used with the high frequency test structure. The need of a controller is due to the nonlinear behaviour produced by TMW devices. The controller helps reduce uncertainty in the test results since the input amplitude and waveform is controlled, and any nonlinearity in results only arises due to the test specimens.

Chapter 2

LITERATURE REVIEW

2.1 Introduction

Depending on the source, tangled metal wire (TMW) devices have had several aliases, including metal rubber and elastic wire mesh. The following literature review standardises all these aliases as TMW devices, regardless of the name used in the text.

TMW devices are an attractive group of materials that have gained recognition in several practical applications due to their enduring mechanical properties in extreme conditions [13]. Theoretical research is still lacking in many ways, primarily due to the microstructure not being fully understood, and hence represented in models.

In this chapter, previous experimental studies on TMW devices are reported. Modelling work that has been carried out thus far on TMW devices, as well as other work relevant to this project, are also reported. This includes a discussion of a similar, but simpler (in terms of microstructure) application (wire rope isolators) in which friction is the primary energy dissipation mechanism, as well as a brief overview on the nonlinearity imposed by fibrous materials.

2.2 Experimental studies

2.2.1 General capabilities of TMW devices

Childs is one of the first researchers to have reported research on TMW devices used as dampers [7]. His study was concentrated on the high-pressure fuel turbopump in the main engine of the space shuttle. He reported that the TMW devices provided stiffness and possessed high damping capabilities. He reported that the asymmetric stiffness (because they have different stiffness characteristics in loading and unloading) provided a stabilising effect in the turbomachinery, although actual test data was not published.

Zarzour [14] found that the stiffness and damping provided by the TMW devices tended to reduce the effects of imbalance in turbomachinery, more so when compared to squeeze film dampers.

Zarzour and Vance [15] tested the response when oil was present in the TMW devices. They found that the damping reduced negligibly, and concluded that damping may not be Coulombic. Note that this observation does not establish that TMW device damping is not dominated by contact friction. One possible explanation is that when oil is present, the damping mechanism partly changes from Coulomb friction to a more pronounced viscous damping. They also studied behaviour at elevated temperatures. They found that the stiffness was reduced as temperature increased, but the damping remained unchanged.

Experiments at cryogenic temperatures were conducted by Ertas, et al. [16]. They found that at temperatures of 83 K, stainless steel friction dampers provided the same amount of damping as they did at room temperature. TMW devices, on the other hand, reportedly had increased damping by 25% at these temperatures.

Al-Khateeb and Vance reported that hysteretic modelling is more appropriate than Coulomb friction modelling for TMW devices [17].

Barnes reported that the performance of the TMW devices depended significantly on the properties of the material used [18]. For example, Burshid noted that TMW devices made from copper provided more damping than those made from stainless steel [19].

Okayasu, et al. reported the use of TMW devices as bearing supports in the LE7 engine liquid hydrogen turbopump [20]. When tested using stiff bearing supports instead, they noted several vibration problems. However, with the use of TMW devices, the engine was able to reach speeds higher than the third critical speed; indicating that significant damping arose from the TMW devices.

Al-Khateeb studied the damping effectiveness of TMW devices over a period of 6 months, and found that it remained consistent [21], indicating that TMW devices are less susceptible to fatigue.

2.2.2 Static and quasi-static testing

Zuo, et al. performed a microscopic investigation on the outer surface of a cuboidal TMW device following quasi-static compression tests [22]. They observed that the force-displacement curves may be split into three stages. Stage I (OA in Figure 2.1) was reported to consist of elastic deformation of coils in the microstructure. In Stage II, it was reported that a combination of nonlinear elastic deformation and microscopic sliding took place, which consisted of a distinct friction mode, labelled as Mode I. In friction Mode I, it was reported that two non-parallel coils at a certain relative angular orientation (crossed contacts) slipped relative to each other, as illustrated in Figure 2.2 (a). Finally, in Stage III (BC on Figure 2.1), the load was shown to increase exponentially with deformation. They reported that this was thought to be caused by both sliding friction and the inelastic deformation of the coils. The plastic deformation occurring in this stage, caused the TMW microstructure to remain permanently deformed when loads were removed. Stage III was thought to consist of friction Mode II, in which a wire segment was pressed out from between two adjacent coils that were at a relative angle to each other, as shown in Figure 2.2 (b).

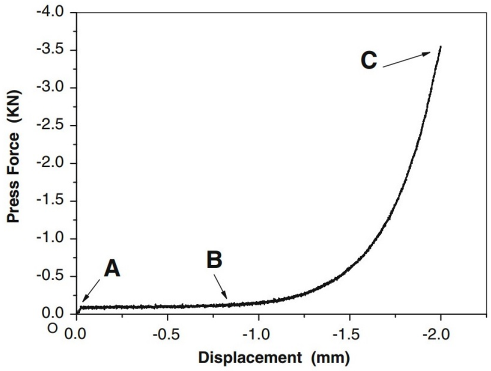

Figure 2.1: Typical force-displacement curve of TMW devices reported by Zuo et al. (Source: [22])

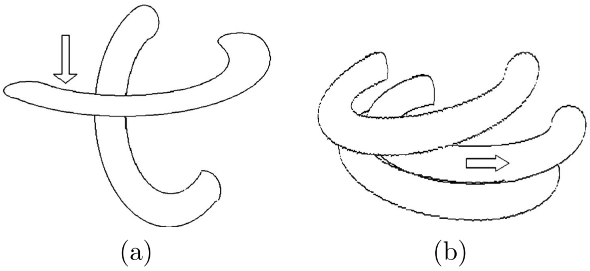

Figure 2.2: (a) Mode I friction mechanism, and (b) Mode II friction mechanism (Source: [22])

Wang, et al. also noted the three stages of the static hysteresis curve [23]. In order to maintain the structural integrity of TMW devices, they stated that it was essential to avoid Stage III, and limit the loading to Stages I and II. The reported reason being that energy dissipation, after the onset of plastic deformation, reduces significantly. They also studied the effects of relative density, wire diameter and coil diameter on the static response of TMW devices, noting that other parameters, studied by Yan and Nie [24] and Ma and Hong [25], such as material, angle of coil orientation, and moulding thickness, affect the response too [23].

Wang, et al. [23] also showed that an increase in relative density caused the stiffness to rise, while loss factor was affected negligibly, with a slight increase in damping before it decreased. This is thought to be because, at higher densities, the wires are closer together, and so there are more contacts, allowing for increased frictional losses between contacts. However, the total amount of slip is limited for much higher relative densities, reducing the energy dissipation. A smaller wire diameter for a given relative density has a lower stiffness, but can dissipate more energy. This can be explained by more contact points being created, which can slip more, and therefore explaining the higher loss factors observed. They reported that the drop in stiffness occurred because stiffness is proportional to the fourth power of radius [26]. Coil diameter was found not to affect loss factor, but because the stiffness is inversely proportional to the cube of coil diameter, stiffness dropped with increased coil diameter.

Wang, et al. also measured the Poisson's ratio of the TMW devices using a 7 megapixel camera, by observing the changes in pixels for consecutive photos following application of a load [23]. They found that the Poisson's ratio was near zero in both the axial and radial directions.

Hong, et al. [12] also mentioned the three stages of the force-displacement curve explained earlier in this review. They reported that Stage I appeared only if the device is not preloaded.

Tan, et al. performed quasi-static compressive testing on aluminium TMW devices [27]. In their study, they also noted the three stages of the force-displacement curves. They found that the stress-relative density relationship followed the Gibson-Ashby equation [28], which follows the power law, and is also used to characterise metallic foams.

Ao, et al. examined the damping characteristics of TMW device isolators under simultaneous axial and tangential loading [29]. They reported that TMW damping is affected to different extents by various microstructural properties, such as relative density, and wire diameter. They noted that the presence of friction introduced nonlinearity into the system

Zhang, et al. studied TMW devices made of a nickel-based superalloy with quasi-static loading [30]. In their work, three sets of specimens of different relative densities were tested for the secant and tangent Poisson's ratios, based on the secant modulus (gradient from origin to a certain point in the stress-strain curve) and tangent modulus (gradient of a specified point in the stress-strain curve).

Some important sources of uncertainty were noted by Zhang, et al. [30]. The main source of uncertainty was attributed to the uneven compression surfaces, especially for small deformations. They advised that, to avoid the issues that arise because of the uneven surface, specimens should be pre-compressed (to the order of 0.02-0.05 strain). They also stated that it was necessary to avoid strains above 0.10, due to possible plasticity fatigue to the TMW device. Other sources of uncertainty were related to the limitation imposed by the video extensometer (used to measure the changes in strain) where it was not able to track large deformations. The video extensometer was used to measure changes in strain between two points in relative motion. Increased strains caused an increase in relative density, and increase in stiffness. This is in agreement with experimental results published by several authors. Additionally, the specimens with higher relative densities had higher tangent moduli and lower loss factors. The loss factors reported by Zhang, et al. [30] for the Nickel based superalloys were between 0.11 and 0.18, which is lower than that of stainless steel, which range between 0.2 and 0.3. The Poisson's ratio increased with increasing relative density and increased strain. This phenomenon was attributed to larger pores available in the microstructure at lower relative densities or strain. Therefore, when compressed, the wires slid transversely within the large pores. Overall, it was reported for smaller deformations, the Poisson's ratio was about 0.01, which rose to 0.1 for higher deformations.

Ma, et al. carried out quasi-static testing to study the effects of TMW dimensions - the height and the cross-sectional area - on specimens with constant relative densities [31]. They found that increasing the height, or reducing the cross-sectional area of a TMW bearing led to a drop in the loss factor. The tangent modulus (which is believed to be their preferred term to the elastic modulus), on the other hand, was reported to increase with height. This is thought to be unusual, because increasing the height should reduce the stiffness of the material. However, if the stiffness coefficients of the TMW specimens were kept constant, the increase in the elastic modulus may be justified.

Ma, et al. [32] performed quasi-static testing of various relative density TMW specimens with different lateral constraints. The study was aimed at understanding boundary effects for better design of TMW devices. As the constraint load increased, the elastic modulus and loss factor increased. These can be explained by the increase in relative density, and higher number of contact points within the microstructure.

2.2.3 Dynamic testing

Dynamic testing, as opposed to the quasi-static testing reported in the previous section, is defined as any test conducted where inertial effects are considered significant.

Hou, et al. [33] tested some TMW specimens over a narrow range of frequencies (1 Hz to 10 Hz), at various amplitudes (0.5 mm to 2.5 mm) and at a broad range of temperatures (243 K to 573 K). The effect of temperature on the loss factor was reported to be negligible although there was a fluctuation of about 15% from the midpoint value of 0.27. The amplitude dependency on loss factor was also shown to be negligible, with loss factor slightly decreasing. It was reported that higher amplitudes cause dry friction to occur over a larger distance. There was a reported increase in pressure between the wires. These acted to increase the energy dissipation. The frequency dependency was found to be the most influential factor affecting loss factor. With increasing frequency, the loss factor reduced in a nonlinear fashion.

Ma, et al. experimentally studied TMW under the context of damping and sound absorption [34]. Like many other researchers, they studied the sound absorption capabilities of TMW with regards to various microstructural properties that included the thickness of wires, porosity, and hygroscopicity (whereby the TMW was immersed in water). In the experimental study of damping, various amplitudes of band-limited random vibration inputs up to 2000 Hz were considered for different TMW devices. For the sound absorption experimental studies, the TMW devices were placed in an impedance tube, and subjected to acoustic excitation at frequencies up to 6000 Hz, and the response was measured using a microphone. Increasing wire thickness and reducing porosity were shown to improve TMW sound absorption.

Dynamic tests, in addition to quasi-static testing, were performed by Wang, et al. [23] to observe the effects of dynamic strain amplitude, pre-compression and vibrating mass on a TMW device connected to a steel tube cantilever beam, excited by a shaker. They studied force and acceleration controlled response. For force controlled response, it was observed that the resonant frequency of the system dropped with increasing force levels. This was reported to occur due to the nonlinear stiffness reduction of TMW devices at increasing amplitudes. In the acceleration controlled response, the stiffness again displayed softening behaviour, while the loss factor was found to increase with higher acceleration. This can be explained by the increase in sliding between wires, which increases energy dissipation, inside the device. The effect of pre-compression is that the wires are closer together (similar to a device with a higher relative density) and there are hence more contacts occurring. However, this causes an increase in stiffness. Lower damping results if a certain limit is exceeded, a characteristic of systems with friction damping. The vibrating mass affected the pre-compression level in their experiments, and hence affected dynamic behaviour. When studying the hysteresis of the TMW device at various displacement amplitudes, it was concluded that the stiffness indeed did reduce in a nonlinear fashion, and that the loss factor increased, also nonlinearly. Tests with various frequencies also indicated the dependency on frequency higher frequencies reduced the dynamic stiffness, but increased the loss factor. The Kramers-Kronig relationship, which was initially developed in electromagnetics, could be used to define the relationship between the elastic modulus changes to the loss factor changes [35]. The relationships are basically a pair of integrals that allow the real part of the complex modulus to be calculated from the frequency dependence of the imaginary part if the imaginary part is known for all frequencies, and it is true for the reverse too. The important assumptions are that the stress-strain relationship is linear, and that the system is a causal one which in the case of all real materials is true. More importantly, it is required that the solutions of the Fourier transform for a given strain function must converge to give the dynamic and loss moduli of the complex modulus.

Wang, et al. [23] compared the TMW device results with results from a near-linear elastomeric material, DC3120 at various accelerations. It was found that the estimated loss factor of the TMW device was up to three times larger than that of DC3120 at high excitation levels.

Ma, et al. used TMW as a bearing support [36]. The TMW bearing support was subjected to two sets of vibration tests: one with excitation using an electrodynamic shaker (up to 240 Hz) and the other, with excitation caused by mass imbalance (up to 6000 RPM). For the shaker experiments, they noted that both stiffness and damping reduced when amplitude of vibration was increased. As frequency increased, the stiffness was found to increase, and the loss factor increased to a maximum, before decreasing. For the mass imbalance experiments, a rotor was tested at its critical speeds. Increasing the imbalance did not change the critical speeds, indicating overall structural linearity. When compared to the use of squeeze film dampers instead, which were found to be highly nonlinear, this was found to be preferable. In the range of mass imbalances tested, the loss factor ranged between 0.1 and 0.5.

Ertas and Luo attempted to characterise the nonlinear stiffness and damping coefficients of TMW devices at various excitation amplitudes, and frequencies [37] using an electrodynamic shaker. Increasing amplitude or frequency led to reduced stiffness and damping trends, similar to the results reported by Ma [36].

Zhang, et al. studied the use of TMW devices as an isolation bearing [38]. In their experiments, they went up to frequencies of 3 Hz and dynamic strains of 20%. The frequency was shown not affect the hysteresis observed for a given amplitude. The damping was noted to increase with amplitude, whereas stiffness correspondingly reduced. They created an experimental model relating the force response of the TMW to the displacement [38]. This included a quintic polynomial to define the stiffness, and a quadratic term with an exponent to define the damping. They identified parameters using the least square error method.

Choudhry performed tests on several TMW devices of different configurations [39]. Although not explicitly stated, the manufacturing style of these devices is slightly different from the TMW devices other researchers have studied. A company called Metex, who produce the devices, employ the "Jersey Stitch" approach in the manufacturing process. By treating the test apparatus as a single degree of freedom (SDOF) system and taking the baseline properties of the test apparatus into account, he was able to obtain the mechanical properties (namely, stiffness and loss factor) of the devices. He found that the devices with increased axial thickness (thickness in the direction of loading) caused higher damping and stiffness. The trend was that with increasing radial strains, these would drop logarithmically. Using a radial thickness parameter (sum of the outer and inner diameters of the damper divided by their difference) as a means of quantifying its effect on damper performance, it was found that both stiffness and damping coefficients had a positive linear correlation with the radial thickness. Next, it was found that, in the limits tested, both stiffness and damping increased with increasing axial compression, with both having a non-linear trend, firstly with a slow rise, and then followed by a more rapid rise. Radial pre-compression was found to have a weakly linear relationship with both stiffness and damping. The effect of increasing displacement amplitude of vibration was seen to cause the stiffness and damping to reduce in a logarithmic manner. The effects of different designs of TMW devices were then studied. Segmented TMW devices were interestingly found to affect the stiffness and damping more than TMW devices that were split. The latter devices had a gap in their annular shape , whereas the former devices had two gaps, and can effectively be considered as two separate TMW devices. This study may prove to be beneficial for widespread use of TMW devices in critical applications, as even "damaged" specimens may provide adequate damping and stiffness support, since the most significant drop in damping was only 20% in the case of the segmented devices.

Jones performed an experimental investigation on TMW devices [11]. Jones conducted two sets of experiments: impact testing and shaker testing, noting the differences between parameter identification of stiffness and damping in the two methods [11]. Like Choudhry, he found that both stiffness and hysteretic damping had a logarithmically decreasing trend. He also performed similar tests to assess the effects of axial interference (referred to as pre-compression in work performed by others) and radial interference (compression in the radial direction). For the axial pre-compression test, the stiffness increased with increasing pre-compression in a weakly nonlinear fashion. The loss factor, calculated in his work as the damping divided by stiffness (not the usual definition of loss factor reported by other researchers), had an initial peak, followed by a decreasing trend with increasing pre-compression. In the radial pre-compression case, the stiffness had a positive linear trend with increasing radial pre-compression. On the other hand, the loss factor had a positive correlation with radial pre-compression, with a parabolic trend. The loss factor seemed to have a positive linear trend after 5 mils of radial pre-compression. Before 5 mils, there was a small trough in the results.

2.2.4 Discussion

It has been seen that several researchers have reportedly observed three stages of the TMW force-displacement curve, with three distinct gradients. The reported drop in the stiffness between the first and second stage is quite questionable. There is no mechanism perceivable that can cause an initially stiff curve to become less stiff (unless sudden slip, or buckling is observed, but these were not reported to occur). If anything, the stiffness should increase even further because during loading at the initial stages, only a few strands of wires on the uneven TMW surfaces are compressed, before the bulk material is compressed. This should stiffen the material even more.

It must be noted here that the internal structure of the TMW devices was not studied by Zuo, et al. [22]. The friction modes that they have reported were obtained by observing changes to the outer surfaces, and therefore it cannot necessarily be accepted as fact that these are the only types of friction modes present i.e. there may be other types of friction contacts in the internal structure.

The effects of Poisson's ratio, reported by Wang, et al. [23] and Zhang, et al. [30] seem somewhat contradictory. Zhang, et al. reported a Poisson's ratio of up to 0.1 at high displacements, but Wang, et al. reported a Poisson's ratio of only 0.03. This could have been due to the fact that at high displacements, the relative density increases to a point where internal deformation cannot take place, and so the bulk material deforms outward instead.

The study by Choudhry [39] and Jones [11] simplified the function of TMW devices by assuming a single degree of freedom system, allowing them to understand the behaviour at a single frequency. Although Choudhry did test various different configurations of TMW devices, the limited nature of his investigations did not allow him to analyse the effect of the microstructure, rather focusing on the bulk material.

Following the review of experimental findings in literature, it is clear that most of the work that has been carried out has concentrated on quasi-static and static type compression tests. Dynamic testing has been carried out, but this is still in its infancy. Furthermore, the frequencies tested in most of the publications are limited to lower frequencies (generally 10 Hz or less when studying the stand-alone compression behaviour of TMW devices). Therefore, this is an area that can be improved upon.

The effects of different material properties have been studied in almost all the literature findings and are clearly an important factors that affect the mechanical properties of the devices. However, most of the explanations given by the respective researchers remain hypotheses - objective evidence that rules out alternative hypotheses is scarce. The reasons for certain changes in behaviour have often been linked to different material properties, and although this provides a good platform for a hypothesis to work towards, the material properties have not been critically analysed to justify the changes in the mechanical properties of the devices. The primary reason for this is because researchers have not been able to access the internal microstructure of the material while the tests were performed, whether static or dynamic. Micro-computed tomography scanning, which is discussed in Chapter 3, rises up as an important tool for this. The fact that the microstructure changes under loading means that it is the most important underlying factor that affects performance. Obtaining a good understanding of the microstructure is vital in determining why certain experimental findings are observed, and how to quantify the effect of different material properties.

2.2.5 Other interesting studies

He, et al. explored the use of titanium TMW devices for load bearing biomedical applications, where conventionally porous titanium materials are used [40]. They studied the pore structure estimated by histograms obtained from image analysis of outer surface scanning electron microscopy (SEM) images for specimens with various relative densities and wire diameters. The distributions showed that specimens with thicker wires (and same relative density as specimens with thinner wires) and lower relative density (with constant wire thickness) specimens had a wider spread of pore sizes. They also studied the mechanical behaviour under uniaxial tensile loading for specimens of varying microstructural properties and found similar results to other researchers, working on compression behaviour, studying the same properties with respect to TMW device behaviour.

He, et al. studied the effects of sintering temperatures on the mechanical properties of titanium TMW manufactured using a sintering process [41]. They found that increasing the sintering temperature increased the elastic modulus (which was calculated from results following 3 point bend tests). However, they also noted that sintering for prolonged periods led to oxidation of the wires, which caused the relative density to increase.

Tan, et al. performed tensile tests to failure of dog-bone shaped TMW devices [42]. They reported that before complete rupture occurred, the tangled wires loosened, and straightened. They reported three stages of the stress-strain curve, relating to these aforementioned physical characteristics of failure.

Liu, et al. carried out impact Charpy testing on TMW devices [43]. They reported that several changes in the TMW microstructure contributed to the energy absorption of the impacts. These included bending, buckling, yielding, and fracture of the wires, in addition to the general densification that occurs when the devices are loaded.

Liu, et al. compared TMW devices made from initially straight and initially coiled wires [44]. The TMW device made from initially straight wires had a higher elastic modulus and yield strength than the device made from initially coiled wires, which produced larger force-displacement hysteresis. They also performed compression tests to failure. For the TMW device made from initially straight wires, they reported that plastic deformation and failure occurred via a combination of translation, rotation, buckling, bending, and joint fracture of the wires. On the other hand, they reported that the device made from initially coiled wires went through bending, interlocking, coil flattening and joint fracture, before failure.

Lui, et al. performed tensile testing to failure of dog-bone shaped TMW devices [45]. They noted four stages of the stress-strain curve, which included an elastic region, yielding of local wires, wire rupture and finally, complete fracture. They noted that specimens with lower relative densities required lower stresses for fracture to occur. Their work, which was supported by scanning electron microscopy (SEM) images, found that the individual wire strands had undergone ductile necking.

Huang, et al. made a few three-dimensional (3D) computer-aided design (CAD) models of cylindrical and washer shaped TMW devices [46]. The microstructure was designed to consist of uniform spiral wires oriented at various angles. They claimed that the models could be used in the future for design optimisation of the devices, but they did not apply the models to any finite element (FE) models.

Safin, et al. obtained noise reduction coefficients (NRCs) for TMW devices [47]. The aim of using TMW was to reduce noise caused by gas turbine engines. The TMW devices were applied as acoustic liners in the intake of the engines. They proposed an empirical mathematical model that could be used to predict the NRCs.

Ma, et al. experimented with an air film damper (AFD) with TMW supports on a rotor [48]. The elastic TMW allowed the AFD to adjust the air film clearance, which adapted to the rotor vibration. They reported that the TMW also contributed with more stiffness and damping to the system.

Ma, et al. studied TMW devices as heat insulators [49]. They studied the heat transfer in the microstructure, noting that conduction occurs in the TMW wires, convection occurs in the air within the confines of the device, and radiation occurs between the wires and the air. They studied heat transfer as functions of wire diameter, helix diameter, and relative density. They found that the thermal conductivity was inversely proportional to wire diameter, and directly proportional to helix diameter and relative density.

Ma, et al. applied magnetic fields to TMW devices in an effort to adapt the microstructure to different conditions [50]. In this study, the experiments were quasi-static in nature, where they applied magnetic fields to the axial loading direction (moulding direction), as well as the transverse direction (non-moulding direction). It was reported that the elastic modulus increased between 2 to 7 times, and the loss factor increased between 20% to 30% in the range of experiments performed.

Ma, et al. looked at shape memory alloy (SMA) TMW in an active vibration control perspective due to its changing properties with amplitude and temperature [51]. They applied the SMA TMW to a rotor support, performing both quasi-static and dynamic testing (up to 500 Hz). As temperature increased, the SMA wires in the microstructure changed phase from martensite to austenite. It was noted that the loss factor dropped from 0.5 at room temperature to 0.2 at 90° following the phase transformation. At the same time, the stiffness was seen to increase. It is interesting to note that the dynamic tests indicated a negative force-displacement slope after the resonant frequency (approximately 450 Hz), indicating negative stiffness. Therefore, they only discussed the results of experiments conducted up to frequencies of 300 Hz. Additionally, their hysteresis curves were quite elliptical, more akin to the response of viscoelastic materials. The author of this thesis believes that the former occurs because the inertial term was not properly accounted for in their results, and hence they should have applied corrections to the measured force. It is possible that the elliptical hysteresis curves were observed either due to the filtering and digital signal processing performed, or was an additional effect of the wrong inertial term being used. Applying a restrictive narrow bandpass filter removes the high frequency content that contribute to the hysteresis curves having sharper, less elliptical shapes.

Ma, et al. added TMW particles of various microstructural properties to the cavities within an auxetic (negative Poisson's ratio) honeycomb structure, essentially acting as a granular fill [52]. They performed quasi-static and sine-sweep (up to 1000 Hz) testing on the structure, without and with the fillers. The frequency response functions showed that the amplitude of vibration at resonance, which occurred at 40 Hz, reduced, and reduced the resonant frequency (due to the added mass of particles). In the quasi-static tests, the addition of the TMW particles affected neither the stiffness, nor the loss factor. This is sensible, since granular fillers only work when enough energy is given to activate them, similar to particle dampers.

Like the work by Ma, et al. (2014), Ma, et al. (2015) also studied SMA TMW as rotor supports [53]. Experiments were conducted on a rotor. Prior to the experiments, a finite element model of the rotor system was designed to obtain the experiment limits. It was found that the critical rotor speed increased from 5000 to 6100 RPM due to the increase in stiffness when the temperature increased from 20° to 90°. The damping reduced once again. They also performed sweep up and sweep down experiments to observe any nonlinearity, but found that the critical speed did not change substantially. The amplitude at the critical speeds reduced by 16% when the SMA TMW support was added.

Ma, et al. followed their previous work, and tested SMA TMW specimens, which exhibited transverse isotropy, nonlinear stiffness, friction damping, and thermodynamic characteristics [54]. They studied the effects of pre-compression, relative density, loading direction, as well as the effects of annealing. It was found that annealing increased the elastic modulus by almost 11 times, since the microstructure changed (the coil diameter decreased significantly).

Tan, et al. studied aluminium matrices reinforced with TMW, essentially making it a metal matrix composite (MMC) [55]. It was found that introducing TMW to the aluminium doubled the yield strength of the structure. They also studied histograms of wire orientations in cross-sectional images, and longitudinal images. It was found that in the cross-sectional images, a TMW specimen with a lower density had a bimodal (two modes) distribution of angular orientation with peaks occurring between 20-30°, and 40-50°, whereas a TMW specimen with a higher relative density had a single mode between 40-50°. In the longitudinal images, the TMW specimen with the lower relative density had a mode between 40-50° and the higher relative density specimen had a peak between 20-30°. The images obtained came from an optical microscope, and interestingly, an office scanner.

Li, et al. also studied MMCs, this time with TMW reinforcing magnesium [56]. They reported that the TMW strengthened the magnesium, and also improved the energy absorption when compared to pure magnesium. In this study, they measured damping over a range of temperatures.

2.3 Analytical and empirical modelling

2.3.1 Physical models

Hong, et al. [12], following initial work by Ao, et al. [29], developed a micromechanical model of TMW devices. This model consisted of spring elements that aimed to replicate the stiffness and loss factors of actual TMW devices. They started off by defining the characteristics of a hysteresis curve. The loading curve $P_1(x)$, for a specimen being loaded to a maximum displacement of A, was calculated as the summation of the elastic force $L(x)$, which was taken as the middle line between the loading and unloading curves, and the friction force $H(x)$. The unloading curve $P_2(x)$ was obtained by subtracting the friction force from the elastic force, i.e.:

$$P_1(x) = L(x) + H(x) \tag{2.1}$$

$$P_2(x) = L(x) - H(x) \tag{2.2}$$

and the average stiffness was calculated as the derivative of the elastic force with respect to displacement.

The definition of loss factor for a single hysteresis curve used by Hong, et. al. was given by:

$$\eta = \frac{\Delta W}{\pi U} \tag{2.3}$$

where,

$$\Delta W = \int_0^A P_1(x)dx - \int_0^A P_2(x)dx \tag{2.4}$$

is the energy dissipation per cycle (area inside one hysteresis loop) and

$$U = \frac{1}{2}\left(\int_0^A P_1(x)dx + \int_0^A P_2(x)dx\right) \tag{2.5}$$

is the potential energy (area under the elastic curve). The loss factor was thus described in terms of the friction force and elastic force i.e.

$$\eta = \frac{2\int_0^A H(x)dx}{\pi\int_0^A L(x)dx} \tag{2.6}$$

In their micromechanical model, they considered three types of arrangements: series, parallel, and no loading, with the stiffness of the spring described by a combination of the three configurations. They considered three types of contacts, namely “open”, “slip”, and “stick”. Since dry friction can only arise during relative motion, it was assumed that the damping only occurred in slip.

To take into account the various material parameters of each microelement into account, Hong, et al. [12] took into account the diameter of each spiral D_L, helical pitch L_J, wire diameter d_s, relative loading angle α, and spiral angle β.

The deformations, and hence stiffness, following application of force, F_z were assumed to be distributed to the axial and radial directions. Formulations for deformation and stiffness were then developed for the three conditions.

The contribution of open, slip and stick was reported to play an important part in determining the dynamic properties of the TMW devices. These contact conditions keep occurring at all times, simultaneously throughout the loading and unloading processes. The combined stiffness of these procedures was reported to be a function of the number of microelements across the layers and heights (N_A and N_L, respectively), the stiffness of each condition, and a contribution ratio ($n_m(x)$, $m = 1, 2, 3$). This ratio (a number between 0 and 1) reportedly defined the proportionality of each contact condition that existed and unfortunately, these were not been fully understood and applied. Note that superscripts (1), (2) and (3) denote the open, slip and stick conditions, respectively, while k_L and k_U denote the loading and unloading stiffness in each case.

The equations for loading and unloading stiffness were given by:

$$K_L(x) = \frac{N_A}{N_L} k_L^{(m)} n_m(x) = \frac{N_A}{N_L} (k_L^{(1)} n_1(x) + k_L^{(2)} n_2(x) + k_L^{(3)} n_3(x)) \tag{2.7}$$

$$K_U(x) = \frac{N_A}{N_L} k_U^{(m)} n_m(x) = \frac{N_A}{N_L} (k_U^{(1)} n_1(x) + k_U^{(2)} n_2(x) + k_U^{(3)} n_3(x)) \tag{2.8}$$

The loss factor was then calculated by:

$$\eta = \frac{\Delta W}{\pi U} = \frac{2(\int\int K_L(x)dx^2 - \int\int K_U(x)dx^2)}{\pi(\int\int K_L(x)dx^2 + \int\int K_U(x)dx^2)} \tag{2.9}$$

Therefore,

$$\eta = \frac{2(k_L^{(2)} - k_U^{(2)}) \int\int n_2(x)dx^2}{\pi\left(\int\int (2k_L^{(1)} n_1(x) + (k_L^{(2)} + k_U^{(2)}) n_2(x) + 2k_L^{(3)} n_3(x) dx^2)\right)} \tag{2.10}$$

Finally, the maximum number of microelements were calculated using the following equation [12]:

$$N_{max} = \frac{L_N \cos(\beta)}{\pi D_L} = \frac{4\rho_{TMW} V_{TMW} \cos(\beta)}{\rho_S \pi^2 d_s^2 D_L} \tag{2.11}$$

Several parameters affect the performance of TMW devices. This prompted Hong, et al. [12] to investigate the effects of parameters such as relative density and wire diameter on the stiffness and loss factor. Results seemed to agree with the theory it was based on. However, they did not publish results comparing experimental findings to the output of the model to determine how effective the model was. The advantage of this model was that it contained physical parameters from the design stage that affected the response. The spring-like nature of the actual TMW devices was also represented.

Hong, et al., (2012) [10] performed a study on a variant of the standard TMW devices, TMW particles (TMWP). Their work considered experimental investigations and attempted to replicate the dynamic properties of the TMWP, namely stiffness and loss factor, in the model, which was a modification of the model proposed by Hong, et al. (2011) [12]. Although these models were very similar, there were some key differences that were based on some broad assumptions, including that two-thirds of the microelements were distributed on the layers and that the remaining were distributed in the axial direction. Based on this, they found the minimum number of elements on each layer, and the maximum number of elements on the axial direction. These values were used to obtain the minimum and maximum densities of microelements in the device.

It was also assumed that before loading, the density was low and that the microelements became engaged (converted) to slipping and sticking phases consecutively through the layers, and that the contributions changed linearly with load. All layers were considered active when the total deformation reached the assumed initial gap between microelements. When loading, sticking was assumed only to occur once all gaps were eliminated, when the density was between the calculated maximum and minimum densities. When unloading, sticking and slipping contacts converted to open contacts midway between the maximum and minimum deflections of one cycle.

With these assumptions in mind, the stiffness in loading and unloading were calculated with the same expression obtained by Hong, et al. (2011) [12], with an additional factor of γ, which is given by:

$$\gamma = \frac{\rho_{TMW}^{3}\rho_{max,TMW}}{\rho_{min,TMW}^{4}} \tag{2.12}$$

No derivation was given on how Equation 2.12 was obtained and no justification was given as to why this term should be used in the expression.

This model was coupled with some experimental quasi-static work that was used to validate the model. The model was able to represent the stiffness of the specimens, of a number of relative densities, relatively well, but the loss factors were constantly underestimated by almost 20%. This clearly had something to do with some of the assumptions made.

Ma, et al. proposed a constitutive model [54], which was an extension of the model proposed by Hong, et al. (2011) [12], and (2012) [10]. This model modified the friction coefficients and contact state within the microstructure. Rendered 3D models produced from micro-computed tomography scans were used to qualitatively explain the microstructural state.

2.3.2 Data fitting models

Empirical data fitting for Jersey Stitch TMW devices

In order to quantify stiffness and damping for various test parameters, Choudhry [39] (testing discussed in Section 2.2.3) developed a relationship that expressed the coefficients of stiffness and damping as a combination of the functions of height of the specimen, radial thickness, axial compression, radial interference (compression in the radial direction), and displacement amplitude. He added further empirical expressions to the relationship that were derived by Al-Khateeb [21] to account for the effects of frequency. He then made an effort to make the functions of the test parameters dimensionless so that it can be fit to more general applications. The percentage error between the measured and calculated stiffness was pretty low (below 5%) varying between over and underestimation, whereas the maximum error in damping was a 10.6% underestimation.

Jones [11] employed a modified relationship of that developed by Choudhry [39] to create a “design workbook” that would calculate the damping and stiffness coefficients of the TMW devices. Since this method is quite empirical, it would require tests to be conducted on sample TMW devices to obtain the complete set of constants required to define the damping and stiffness coefficients. Unfortunately, no quantification was given on the accuracy of this model prediction workbook.

Black-box model of TMW device behaviour

Zhang, et al. [13] created a 'black-box' procedure to pick out several coefficients to characterise the dynamic response of the specimens. They delivered a semi-constitutive model that included various properties of the TMW devices, including the nonlinear damping (viscous damper), elastic stiffness (elastic spring), and bi-linear hysteretic damping (hysteretic Coulomb damper) parallel to each other. The parameters of the hysteretic Coulomb damper were approximated by the Chebyshev polynomials of degree 1. It has to be noted that the hysteretic Coulomb damper is reliant on the current deformation, and also the history of loading, due to its memory characteristics.

Chebyshev polynomials of the first kind are solutions to the Chebyshev differential equation. They are a series of orthogonal polynomials (sequential polynomials that have an inner product value of 0), and are known to give high accuracy approximations of the nonlinear characteristics of the hysteresis curves [57]. After obtaining the first approximation of this model, noise effects were taken into account to give a more generalised model, using a NARMAX (Nonlinear Auto Regressive Moving Average with eXogenous input) model. Details of the NARMAX model can be found in Chen and Billings' work [58]. Zhang, et al. [13] utilised the Orthogonal Least Square (OLS) algorithm, in combination with the Adjustable Prediction Error Sum of Squares (APRESS) criterion to characterise the model parameters of the TMW devices. The OLS algorithm makes associated terms orthogonal to each other, maximises the error reduction ratio and therefore selects only the most relevant terms in a forward stepwise manner. APRESS was used as an aid to find the optimal number of parameters to be used. OLS' inherent orthogonal property allowed the noise and dynamic model terms to be decoupled, reducing computational effort. These results were backed up by nonlinear validity tests. An additional benefit is that the parameters can be related to the sensitivity of real data.

Another example of the implementation of the Chebyshev polynomials was when Ulanov and Lazutkin [57] obtained the middle line of the hysteresis curve and the friction force, $L(x)$ and $H(x)$ respectively of a DKU vibration isolator using the Chebyshev polynomials of the third kind. Their work was based on the Masing Principle, which involves duplication, translation and rotation of the force-displacement loading curve to define the loading process. This principle is applicable to spring and constant friction elements, which are a feature in TMW devices. In the implementation of their work, they eliminated the non-zero stiffness term by subtracting the loading curve by the middle line. This was followed by the friction displacement dependency by dividing the new coordinate by the friction force this coordinate system contains a constant friction element with a unit friction force. The final transformation was a similarity transformation in the displacement axis. These transformations were used for every loading and unloading process. The end result was that coefficients that characterised the hysteresis curve were formed for different displacement axes i.e. axes where the test specimens are loaded. In their work 25 non-zero coefficients of load, friction and constant coefficients were required, with 8 describing the primary loading process to give an error of less than 3% between experiment and calculations [57].

2.3.3 Discussion

From the literature studied so far, only the models by Hong, et al. (2011) [12], Hong, et al. (2012) [10], and Ma, et al. [54] have been physically driven. The fact that the model has attempted to take the microstructure of the material is very useful in terms of quantifying their effects on a macroscopic scale. The model also takes the interfacial interaction into account, by including Coulomb friction terms, in the 'slip' contact condition. However, some of the assumptions, such as the contribution of each contact condition, and the fact that the 'stick' condition appears only after all the 'open' microstructure conditions have been transformed to the 'slip' condition, are very broad and unjustified. This is reflected on the results of loss factor being underestimated. To get a more justified model, statistical tools need to be employed to capture the random nature of TMW devices: not only the contribution of all the different types of contacts, and angular orientations, but also the variations between different specimens. It should be appreciated that in the work by Ma, et al. [54], advances were made to take the statistical variations in angular orientations of the wire coils into account, and these variations were included in the model they proposed.

Even though the models produced by Choudhry [39] and Jones [11] may have been good at estimating the coefficients of damping and stiffness, it must be noted that the model is produced via a means of data fitting. This implies that TMW devices having different properties to those studied by them cannot be modelled using these relationships. It is also essential for the test conditions to be similar to the experiments they performed. However, in reality, the environmental conditions may vary significantly, especially in applications such as engines.

Finally, the ‘black-box’ model proposed by Zhang, et al. [13] also fits into the category of data fitting. What makes this data fitting model more appealing than those proposed by Choudhry and Jones, is that it is semi-constitutive in nature, allows for noise reduction from data, can be applied to different types of dampers (due to the algorithm employed) and can assess the sensitivity of the dampers to real test data. The drawback is that the model is reactive, rather than proactive, for analysis purposes i.e. the parameters are obtained only after experimental data is obtained.

One of the main objectives of this project is to deliver a more representative, physically inspired model, rather than a simple data fitting model, and so focus will be concentrated on pursuing a constitutive, microstructure model that will link the microstructure of the specimens to the bulk material properties observed experimentally.

2.4 Other related work

2.4.1 Wire rope isolators

Another friction based damping device, the wire rope isolator (WRI), was studied by Tinker and Cutchins [59]. WRIs provide inherent frictional damping when individual cables of the helical isolator move relative to each other. In their work, they focused on creating a semi-empirical model to capture the stiffness, hysteresis, frequency response, and the phase-plane trajectories, observed in experimental studies. A model with only Coulomb friction or classical viscous damping was ineffective to model the experimentally observed hysteresis curves. Viscous damping models produce elliptical hysteresis curves, and Coulomb friction hysteresis curves have flattened ends, whereas the experimental hysteresis curves actually have pointed ends. Therefore, they carried out simulations based on the n^{th}-power velocity damping proposed by Dahl and Rice [60] which was created for viscoelastic materials.

$$m\ddot{z} + k[(z-u) \pm \varepsilon^2 (z-u)^3] + c_n|(\dot{z}-\dot{u})^n| \operatorname{sgn}(\dot{z}-\dot{u}) = 0 \tag{2.13}$$

where z is the displacement of the centre mass of the isolator, u is the displacement of the frame, ε is a nonlinearity parameter and m, k and c_n are the mass, stiffness and n^{th}-power damping coefficients respectively. Dahl and Rice [60] reported that $n = 0$ results in Coulomb friction, and $n = 1$, results in viscous damping. For values of n greater than two results in hysteresis curves with pointed/sharp ends.

The n^{th}-power velocity damping method provided results that matched the experimental results well, but it was lacking the Coulomb friction phenomena. This prompted the inclusion of a Coulomb friction term into the equation of motion.

$$m\ddot{z} + k[(z-u) \pm \varepsilon^2 (z-u)^3] + c_n|(\dot{z}-\dot{u})^n| \operatorname{sgn}(\dot{z}-\dot{u}) + f \operatorname{sgn}(\dot{z}-\dot{u}) = 0 \tag{2.14}$$

where f is the Coulomb friction force.

However, comparison with experimental hysteresis curves suggested that the model had a worse fit than the n^{th}-power velocity damping model. In an effort to conserve the Coulomb friction term in the model, some additional terms were added to the Coulomb friction term that took into account the changes in frictional forces on the cables with changes in relative displacement. Additionally, with this model, rather than using the static stiffness, the dynamic stiffness was used (by taking the average of the loading and unloading phases).

$$m\ddot{z} + r(k[(z-u) \pm \varepsilon^2 (z-u)^3] + b) + (c_n|(\dot{z}-\dot{u})^n| + f[1 - a(z-u)^2]) \operatorname{sgn}(\dot{z}-\dot{u}) = 0 \tag{2.15}$$

where r is a multiplier used due to the approximation of the dynamic stiffness, a is a variable that is altered to give better correlation with experiment, and b is the distance that each curve lies above the origin at zero relative displacement.

The results, when compared to experimental results, seemed to capture the hysteresis, and other characteristics of the isolator quite effectively. The hysteresis curves shapes, in particular, also agreed to other frictional damping experimental findings reported by Kerley [61], and Pivovarov and Vinogradov [62], and pointed out that majority of the damping did indeed arise due to friction in such isolators. The drawbacks were that at certain frequencies, the semi-empirical model produced low stiffness at the extreme negative displacement, while slightly too high at extreme positive displacement. This was reportedly due to the stiffness approximation used in the model. Also at lower frequencies, the damping was overestimated, but altering the effective mass in the equation of motion allowed a better correlation.

A numerical method was reported by Tinker [6] to compute these models analytically and obtain any coefficients and constants that were present in the model. It was found that the n^{th}-power damping mechanism provided a stabilising effect to the Coulomb friction model, as a model with dominant Coulomb friction would result in large response behaviour. By using the numerical method, which allowed active modification of the parameters, Tinker was able to identify the parameters that had this effect on the model.

2.4.2 Investigations on nonlinearity posed by fibrous materials

Shin [63] performed an investigation on the static and dynamic properties of fibrous materials. His experimental work considered macro-scale models, consisting of idealised elements e.g. steel rods stacked on layers. The macroscopic models were intended to resemble the microscopic behaviour of fibrous media. In doing so, he studied the nonlinear behaviour produced by these macroscopic models. Hertzian contacts are a well known source of nonlinearity because as force varies, the area of an elastic contact between two elements changes, causing a nonlinear force-displacement relationship [64]. Shin [63] found that the nonlinearity imposed by the Hertzian contacts had a very negligible contribution to the overall nonlinearity of the system, and that nonlinearity due to the increase in contacts and bending mechanism were the main culprits to the phenomenon.

Baudequin, et al. [65] performed an analysis on the elastic nonlinear phenomenon in fibrous material. The creation of new contacts, and therefore increase in contacts with increasing compression was thought to be the main source of nonlinearity. The only length scale that was considered was the length of the fibre, with the diameter of the fibres assumed to be constant, and elongation and compression of fibres assumed to be negligible. It was also assumed that slip, friction and damage were non-existent. Therefore, bending of the wires was the only physical effect of the compression force, along with creation of new contacts. The length of the fibre between contacts was considered to have a statistical distribution, and a probability of a certain length of fibre to come into contact with another fibre with a small increment of stress was also factored into the analysis. It was found that the most significant factor on the elastic behaviour of the fibres was the inverse cubic dependence of the transfer stiffness on the length of fibres between contacts. They used a scale transformation to derive a power-law relation between the length scale and compression stress (and thus, strain). Experimental results validated the power-law dependence in the high strain region. In the low strain region, it was noted that the elastic behaviour was governed by the mean distance between the chemically bonded fibre connections, rather than the power-law relation.

When considering a three dimensional contact model, with three contacts, Shin [63] noted that there was a discrepancy in the force-displacement curves of the model when the second contact occurred. This was attributed to possible sliding between the elements in the model. This feature was added to the model using a ‘sliding factor’. A number of sliding factors were tested, and it was found that the sliding factor found to fit the model was similar to the coefficient of friction, although he noted that they were not necessarily the same. To model the nonlinearity, it is necessary to know several terms beforehand, e.g. gap between contacts, location of new gaps, or else the sets of nonlinear equations would be statically indeterminate.

Shin [63] studied the relationship between contacts and electrical resistance, starting with a single contact, followed by a network of four contacts. He noted that because the material was susceptible to oxidation, and the possibility of asperities present made it difficult for the theoretical model to agree with experimental work. The use of a terminal resistance, which takes into account of such issues, allowed closer agreement. The general trend was that as the strain increases, the resistance decreases, with a decreasing rate. However, Shin noted that the network of fibres in real materials, or in our case, TMW devices, may be too complicated for such theoretical models to be applied to it [63].

Shin [63] studied different bending models in relation to the fibrous materials. For the linear model, he assumed an idealised structure of symmetrically stacked cylindrical rod elements, and also assumed that the elements were subjected to pure bending. Elastic work was assumed to arise because of the bending moment between the links. Using this relationship, Castigliano's second theorem, and a few other parameters, such as number of layers, and total deflection of the structure, a stress-strain relationship was derived. A simple non-linear bending model was then obtained from the linear model, by including the strain-dependent change in solid fraction of fibres, which are isotropic in the x and y directions. It must be noted that due to the symmetry condition, the rods were not allowed to rotate at the ends, making them essentially clamped, although in reality, the ends were simply supported. Deviations from the simply supported model, in the presence of external forces, were expressed as additional moments. This “modified nonlinear bending model” (MNBN), along with the simple non-linear model, and a power-law model were compared to experimental findings on some fibrous materials. For fibrous materials, the MNBN was found to produce accurate stress-strain behaviour. The simple nonlinear model was found to be accurate only for lower strains, whereas for higher strains, the results from the model and the experimental data tended to diverge. The power-law model studied was only accurate at higher strains.

While studying the dynamic behaviour of fibrous materials, Shin [63] found that the dynamic modulus may approach the static modulus of elasticity at higher excitation. It was also found that the main mechanism causing nonlinearity in the dynamic modulus was that the number of contacts was changing, similar to the nonlinearity encountered in the static case. This was noted because when testing the idealised, transversely isotropic model, dynamic behaviour was found to be almost independent on the type or level of excitation.

2.5 Conclusions

Following the study of literature, the following statements summarise the current state of the art:

- There have been numerous studies of quasi-static and low frequency compression behaviour. Researchers have particularly looked at comparisons between TMW devices of varying microstructural properties. Additionally, there are many theories proposed by various researchers as to why TMW devices behave as they do.

- TMW device behaviour at high frequencies (greater than 10 Hz) has received little attention.
- The microstructure of TMW devices is complex, and its understanding has been quite limited. Thus far, the microstructure has been studied qualitatively, rather than quantitatively. Understanding the microstructure is particularly important in deriving a representative physical model.
- There are a few models found in literature. Many models that can be considered as "black-box" exist, where researchers use polynomials to define the loading and unloading curves. There are a few physically inspired models, but in general, they can be very complicated, and would hence find limited use.

Therefore, the aims and objectives can be reiterated. This thesis aims to:

i Develop methods to study the microstructure.

ii Study and explain quasi-static and low frequency behaviour objectively.

iii Study and explain high frequency behaviour objectively.

iv Study and develop more representative, physically inspired analytical models that explain the observed hysteretic behaviour.

Chapter 3

Microcomputed Tomography and Use of Image Processing

3.1 Introduction

While the wires used in the manufacture of tangled metal wire (TMW) devices are initially spiral in nature, the process of weaving and the influence of contacts on the microstructure of the device, as a whole, means that the microstructure will not contain purely spiral wires, but instead contain combinations of spiral and straight wires. Analytical models proposed in the past [10], [12] have fallen short in characterising mechanical properties because the basic assumption is that the microstructure can be simplified into a set of linear springs, directly related to the flexible nature of the wires, at different angles, relating to the general orientation of the spiral wires.

In reality, the microstructure of these devices, and of other variants that consist of tangled, fibrous materials, are extremely complicated. Depending on the type of device, the microstructure consists of several contact points. In between these contacts, wires are present in a variety of configurations. The connecting wires between contact points may be simply uniform and straight, wavy, or spiral, to name a few examples. Within these different connection configurations, there are other parameters that vary, including length and orientation. As a result, the microstructure contains regions with varying mechanical properties, such as stiffness and damping. The wires in a stiffer region are less likely to deform, and so the contacts within the region are more likely to slip than contacts in a more flexible region for a given loading. This influences the amount of friction, and hence damping present in the system.

There are benefits in understanding how the microstructure deforms before progressing towards studying the dynamic behaviour, or proposing any analytical model. The approach finally selected for investigating the microstructure of TMW was defined following consideration of several alternatives. These are discussed briefly below.

- The first method involved using a microscope to analyse the devices. This was rejected because the study would only cover the outer layers, whereas wires turn back towards the interior of the device, and are primarily spiral in nature.
- To view the microstructure beneath the surface, one approach considered was to cut the device into thin slices. Impregnating the device with low viscosity epoxy resin before slicing was thought to be a suitable way to maintain the wire positions. However, this is a destructive technique, and the information that could be gathered is limited to the number of slices used, and the information in between the slices is neglected in the analysis.
- A more comprehensive approach would require information from many slices, without damaging the device under study. This led to the final iteration of the analysis options: microcomputed tomography (μ-CT).

Figure 3.1 shows an example of a TMW device considered in this research.

Figure 3.1: Tangled metal wire device

The specimens used in this thesis were made from Grade 304 stainless steel spiral wires that have a nominal wire diameter of 0.15 mm. The spiral wires were first drawn out using wire-drawing. They were then woven to form an amorphous body, and compressed in a mould at high pressures to produce the final washer shaped device, as shown in Figure 3.1. It should also be noted here that due to the discontinuity present in the hollow section of the specimens, the microstructure is more complicated than bulk TMW devices that have been studied by other researchers. In bulk TMW devices, the wires microstructure are distributed in a more uniform manner, whereas the discontinuity at the centre disrupts the microstructural state. This makes the response behaviour of the devices studied in this thesis both different, and unique.

This chapter contains an introduction to the concept of μ-CT, which was extensively used to gain an understanding of the TMW device microstructure. An in-depth description is given for the image processing algorithm that was developed to identify the “skeleton” structure of TMW. This is complemented by an introduction to image processing, with attention given to the algorithms and functions used in this work for purposes of microstructural analysis.

The chapter also discusses the experimental work carried out in parallel to the image processing work reported. The experimental work consisted of using a bespoke test rig that allowed TMW devices to be maintained at a compressed state in a μ-CT scanner while scan data were being acquired. In doing so, this enabled the study of how the microstructure evolved when TMW devices were loaded and unloaded.

Figure 3.2 gives an overview, in the form of a data flow diagram, of the processes involved to achieve the final goal of identifying the state of the microstructure of TMW devices such as that seen in Figure 3.1. This can be referred to during the later stages of the chapter and it will help ease the reader into the complexities this chapter contains.

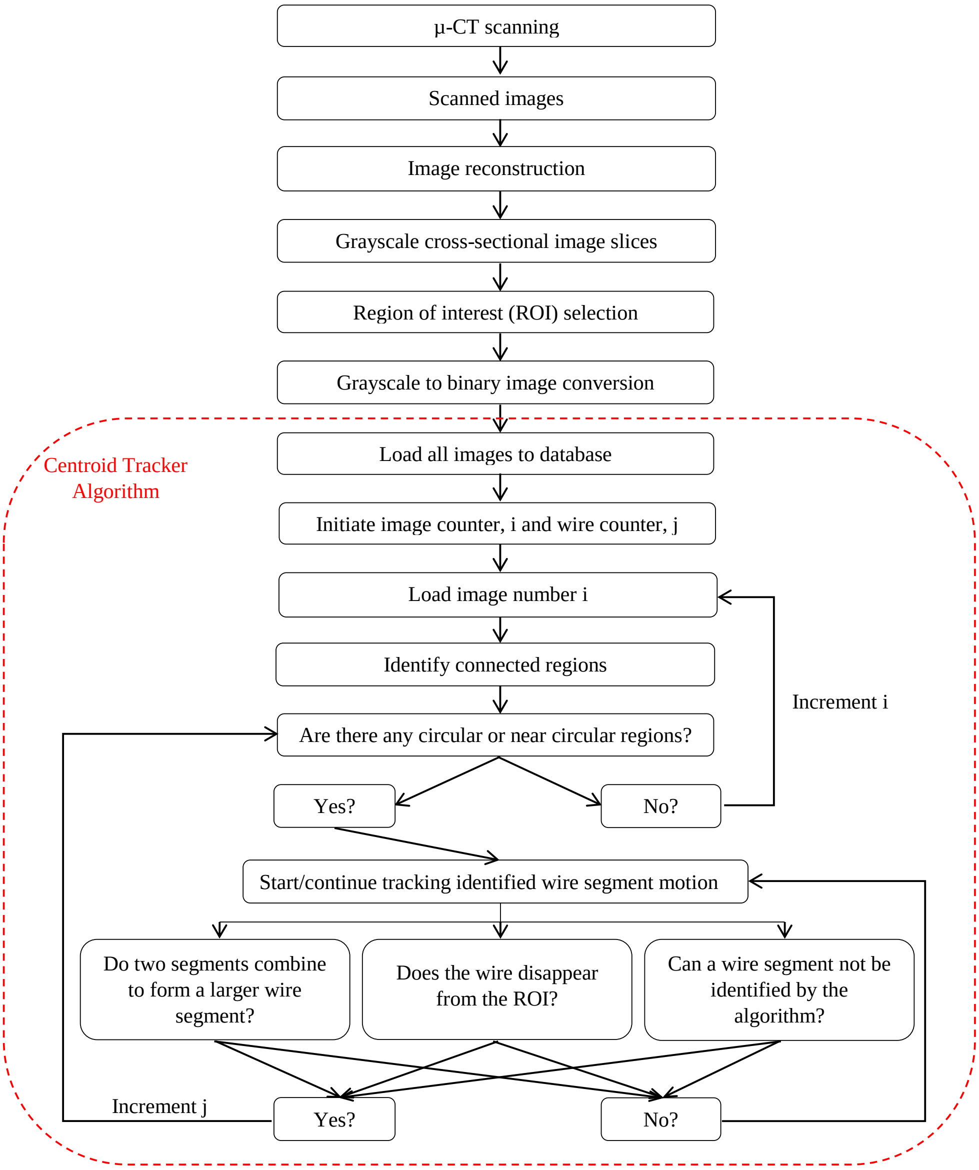

Figure 3.2: Data flow diagram for identifying the state of the microstructure

3.2 Microcomputed tomography

Advances in computing capabilities over the past two decades have resulted in the improvement of microcomputed tomography (μ-CT) to the extent that it is now a viable approach for analysing materials with complicated internal geometries. X-rays are projected onto a specimen that is located at the centre of a scanner. On the opposite side of the X-ray source is an X-ray detector that measures the changes in the intensity of the rays from the source after they pass through a material. This change is brought about by some of the X-rays being absorbed by the material under test. The measured X-ray intensity, I, is related exponentially to the distance that the X-ray travels, x, according to,

$$I = I_0 \exp(-\mu x) \tag{3.1}$$

where I_0 is the initial X-ray intensity at the source, and μ is the linear attenuation coefficient of the material under test [66]. The attenuation coefficient is a measure of the ability of a material to absorb the rays from the source. A higher attenuation coefficient means that a material retards more X-rays, resulting in better contrast between the material and its surroundings, typically air, in the images being captured by the detector. The attenuation arises due to a combination of the Compton and photoelectric effects.

When X-ray photons go through a medium, they interact with the outermost electrons present in its atoms. This causes the photons to scatter in an inelastic fashion, which decreases their energy. This effect is known as the Compton Effect [67], named after Arthur Holly Compton, who discovered this scattering. On the other hand, in the case of the photoelectric effect, low energy photons from the X-ray source dislodge an electron from the shell of an atom. The discharged electron is called a photoelectron. The photons get absorbed by the material, which as a result emits an electron [68] (the electromagnetic energy is converted to internal thermal energy of the material), and hence leads to a difference in intensities between source and detector.

If a material absorbs the X-rays completely, the detector is not able to capture any signal. Large or dense materials therefore require a high energy of X-rays from the source, which drives up power consumption. For this reason, TMW devices were specially crafted to allow enough X-rays generated within the available scanner to penetrate through the device medium. These devices were washer-shaped, with a nominal outer diameter of 18 mm and an inner diameter of 8 mm. The height of the specimens were approximately 5.8 mm. The complete specifications of the devices are detailed in Tables 3.9 to 3.12. These dimensions were chosen after running preliminary scans on other TMW specimens, and drawing conclusions from the quality of images produced.

The μ-CT scans were performed on a Skyscanner 1172 model at the Mellanby Centre for Bone Research in the Medical School at the University of Sheffield. In CT scanning, a specimen is placed at the centre of the scanner on a rotating support, with an X-ray source on one end of the scanner, and an X-ray detector on the opposite end. While the specimen is being rotated at small incremental angles, several projection images are captured by the detector. At each increment, several images are captured, which are used to mitigate noise via averaging. If the specimen is symmetric, the specimen only needs to be rotated 180° to gather all the information required for image reconstruction. The scanner uses the cone-beam CT approach, rather than the traditional fan-beam CT approach. In cone-beam CT, as the name suggests, a cone beam is projected through the specimen (both in the axial, and circumferential directions) onto the detector, while in fan-beam CT several projections are made along the axial direction of the specimen. Cone-beam CT allows faster data acquisition since more information is captured per projection. While the speed of data acquisition for scanners using cone beams is higher, there is one fundamental drawback. Since each image obtained from cone-beam CT is made up from a composite of several projections, the images captured have reduced contrast and clarity, and can be tarnished with noise, especially while scanning large or dense objects. Averaging is the most popular way of filtering these effects. In both methods, image reconstruction is a separate task.

Image reconstruction is a computer intensive process. During this process, there are several adjustable parameters that a user can input. Each of these adjustments come with a trade-off. For example, if one wants images to be constructed with low noise, one can adjust the standard deviation variable of a Gaussian filter, with the cost of sacrificing spatial resolution (or image sharpness). The process of image reconstruction is out of scope for this project, but further information can be obtained in the review performed by Pan, et al. [69].

The image reconstruction process yields stacks of cross-sectional 8-bit grayscale images (slices) of the specimen. These are often a combination of top, and side views of the specimen that has been scanned. The majority of image processing tools, which will be discussed extensively in the following section, generally use binary images to perform their respective tasks. The grayscale images are therefore converted into binary images using thresholding techniques. The grayscale images are essentially matrices of numbers ranging from 0 to 255. Thresholding techniques convert numbers below or equal a calculated threshold to a binary value of 0, and the numbers greater than the threshold to a binary value of 1. Otsu's method was the chosen technique for calculating the threshold due to its availability in the MATLAB Image Processing Toolbox [70], and its simplistic implementation. However there are other histogram methods available that perform the same task but would yield slightly different results. These include the minimum error thresholding, [71] and iterative histogram thresholding method [72], among many others [73], [74].

Otsu's method assumes that the image intensities possess bi-modal histograms, referring to the back and fore grounds. An optimal threshold that minimises the variation for each mode of the histogram is then derived. Once all the grayscale images are converted to binary images, they are ready to be processed using image processing tools.

The MATLAB Image Processing Toolbox was chosen because it contained convenient functions that catered for a broad set of requirements, ranging from simple image visualisation to more complex image registration [70]. Most importantly, it allowed algorithm development.

3.3 *centroidTracker* algorithm

This algorithm works on the principle that out-of-plane wires possess either a circular, or elliptical shape, whose minor axis is the wire diameter - which is assumed to be a constant value. The algorithm attempts to identify centroid locations for each set of out-of-plane wires, and groups them together. Special rules and techniques are developed for conditions where wires in contact create agglomerations rather than discrete circles/ellipses. This is performed because standard image processing tools cannot segment objects that are in contact. It should be noted that any text in *italics* is either a MATLAB function (both pre-defined, and developed for this work), or a control flow statement (i.e. *for*, *if*, and *while* statements).

centroidTracker is the main algorithm that encompasses all the functions involved with tracking the centroid locations of the wires in the images (this is indicated in the red section of Figure 3.2). The details of individual functions will be discussed in Section 3.4.

centroidTracker starts by loading all the binary images from the scans. A variable for the wire counter (j on Figure 3.2, which keeps track of the number of wires identified by the algorithm) is initiated, along with constants for the spacing between images (which is used to develop the three-dimensional geometry of the scanned TMW devices), and horizontal and vertical sizes of the images.

A nested outer *for* loop then goes through each image till the end of the image stack (using image counter, i on Figure 3.2), and properties of the objects (e.g. centroid locations, orientation, etc.) in each image are calculated using *regionprops*. The nested inner *for* loop goes through the number of regions recorded by *regionprops*. If one object, or wire segment, resembles an out-of-plane wire, i.e. a near-circular, elliptical object, with a minor axis length within the range of the characteristic radius of the wires, it is considered for further investigation.

The wire counter variable is incremented by one. A set of Boolean indicator variables are also initiated with a 'false' value. The algorithm loops through the objects and images until a defined condition is met. The Boolean indicators are used to keep track of the condition that caused the algorithm to stop performing its tasks. The properties of the object are then stored in a structured array. These include the three-dimensional centroid coordinates on the images, both in pixels and in standard units, the major and minor axis lengths, the orientation and the area of the wire segment. The details of the image dimensions, the wire segment centroid locations and orientation, and a pre-specified major and minor axis lengths are then fed into the *drawEllipse* function to create an ellipse. The pixel list output by *drawEllipse* is used to convert corresponding foreground pixels to the background (i.e. change the pixels from white to black). Since the major and minor axes are pre-specified, only a small segment of the entire wire segment is eradicated from the image, rather than the whole wire segment. This is performed to indicate that the wire segment has already been processed, and so it will not be identified again as the algorithm goes through the images (there is a condition in the algorithm that any identified object should not be hollow). An additional benefit of substantially hollowing out a wire object is that the wire object can be easily removed from an image through some manipulation ("opening" an image, which will be discussed shortly). If not enough of the wire is hollowed out, the "opening" of the image will leave a residue of the wire object, which can complicate wire identification later in the algorithm. An example of a marked image is shown in Figure 3.3, where a wire object on the top left corner has been identified and marked.

Figure 3.3: Wire object on the top left corner of image has been marked to indicate that it has been identified

This image is then ‘opened’, and a new variable is created for this opened image. Opening is a process of eroding an image, followed by dilating it. It allows objects with a hollow centre to disappear completely from the image. Removal of an object through the ‘opening’ process is more preferable and beneficial than removing an object of fixed size since there is always some uncertainty in the actual size of a wire object, especially when wire objects agglomerate to form one image object, which could lead to chunks of other wire objects being removed).

The algorithm separately subtracts the current, opened image from both the preceding image and following image. Subtracting two successive images checks the differences between them, and allows the identification of wire segments that have evolved between them. By ‘opening’ the processed image, eradicating the identified wire segment, and using this image in the subtraction process, the evolution in the wire segments is even more pronounced, especially when considering the current wire being tracked. The closest large object (to the identified wire object in the current image) in the subtracted image will only consist of the wire segment under investigation, and will mostly contain residual boundary traces of other wire segments that have moved. Figure 3.4 (a) shows an object where an object has been identified and marked, (b) shows the same image after it has been ‘opened’, (c) shows the next image, and (d) shows the result of the image subtraction.

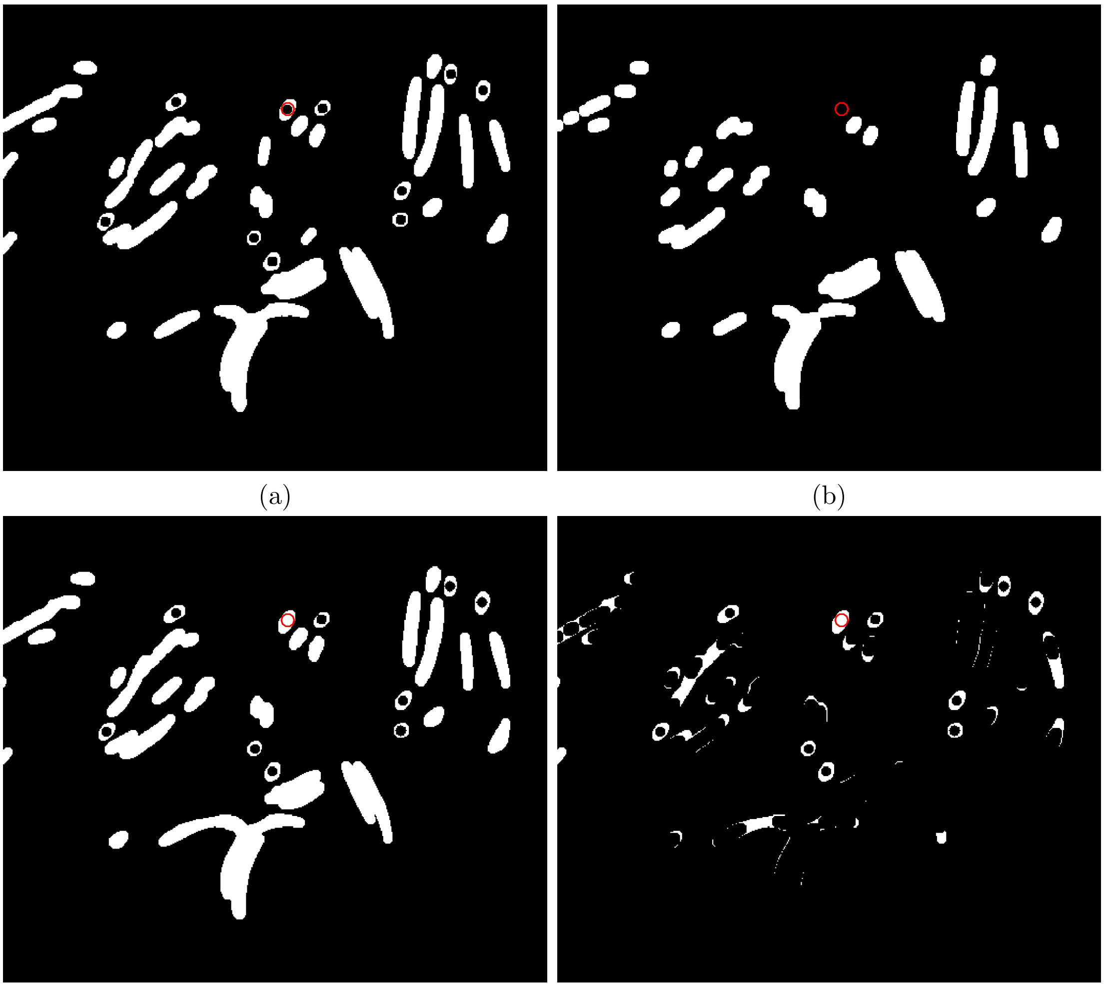

(a) (b) (c) (d)

Figure 3.4: (a) Identified and marked wire segment, (b) image (a) 'opened', (c) succeeding image where the wire segment belonging to the identified wire in image (a) is present, and (d) image subtraction carried out between images (c) and (b)

While it may not seem obvious as to why image subtraction is performed for the example in Figure 3.4, the process is useful when the wire segment of interest in the following/preceding image is in contact with another wire segment. This allows segmentation (i.e. separating and identifying a wire object from an agglomeration of other wire objects), and wire centroid identification to continue to the next stages.

The loop that goes through the objects in the image is exited if either of the following cases is true:

- The Euclidean distance between centroid locations of the new wire segment and that of the saved wire segment (i.e. from a previously processed adjacent image) is greater than a specified tolerance: This deals with situations where a wire segment disappears from the images, occurring especially at the image edges.

- The area of the new wire segment is greater than 1.5 times the area of the saved wire segment: This can occur when the identified object represents either the top or bottom end of an in-plane wire. It can also occur when an out-of-plane wire turns in-plane, where a relatively small elliptical shape combines with another to form a large elliptical shape (see Figure 3.5). When either of these cases are met, there is a large change in area between wire segments in successive wires.

(a) (b)

Figure 3.5: Two out-of-plane wires combine to form a large elliptical wire (in-plane wire): (a) two out-of-plane wires (marked by Xs), and (b) out-of-plane wires merge and wire turns in-plane

If either of these occur at the start of the wire detection (i.e. the wire identified only spans for a few images), the data stored in the structured array for that particular wire is deleted from the data set, and the identified wire segment that was removed from the image foreground is reapplied to it. The algorithm then identifies another object on the same image that resembles an out-of-plane wire segment (i.e. on Figure 3.2, wire counter, j is incremented by one, and the algorithm continues). If there are no more to be found, the next image is loaded, and the process continues in the same fashion (i.e. on Figure 3.2, i is incremented by one, and the algorithm continues).

If the algorithm continues running without exiting, the next step is to loop through the image dataset backwards and identify objects that belong to the same cluster of wire segments in the preceding images. This is performed because there are wire segments present in the preceding images that could not initiate the tracking algorithm because they did not meet the requirements for the algorithm to commence. Once no more wire segments are found in the preceding images, the algorithm goes back to the image where the first wire segment was identified, and performs the same procedure *while* looping forward through the images.

The process of identifying objects in either preceding or subsequent images is performed using two separate *while* loops. Apart from the fact that these loops are either moving backward or forward through the images, the only difference between the two is the way the identified wire segment data is logged into the structured arrays. While the backward moving loop is running, the previously stored data needs to be shifted by one cell to accommodate data coming in from the newly identified wire segments, whereas in the forward moving loop, new data can simply be appended to the array. Stored data will hence be well organised. This is clarified in Figure 3.6. In Figure 3.6 (a), the algorithm is looping backwards from "Image 431", where a wire segment was first identified (highlighted in red to indicate the start of wire identification), through "Images 430-425" (highlighted in green to indicate data has been recorded) to "Image 424" (highlighted in gray to indicate data has not been recorded yet). When data needs to be recorded from "Image 424", the cells of the previously recorded data need to be shifted to the right by one cell, to allow the data in "Image 424" to be added to the array. This process is straightforward in Figure 3.6 (b), which corresponds to the same wire seen in Figure 3.6 (a), since incoming data from "Image 438" is simply appended to the array. Note that in this illustration, just as it is in the algorithm, the backward *while* loop always occurs first, before the forward *while* loop occurs.

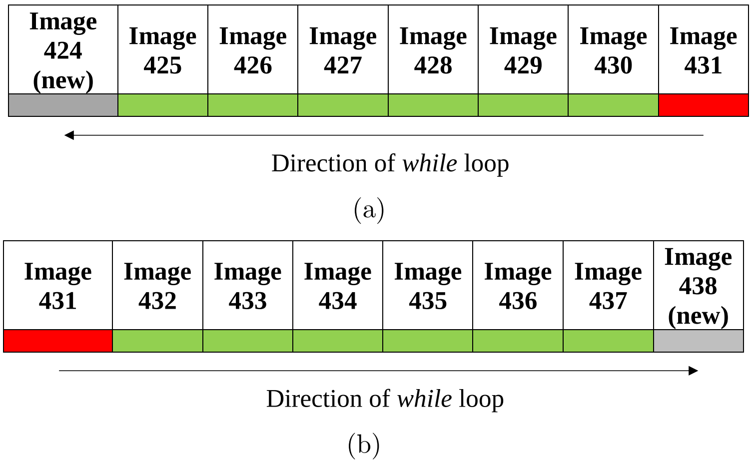

Figure 3.6: Storing data when: (a) the *while* loop is moving backwards, and (b) the *while* loop is moving forwards

The *while* loops require information regarding the major and minor axis lengths of the wire segment under consideration. Euclidean distance calculations are performed on either the preceding image or the subsequent image, prior to the loops, to identify, dictated by the smallest Euclidean distance, the wire segment that belongs to the family of wire segments being tracked, and obtain its properties. The same properties are calculated within the *while* loops until a wire segment that has a major axis length to minor axis length (i.e. the aspect ratio of elliptical segments) greater than a predetermined value, which indicates that the out-of-plane wire has turned in-plane (see Figure 3.5). This value was obtained by looking at average in-plane wire segment aspect ratios.

Within each *while* loop, the first task is to save the incoming data. The image number, i is then either decreased or increased by one, depending on the direction the loop is travelling through the set of images. The new image is mathematically squared using *imageSquare*, which improves the contrast in wire object boundaries, and converted to produce a corresponding binary image. Next, the most probable position of the next centroid is evaluated using *predictMethod*. *regionprops* is then used to identify all the objects in the new image, and the object that is located in the predicted centroid locations is determined. This object does not necessarily need to be the single wire segment under consideration, and could contain the wire segment of interest, as well as other segments in contact with it. Finding the object verifies whether the wire segment is still present in the images or not, and is especially crucial at the extremes of an image because wire segments can disappear from the region of interest (discussed and justified later on in this chapter). If the wire segment does disappear, the *while* loop is broken, and the algorithm attempts wire tracking in the forward *while* loop. Otherwise, the algorithm moves onto the next object in the original image from which tracking was commenced (and wire counter, j is incremented), or to the next image (and image counter, i is incremented).

The pixel list, along with the image number, and the predicted centroid locations, of the object where the centroid is located is fed into the function, *erodeImage* that attempts to find the true centroid of the wire segment under consideration. If it cannot successfully find a centroid, the code will progress onto a secondary method to determine the centroid. In the secondary method, the previous image is 'opened' and the 'opened' image is subtracted from the output image from *imageSquare* in an effort to separate a wire segment from an agglomeration of wire segments. As mentioned earlier, the residual image would contain the wire segment sought, whose centroid properties, and other parameters can be easily calculated. This secondary method is especially suited to wires that are purely out-of-plane, as was seen in Figure 3.4. It is, however, inaccurate when in-plane wire segments are involved, because subtracting an elliptical out-of-plane moving segment (that is removed from the image by 'opening' it) from an elliptical in-plane segment will produce a discontinuous elliptical object whose centroid location would be wrong by a factor of half the size of out-of-plane wire segment. An example of this is seen in Figure 3.7.

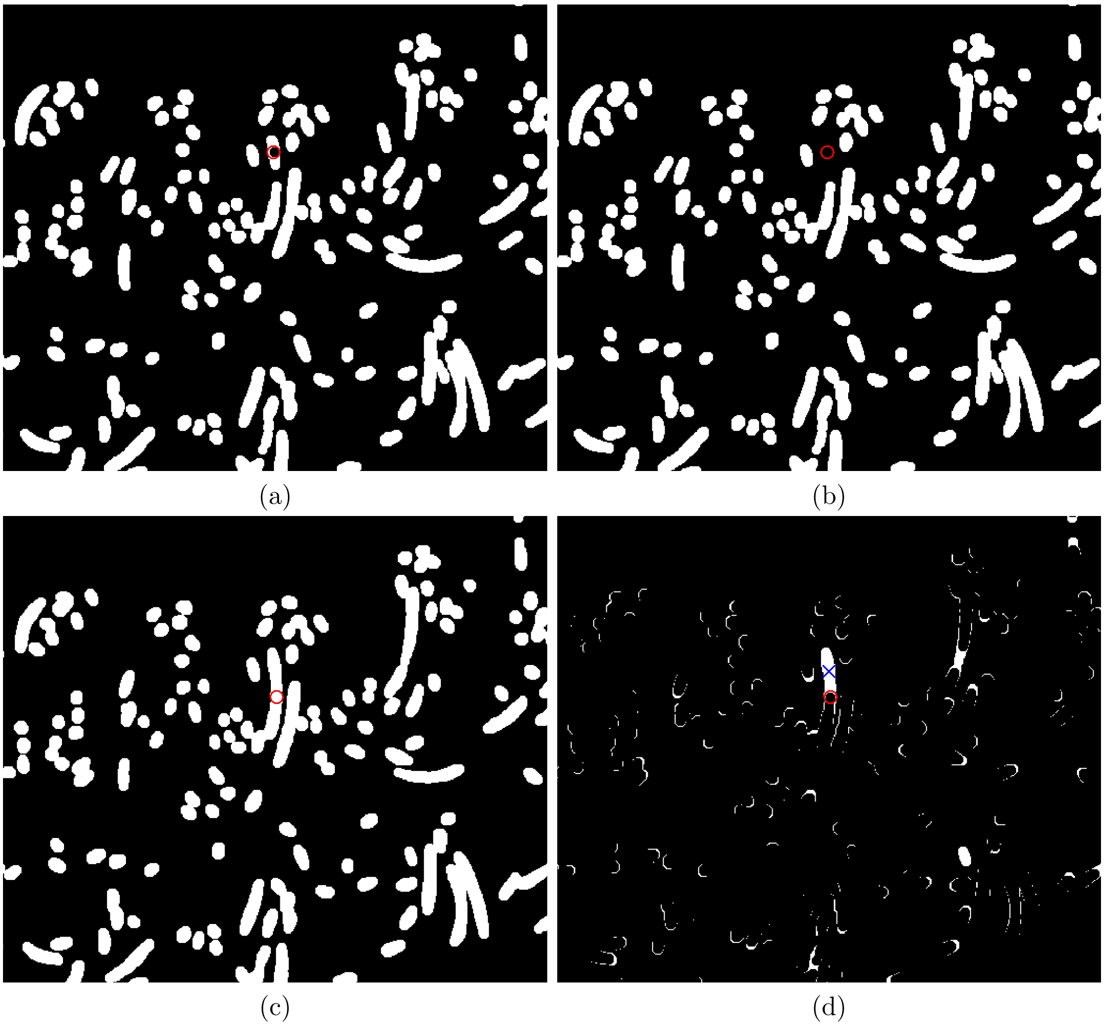
(a) (b) (c) (d)

Figure 3.7: Image subtraction performed for an in-plane wire segment: (a) Identified and marked out-of-plane wire segment, (b) image (a) 'opened', (c) succeeding image where the wire segment belonging to the identified wire in image (a) is present, and is now in-plane, and (d) image subtraction carried out between images (c) and (b)

It can be seen in Figure 3.7 (d) that the actual centroid should be at the location marked by the red 'O', but the image subtraction leads to the misidentified centroid, as indicated by the blue 'X'.

If the Euclidean distance between the predicted centroid location, and the centroid of a segment from the subtracted image is within a suitable tolerance, the centroid locations may be recorded. If, however, the Euclidean distance exceeds the tolerance, a third, and final attempt is made to locate the centroid coordinates using the tertiary function *centroidFinder*. This function is used as a last resort because it is significantly more computationally expensive than the other two methods. If this final attempt fails, the loops are broken and the algorithm moves on to the next object in the current image (and j is incremented by one), or to the next image if no more objects are found to be acceptable in the current image (and i is incremented by one).

Once the centroid coordinates are determined using one of the three centroid finding functions, *drawEllipse* is used to mark the wire as identified, and the algorithm repeats its procedures until the end of the image dataset.

Once the first run of the *centroidTracker* algorithm is complete, the marked objects can be 'opened' to eradicate them from the data set, and the algorithm can be run a number of times to detect objects that were previously undetectable. For example, if an object in an image contains three wire segments, two of which were detected in the first run of the algorithm, it would now be possible to detect the third segment very easily, since it will be the only object left once the opening procedure is performed.

The final output of the *centroidTracker* algorithm now contains all the information required to perform further data analysis to understand the state of the TMW microstructure (e.g. wires that are free, or in contact).

3.4 Description of functions

This section explains the core functions used in the main algorithm developed to analyse the binary images. These functions include the in-house functions that can be found with the MATLAB Image Processing Toolbox, and also custom functions that have been created to supplement the former functions. The in-house functions will be introduced with short summaries (they are explained first to show how they were used in *centroidTracker* algorithm, and the custom functions made to complement the algorithm), whereas the custom functions are explained in more detail.

3.4.1 Functions with MATLAB Image Processing Toolbox

regionprops

regionprops is used to calculate various properties of objects (or regions) for a binary image. The properties are based on the assumption that the object shape is elliptical. This function considers white pixels as the foreground, and black pixels as the background. Regions are detected based on pixel connectivity. For a two dimensional image, there can be either four or eight connectivity neighbourhoods. As the word neighbourhoods suggests, if a neighbouring pixel is white, the region is considered connected and is hence considered as one object. For the four neighbourhood connected option, the pixels considered are situated north, south, east and west to the pixel under consideration. For the eight neighbourhood connected region, the directions considered are northeast, northwest, southeast and southwest, in addition to the aforementioned directions. Figure 3.8 shows an image which shares a single point of contact between the two objects, which is circled on the figure. If the connectivity parameter was set to four, two distinct wire segments would be detected, and if the connectivity parameter was set to eight, then the object would be identified as a single, larger object.

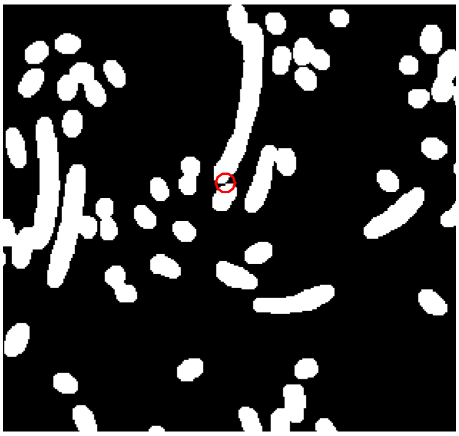

Figure 3.8: Two wire segments sharing a single pixel at their borders. If the connectivity parameter is four, two distinct wire segments are detected, and if the connectivity parameter is eight, only one object is detected by *regionprops*

There are a total of 22 different properties measured using *regionprops*, but not all of them are used in the proposed algorithm. The important ones are stated as follows.

`Area`: Counts the number of foreground pixels in an object.

`Centroid`: Calculated mass centre of the foreground, measured in terms of the pixel x and y coordinates.

`MajorAxisLength`: Length of the longest axis of the ellipse.

`MinorAxisLength`: Length of the shortest axis of the ellipse.

`Orientation`: Calculated angle between the major axis length and the horizontal axis of the image.

`PixelIdxList`: Lists the x- and y-coordinates of all the foreground pixels contained within an object.

`PixelList`: Lists the element numbers of all the foreground pixels contained within an object.

`Solidity`: Ratio of foreground pixels to total pixels present in an object.

im2bw

im2bw is used to transform a grayscale image to a binary image using thresholding. The thresholds are determined by using Otsu's method.

imopen

imopen is a morphological operation that first erodes objects in an image, followed by dilating them. This is a very important tool which was used to remove wire objects that were marked (i.e. hollowed objects). An example of this was seen in Figure 3.7 (b), which showed an 'opened' image of Figure 3.7 (a). A structuring element is required to perform this operation. Structuring elements come in the form of several shapes: diamond, disk, rectangle, and line, to name a few, and the sizes of these shapes is an input that the user can choose. Erosion can be thought of as an eraser that removes foreground pixels from the image, and dilation can be thought of as a filler that adds foreground pixels into the image. The size and shape of the eraser and filler dictates the way an image is 'opened'. If all the pixels in an object are eroded (or erased), dilation (or filling) is not performed, since there are no pixels left to dilate. This highlights the importance of marking an identified object to help removing them from the image dataset.

bwsubtract

bwsubtract performs simple subtraction between two images. It is most advantageous when used to spot the changes that have occurred between two successive images. Examples of *bwsubtract* were shown in Figures 3.4 and 3.7.

3.4.2 Custom made functions

predictMethod

The *predictMethod* function predicts the position a wire is likely to be in a particular image using information from the previously known and stored centroid locations. This is done by calling up to four stored centroid values from previously processed images, applying a smoothing filter (to reduce the minor deviations that can potentially cause divergence in predictions in the future), and applying a polynomial fit to both the abscissa and the ordinate. Since the physical bend of a wire can be described quite well by a quadratic equation, the polynomial is a second order one. Once the polynomial equation is found, the known values of the z-axis (i.e. spacing between images) is used to evaluate the functions and obtain the predictions.

Table 3.1 summarises the inputs and output of the *predictMethod* function.

Inputs	**Outputs**
centroid, x, centroid, y, centroid, z, image number, length of tracked wire	predicted centroid, x, predicted centroid, y, predicted centroid, z

Table 3.1: Inputs and outputs for *predictMethod*

distanceFinder

The primary task of *distanceFinder* is to locate the one object in an image that belongs to the 'family' of objects previously recorded by the algorithm. This is performed by finding the centroid locations of each object in an image, and measuring the Euclidean distance, Equation 3.2, from each of these objects to the predicted centroid from the wire being tracked.

$$d = \sqrt{(x_2 - x_1)^2 + (y_2 - y_1)^2} \tag{3.2}$$

where d is the Euclidean distance, x and y are Cartesian coordinates, and the subscripts 1 and 2 denote two distinct points on the Cartesian space.

The object that belongs to the wire family would have the minimum Euclidean distance of all the measured distances. The secondary task of *distanceFinder* is to calculate the properties for the identified object using *regionprops*. Since the main algorithm does not require all properties every time, there are several conditional *if* statements that retrieve and output the properties as needed to ensure efficiency.

Table 3.2 summarises the inputs and output of the *distanceFinder* function.

Inputs	**Outputs**
binary image, predicted centroid, x, predicted centroid, y, orientation	minimum distance, new centroid, x, new centroid, y, minor axis length, major axis length, pixel list, orientation

Table 3.2: Inputs and outputs for *distanceFinder*

imageSquare

imageSquare is a simple function used to supplement the *im2bw* function. *imageSquare* uses the image number of the image that is under analysis and the `PixelList` of the object that has been identified to be part of the same family of wires as an input. This object can be that of a single wire, or an agglomeration of wires in contact. *imageSquare* first loads the grayscale image that corresponds to the image number input (Image 1), and also creates a grayscale image full of zeros (Image 2), which has a datatype of unsigned 8 bit integers, of the same size as the images being analysed. Only the grayscale components of the object under consideration is superimposed from Image 1 to Image 2 using the `PixelList`. The datatype of Image 2 is then converted into *double* format in order to square the image. If this conversion is not performed, the pixel values would be capped at 255 (i.e. $2^8 - 1$) since it is an unsigned 8 bit integer image. Squaring the image is useful as it helps increases the contrast between the background and the foreground. The image is converted back to unsigned 8 bit integer format before it is converted into binary format. This process contributes to the segmentation of objects that are in contact because contrast between foreground and background is higher, and hence the thresholding procedure is made easier. Figure 3.9 (a) shows an original reconstructed image, and (b) shows the squared image produced by the *imageSquare* function.

(a) (b)

Figure 3.9: (a) Original unmodified grayscale image, and (b) image (a) is squared

Table 3.3 summarises the inputs and output of the *imageSquare* function.

Inputs	**Outputs**
image number, pixel list	binary image

Table 3.3: Inputs and outputs for *imageSquare*

drawEllipse

drawEllipse is used to form an ellipse based on major and minor axis lengths and orientation. The general equation used to draw the ellipse is described by Equation 3.3.

$$\left(\frac{(x-x_c)sin(\theta)+(y-y_c)cos(\theta)}{a}\right)^2+\left(\frac{(x-x_c)cos(\theta)-(y-y_c)sin(\theta)}{b}\right)^2=1 \tag{3.3}$$

where x and y are two dimensional Cartesian coordinates, x_c and y_c are the centroid values in the Cartesian space, θ is the orientation of the ellipse, and a and b are the minor and major axis lengths, respectively.

If a pixel fulfils the criteria dictated by Equation 3.3, its binary value is changed from 0 to 1. To ensure that the function runs efficiently and quickly, the ellipse is created on a smaller image (Figure 3.10 (a)). It is then superimposed onto a larger image (Figure 3.10 (b)), using translation, that has the same size as the main images being analysed. *regionprops* is then used to identify the list of pixels (`PixelList`) that the ellipse occupies, which is the output of the function.


(a)

(b)

Figure 3.10: (a) Ellipse created on a small image (100x100 pixels), and (b) Ellipse superimposed on the full-sized image (725x725 pixels)

Table 3.4 summarises the inputs and output of the *drawEllipse* function.

Inputs	**Outputs**
image size, x, image size, y, centroid, x, centroid, y, orientation, minor axis length, major axis length	pixel list

Table 3.4: Inputs and outputs for *drawEllipse*

erodeImage

erodeImage is used to separate agglomerations of wire segments to help identify the centroid locations of wires of interest. Before continuing with the details behind the function, *erodeImage*, it is worthy to note an important underlying function used with *erodeImage*, *imerode*. *imerode* is an in-built MATLAB function that performs morphological erosion of an image. Erosion takes away layers of pixels from the object, based on the size of a specified structuring element, as with the *imopen* function.

An example of image erosion is shown in Figure 3.11 (b), which performs erosion on the image seen in Figure 3.11 (a).


(a) (b)

Figure 3.11: (a) Unmodified image, and (b) erosion of unmodified image

However, it must be noted that the erosion in this example was performed to remove several layers of a wire object in one go for illustration purposes. With *erodeImage*, the erosion process removes one layer of the wire objects at a time, as detailed in the following text.

The first step *erodeImage* performs is mathematical squaring of the image, with the same procedure as described by *imageSquare*. Prior to converting the image back to binary, however, the image is eroded one layer at a time to help separate wire agglomeration. The eroded grayscale image is then converted to binary to calculate the new centroid location using *regionprops*. The minimum Euclidean distance is then calculated between the object(s) and the predicted centroid locations, which are fed into *erodeImage* as inputs. The minimum distance is used as the condition to run a *while* loop. This *while* loop repeatedly performs the tasks of eroding the grayscale image with a unit disk, converting it to binary, finding the new centroid(s) using *regionprops*, and calculating the minimum Euclidean distance (between the predicted centroid location and the new centroid location) until the value gets below a distance of one pixel. Once this occurs, the final eroded image is output. Note that continued erosion can cause the object to disappear completely. For this reason, there is a condition that breaks the *while* loop, and avoid an infinite loop.

Table 3.5 summarises the inputs and output of the *erodeImage* function.

Inputs	**Outputs**
image number, pixel list, predicted centroid, x, predicted centroid, y	binary image

Table 3.5: Inputs and outputs for *erodeImage*

centroidFinder

centroidFinder is the another vital function utilised by the main algorithm. *regionprops* only finds the centroid of an entire agglomeration, while *centroidFinder* attempts to find the centroid of a wire segment within the agglomeration. The inspiration to create this function came from the method of finding the centre of gravity for irregularly shaped objects, whereby the object is suspended from different locations within the body, straight lines are drawn pointing downward, and the intersection of all the lines is the true centre of mass. With *centroidFinder*, however, the method of finding the centre of mass is slightly different. Starting from a point within an object, a line is first drawn at zero degrees, up to the borders of the object on either side of the point. The midpoint of the line is then evaluated and is used as the starting point to draw the next line at an incremented angle either side of it up to the border of the object. A new midpoint is found, and the process is repeated for all angles up to 360°. In this manner, the *centroidFinder* function 'walks' to the centre of mass of the object in an iterative fashion. Because the objects comprise of a discrete number of pixels, this method of finding the centroid is prone to fluctuations about the centroid. For this reason, the entire algorithm is repeated three times and the centroid is evaluated by taking the median of all the points. Figure 3.12 shows how the estimated centroid can move from a starting position, purposely positioned far away from the real centroid for illustration purposes. The centroid iterates towards the estimated centroid for a circular wire segment, with the angles incremented from 0° to 175° in Figure 3.12 (a) - (e).

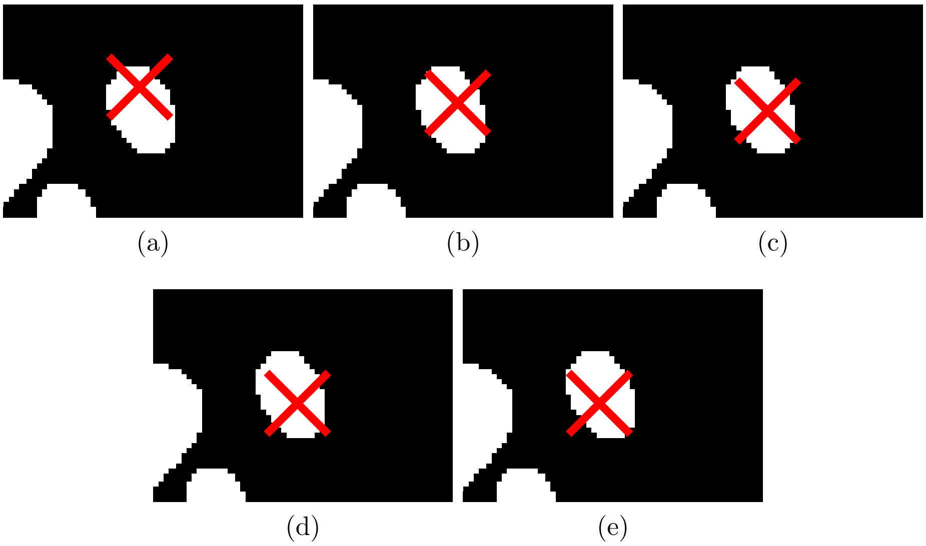
(a) (b) (c) (d) (e)

Figure 3.12: *centroidFinder* iteratively 'walks' towards the estimated centroid from a position located far away from the real centroid. The calculated centroid locations are shown for: (a) 0°, (b) 45°, (c) 90°, (d) 135°, and (e) 175°

centroidFinder, on its own, can only successfully find the centroid of an object that represents a single wire segment. If two wires are in contact, for example, and *centroidFinder* is run as it has been described thus far, the centroid would be dragged away from the wire segment of interest. This would occur because the lines constructed from the respective midpoints till the border of the object would extend to the second body and the new midpoint would most likely lie on the hypothetical border between the two wire segments.

This pitfall is overcome using supplementary functions that help in the selection of which lines can be used in order to avoid divergence from the true wire segment centroid. These are *lengthChecker* and *angleChecker*.

Table 3.6 summarises the inputs and output of the *centroidFinder* function.

Inputs	**Outputs**
binary image, predicted centroid, x, predicted centroid, y	centroid, x, centroid, y

Table 3.6: Inputs and outputs for *centroidFinder*

lengthChecker

lengthChecker progressively grows a line at a specified angle from a location within an object under consideration up to the point where the pixel changes from white to black, i.e. at its border. This is performed using two *while* loops, one that creates the line forward in the image, from left to right, and one that creates the line backward in the image, from right to left. For each line, the Euclidean distance is calculated and output along with its corresponding orientation.

Table 3.7 summarises the inputs and output of the *lengthChecker* function.

Inputs	**Outputs**
binary image, predicted centroid, x, predicted centroid, y, line orientation	forward line length, backward line length, forward line orientation, backward line orientation

Table 3.7: Inputs and outputs for *lengthChecker*

angleChecker

angleChecker uses the data from *lengthChecker* to identify the lengths and orientations that are valid for the calculation of the midpoint, and those that should be ignored. It uses simple differences to trigger the commencement of an outlier, where the length increases rapidly between successive orientation angles. While developing this function, several different cases of wire segments were chosen to gain an understanding of the intricacies of outlier identification, and more importantly, where the outlier ceases to exist.

The wire segments, shown in Figure 3.13, were chosen from an image that contained a diverse range of wire segments, and the algorithm was later verified and validated on other images for a range of wire segments.

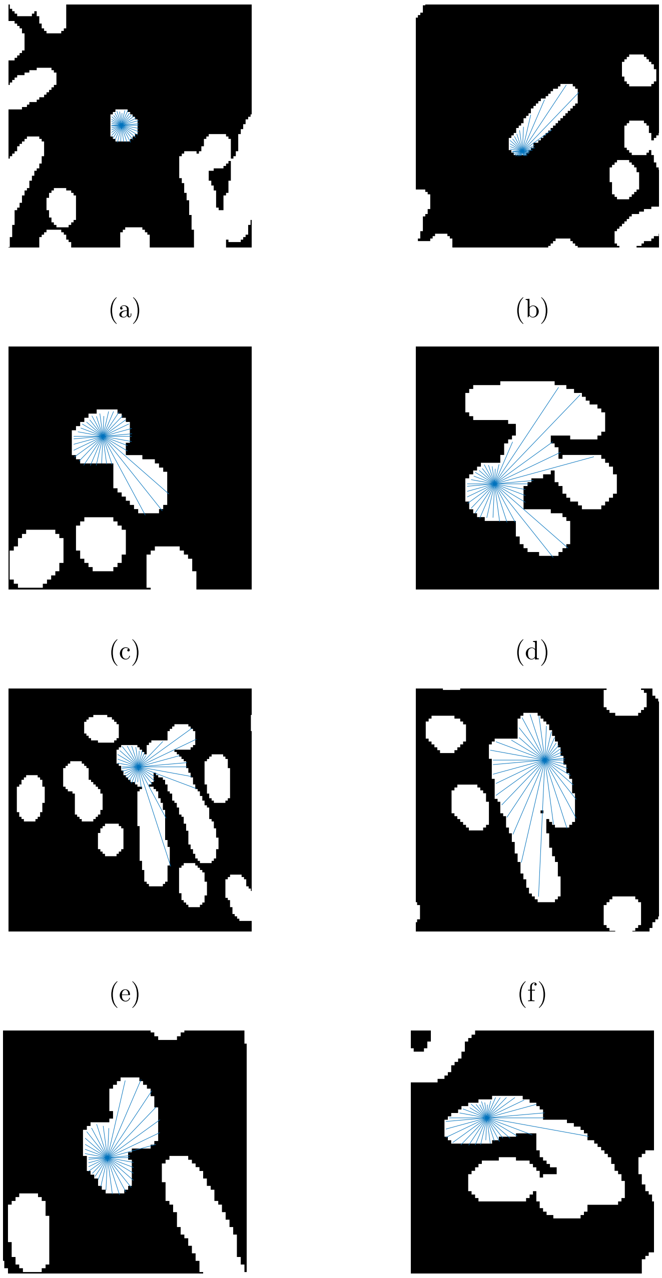

(a) (b) (c) (d) (e) (f) (g) (h)

Figure 3.13: (a) a circular wire segment, (b) an elliptical wire segment, (c) two circular wire segments, (d) multiple wire segments, (e) a circular wire segment, neighboured by an elliptical wire segment that is neighboured by another circular wire segment, (f) two neighbouring elliptical wire segments, Example 1, (g) two neighbouring elliptical segments, Example 2, and (h) two neighbouring elliptical segments, Example 3

The following discussion covers eight different types of wire segments illustrated in Figure 3.13 (a) - (h). Each segment possesses a different shape for the ‘length of line vs. angular orientation’ diagrams shown in Figure 3.14, both in terms of inter and intra-shape contact types. The description of each example includes new features learnt from such a curve, and something that the algorithm would need to handle. It is noteworthy that the angular orientations are plotted twice along with their corresponding line lengths and hence covers 720°. An outlier occurring at the beginning of the plot may not be detected if this operation is not performed.

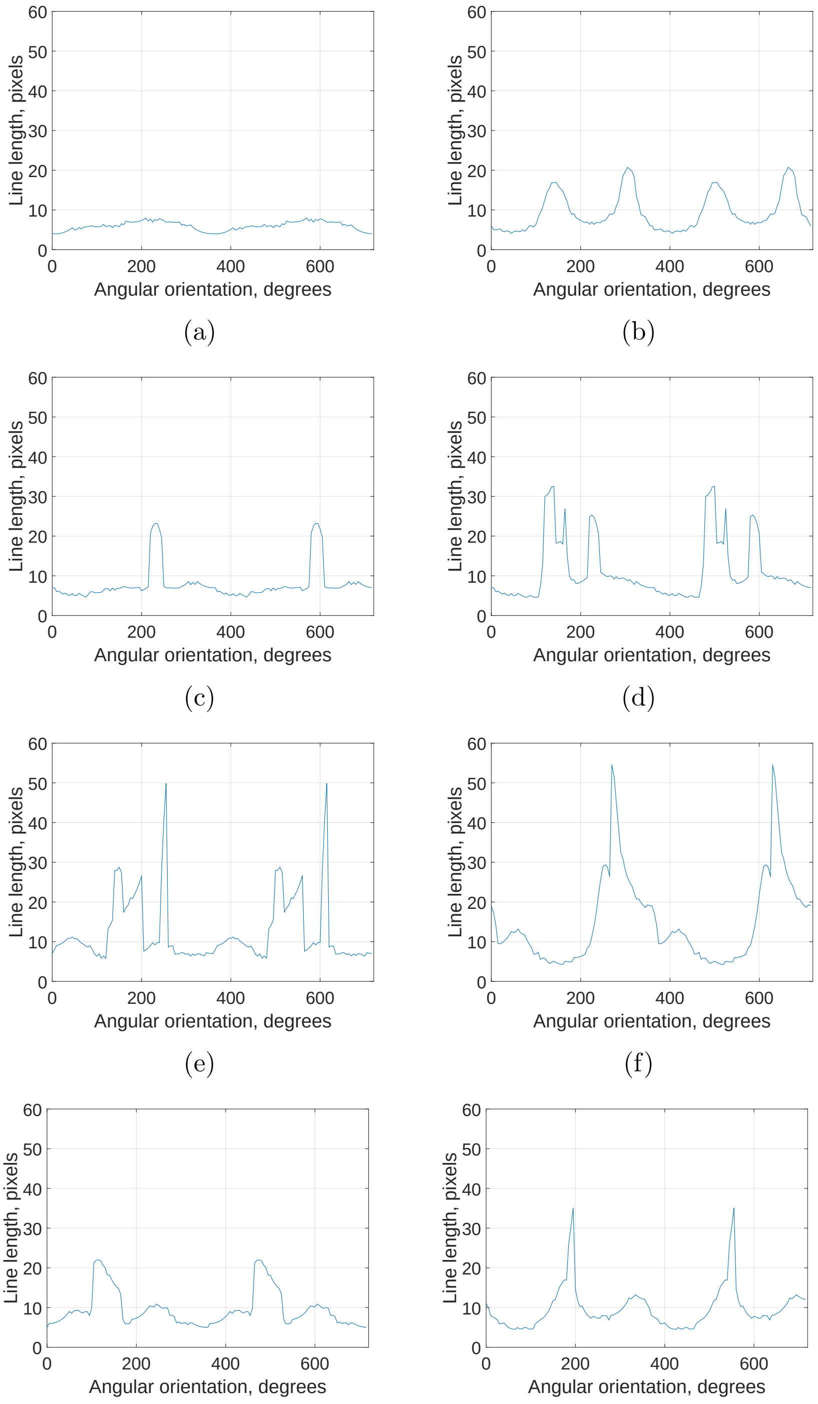

(a) (b)

(c) (d)

(e) (f)

(g) (h)

Figure 3.14: Line length vs. orientation angles for: (a) a circular wire segment, (b) an elliptical wire segment; (c) two circular wire segments, (d) multiple wire segments (e) a circular wire segment, neighboured by an elliptical wire segment that is neighboured by another circular wire segment, (f) two neighbouring elliptical wire segments, Example 1, (g) two neighbouring elliptical segments, Example 2, and (h) two neighbouring elliptical segments, Example 3

Case study 1: Circular wire segment

Figure 3.14 (a) does not contain any abrupt increase in length over the full range of orientations because it is a simple circle in the image. There are a number of local peaks and troughs that occur due to the imperfect shape at the borders of the segment, and the algorithm would need to handle such minor variations.

Case study 2: Elliptical wire segment

Figure 3.14 (b) indicates two pairs of peaks over the range of angular orientations. Each peak refers to a line approaching and/or moving away from the length of the major axis. The peaks are 180° apart because the two ends of the major axis are opposite each other. Every peak is followed by a gradual decrease to a local minimum, as expected, because the minor axis is being approached. The gradient of the curves are quite smooth, indicating that the object under analysis is a single wire segment.

Case study 3: Two circular wire segments

There is a clear distinguishing feature in Figure 3.14 (a) that separates the object identity from Figure 3.14 (c) - the sharp change in line length between 215° and 250°. The narrow width of the peak indicates that the discontinuity is not caused by a large wire segment. Any discontinuity disregarded by the algorithm would also have to disregard the corresponding set of lines (and hence angles) that occur 180° apart. Therefore, while the lines occurring between 35° and 70° remain within the perimeter of the circle under study, it would not be taken into account.

Case study 4: Multiple wire segments

The case of three circles is much more complicated from the other cases involving circles discussed thus far. There are essentially two discontinuities observed in Figure 3.14 (d). There is a sharp discontinuity at 110°, followed by a small sharp dip, which increases again before dropping sharply. This is followed by another discontinuity between 215° and 245°. This example shows that a sharp fall does not necessarily mean that it is the end of a discontinuity. The algorithm also cannot simply look for a single set of outliers.

Case study 5: Circular wire segment neighbouring an elliptical wire segment neighbouring another circular wire segment

Figure 3.14 (e) is another case of high complexity. There are essentially three sets of outliers. There is one discontinuity at 125° followed by another one at 140°. The first discontinuity occurs when the line encroaches the space of the ellipse, whereas the second discontinuity occurs when the line extends to the space of the circle neighbouring the ellipse. The third and final discontinuity is due to the ellipse neighbouring the circle under study at 245°.

Case study 6: Two elliptical wire segments, Example 1

The peaks occurring at 65° and 245° in Figure 3.14 (f) are the true ends of the ellipse being examined. The discontinuity occurring at 265° occurs because the line extends into a neighbouring parallel ellipse. The gradual drop happens within the limits of the neighbouring ellipse, and the small local peak seen at 355° is at its major axis. The local minima seen at 375° (same as the one at 15°) is the point where the line retracts to within the boundary of the primary ellipse. The algorithm would hence need to distinguish between peaks that belong to the object under study, and those that do not.

Case study 7: Two elliptical wire segments, Example 2

Figure 3.14 (g) is a simpler case of a small ellipse being neighboured by another small ellipse to its northeast. The discontinuity occurs between 105° and 170°. This is followed by a small rise to a peak, which is the approach towards the major axis length, followed by a drop. There is another peak 180° apart, which is the other end of the major axis length.

Case Study 8: Two elliptical wire segments, Example 3

In the case of Figure 3.14 (h), the mid-sized ellipse under study is neighboured by another mid-sized ellipse, positioned to its southeast direction. It occurs nearly at the point coinciding with the major axis length. The trends observed here are very similar to other examples of neighbouring ellipses, bar the point where the discontinuity occurs.

These subtle differences need to be dealt with in slightly different approaches, and yet the core data extracted from the algorithm needs to be the same.

angleChecker, first and foremost, finds the minimum value of the line length data to form a starting point, and then finds the difference between this and its neighbour. If the difference is greater than a specified threshold, a *while* loop modifies the element number until the difference between subsequent values falls within the threshold. It also performs smoothing on the length data, as a new variable, to remove noise and variability from the data. It is created as a new variable because the smoothing operation can modify important characteristics from the data, such as the peak values found at the major axis lengths, which may need to be preserved. A nested *while* loop that incrementally calculates differences between successive points is then commenced. If the difference exceeds the previously used threshold value, the element identity number is saved for reference, and the second, inner *while* loop is triggered. This loop identifies sets of outliers from the data.

The features that were considered most important when considering the outliers found in all the cases studied can be independently summarised as follows:

i After a sharp increase in line length occurs, there is generally a sharp drop that occurs. This drop needs to be followed by sequence of line lengths that is approximately unchanged statistically. If this does not occur, the points are still considered as outliers.

ii Sharp rises can be followed by a gradual drop. This occurs when the lines are in the vicinity of a neighbouring wire segment in the shape of an ellipse. The gradual drop typically ends in a valley. A sustained positive gradient indicates that the line is back in the space occupied by the wire segment under study.

iii If the line length drops to a value that is below the characteristic length of twice the minor axis length, and does not fit the description of the preceding statements, the point/points can be considered not to be outliers, by default.

The flat sequence of data described in (i) is identified by calculating the standard deviation and absolute difference between mean values of five consecutive points and the current value following each point in the length data. If both these values are below a value of 0.15 (this number was obtained by testing out sequences of data), the values in between are flagged using an Boolean indicator (i.e. the values are set to true).

The outlier detection described in (ii) is stopped by using differences to identify the minimum point of the valley (e.g. the valley seen in Figure 3.14 (f)). As the inner *while* loop sifts through the data point by point, a check is carried out to find changes in gradients before and after each point. To ensure that a current point is indeed a minimum point in a valley, two successive points need to have a negative gradient prior to the current point, and six consecutive points need to have a positive gradient following the current point. When this occurs, the values are flagged using the Boolean indicator.

The third, and final, item (iii) is simply dealt with by using the value of the length data for a point in the iteration, and the values are flagged using the Boolean indicator.

Within the inner *while* loop, once a value is flagged via the Boolean indicator (as a true value), the values of the line length data, starting from the reference element identity number up to the current element identity number, are changed to infinity, and the computation resumes to the nested *while* loop until the entire range of data is covered by the algorithm. On exit from the *while* loops, the data is reviewed once again. For any data value that is infinite, the algorithm changes the length data that lies 180° apart to infinity too. To complete the algorithm, the angles for which length data are real numbers, and not infinity, are selected and output.

Finally, to conclude the cases studied, Figure 3.15 shows the comparison of the line length data with the corresponding length data that the algorithm deems valid.

As depicted in Figure 3.15, *angleChecker* eradicates the problematic data points. The rest of the data points can then be successfully applied to the *centroidFinder* algorithm to calculate the centroid co-ordinates.

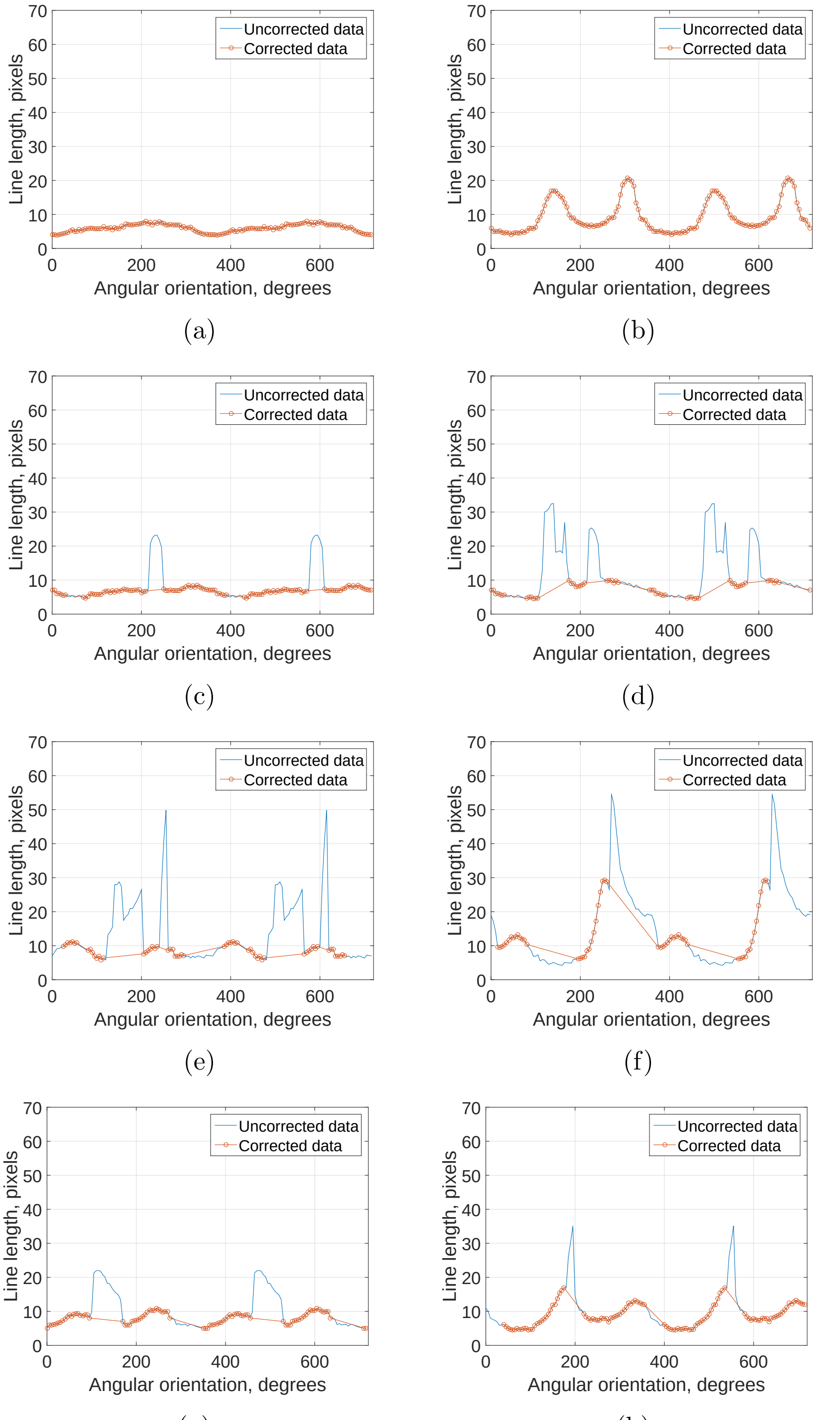

(a) (b)

(c) (d)

(e) (f)

(g) (h)

Figure 3.15: Uncorrected and corrected line length vs. orientation angle data for: (a) a circular object; (b) an elliptical object; (c) two circular objects; (d) three circular objects (e) a circular object; neighboured by an elliptical object that is neighboured by another circular object; (f) two neighbouring elliptical objects, Example 1; (g) two neighbouring elliptical objects, Example 2; and (h) two neighbouring elliptical objects, Example 3

Table 3.8 summarises the inputs and output of the *angleChecker* function.

Inputs	**Outputs**
forward line length, backward line length, forward line orientation, backward line orientation	valid line length, valid line orientation

Table 3.8: Inputs and outputs for *angleChecker*

3.4.3 Summary

The *centroidTracker* algorithm, its functions and sub-functions, have been described in detail. It has been designed to:

- Identify and store centroid locations of out-of-plane wires.
- Cluster 'families' of out-of-plane wires.
- Separate wire agglomerations to enhance wire centroid identification.

While efforts were made to identify in-plane wires as well (not reported), it was found that in-plane wires had complicated structures, which made centroid tracking difficult and cumbersome. This was because of a number of reasons, including:

- In-plane wires would be visible in images where the true wire centroid will not lie (i.e. only one centroid would be required from a range of images).
- In-plane wires tend to agglomerate with other in-plane wires, making matters complicated.

Taking the above statements into consideration, the experimental work carried out with respect to micro-computed tomography scanning, and the respective image processing, are discussed next.

3.5 Experimental methodology

3.5.1 Specimen selection

A total of 10 TMW specimens were specially manufactured at Beihang University in 2014 using 0.15 mm nominal diameter Grade 304 stainless steel wires, enabling experimentation in conjunction with micro-computed tomography scanning of the specimens. The specimens were split equally into two groups of varying relative densities ($\tilde{\rho}$) 0.18, and 0.23, all with similar dimensions. Relative density is a measure of ratio of the mass of the specimen divided by the volume of the wires in the microstructure relative to the mass of a solid block of same geometry to its volume.

There was quite a noticeable inter and intra specimen variability in dimensions for each of the groups of TMW. While the manufacturing process for each group of TMW specimens was the same, the differences in dimensions were partly attributed to the complicated manner of the wire weaving that was carried prior to the moulding procedure. As a result of this, the internal loads that the wires and the contacts carry may vary considerably over the microstructure, leading to microstructure relaxation to varying degrees, which consequently influence changes in geometry.

Tables 3.9 - 3.12 show the specifications of mass, inner diameter, outer diameter, and height of the manufactured TMW specimens, respectively. An electronic weighing scale (with resolution 0.01 g) was used to measure the mass, whereas a Vernier caliper was used to measure the dimensions. For the values shown in Tables 3.10 - 3.12, three readings of each parameter were considered at different corresponding cross-sections of the specimen. The standard deviation is also displayed to gauge the degrees of inter and intra specimen dimension variability.

Relative density	Specimen ID	Mass, g	Inter specimen	
			Mean, g	STD, g
0.18	1	1.74	1.73	0.008
	2	1.72		
	3	1.73		
	4	1.73		
	5	1.74		
0.23	1	2.22	2.21	0.008
	2	2.20		
	3	2.21		
	4	2.20		
	5	2.21		

Table 3.9: Mass of TMW specimens

Relative density	Specimen ID	Measurement no.			Intra specimen		Inter specimen	
		1, mm	2, mm	3, mm	Mean, mm	STD, mm	Mean, mm	STD, mm
0.18	1	7.61	7.79	7.66	7.69	0.093	7.73	0.063
	2	7.75	7.79	7.77	7.77	0.020		
	3	7.74	7.74	7.78	7.75	0.023		
	4	7.69	7.73	7.82	7.75	0.067		
	5	7.75	7.68	7.62	7.68	0.065		
0.23	1	7.85	7.83	7.84	7.84	0.010	7.84	0.037
	2	7.87	7.83	7.85	7.85	0.020		
	3	7.74	7.87	7.82	7.81	0.066		
	4	7.86	7.84	7.89	7.86	0.025		
	5	7.78	7.85	7.86	7.83	0.044		

Table 3.10: Inner diameter of TMW specimens

Relative density	Specimen ID	Measurement no.			Intra specimen		Inter specimen	
		1, mm	2, mm	3, mm	Mean, mm	STD, mm	Mean, mm	STD, mm
0.18	1	18.47	18.48	18.44	18.46	0.021	18.38	0.074
	2	18.35	18.42	18.37	18.38	0.036		
	3	18.24	18.34	18.36	18.31	0.064		
	4	18.25	18.33	18.39	18.32	0.070		
	5	18.42	18.38	18.48	18.43	0.050		
0.23	1	18.39	18.41	18.36	18.39	0.025	18.39	0.049
	2	18.49	18.37	18.33	18.40	0.083		
	3	18.37	18.41	18.44	18.41	0.035		
	4	18.29	18.40	18.45	18.38	0.082		
	5	18.36	18.41	18.38	18.38	0.025		

Table 3.11: Outer diameter of TMW specimens

Relative density	**Specimen ID**	**Measurement no.**			**Intra specimen**		**Inter specimen**	
		1, mm	**2, mm**	**3, mm**	**Mean, mm**	**STD, mm**	**Mean, mm**	**STD, mm**
0.18	1	5.68	5.78	5.97	5.81	0.147	5.92	0.147
	2	5.68	5.82	5.75	5.75	0.070		
	3	6.12	6.02	6.05	6.06	0.051		
	4	5.97	5.89	6.04	5.97	0.075		
	5	5.99	6.10	6.00	6.03	0.061		
0.23	1	5.68	5.91	5.76	5.78	0.117	5.81	0.165
	2	5.87	5.78	6.10	5.92	0.165		
	3	6.00	6.09	5.91	6.00	0.090		
	4	5.68	5.70	5.74	5.71	0.031		
	5	5.66	5.60	5.61	5.62	0.032		

Table 3.12: Height of TMW specimens

Once these specimens were acquired, a preliminary micro-computed tomography scan was carried out on one of the $\tilde{\rho} = 0.18$ TMW specimens. Cross-sectional images were then obtained following an image reconstruction procedure. These images gave an early indication of the expected quality of the scans. An example of one such image is shown in Figure 3.16.

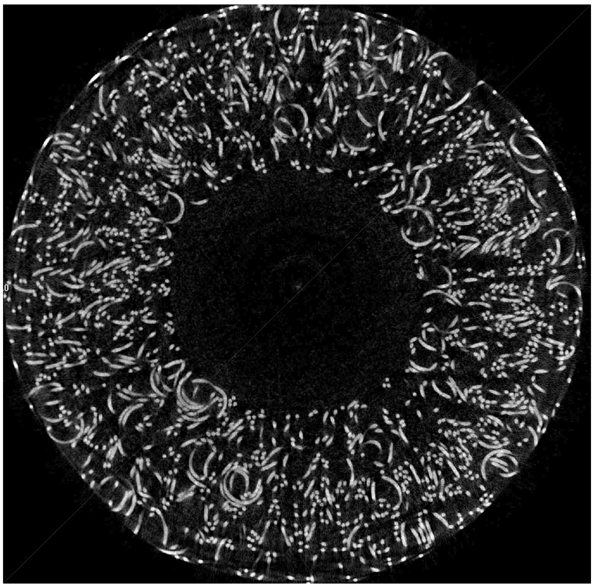

Figure 3.16: Exemplar cross-section image of a TMW device obtained following image reconstruction

Figure 3.16 shows that the image quality is relatively low, as attested by the poor contrast between the pixels. Neighbouring wires in contact, in particular, appear to have no gap in between them. This scan therefore helped conclude that for any valuable analysis to be carried out between experimental and image processing results, only a selective number of specimens should be used. Furthermore, because the quality of images would only depreciate when moving on to the $\tilde{\rho} = 0.23$ specimens, more emphasis should be placed on the $\tilde{\rho} = 0.18$ specimens. The discussions in this chapter, and following chapters, will henceforth focus on three $\tilde{\rho} = 0.18$ and two $\tilde{\rho} = 0.23$ TMW specimens randomly selected from the population of specimens available.

3.5.2 Pre-conditioning and loading regimen

The specimens were pre-conditioned prior to the μ-CT scanning. From previous testing and analysis [75], it was known that the quasi-static and dynamic properties of TMW devices changed significantly between load cycles, prompting the necessity of pre-conditioning. Pre-conditioning a specimen involves loading a specimen to a strain level higher than it would be subjected to in normal operation. In the case of TMW microstructure, it would force the wires to be held in place via a combination of new contacts being formed and friction stopping contacts from slipping.

The hydraulic ram of an MTS 858 Table Top dynamic test system, which is discussed in more detail in Chapter 4, was lowered down to the top surface of each TMW device until complete contact between the two surfaces was made. The TMW devices were then subjected to a static strain of 0.07, and a dynamic strain amplitude of 0.05, i.e. the hydraulic ram oscillated between amplitudes equivalent to device strains of 0.02 and 0.12, about a pre-compression strain of 0.07. The frequency of these oscillations was set to 5Hz, with 1000 cycles chosen for each pre-conditioning exercise. Once pre-conditioning was complete, a quasi-static ramp test was performed up to a strain of 0.10 for each device to estimate the forcing applied during compression on the compression test rig. The ramp tests were also repeated to gauge the success of the pre-conditioning exercise. Figure 3.17 (a) and (b) show the hysteresis loops produced from the ramp tests of the TMW devices with relative densities ($\tilde{\rho}$) of 0.18 and 0.23, respectively.

The results from Figure 3.17(a) show that Specimens 1 and 3 behave in a similar fashion, and are suitable for direct microstructural comparison (and hence, inter specimen/intra group variability) using image processing. Specimen 2, on the other hand, behaves consistently between the two cycles, making it suitable to study the microstructure evolution during load and unload cycles. Additionally, due to the ability of Specimen 3 to follow the load path closely compared to Specimen 1, it was chosen to study intra specimen variability between successive load cycles.

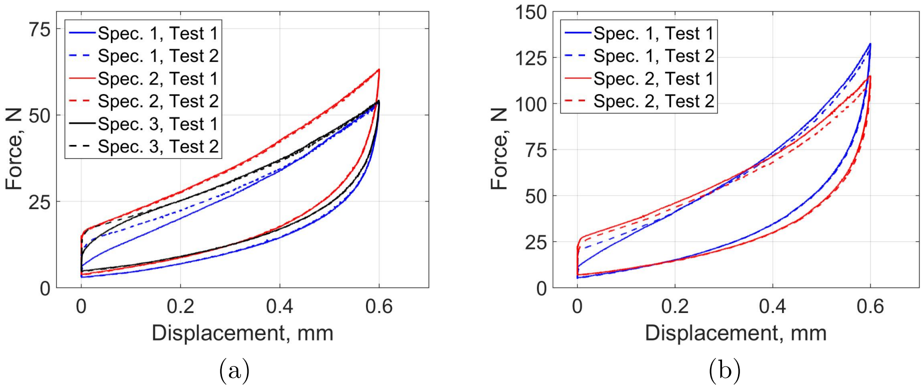

(a) (b)

Figure 3.17: Hysteresis curves of the TMW specimens of (a) $\tilde{\rho} = 0.18$, and (b) $\tilde{\rho} = 0.23$ following the pre-conditioning regimen

Only one specimen, Specimen 1, of the 0.23 relative density group (Figure 3.17(b)) was chosen for scanning to gauge inter group variability. This was because it was predicted that the scan images from a higher density device would possess lower quality due to the lower spatial resolution.

Table 3.13 shows the loading regimen followed for each specimen during the μ-CT scanning. These will be referred to later on in this chapter, when discussing the image processing results.

Relative density	Specimen ID	Loading regimen, strain (%)
0.18	1	0 - 5 - 10
	2	0 - 5 - 10 - 5 - 0
	3	0 - 5 - 10; 0 - 5 - 10
0.23	1	0 - 10

Table 3.13: Loading regimen followed for μ-CT scanning

3.5.3 Test rig description

A compression test rig was designed and manufactured using Perspex due to its known radiolucent properties. Radiolucency is the tendency of a material to allow

X-ray photons to pass through it without any significant attenuation. It is therefore ‘transparent’ during μ-CT scanning, allowing the material being scanned to be the primary X-ray attenuator. The test rig was designed to apply and maintain compressive loads to the TMW devices while they were in the scanner, and μ-CT scanning was taking place.

The bottom of the test rig, shown Figure 3.18, consisted of a protrusion that was used as a fixture to the Skyscan 1172 μ-CT scanner. The main body of the rig was 21 mm in diameter, and 65 mm tall to ensure that a loaded specimen sat comfortably within its confines, and was aligned with the X-ray source and detector, respectively. The top of the test rig consisted of a threaded bolt, which complemented a loading nut that applied the compressive loads when tightened. A washer, which was held when tightening the bolt, was used to reduce torsional loads being transferred to the specimens from the nut. Figure 3.18 (a) shows a schematic of the compression test rig, and Figure 3.18 (b) shows the interior of the scanner with compression test rig installed.

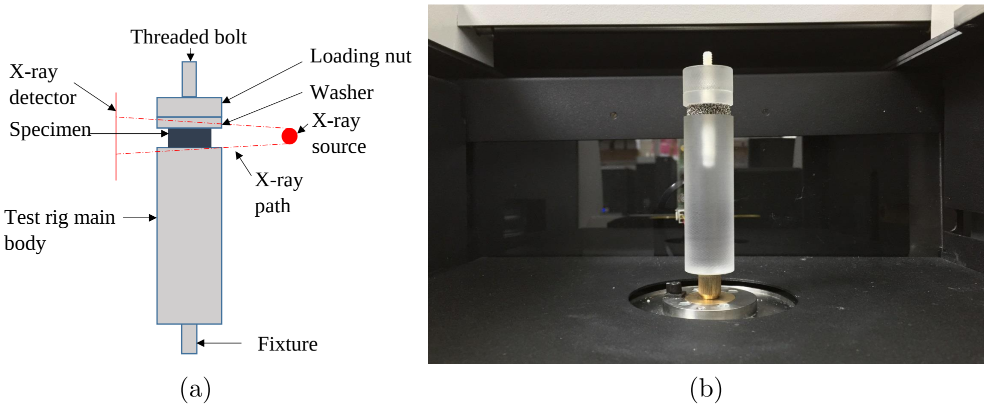

(a) (b)

Figure 3.18: Images showing: (a) schematic of the compression test rig, and (b) interior of scanner with compression test rig installed

The fixture connecting the test rig and the scanner was a source of concern during the scanning. Slight misalignment in the fixture tended to cause the specimen being scanned to go out of view in the X-ray images, because the X-ray source and detector were within a close proximity to the specimen. Due to this, the loading and/or unloading process had to be performed carefully to ensure that the specimen was centrally placed in the rig. Additionally, a spirit level was used to verify that the rig was well aligned within the scanner at various orientations. Even with these measures, with the X-ray source and detector so close to the specimen, the loaded specimen was seldom perfectly aligned, and adjustments were made iteratively after loading the specimen in the scanner, and observing the X-ray images at several angular rotations (up to 180°).

Figure 3.19 (a), (b), and (c) show the test rig taken by a camera installed in the scanner, the X-ray image of the test rig and the X-ray image of the out-of-view specimen, respectively, and is one such example of a minute misalignment causing the specimen to go out of view from the X-ray images.

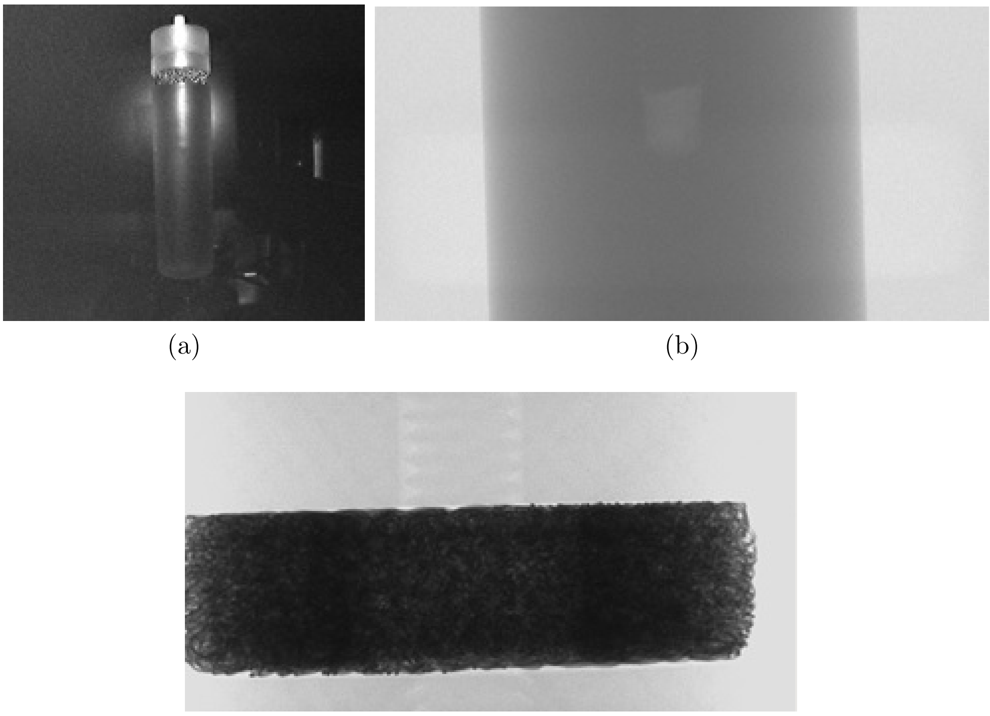
(a) (b)

(c)

Figure 3.19: Images showing: (a) test rig from camera in the μ-CT scanner, (b) X-ray image of test rig, and (c) X-ray image of out-of-view specimen

3.5.4 Testing protocol and scan settings

The order in which the scans were performed are listed below.

- Scan of $\tilde{\rho} = 0.23$, Specimen 1 at 0% strain, followed by a scan of the same specimen at 10% strain - 2 scans.

- Scan of $\tilde{\rho} = 0.18$, Specimen 1 at 0% strain, followed by a scan of the same specimen at 10% strain. The specimen was then unloaded completely, before reloading the specimen and performing the scan at 5% strain - 3 scans.
- Scan of $\tilde{\rho} = 0.18$, Specimen 3 at 0% strain, followed by a scan of the same specimen at 5% strain during unloading (i.e. it was compressed up to 10% strain and decompressed to 5% strain). The specimen was then loaded to, and scanned at, 10% strain - 3 scans.
- Scan of $\tilde{\rho} = 0.18$, Specimen 2 at 0% strain, followed by a scan of the same specimen at 5% strain, and then again at 10% strain. The specimen was then unloaded to, and scanned at, 5% strain and 0% strain, respectively - 5 scans.
- Scan of $\tilde{\rho} = 0.18$, Specimen 3 at 0% strain, followed by a scan of the same specimen at 5% strain and at 10% strain. - 3 scans.

The most dense specimen ($\tilde{\rho} = 0.23$) was scanned first to ensure that the quality of the reconstructed images were acceptable. It was decided that, based on the quality of the result of the image reconstruction, the rest of the specimens would retain the same scan settings. This helped ensure that the results were consistent. Note that the quality of an image is defined by the contrast between background, and foreground pixels. A high quality image is one that has a sharp contrast between the two sets of pixels, with well defined boundaries of the foreground pixel. However, due to noise and other effects, this cannot be realised in practice.

It was found that the first scan resulted in poor spatial resolution for the wires in the images, requiring the scan settings to be modified. As the X-ray scanner was already running at its maximum power capacity (100kV and 90μA), the only other parameter that affected the image quality was the X-ray exposure time, which, as a consequence, was increased from 2000 ms to 3000 ms. The image quality improved, but not to a great extent, and keeping in mind the cost of the scanning, the new exposure time was deemed sufficient. Further increase in this parameter would have improved the image quality further, but it would have also significantly increased the scan time (the scan time for a single specimen rose from 1 hour, 58 minutes to 2 hours, 50 minutes).

Table 3.14 summarises the scan parameter settings.

Parameter	**Options**	**Setting**
Voltage	0:100 kV	100 kV
Current	0:90 μA	90 μA
Camera Position	Near/Middle/Far	Near
Pixel Size	Small/Medium/Large	Medium
Filter	No filter/Al (1 mm)/Al (0.5 mm)	Al (1 mm)
Exposure Time	0:10000 ms	3000 ms

Table 3.14: Settings chosen for X-ray scanning procedures

The “Camera Position” and “Pixel Size” settings, shown in Table 3.14, were chosen to maximise the area occupied by the specimen in the images without going out of view. A 1 mm aluminium filter was used in the scanner to attenuate low energy X-rays that are known to degrade image quality. In medical applications, adding a filter to μ-CT scans has an added advantage of lowering radiation doses applied to specimens, especially if a scan is being performed in-vivo [76]. However, Meganck, et al. [76] also reported that the inclusion of a filter reduced the image contrast and increased image noise in their study.

3.5.5 Image reconstruction settings

Following the scans, the X-ray images go through a reconstruction procedure to produce slices in the transaxial (X-Y) plane. The reconstruction process, which was performed on a software called “NRecon Reconstruction”, required the implementation of more settings to obtain good quality images.

The first task was to load all the images from the dataset into the software. Before complete image reconstruction was performed, a single transaxial image from the axial direction was reconstructed, previewed, and its settings altered to a desired level. These settings were then applied globally for the entire dataset.

Table 3.15 shows the settings used during reconstruction.

Parameter	**Options**	**Setting**
Misalignment Compensation	Program controlled (PC)	PC
Beam Hardening Correction	0:100	50
Ring Artifact Reduction	1:20	10
Objects Larger than Field of View	Yes/No	Yes
Smoothing	None/Box (asym./sym.)/Gaussian	None
Level of Smoothing	0:10	0
Dynamic Image Range	(-1:1):(-1:1)	0.008:0.136

Table 3.15: Settings chosen for image reconstruction

Minute misalignment can occur during scanning, especially if the test rig moves slightly within the specimen holder as it rotates. This movement may cause slight blurring during image reconstruction. The effect of misalignment was reduced by using the "Misalignment Compensation" [77]. While this option could have been modified, the software was allowed to choose an appropriate parameter value, which was calculated using reference points captured during the scanning. A wrong value can cause tails (i.e. the foreground, in this case, the wires, becomes unrealistically slender), doubling (foreground becomes too thick: again, not realistic), or image blurring.

Beam hardening is seen in images as a combination of bright and dark streaks, especially in regions where there is a high X-ray attenuating medium present [78]. This is unavoidable when a material such as stainless steel, which is the primary constituent of TMW devices, is scanned using X-rays, hence these need to be reduced in post-processing using the "Beam Hardening Correction" option.

Ring artifacts are formed when an X-ray detector is not properly calibrated, or is defective. The result of this is the presence of rings around the centre of the rotation of the specimen [78]. If the detector cannot be re-calibrated or changed, the rings need to be artificially reduced in the post-processing phase of the image reconstruction.

The "Object Larger than Field of View" option is selected if the extremes of the specimen are close to the image borders.

The "Smoothing" option allows one to choose between three different types of filters that try to reduce image noise to various degrees, depending on the "Smoothing Level" set.

The “Dynamic Image Range” is perhaps the most sensitive option amongst those shown in Table 3.15. The range chosen dictates how the floating-point real numbers from the scan images are converted to integers in the grayscale output images. The “correct” range is chosen manually by previewing the images, and finding a balance between the background noise, and foreground illumination. Typically, the noise/illumination cannot be eliminated/kept without interfering with the topology of contact interfaces. It is important to note here that the image slice chosen to select the “Dynamic Image Range” came from the densest region in the scanned specimens since the densest regions posed the “worst-case” scenarios in terms of image noise. These settings were then implemented globally to all regions.

Once the settings were applied, the image reconstruction was started, covering the entire dataset, and the result was a stack of transaxial plane (X-Y) grayscale images. Note that the images may be viewed in further detail, using another software provided by SkyScan, called “DataViewer”, in the following planes:

- the coronal plane (X-Z)
- the sagittal plane (Z-Y)

The images from these two planes can then be exported as further stacks, converted to binary images and the *centroidTracker* algorithm may obtain the microstructural information of the TMW devices from them. However, this option was not pursued further, and can be considered for further work in the future. The benefit of using these images would be that the in-plane wires would be out-of-plane in another plane, and therefore easily identified. This allows a more complete representation of the microstructure to be obtained.

3.6 Image processing procedure

3.6.1 Trade-off study: time vs. complete microstructural representation

The transaxial plane cross-sectional grayscale images produced were 2000 x 2000 pixels, and contained numerous foreground pixels that indicated wire segments.

As a result of this, the processing of an entire specimen took several days on a standard PC to complete. Images of dimensions 725 x 725 pixels were used during the development of the *centroidTracker* algorithm, and a single tracking run took approximately 18 hours to run, whereas a run on a full dataset took approximately four and a half days to complete.

An analysis of binary images of various dimensions was performed to identify a compromise between the image size and processing time. This analysis simply used the specimen porosity, found as the ratio of the area covered by the foreground pixels (i.e. the wires) to an estimated area of the specimen footprint, for various image dimensions. The aim of this exercise was to identify the image size at which the porosity of the images changed, and hence this was used as an indicator to show that images smaller than a certain image size cannot be used in the analysis. The areas of the foreground pixels were obtained directly from the Image Processing Toolbox on MATLAB. The area of the full specimen was estimated using its known inner and outer radii (in pixels). For other irregularly shaped segments of the specimen, the areas were calculated graphically through a combination of curve fitting a 4^{th} order polynomial to user-selected points around the segments, and the trapezoidal rule numerical integration technique. Areas not covered by the specimen footprint were not used in the calculations as these introduced bias in the porosity calculations, caused by these backgrounds. For image dimensions that fitted within the confines of the specimen footprint, the areas were simply that of the image size.

Tables 3.16 and 3.17 illustrate the image dimensions considered, the calculated foreground areas, the estimated total areas, as well as the respective estimated porosities for image numbers 238 and 436 from a stack of 638 images, shown in Figure 3.20.

Image dimensions	**Foreground area**	**Total area**	**Porosity**
300 x 300	20020	90000	0.222
500 x 500	53710	250000	0.215
725 x 725	93987	423253	0.222
1000 x 1000	144563	665176	0.217
2000 x 1000	241680	1142434	0.212
2000 x 2000	484448	2224872	0.218

Table 3.16: Porosity estimations for images of various dimensions, performed on image 238

Image dimensions	Foreground area	Total area	Porosity
300 x 300	21153	90000	0.235
500 x 500	55992	250000	0.224
725 x 725	97569	421503	0.231
1000 x 1000	155347	655035	0.237
2000 x 1000	252862	1114419	0.227
2000 x 2000	497663	2224872	0.224

Table 3.17: Porosity estimations for images of various dimensions, performed on image 436

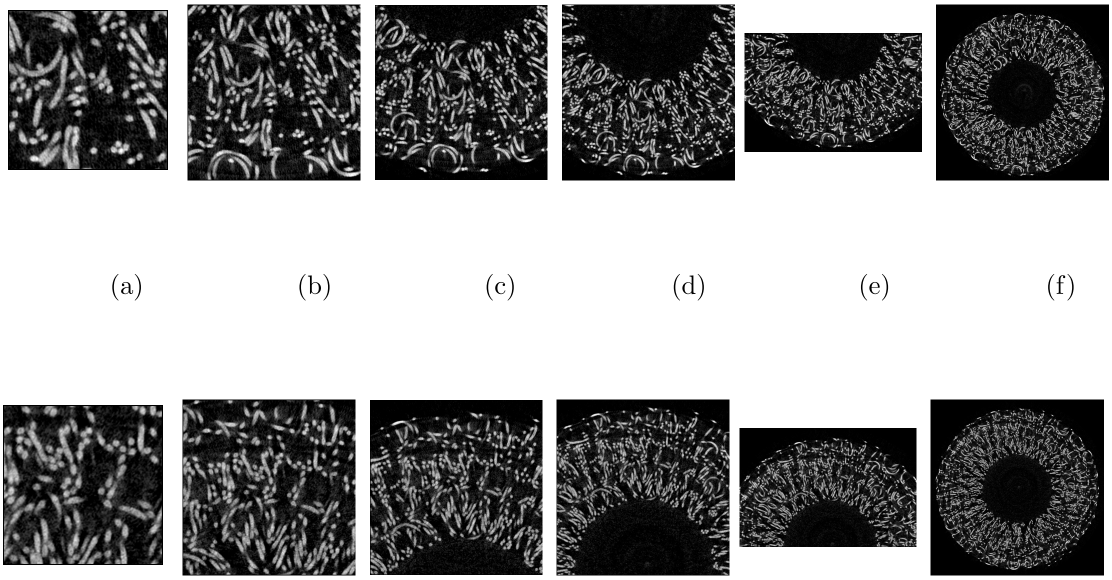

(a) (b) (c) (d) (e) (f)

(g) (h) (i) (j) (k) (l)

Figure 3.20: Images considered for porosity calculations. (a) - (e) and (f) - (l) belong to images 238 and 436, respectively. The images shown, scaled down for illustration purposes, correspond to the image dimensions outlined in Tables 3.16 and 3.17

The consistency of the porosities for both images at the different dimensions indicate that even small images could be used for analysis purposes, without losing integrity of obtained data. However, the smaller the dimension of the image, the less likely a feature that may be important would appear in the stack of images. Therefore, it was decided that the images that would be analysed would be 725 x 725 pixels, a compromise between time and total representation of features in the images. An image of 725 x 725 pixels corresponds to a physical size of approximately 7.2 x 7.2 mm. The largest microstructural feature is the coil diameter, and the chosen image size could fit in 5 or 6 coils in any direction. This was a second measure of justifying the use of smaller image sizes.

3.6.2 Pre-processing

The specimens moved within the confines of the compression test rig due to the manual handling (loading/unloading) of the specimens after the respective scans were performed. For this reason, the images from different scans were rotated by an estimated angle using some features as a reference, such that the *centroidTracker* algorithm could track the same set of wires at successive compression levels for the same specimen. This gave a direct representation of the change in microstructural properties within the TMW devices.

The final step, following the image rotations, was to run the *centroidTracker* algorithm. It was decided that the algorithm would be set to run three times (three passes) for each stack of transaxial images of each specimen at each compression level. In between each pass of the algorithm, the images were ‘opened’ to get rid of wires that had already been identified. This helped wires that were not identified in the one pass to be identified in the successive passes. An example of this can be seen in Figure 3.21.

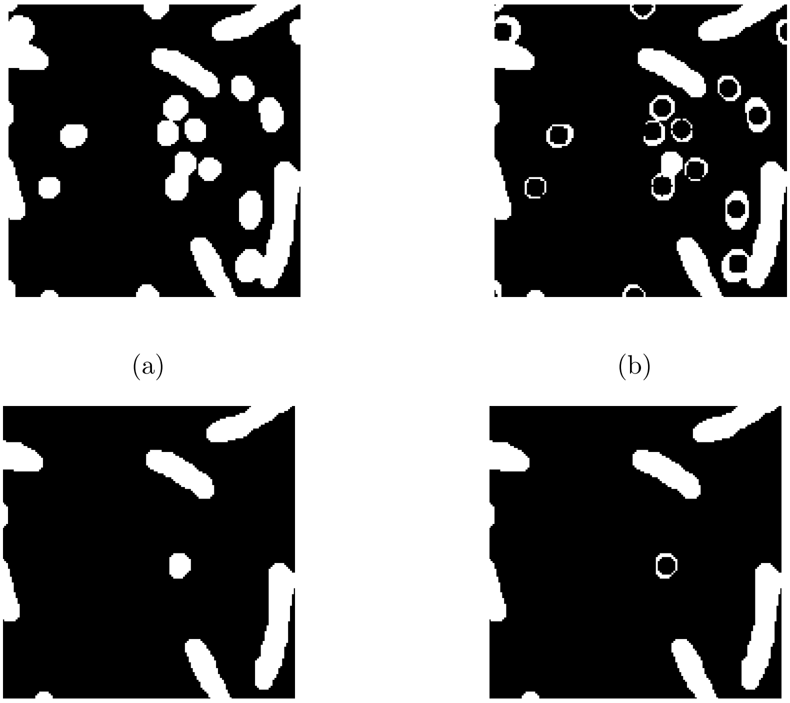

(a) (b)

(c) (d)

Figure 3.21: Image ‘opened’ in between successive passes to allow unidentified wires in one pass to be identified in successive passes: (a) original image, (b) image after first pass, (c) image ‘opened’, (d) unidentifiable wire object in previous pass identified in current pass

A script was written for the images of each compression level of each specimen to do the following:

1. Read grayscale images, and convert to binary. ‘Open’ and clean each binary image to remove wire objects that are too small. Save all images.
2. Run first pass *centroidTracker* algorithm, which saves the information extracted from the images at the end of the algorithm.
3. Load and ‘open’ the processed images to remove wire objects that have already been identified.
4. Run next pass of *centroidTracker* algorithm. The algorithm adds to the information already obtained from the previous pass and saves the new, updated information.

5. Repeat Step 3 and 4 for the final, third pass.

The algorithm was run on several computers in an effort to minimise processing time.

3.6.3 Post-processing

A simple analysis was performed on a representative image midway along the axial length, where the wire density was the highest, to gauge the success rate of the algorithm for the wire detection. This was calculated by manually counting the number of wire segments present in an image before the algorithm performed its task, after the first pass, second pass, and finally, the third pass. Table 3.18 breaks down these results, showing the number of "unidentified" wire segments, following multiple passes of the *centroidTracker* algorithm. The percentage of wires detected following the third pass was around 77.5%. Given that the algorithm was created to detect the evolution of out-of-plane wires, and the remaining wire segments after the final pass were mostly in-plane wires, algorithm was considered a success.

	Original	**First pass**	**Second pass**	**Third pass**
Number of unidentified wire segments	373	113	98	84
Wire segments identified, %	-	69.7	73.7	77.5

Table 3.18: Number of unidentified wire segments, and percentage of identified wire segments following the respective passes of the *centroidTracker* algorithm

After the microstructural information was acquired, the next task was to analyse the data to extract meaningful information. The information sought out was the distribution of free, and contact length information.

A script was created to assess the state of the contacts within the microstructure. The code iterated through each co-ordinate in every group of wire strands, and performed calculations to evaluate the three dimensional Euclidean distance between neighbouring wires. If the Euclidean distance was less than or equal to a nominal value, two wire co-ordinates from different wire strands were considered to be in contact, and if the Euclidean distance was greater than the nominal value, the wire co-ordinate was considered free. The nominal value was obtained by taking average minor axis lengths, with a small tolerance, from randomly chosen independent objects from randomly chosen images. The result of whether a co-ordinate was free or in contact was indicated as a separate variable, and was added to the structured database that carried all other information.

Once all the coordinates in the datasets were analysed for contacts, the next step was to perform a set of calculations to assess the lengths of the free, and contact lengths. Another script was created to calculate these lengths. For each group of wires, the code iterated through the respective co-ordinates, and checked whether a co-ordinate was free or in contact with a neighbouring group of wire.

- If two or more successive co-ordinates from a single wire strand were free (or in contact), the Euclidean distance was calculated and added to the running sum of free (or contact) lengths for that wire.
- When a wire strand changed from being free to being in contact (or vice versa), Euclidean distances were calculated and added to the running sum for the new state.

3.7 Results and discussion

Figures 3.22 and 3.23 illustrate examples of the three-dimensional skeletal microstructure of TMW devices. Figure 3.22 show the full microstructure at 0% static compression, captured by the *centroidTracker* algorithm, whereas Figure 3.23 (a) - (c) illustrates the evolution of the TMW device skeletal microstructure following the application of 0%, 5% and 10% static compression. It is clearly not possible to distinguish any meaningful result from either of these figures, simply due to the high number of wires identified by the *centroidTracker* algorithm.

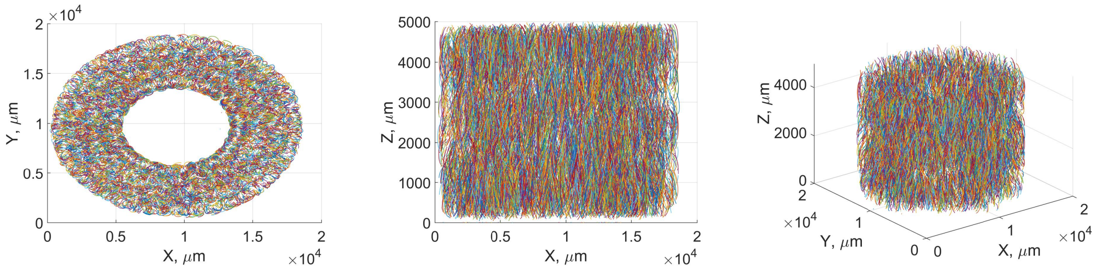

(a) (b) (c)

Figure 3.22: 3D skeletal microstructure of TMW device following three passes of *centroidTracker* algorithm on the full specimen ($\tilde{\rho}$ = 0.18, Specimen 2; image size: 2000 x 2000 pixels) for 0% static compression. (a), (b), and (c) show the same microstructure at different viewing angles

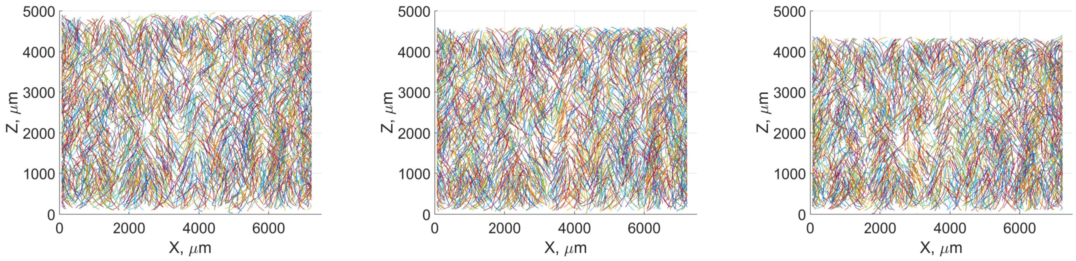

(a) (b) (c)

Figure 3.23: 3D skeletal microstructure of TMW device following three passes of *centroidTracker* algorithm on a section of the specimen ($\tilde{\rho}$ = 0.18, Specimen 2; image size: 725 x 725 pixels) for: (a) 0% static compression, (b) 5% static compression, and (c) 10% static compression

Due to the sheer volume of wires identified, the results obtained for each specimen were analysed using histograms to understand the microstructural state of the population of wires for the three levels of compression applied to them. These were divided into two categories, free and in-contact wires. A free wire was defined as a wire that did not have a neighbouring wire, located within a length of the diameter of the wire (and a small tolerance). An in-contact wire was defined as the opposite of a free wire.

3.7.1 Full range vs. region of interest

Figure 3.24 shows the free and contact length distributions for the full specimen range, and a selected range of interest (ROI). It can be seen that both distributions for the full specimen range are much smoother than that of the selected ROI. This is not unexpected because the population of the former is much greater than the latter. Due to the overall trends being nearly identical, this further justified the use of the ROI over the full specimen range. It is appreciated that there are an unrealistic number of short wires (both free and in-contact) in the histograms shown here, and those that follow. They are unrealistic because they have lengths shorter than the wire diameter. Hence, the most trustworthy results are those that occur greater than a length of 150 μm (the diameter of the individual wires in the microstructure).

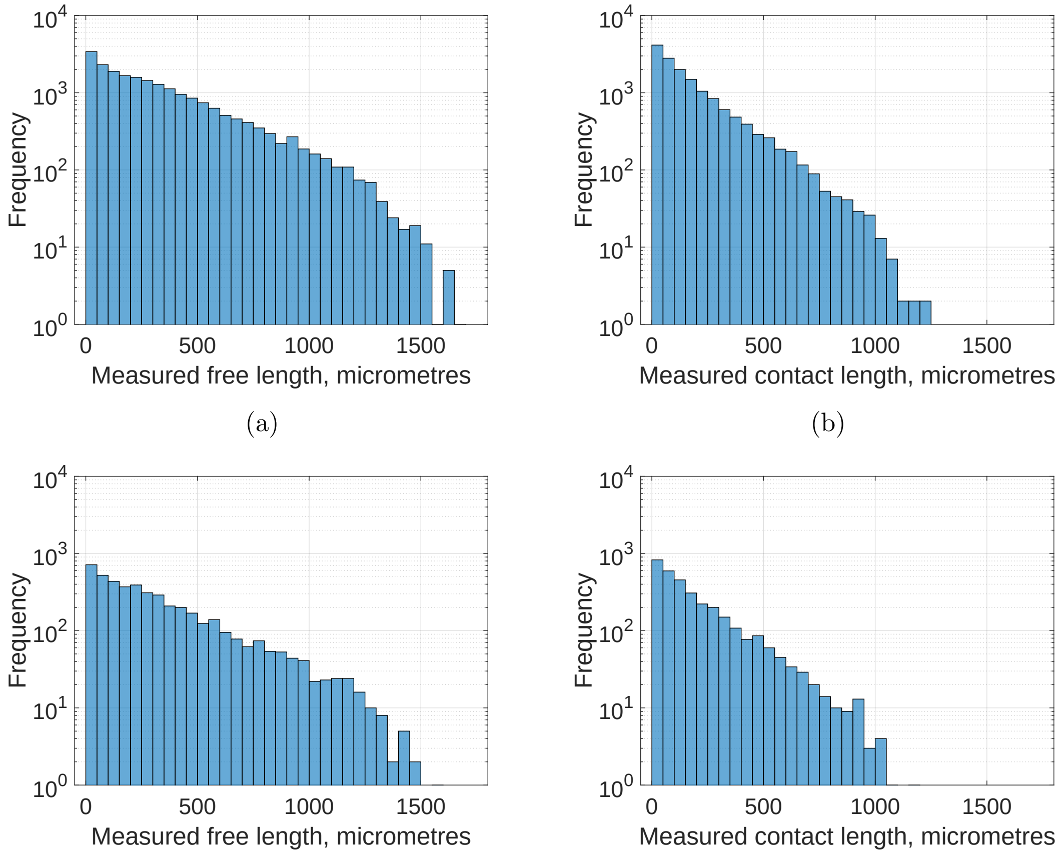

(a) (b)

(c) (d)

Figure 3.24: Free and contact length distributions for: (a - b) the full specimen range, and (c - d) a region of interest, respectively. The specimen used for this study was $\tilde{\rho} = 0.18$, Specimen 2

A final evaluation of the *centroidTracker* algorithm was performed to gauge its success in identifying wires in the microstructure. This evaluation used the wires identified for the full specimen. The total length of wires was calculated (i.e. sum of the free and in-contact wire lengths), and multiplied by the nominal cross-sectional area of the wires (with a diameter of 0.15 mm) to obtain the volume. This was then multiplied by the material density (stainless steel, 7900 kg/m^3) to obtain the mass of identified wires. The total length of wires identified by the algorithm was calculated to be 8.85 m, and the calculated mass based on the corresponding volume was 1.24 g. When comparing this to the masses reported in Table 3.9, it was found that the algorithm identified 72% of the wires. When considering that the algorithm was designed to primarily identify out-of-plane wires, the *centroidTracker* algorithm was a resounding success.

3.7.2 Quick note

Prior to the discussions that follow, it is important to note what is being seen in the figures. Depending on the figure, there are a number of different results overlaid on each other. The overlaying of figures causes the colours of the histograms to appear different from those shown in the legends.

3.7.3 Compression

Figure 3.25 shows how the free and contact lengths evolve following the application of compressive loads. It can be noted that the distributions are skewed, with an elongated tail to the right (positive skewness). This is expected due to the relatively high packing densities of the wires, resulting in a higher volume of short wire lengths than long ones.

With an increase in compression, it can be seen that the positive skewness increases. As the compression is increased, the number of long wires reduces, whereas the number of short wires increases. There is one case, Figure 3.25 (e), where interestingly, there are two very long free wires identified when the compression is increased to 10%. While the probability of this occurring is low, it is still possible for such a case to occur, especially if contacts on either end of a free wire move apart following the application of a load. As loading increases, contacts are generally forced to get closer to each other. Furthermore, there are also many new contacts created. A combination of these lead to a drop in the free wire length.

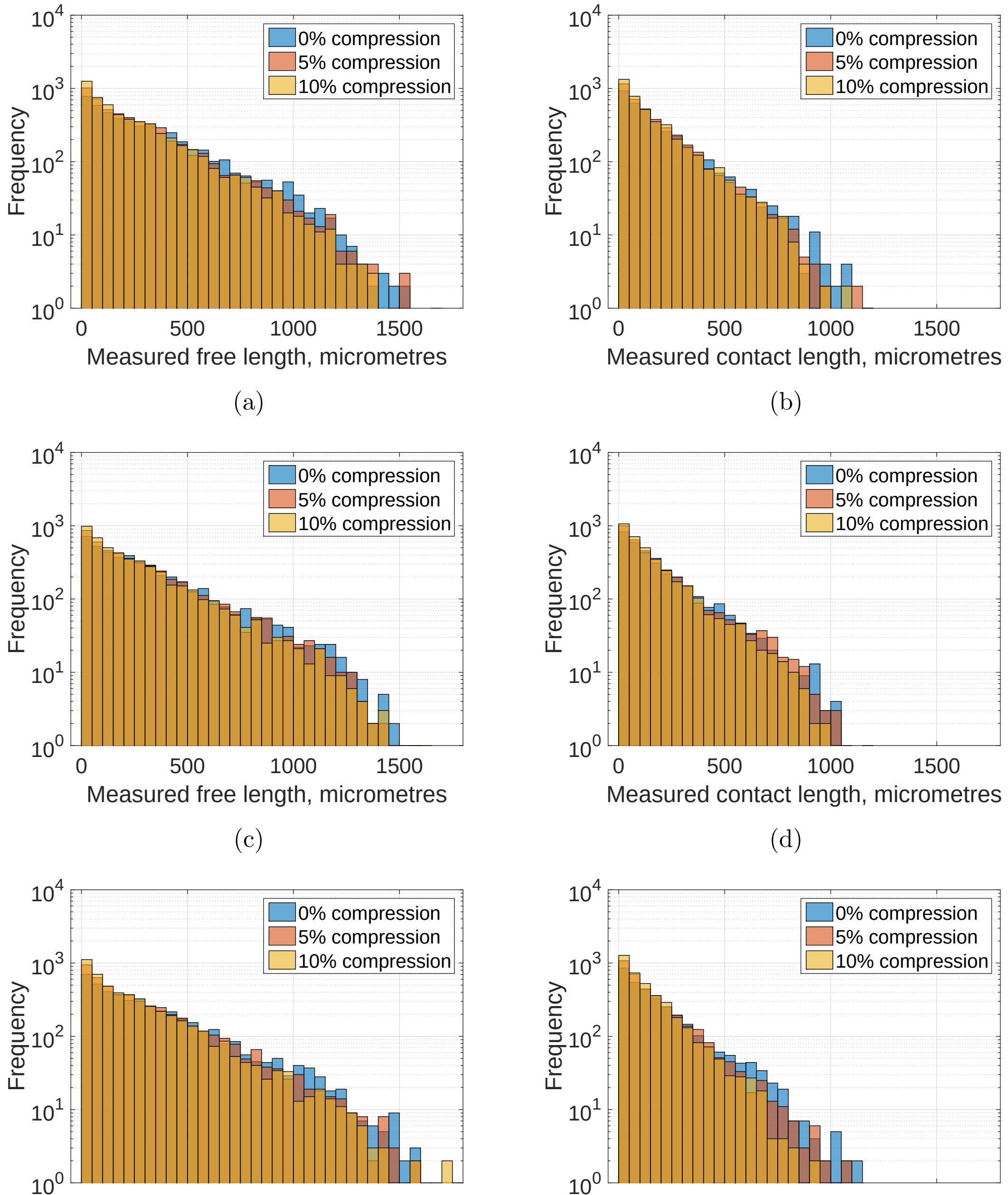

(a) (b)

(c) (d)

(e) (f)

Figure 3.25: Free and contact length distributions following the application of compression loads for: (a) and (b) Specimen 1, (c) and (d) Specimen 2, (e) and (f) Specimen 3. All specimens are from the specimen group $\tilde{\rho} = 0.18$

As the compression is increased, the relative density of the TMW devices also increases. As a result, the X-ray penetration through the specimen is reduced. When this happens, wire agglomerations increase, making them more difficult to separate and gain a quantitative understanding of the contact lengths. Since the wires are naturally spiral, when loading is applied, the wires move from one contact state to another, whereby two or more parallel wires slip, making them non-parallel, and hence the lengths of the contacts decrease. From these histograms, there are clear increases in the number of shorter wires, which indicates that many new contacts are being generated.

3.7.4 Compression vs. decompression

The distributions in between the compressions and decompressions in Figure 3.26 have very few noticeable changes between them, both for the free lengths and the contact lengths. The fact that the microstructure is almost unchanged between compressions and decompressions may point to a device that is completely elastic. However, this is not the case, as justified by the size of the hysteresis loops observed during the pre-conditioning exercise (and testing carried out in Chapters 4 and 5). It must be noted that the preparation times of applying the different loading conditions, as well as the scanning procedure itself were quite lengthy. This gave sufficient time for the microstructure to relax considerably such that it returned to its original state. It is therefore fair to state that μ-CT imaging is not appropriate in understanding short term dynamics occurring in any material. However, the lessons learnt in a static setting can be applied to understand the dynamic behaviour.

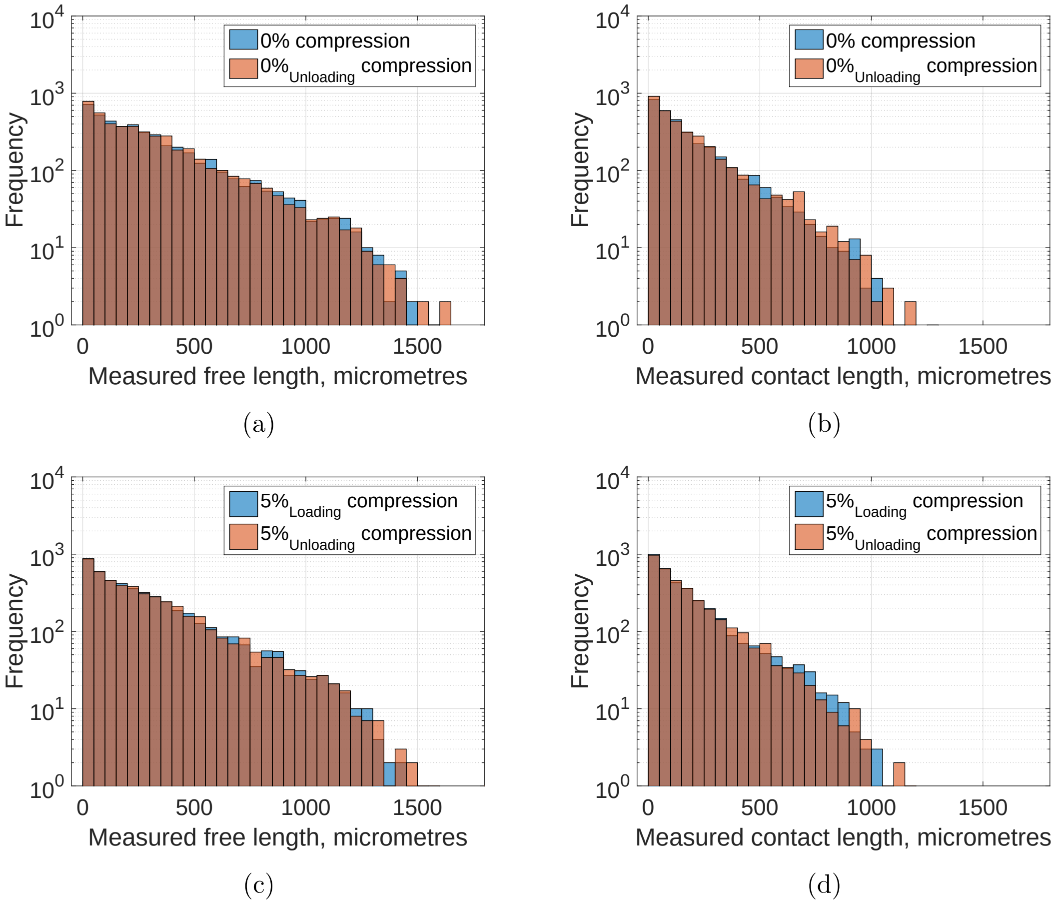

(a) (b) (c) (d)

Figure 3.26: Free and contact length distributions following the application of compressive loads from 0% strain, up to 10% strain, and then back to 0% strain. The specimen chosen for this study was $\tilde{\rho} = 0.18$, Specimen 2

3.7.5 Repeatability

Following the discussion in the previous section, it is expected that the microstructure distributions would remain fairly consistent following repetitions of the same loading regimen. There are a few variations in the results observed in Figure 3.27, but they do not possess a significant bearing.

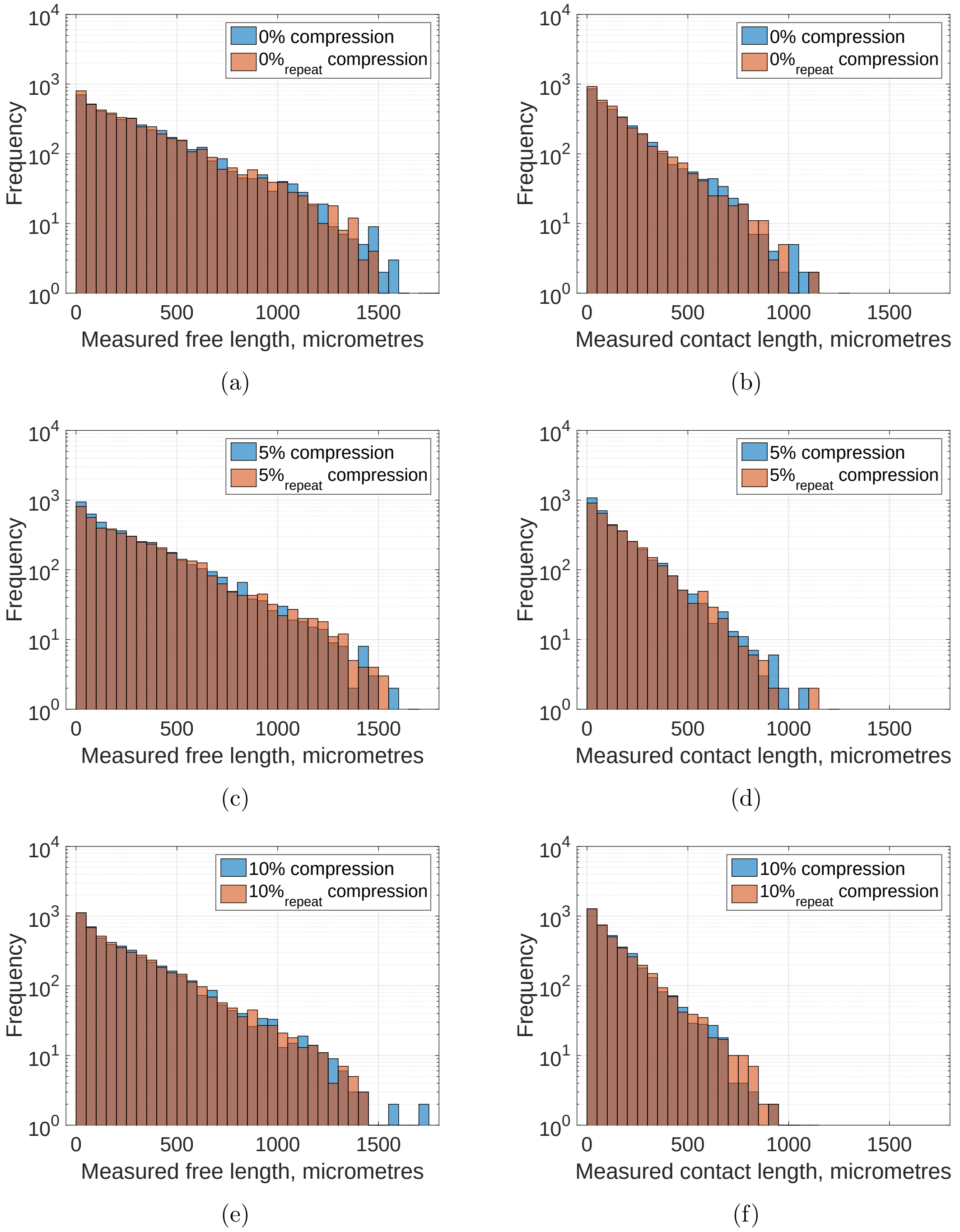

(a) (b)

(c) (d)

(e) (f)

Figure 3.27: Free and contact length distributions following the application of compressive loads from 0% strain, up to 10% strain, and then repeated with the same compressive loads. The specimen chosen for this study was $\tilde{\rho} = 0.18$, Specimen 3

3.8 Conclusion

It has been well documented, and widely accepted, in the research community that the internal microstructure of TMW dampers was previously unknown. While microcomputed tomography (μ)-CT technology has been around for a few decades, its use has mostly been restricted to the medical field. Some researchers have used μ-CT imaging as a means to explain the microstructure, but have not used it quantitatively. In the cases reviewed, a few images were shown to qualitatively support the physical response of the tangled metal wire (TMW) devices. As such, this method of analysis does not paint a global picture, and can hence not be used to deterministically explain the dynamics of TMW devices.

This chapter delved into understanding the microstructural state of TMW devices in a global sense. The *centroidTracker* algorithm was developed to track the evolution of wires through the axial cross-sectional images produced from μ-CT scanning. Along with the algorithm, several other functions, which are encompassed within the *centroidTracker* algorithm, were explained.

A total of five specimens were chosen from a population of 10 specimens for $\mu - CT$ scanning (three with a relative density ($\tilde{\rho}$) of 0.18, and two with 0.23). These specimens were preconditioned to ensure minimal changes to the microstructure in between load cycles. A compression test rig was designed and manufactured to provide compressive loads on the TMW devices while they were being scanned. The images resulting from the μ-CT scans were reconstructed to produce axial cross-sectional images of the TMW devices. It was found that the scans of the higher relative density specimen produced low quality images, and hence further analysis work was not carried out for this specimen. During the scanning procedure, the specimens moved when they were being compressed or decompressed and re-attached to the scanner. Due to this, the axial images for successive load/unload cycles were rotated to align wire locations between the respective sets of images. The images were then narrowed down to a region of interest. The basic assumption in doing so was that the average behaviour was the same for all regions in the images. The benefit that arose from this was minimising time, whilst still being accurate enough to capture sufficient features from the images. Results from the full specimen were also evaluated, and it was found that 72% of the wires were identified. When considering the primary goal of the algorithm (track out-of-plane wire motion), the algorithm was deemed to be successful.

The cropped stack of images were then fed into the *centroidTracker* algorithm, which extracted the centroid information of wire objects, and constructed a three dimensional skeletal structure of the TMW devices. The results from the centroid co-ordinates were then used to indicate whether a wire was in contact with neighbouring wires or not. Furthermore, measurements of the lengths of the free and in-contact wires were made. The vast population of wires that were either free or in contact were then studied statistically to observe quantitatively, for the first time, how the microstructure of TMW devices evolve between static load cycles. It was found that following the application of compressive loads, the length of the free wires generally became lower, and there were more short wires. It was also seen that there were a higher number of wires in contact following the application of a compressive load, but the length of the wires in contact tended to also reduce. This was justified by the spiral nature of the wires. Wires that agglomerated in parallel to one other deformed relative to each other following the application of a compressive load, making the contact lengths between them shorter. In terms of changes in the microstructure between load/unload cycles and separate load cycles, it was seen that the microstructure remained relatively unchanged. The results of this repeatability is seen in more detail in Chapters 4 and 5, where the experimental hysteresis curves between load cycles are shown to be repeatable.

Now that the microstructural behaviour of the TMW devices have been shown in a static setting, it forms the basis for the quasi-static and dynamic behaviour to be tested and discussed, before revisiting the results from this chapter to discuss the analytical modelling performed in Chapter 6.

Chapter 4

EXPERIMENTAL STUDIES: QUASI-STATIC AND LOW FREQUENCY DYNAMIC TESTING

4.1 Introduction

Viscoelastic materials have traditionally been employed in damping energy from mechanical vibrations. The manufacturing process of these materials can be manipulated to accommodate specific properties. Whilst they are effective over particular temperature and frequency ranges, these materials are known to under-perform in extreme working conditions, such as high temperature or corrosive environments. A solution to this issue comes in the form of Tangled Metal Wire (TMW) devices, which possess elastic modulus and damping properties similar to that of some elastomeric rubbers.

In Chapter 2, it was reported that Zuo, et al. [22] and Hong, et al. [12] studied the force-displacement behaviour of TMW devices. The authors of these two publications noticed that there were three distinct stages on the curves. The first stage was reportedly short, where the load rose rapidly with displacement. The second stage, which was reportedly the longest of the three stages, involved a drop in stiffness as the load gradually increased with displacement. The final stage involved an exponential increase in load with displacement. It must be noted that there were only two distinct stages reported by Chandrasekhar, et al. [75], with the first stage having a lower stiffness than the second stage.

The experimental study for this chapter was carried out to observe the amplitude and frequency dependency of the TMW devices, and to explain the resulting behaviour in terms of the microstructural properties. Previous research has primarily focused on quasi-static behaviour, whereas reports on dynamic behaviour have been limited. Testing was carried out using an industrial hydraulic test system, the MTS 858 Table Top dynamic test system. The investigations here have two different aspects. In the first case, displacements were applied to the specimen at a low rate. As a result, the inertial effects had negligible effects on the loading of the specimen and were hence ignored. For simplicity, this loading is referred to as quasi-static. In the other set of tests, the applied displacements were dynamic, at different frequencies and amplitudes.

4.2 Quasi-static testing

4.2.1 Experimental methodology

Steady state, quasi-static tests were carried out on the washer shaped TMW specimens detailed in Chapter 3 using an MTS 858 Table Top dynamic test system. It employs a hydraulic ram to apply compression whilst acquiring displacement and force data.

The experiments were displacement controlled. To maintain structural integrity and avoid induced plasticity in the wires, the tests were restricted to a maximum nominal specimen strain of 0.1, noting that pre-conditioning exercises were performed on all specimens to nominal specimen strains of 0.12.

Compression was applied with increments of 0.06 mm to a maximum displacement of 0.6 mm (i.e. steps of 0.01 strain to 0.1 maximum), and then unloaded back to the initial position. The applied compression rate was 0.006 mm/s (in terms of strain rate, 0.001/s). There were negligible changes to the specimen height after the first quasi-static loading and unloading cycles. These changes are partially attributed to flattening of the uneven TMW surfaces. Previous research, for example the work carried out by Chandrasekhar, et al. [75], had shown much more drastic changes in specimen dimensions than those observed in this present research. In the research carried out previously by Chandrasekhar, et al., specimens were tested with no prior pre-conditioning, and also with no knowledge of previous loading histories of the specimens tested. The pre-conditioning exercises on each of the tested specimens helped in curtailing the significant changes in dimensions. Theoretically, because the specimens have already faced higher strains, testing carried out at lower strains should produce more repeatable results. A similarity can be seen in fibrous materials when these materials face a high strain, the fibres damage and the elastic stiffness reduces, but when the strains are lowered, no further damage takes place and so the material is normalised for subsequent tests [65]. In the case of TMW devices, the changes in plasticity will be reduced because the wires that deform plastically have already done so at the higher loads, and so the specimens would be expected to behave similarly in the tests that follow.

The tests were carried out three times to ascertain repeatability of each specimen. For the first load/unload cycle, a pre-compression force of 20 N was applied for each specimen. This ensured that there was complete contact between the surfaces of the hydraulic ram and specimens tested. For the succeeding set of experiments on each specimen, the starting position of the hydraulic ram and the compression displacements were maintained, noting that there was a negligible change in specimen dimensions after the first cycle. This allowed for comparison of the changes in properties. In the work carried out by Chandrasekhar, et. al. [75], it should be noted that all experiments were repeated on a separate day due to consistently changing hysteresis behaviour between the first three experiments. As shall be seen in Section 4.2.2, this was not merited in this work because the hysteretic behaviour of all specimens proved to be consistent between the respective tests, thanks to the pre-conditioning regimen followed.

4.2.2 Results and discussion

Figure 4.1 illustrates an example of the displacement time history of these quasi-static tests for $\tilde{\rho} = 0.18$, Specimen 1. After each displacement, the specimen was given a dwell time of 10 seconds so that it could stabilise. Figure 4.2 shows an example of the force time history for the same specimen. Noise on the raw force signal was noticeable but as the standard deviation was approximately 0.8 N, it was decided that the data collected were acceptable for these investigations. As the experimental procedures for the rest of the specimens are identical, the respective time histories of displacement and force are not shown.

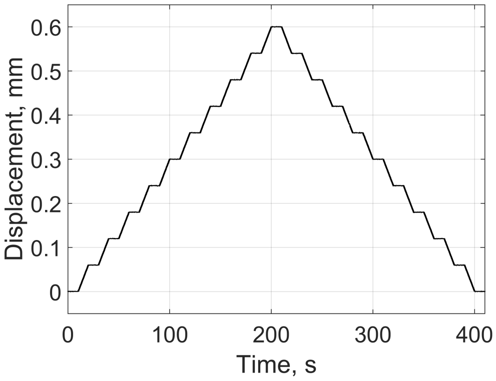

Figure 4.1: Quasi-static displacement time history for $\tilde{\rho} = 0.18$, Specimen 1

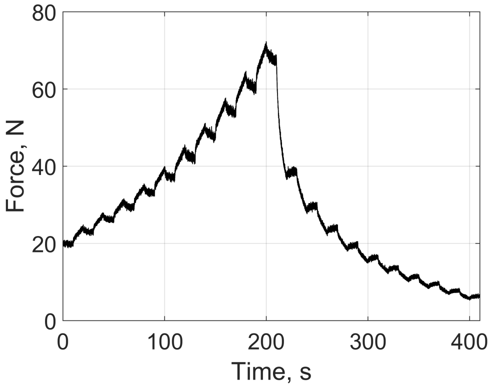

Figure 4.2: Quasi-static force time history for $\tilde{\rho} = 0.18$, Specimen 1

In Figure 4.2, it can be seen that each time the loading increases, noticeable relaxation occurs, in an exponential manner. The magnitude of this relaxation increases for higher loads. A possible explanation is that compression increases the number of contacts in the microstructure which restrict the rate at which the wires are able to reorganise their positions. This in turn increases relaxation time.

During the unloading process, the force reduces significantly for the first load step, and the rate of the drop in force reduces as the specimen is unloaded. Relaxation is also seen to occur in the unloading process, this time in the opposite direction. The trend is similar to the loading process, in that the magnitude of the relaxation and relaxation time reduce at lower loads. Another important deduction is that the force almost returns to zero before the hydraulic ram reaches its starting position i.e. in the final part of the test there is only a small contact between the hydraulic ram of the test machine and the specimen surface. There is a net difference between the magnitudes of the relaxation forces in loading and unloading. One explanation for this is that the wires, which store deformation energy, become 'locked' in position by friction at the contact points. These locked wires can only be released if a force greater than the friction force is supplied. When unloading, the restoring forces are unable to provide this.

Figure 4.3 illustrates the quasi-static force-displacement curves that correspond to the data in Figures 4.1 and 4.2, which takes the form of a hysteresis loop.

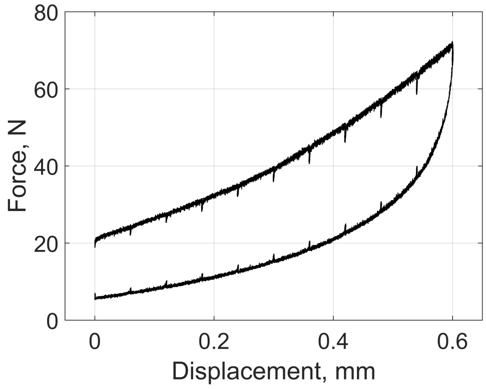

Figure 4.3: Quasi-static force-displacement curve for $\tilde{\rho} = 0.18$, Specimen 1, Test 1

Figure 4.3 indicates the 20 N pre-compressive load added to the specimen at the start of the loading stage. It can be seen that the force returns to a value of 5 N at the end of the unloading stage. The second experiment carried out on the specimen resumed the loading from the same starting position as the first, i.e. from 5 N. Figure 4.4 shows the hysteresis loop of the second load/unload cycle for the same specimen essentially starting and stopping at a force of 5 N, indicating no changes in the geometric dimensions of the specimen.

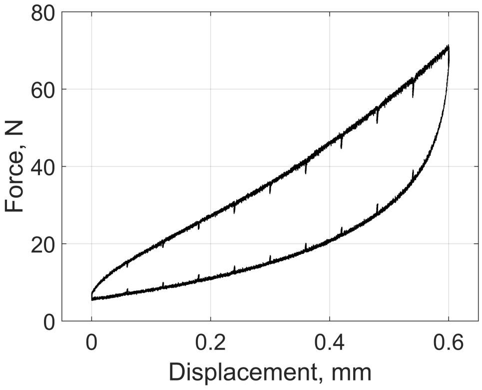

Figure 4.4: Quasi-static force-displacement curve for $\tilde{\rho} = 0.18$, Specimen 1, Test 2

The relaxation behaviour of the specimen can be seen as spikes on the data. The loading curve is moderately nonlinear, with the specimen gradually stiffening with increased compression, whereas the unloading curve is more nonlinear, with the largest changes occurring at the greatest deflection.

An explanation of the observed behaviour is as follows. New contacts and therefore, contact forces, within the specimen are created as the material is progressively deformed. The microstructure deforms both elastically and in a plastic-like manner. This quasi-plastic behaviour occurs because of a number of reasons. These include friction locking of wires after they have moved under load, plasticity at wire-to-wire contacts, and plasticity in the wires themselves due to bending and torsion. It is possible that the quasi-plastic behaviour could dictate the rate dependency observed. Due to the microstructure, the load is shared such that the overall stiffness increase is gradual. At maximum displacement, there are a number of new contacts and contact forces compared to the undeformed state. As the specimen is unloaded, the spring like nature of the elastically deformed wires causes the number of contacts (and contact forces) to decrease much more rapidly, making the stiffness drop rapidly. The quasi-plastic deformations also begin to unload at the same time, but the contribution of this process is slower, and the change in the number of contacts reduces, thereby making the stiffness drop more gradual.

Figure 4.5 shows a comparison of the force-displacement results from the three tests for Specimen 1 of $\tilde{\rho} = 0.18$. The benefit of pre-compressing the specimen in the first load/unload cycle is clearly seen here. It enforced the surface to be even, and when unloaded and reloaded, the results were highly repeatable.

It can be seen that there is a change in stiffness between Test 1 and Test 2, attributed to the pre-load being applied. The results for Test 2 and Test 3 indicate similar stiffness characteristics both in loading and unloading

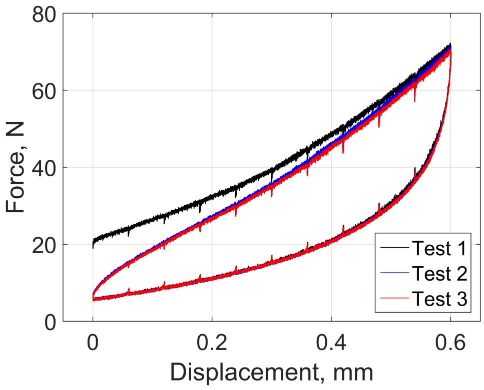

Figure 4.5: Quasi-static force-displacement curves of all tests performed on $\tilde{\rho} = 0.18$, Specimen 1

Figure 4.6 shows the quasi-static test results for the remaining specimens. It is clear the hysteretic path followed by each specimen is nearly identical. It is interesting to note that $\tilde{\rho} = 0.18$, Specimen 3 is much stiffer compared to Specimens 1 and 2 of the same relative density. In fact, $\tilde{\rho} = 0.18$, Specimen 3 is comparable with $\tilde{\rho} = 0.23$, Specimen 2. However, these differences are not completely unexpected, and give further evidence of the random nature of the TMW microstructure.

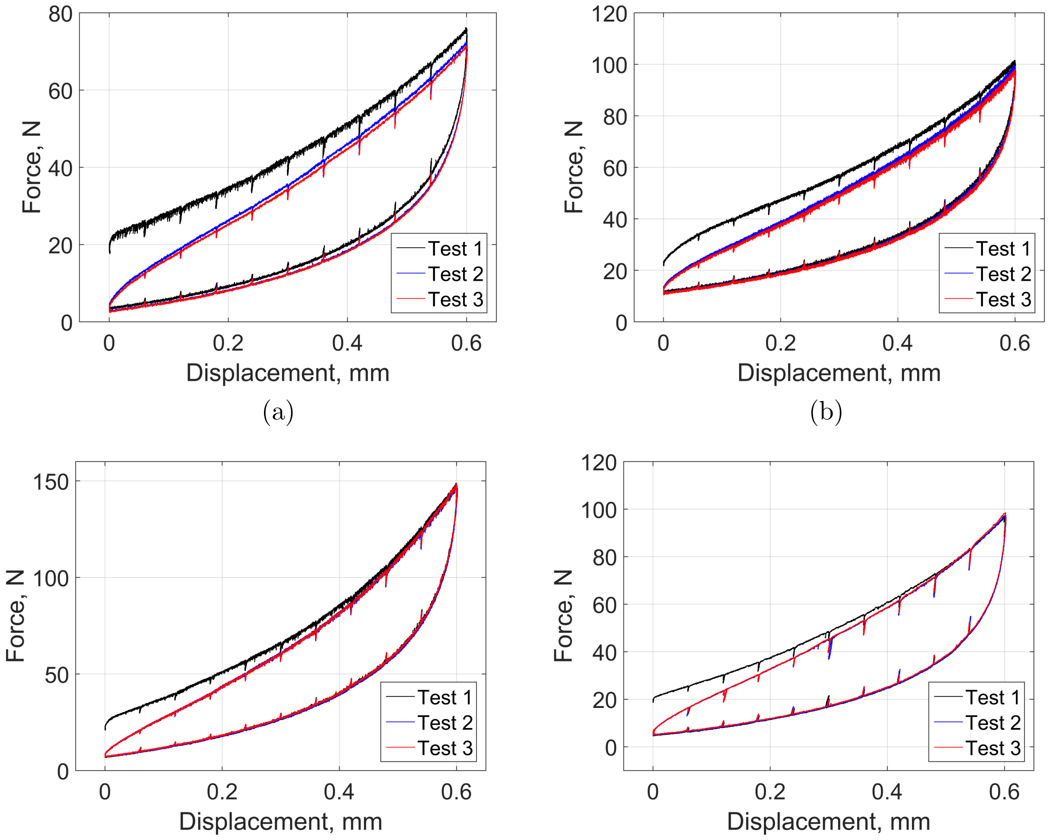

(a) (b)

(c) (d)

Figure 4.6: Quasi-static force-displacement curves of all tests performed on: (a) $\tilde{\rho} = 0.18$, Specimen 2, (b) $\tilde{\rho} = 0.18$, Specimen 3, (c) $\tilde{\rho} = 0.23$, Specimen 1, and (d) $\tilde{\rho} = 0.23$, Specimen 2

Table 4.1 summarises the average coefficients of stiffness calculated for the results shown in Figures 4.5 and 4.6. These coefficients of stiffness were estimated by fitting a polynomial to the elastic part of the force-displacement curves, and then computing the gradient of the polynomial at the midpoint of these curves. The method is described in further detail in Section 4.3.1. Note that the stiffness coefficients were not computed for the first tests of each TMW specimen since the hysteresis curves were not complete, as seen in Figures 4.5 and 4.6.

Relative Density, $\tilde{\rho}$	**Specimen ID**	**Average Stiffness, N/mm**	
		Test 2	**Test 3**
0.18	1	73.9	72.3
	2	77.6	76.7
	3	98.9	98.0
0.23	1	152.1	154.0
	2	95.2	96.6

Table 4.1: Estimated average coefficients of stiffness of quasi-static tests performed on the respective specimens

Comparison with literature

Table 4.2 provides an indication of the approximate range of TMW device coefficients of stiffness reported by other researchers in literature, as well as the results reported in this thesis. In the reported results shown below, the TMW devices were all made of stainless steel.

Author	**Coefficients of stiffness**
Hong, et al. [12]	25 - 500 N/mm
Wang, et al. [23]	2.4 - 7.4 N/mm
Ao, et al. [29]	60 - 140 N/mm
Chandrasekhar, K. [present work]	74 - 154 N/mm

Table 4.2: Range of TMW coefficients of stiffness reported in literature for quasi-static testing, as well as those reported in this thesis

The reported stiffness coefficients occupy a wide range of values, as seen in Table 4.2, even though all the studies involved TMW devices made from stainless steel. One of the reasons for these discrepancies is that the TMW devices studied had various configurations, ranging from different shapes, dimensions, relative densities, wire thicknesses, and so on. Additionally, the TMW devices were subjected to different extents of quasi-static loading. Readers are encouraged to read the publications listed above for further details on the work carried out by the respective researchers.

4.3 Low frequency dynamic testing

4.3.1 Experimental methodology

The TMW specimens were subjected to dynamic loading, at different pre-compressions and dynamic displacements on the same MTS test system. The TMW specimens were tested at four frequencies 1Hz, 3 Hz, 10 Hz, and 20 Hz, for each of the static and dynamic strains illustrated in Table 4.3. As with the quasi-static tests, displacements were chosen according to the strains that the specimens would face in the tests, and the tests were displacement controlled.

Static Strain	**Dynamic Strain**
1%	1%, 2%
5%	1%, 2%, 5%
9%	1%, 2%
1% (unloading)	1%, 2%

Table 4.3: Range of static strains and dynamic strains examined

Between each test, a dwell time of 10 seconds was allocated in order for the specimen to recover, and when the pre-compression was increased, the applied strain rate was 0.001/s. A set of experiments was also performed on the specimens during the unloading process, allowing a comparison to be made on the change in properties, before and after the core dynamic experiments.

Figure 4.7 shows an example of the dynamic test data (the displacement time history).

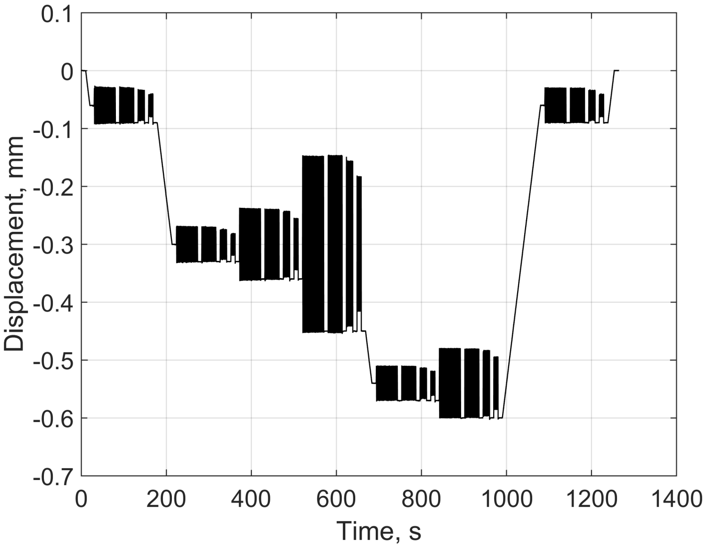

Figure 4.7: Displacement time history of dynamic test data

In order to allow the specimen to stabilise, the test was run for a number of cycles, depending on the frequencies being tested. These can be summarised in Table 4.4.

Frequency, Hz	**Number of cycles**
1	50
3	100
10	150
20	200

Table 4.4: Number of cycles at the different frequencies tested

Each block of static strains shown in Figure 4.7 contains the four frequencies tested, and also different dynamic strains applied. It was noted that the dynamic amplitudes reduced as the frequencies were increased, and this reduction was attributed to the hydraulic test system surpassing its loading capacity. A low pass filter was applied to the force and displacement data to suppress high frequency noise.

As with the quasi-static data, the resulting force-displacement hysteresis curves were nonlinear and asymmetric. In order to relate behaviour to well-understood terms, the curves were processed to give a mean stiffness coefficient (at the midpoint of the hysteresis curves) and an effective loss factor using the procedure described below.

1. The origin for the force and displacement values was reset half way between the maximum and minimum values.

2. The force-displacement hysteresis curve was “split” into 100 distinct vertical slices across the span of the displacement axis. A mean value was then obtained for each slice.

3. A fifth order polynomial was fitted to the filtered, and averaged force-displacement data. The averaging of the slices helped improve the fit. The fit gave a polynomial equation, which represented the elastic part of the hysteresis curve - shown in Figure 4.8 as the solid black curve. The average dynamic stiffness was then estimated from the derivative of the polynomial equation at the mid-point. The order of the fit was assessed based on its shape, with respect to the overall shape of the hysteresis curve. It was noted that the fit ensured that the polynomial curve intersected with the sharp ends of the hysteresis curves, but also made the fit “bumpy”.

4. The energy dissipated per cycle was calculated by numerical integration as was the total potential energy shown in Figure 4.8 as the grey shaded area.

The damping inherent in materials is often described as a loss factor. As TMW is nonlinear, the loss factor is defined using the energy loss per cycle, $\triangle W$, and the total strain energy, U, to give,

$$\eta = \frac{\triangle W}{\pi U} \tag{4.1}$$

The total potential energy is calculated as the area under the elastic curve (solid black line), which is highlighted in grey in Figure 4.8. This is,

$$U = \int_0^{x_{max}} F(x)dx + \int_{x_{min}}^{0} F(x)dx \tag{4.2}$$

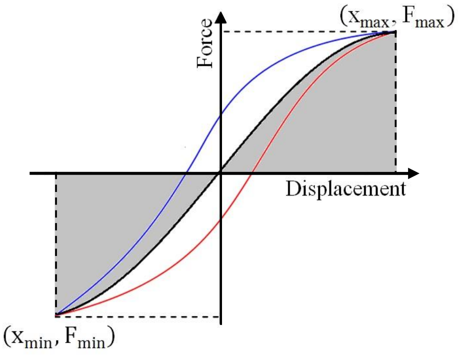

Figure 4.8: Example of a hysteresis curve with origin beginning at the midpoint of force-displacement data

For a linear system, $F_{min}x_{min} = F_{max}x_{max}$, and therefore,

$$U = F_{max}x_{max} \tag{4.3}$$

The maximum potential energy is the potential energy in the first quadrant of Figure 4.8, where force-displacement data is positive (or negative, if the force and displacement data are negative, and in the third quadrant). Therefore, $U = 2U_{max}$ and loss factor,

$$\eta = \frac{\triangle W}{\pi U} = \frac{\triangle W}{2\pi U_{max}} \tag{4.4}$$

Equation 4.4 is the conventional loss factor formula for a linear system. The system in the present study is nonlinear. To get a better approximation of loss factor, the form of Equations 4.1 and 4.2 must be used. The trapezoidal numerical integration method was used to calculate the total strain energy from the hysteresis curves.

4.3.2 Results and discussion

Average dynamic stiffness

The average dynamic stiffness and loss factors were studied as a function of dynamic amplitude, over the range of static and dynamic loading. The hypotheses tested for the changes in average dynamic stiffness can be stated as follows:

1. As the pre-compression is increased, there is an increase in the number of contacts, and new contact forces are created. Therefore, the average dynamic stiffness increases for a given dynamic displacement.

2. For a given pre-compression, an increase in the dynamic displacement allows greater travel of the wires. This leads to a reduction in the average dynamic stiffness of the specimen.

3. As the frequency increases, the wires oscillate at a faster rate, reducing the time for the slow relaxation processes to take place. This results in an increase in stiffness.

The results for the average stiffness can be observed in Figure 4.9. Note that, "SS" in the legends stands for static strain.

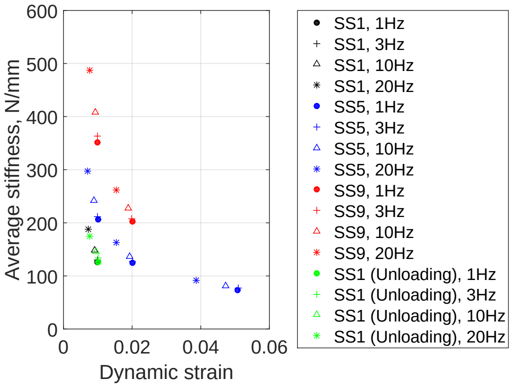

Figure 4.9: Average stiffness variation with dynamic strain over range of static strains and frequencies for $\tilde{\rho} = 0.18$, Specimen 1

The results from Figure 4.9 clearly support the first two hypotheses. The static and dynamic strains have a distinct effect on the average stiffness. The results are also partly in agreement with the third hypothesis over the range of frequencies tested. Although there is a significant reduction in dynamic strains in the range of frequencies tested, there is a negligible, but noticeable, increase in average stiffness as frequency increases. This is especially true on the left hand side of Figure 4.9, where the dynamic strains at 1 Hz and 3 Hz are similar. However, it is not possible to confirm if this is an effect of the applied frequency, or if it is introduced due to uncertainties in the test system. Therefore, it must be stressed that the drop in dynamic amplitude as the frequency increases could mean that the specimen may be operating on a stiffer region of the force-deflection curve.

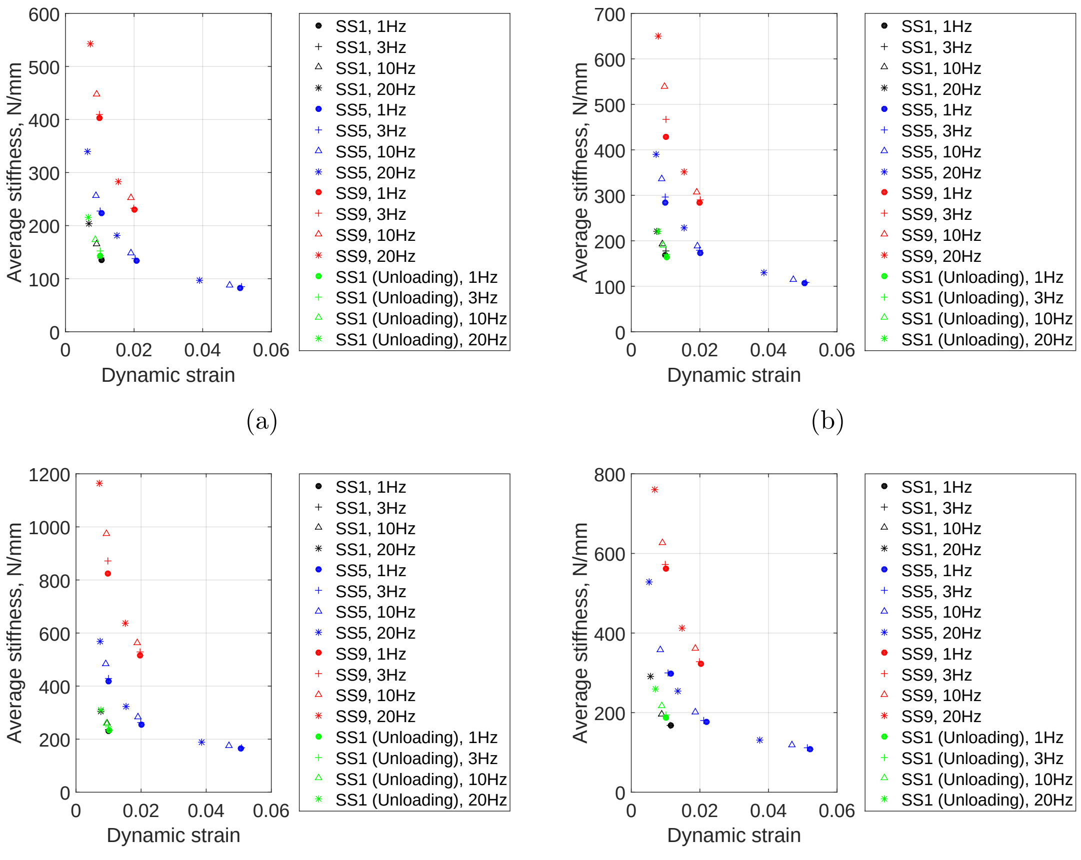

(a) (b)

(c) (d)

Figure 4.10: Average stiffness variation with dynamic strain over range of static strains and frequencies for: (a) $\tilde{\rho} = 0.18$, Specimen 2, (b) $\tilde{\rho} = 0.18$, Specimen 3, (c)$\tilde{\rho} = 0.23$, Specimen 1, and (d) $\tilde{\rho} = 0.23$, Specimen 2

Overall, from the results seen in Figures 4.9 and 4.10 (a) - (d), it can be concluded that the most important parameters affecting the average dynamic stiffness are the static (pre-compression) and dynamic strains acting on the specimen. The average stiffness is seen to rise exponentially with a reduction in dynamic strains. The effects of frequency are not shown to a significant extent, and it can hence be assumed that there is no obvious frequency dependence, which is a characteristic of Coulomb friction systems.

It is interesting to note that the hysteresis curves become narrower with increasing frequency, as seen in Figure 4.11. This trend is in agreement with the relaxation spikes (which are essentially high frequency phenomena) seen in the study of the quasi-static tests, which is also seen in Figure 4.11. This can be used to indicate that higher frequencies will cause narrower hysteresis curves.

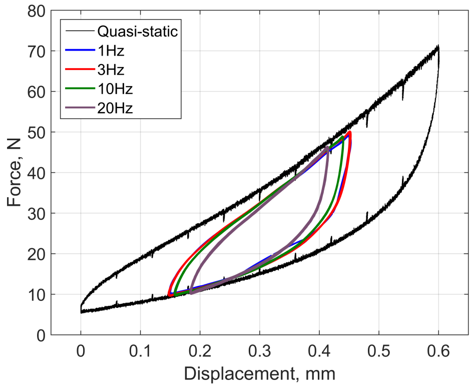

Figure 4.11: Comparison of quasi-static and dynamic stiffening behaviour at a static strain of 5% and dynamic strain of 5%

Loss factor

The primary energy loss mechanism in TMW devices is widely accepted as friction. Under these conditions, it is hypothesised that:

1. As the static displacement is increased, there are several new contacts being formed between the wires. As the specimen is subjected to oscillatory motion, the contacts begin to slide relative to each other. After a critical level of pre-compression is surpassed, the new contacts might pose a restriction to the sliding that occurs in the microstructure. Additionally, if it is assumed that plasticity effects at high compression might be induced, the contribution of plastic wires will be lower than that of elastic wires in sliding. Due to a combination of these, the loss factor might be restricted to a maximum value, or may drop instead.
2. For a given static displacement, increasing the dynamic displacement means that the contacts would slide against each other for a longer travel. As long as plasticity is not induced before this sliding, the loss in the system should increase.

3. As the frequency increases, the time required for the slow reacting quasi-plastic contact and wire behaviour reduces, leading to dynamic stiffening of the affected wires and contacts. This could lead to a drop in loss factors because the contribution of quasi-plastic contacts and wires to damping is lower than elastic ones. It should be noted that if the contacts and wires do get stiffer, and plasticity is not induced, more sliding should occur for a given overall deflection and so, the friction increases, leading to higher losses. Elastoplastic behaviour may be seen in circumstances where local plasticity is induced, whereby both the elastic and plastic contacts/wires will interact with each other to change the friction characteristics.

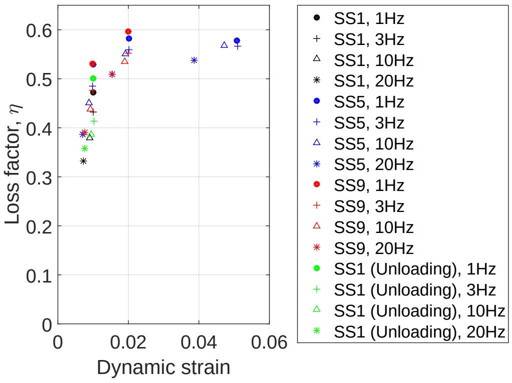

Figure 4.12: Loss factor variation with dynamic strain over range of static strains and frequencies

The specimen supports Hypothesis 1, as seen in Figure 4.12. As the static compression is increased, the loss factor increases, albeit quite negligibly. The hypothesis for a drop in loss factor after a given static compression is not always seen. This can be credited to high levels of static and dynamic strains, where the contacts can provide restrictions to motion within the microstructure, not being applied to the specimen. Noting this, an example of the drop in loss factor for increasing static pre-compressions can be seen for the case of “SS1, 3Hz” to “SS9, 3 Hz”. A closer view of this can be seen in Figure 4.13. The loss factor increases between static strains of 1% and 5%, before dropping at a static strain of 9%.

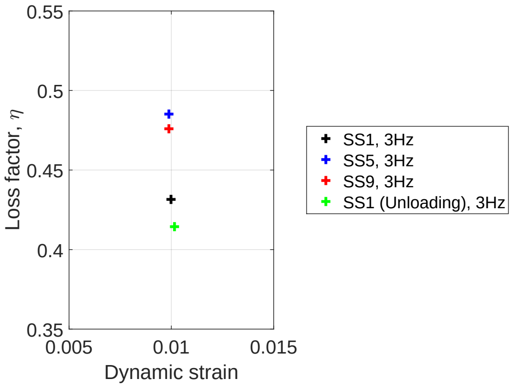

Figure 4.13: Close-up view of reduction in damping when static strain is increased

The results observed are in agreement with Hypothesis 2. The higher travel of the wires with increased dynamic strain causes an increase in the loss factors. At high dynamic amplitudes, the loss factor can be seen to reach a plateau. As dynamic amplitudes are increased further, it can be predicted that the loss factors would start reducing. This is another characteristic of systems with Coulomb friction.

For the frequency dependency of loss factor, it is seen that in all tests conducted, the loss factor drops at the highest frequency tested, agreeing with Hypothesis 3. Unfortunately, it is impossible to judge whether this is as a result of increasing frequency, or the drop in dynamic strain amplitudes at the higher frequencies. Because the frequency related effects are barely noticeable, it can be assumed, like in the case of the average stiffness, that the frequency dependency can be considered negligible, or non-existent.

Figure 4.14 (a) - (d) show the results for the remaining specimens. There is a clear trend between all the results for the loss factor to increase to a plateau, in a logarithmic manner.

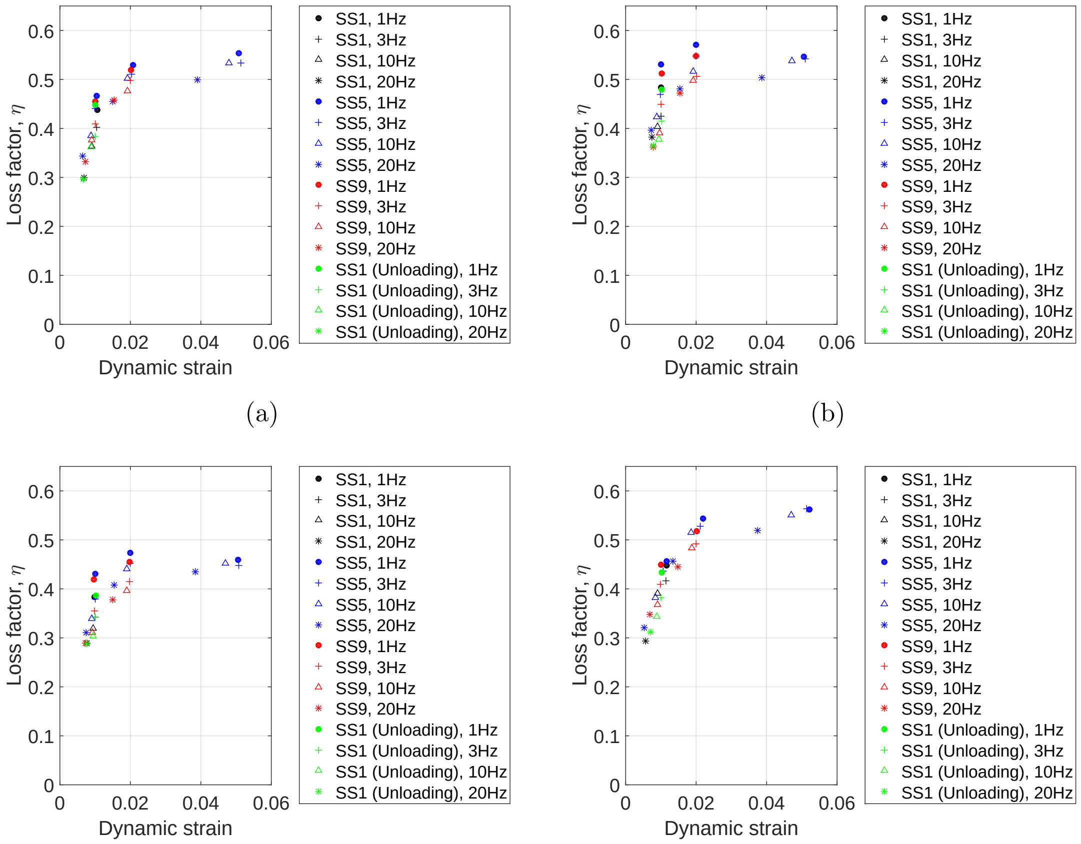

(a) (b)

(c) (d)

Figure 4.14: Loss factor variation with dynamic strain over range of static strains and frequencies for: (a) $\tilde{\rho} = 0.18$, Specimen 2, (b) $\tilde{\rho} = 0.18$, Specimen 3, (c)$\tilde{\rho} = 0.23$, Specimen 1, and (d) $\tilde{\rho} = 0.23$, Specimen 2

Validation of calculations

In an effort to validate the results of the mechanical properties for the experimental hysteresis curves, the calculations were applied to a simulated linear hysteretic system of a known loss factor. The simulated displacement and force took the form of Equations 4.5 and 4.6, respectively.

$$x = X \exp(j\omega t) \tag{4.5}$$

$$f = k(1 + j\eta) \exp(j\omega t) \tag{4.6}$$

where X is the amplitude of the displacement, k is the stiffness, j is the square root of -1, and η is the loss factor, which can be calculated using Equation 4.7.

$$\eta = \frac{c_{eq}\omega}{k} \tag{4.7}$$

where c_{eq} is the equivalent coefficient of damping for the hysteretic system.

Table 4.5 illustrates the parameters used during the validation during these calculations, as well as the theoretical loss factor, η.

Parameter	**Value**
X, mm	1
ω, **rad/s**	31.4
k, N/mm	1
c_{eq}, **Ns/mm**	0.01
η	0.3142

Table 4.5: Parameters used during validation, and calculated loss factor, η

Two slightly differing methods of calculating the loss factor were then compared, one where a polynomial was fitted to the entire force displacement hysteresis curve (which is traditionally used), and the second method was the one described in the previous section. The former method resulted in a calculated loss factor value of 0.3112 (an underestimate of 0.955% from the theoretical value), whereas the latter method showed the loss factor to be 0.3111 (an underestimate of 0.986% from the theoretical value). It can be seen that the performance of the two methods produced nearly identical results. However, it must be noted that for a nonlinear system, polynomials applied to the entire force-displacement hysteresis curves would provide poorer fits when compared to polynomials applied to the approximated midpoints of the force-displacement hysteresis curves.

As an example, when the two methods were applied to an experimental hysteresis curve of a TMW specimen ($\tilde{\rho} = 0.18$, Specimen 1, SS = 9%, DS = 1%), it was found that the traditional method calculated a loss factor of 0.603, whereas the method used in the calculations reported in this thesis calculated a loss factor of 0.598, which is lower since the polynomial fit over the force-displacement midpoint curve follows the experimental elastic curve more accurately. It should be noted that the method of calculating the energy dissipation per cycle for each of the above methods was maintained.

Comparison with literature

Table 4.6 provides an indication of the approximate range of TMW device coefficients of stiffness and loss factors, as reported by other researchers in literature, as well as the results reported in this thesis. In the reported results shown below, the TMW devices were all made of stainless steel.

Author	**Frequency range**	**Coefficients of stiffness**	**Loss factors**
Hou, et al. [33]	1 - 10 Hz	≈ 500 N/mm	0.17 - 0.32
Chandrasekhar, et al. [75]	1 - 20 Hz	30 - 85 N/mm	0.14 - 0.33
Chandrasekhar, K. [present work]	1 - 20 Hz	72 - 1170 N/mm	0.29 - 0.61

Table 4.6: Range of TMW coefficients of stiffness and loss factors reported in literature for low frequency testing, as well as those reported in this thesis

The reported stiffness coefficients and loss factors are once again wide in range, as seen in Table 4.6. As mentioned in Section 4.2.2, the TMW devices studied in literature have various designs and dimensions, as well as different extents of loading, meaning that a direct comparison in results would not be meaningful. However, the above results show the capabilities of TMW devices, especially when considering the relatively high damping they offer. Once again, readers are encouraged to read the publications listed above, and others, for further details on the work carried out by the respective researchers. It must be noted here that in the work by Hou, et al. [33], and Chandrasekhar, et al. [75], the average stiffness coefficients and loss factors were studied as a function of frequency. Therefore, the observed frequency dependence in their work may be inaccurate, since it has been shown in this chapter that the dynamic amplitude decreases at higher frequencies, and if these properties are studied in terms of dynamic amplitudes, frequency dependence is not observed.

4.4 Conclusion

The main result from the quasi-static tests revealed that the TMW device microstructure evolves with different loading regimes. The changes in microstructure were somewhat curtailed by the pre-conditioning exercises observed before the quasi-static and dynamic experiments. The specimen followed the hysteretic load path for the succeeding two tests after the first load-unload cycle. The relaxation forces, which oppose the loading direction, highlight an interesting trend. On the force-displacement curve, they were seen facing inward. Because these relaxation forces are essentially short-term, high frequency phenomena, this means that at higher frequencies, the hysteresis curves become narrower.

Increasing the pre-compression increased the stiffness of the material, in a nonlinear manner. Increasing dynamic amplitudes reduced the stiffness, due to larger travel of the wires in the microstructure. This was also seen to be nonlinear. Increasing the pre-compression increased the loss factor because there are more contacts with higher contact pressures that can slip in the microstructure. Increasing the dynamic amplitude of the cyclic compression also increased the loss factor due to the larger level of slip.

In general, there is primarily an amplitude dependency in the response of the TMW devices. This phenomena is in line with classic Coulomb friction behaviour. Nonlinearity arises both due to the friction mechanism, as well as the nonlinear changes in the number of contacts, and contact areas, formed during load cycles. Nonlinearity due to plasticity may also be a contributing factor. However, this was considered to not be significant because the nominal strain levels were restricted to a maximum of 10%.

Chapter 5

EXPERIMENTAL STUDIES: HIGH FREQUENCY DYNAMIC TESTING

5.1 Introduction

Reviewing research on tangled metal wire (TMW) devices has shown that experimental studies have focused on dynamic behaviour in the lower frequency spectrum, generally studying behaviour at 10 Hz or below. Most of the work published relates TMW material properties, and other related physical properties (e.g. wire diameter, and coil orientation) to behaviour observed in quasi-static conditions, where inertial effects are not observed to a significant extent.

This is believed to be because most industrial dynamic test systems are hydraulic in nature, and are hence only capable of driving high amplitudes at low frequencies [79]. Some test systems also use power screws that are driven by an electric motor [80], which allow excitation at even lower frequencies. On the other hand, there are very few custom-designed experimental test systems that are capable of driving desired amplitudes at high frequencies. An additional constraint that any test system may face is the presence of structural resonances within the range one may want to perform testing. These resonances can add uncertainty to the collected data due to the increased inertia of the test structure itself, and hence interfere with the validity of such tests.

For these reasons, a new test structure was specially designed, and manufactured to operate over a wider band of frequencies, up to 500 Hz. The test structure was designed to have its fundamental natural frequency beyond the high end of the frequency range considered for the experiments. During the design of the test structure, the dynamic amplification that structural resonances cause, away from the natural frequency of the system, was also considered. The main aim of the test structure was to apply sinusoidal compressions to the TMW devices, whilst maintaining a fixed pre-compression, and measuring dynamic forces with accuracy sufficient to allow the hysteresis curves of the TMW devices to be investigated.

The work presented in Chapter 4 indicated that TMW devices may be classed as nonlinear systems. By their nature, they are sensitive to input loading conditions. To reduce uncertainty in the results, and hence simplify analysis, it is important for the input not to deviate from what is desired. This requires the incorporation of a good control mechanism. The use of a Proportional-Integral-Derivative (PID) controller was explored, and a Proportional-Integral (PI) control strategy was chosen to tackle this goal. A brief background of PID control, and the development of the PI controller, deployed on a National Instruments CompactRIO Industrial Controller, for the work carried out in this chapter is reported in Appendix A.

This chapter starts with a discussion of a pre-existing test structure, and the problems faced when using this structure to test TMW devices. This is followed by a detailed description of a new test structure, which was aimed at overcoming the problems faced in the old test structure, and was designed to provide compressive loads at high frequencies. The experimental methodology is then described, which includes the validation of the new test structure using a material of known properties, and the high frequency behaviour of TMW devices are shown and explained. Since it has already been shown that TMW devices are nonlinear in nature, it should be noted that the experimental results presented in this chapter are linearised results of a nonlinear system, i.e. the results are approximated over a point on the force-displacement hysteretic curves.

5.2 Test structure description

5.2.1 Pre-existing test structure

A dynamic test structure that was available before the commencement of this work is shown in Figure 5.1. This had previously been used to test granular viscoelastic materials [81], [82]. The structure was constructed primarily from square-section steel tubes.

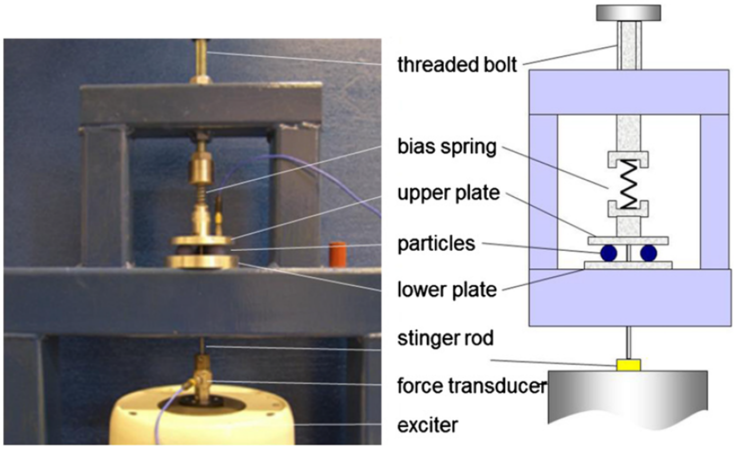

Figure 5.1: High frequency test structure used to test granular viscoelastic materials (Source: [81])

When testing was performed on some TMW devices, it became apparent that there were a number of problems with its applicability in testing such devices. Firstly, it was noted that the upper plate, which was connected to an electrodynamic shaker via a stinger rod, was vibrating with a flapping motion (where two opposite ends of the plate were vibrating out-of-phase), meaning that the specimens being tested were not being compressed uniformly. Secondly, at particular frequencies, ringing noises were heard from the stinger coming in contact with the test structure.

On further investigation, it was found that the first problem was caused by the screw used to attach the upper plate to the slender stinger. As the screw was tightened, the stinger deformed, causing the upper plate to also slant. Furthermore, the uneven surfaces of the TMW devices contributed to the flapping motion. The second issue was also a consequence of the stinger, but the issues were amplified due to structural resonances. Impact testing using a calibrated force hammer was performed to observe the behaviour of top-to-bottom and side-to side motion on the upper and lower supports. In the FRFs (not shown here), there were a large number of resonance peaks, starting at approximately 55 Hz. One option was to avoid the frequency zones around the FRF peaks when performing the experiments on this test structure. However, this limited the range of experiments that could be performed, hence warranting a complete structural redesign.

Learning from the problems faced with the old test structure, the first issue tackled was the connection between the electrodynamic shaker and the moving plate. Having a slender stinger led to its bending when screws were used for attachment to the shaker armature and upper plate, along with slight necking of the stinger at the points of contact. The effects of these issues were considered to be reduced using the same attachment mechanism, but having broader stingers. To completely mitigate this problem, however, the use of screws was abandoned, using a threaded rod of a significantly wider diameter instead.

Electrodynamic shakers are typically designed to supply loads in only one direction. An important consideration to be made with a wider rod mechanism is that a small inclination of the rod may cause lateral (off-axis) forces on the shaker. In order to ensure that the off-axis forces experienced by the shaker could not potentially exceed the limits it was designed for, the rod and shaker connections were finely threaded to ensure that the rods were not inclined.

Because the previous test structure only consisted of two long, hollow supports that were clamped to the testing table, its transverse stiffness was not high, and even though its mass was relatively low, natural frequencies of the structure started from a relatively low value. Keeping this in mind, it was concluded that the new test structure should have short, solid pillars connecting a base, attached directly to the shaker, to the top support structure, essentially making it a stand-alone system.

5.2.2 Redesigned test structure

Prior to the design phase, a list of minimum requirements was generated for the new test structure to meet. There were three essential characteristics it needed to possess, which can be stated as follows:

- Apply compressive loads: The test structure should have the ability to apply compressive sinusoidal loads to a test specimen. Additionally, the magnitude of the compressive loads, and the frequency of the compressive loads should be modifiable.
- High first structural resonant frequency: The main reason behind the overhaul of the old test structure was to increase the range of experiments that could be

performed. The advantage of having a significantly higher first resonant frequency is that it would allow a higher number of experiments to be performed at frequencies where the dynamic amplification is relatively low.

- Minimise nonlinearity: The old test structure had several sources where nonlinearities were a concern. There were several joints, where nonlinearities due to contact friction occurred. The slender stinger also had the potential for large deflections at its resonant frequencies.

- Versatility: Having a test structure that could be adapted to test various shapes and sizes of compressive devices would be beneficial, of course, without compromising the dynamic characteristics of the test structure.

A ring shaped structure was designed to attach directly, and permanently, to a Gearing & Watson (GW) V20 shaker. Table 5.1 details the dimensions of the shaker, which formed the primary size constraints of the test structure dimensions.

Dimension	**Value, mm**
Armature diameter	50
Outer diameter	150
Height	199

Table 5.1: Dimensions of the GW-V20 shaker

The structure base accommodated a number of pillars, which were used to attach another ring shaped support. The centre of the upper support was threaded to accommodate a loading bolt. Figure 5.2 illustrates various views of a computer-aided design (CAD) model of the initial plan for the test structure.

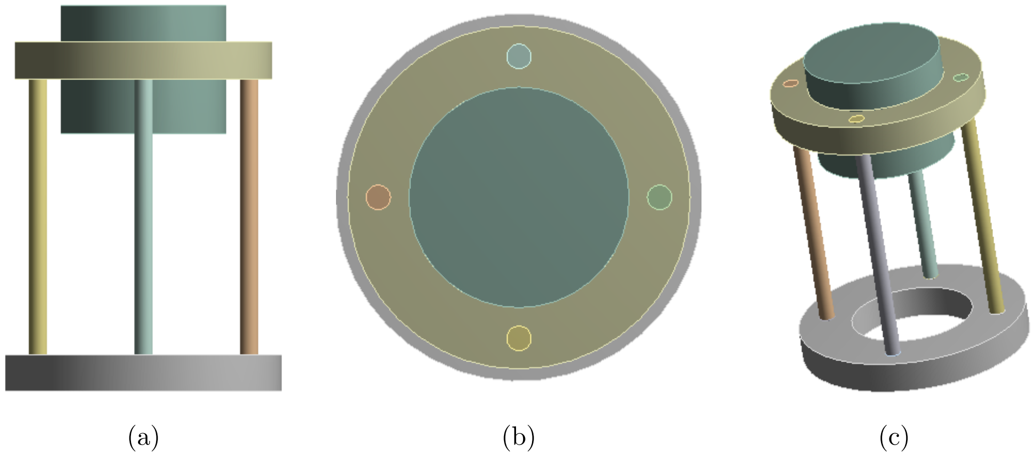
(a) (b) (c)

Figure 5.2: Various views of CAD model of planned test structure

Once design constraints were noted, a Finite Element (FE) model of the test structure was created to perform modal analysis simulations to help finalise dimensions and the materials that the test structure possessed. The focus of the FE work performed here was solely to identify the natural frequencies (eigenvalues) and mode shapes (eigenvectors) of the model. The discussion on the FE aspects of this study will therefore be brief - more details on FE techniques are available in textbooks [83], [84].

As a starting point, the test structure was designed to have four equally spaced pillars with circular cross-sections. The outer diameter of the structure base was the same as that of the shaker, whereas the outer diameter of the upper support was 140 mm. The inner diameter of the structure base and upper support were set to 80 mm. The height of the upper support was set to 20 mm. The material properties of the entire structure were that of stainless steel. Each pillar was initially 150 mm tall, with a 10 mm diameter. Table 5.2 summarises the boundary conditions of various constituent parts of the test structure for the analysis.

Part	**Boundary conditions**
Structure base	Clamped
Structure base - pillars	Bonded
Pillars - upper support	Bonded
Upper support - loading bolt	Bonded

Table 5.2: Boundary conditions of FE model

The chosen element type for the design was SOLID185. Contact elements (Conta174) were used to model the bonded contacts. As modal analysis only uses the stiffness and mass matrices to estimate natural frequencies and mode shapes, small refinements in element sizes typically lead to rapid convergence to give mesh independent results. By experimenting with a few mesh densities, it was concluded that a nominal element size of 10 mm was sufficient to give results that were mesh independent.

The natural frequency for a single degree of freedom (SDOF) system is defined as,

$$\omega_n = \sqrt{\frac{k}{m}} \tag{5.1}$$

where ω_n is the natural frequency (in rad/s), k is the stiffness (in N/m), and m is the mass (in kg). In practice, systems are continuous, with infinite degrees of freedom (MDOF), where each vibration mode will have a respective modal stiffness and mass. If each natural frequency for a continuous system is spaced well apart from each other, each peak can be considered as an SDOF system, with its own stiffness and mass.

By analysing the mode shape and the fundamental natural frequency of the first analysis, it became apparent that the test structure needed to be stiffer and lighter in appropriate places. The fundamental natural frequency of the structure from this analysis was found to be 79 Hz.

There were only two realistic materials to be used for the design of the test structure, taking material availability and cost into consideration, namely, stainless steel and aluminium. Their characteristics were analysed. Firstly, stainless steel has a higher Young's modulus (typically 200 GPa), as well as a higher density (typically 7900 kg/m^3). Aluminium, in comparison, has a lower Young's modulus and density (typically 72 GPa and 2700 kg/m^3). However, they both have a similar specific modulus (i.e. the ratio of Young's modulus to density for a material). For the typical properties quoted here, the specific modulus of stainless steel is 25.3×10^6 m^2/s^2, whereas the value for aluminium is 26.7×10^6 m^2/s^2. This means that two identical structures, one made of stainless steel, and the other made of aluminium, would have almost identical eigenvalues.

The first mode shape of the model showed that the response was dominated by the mass of the upper support and loading bolt. It was therefore decided that changing the material from stainless steel to aluminium could help achieve the goal of increasing the fundamental natural frequency. Given the argument that the specific modulus for both materials is almost identical, it is fair to assume that the change in material would not affect the system dynamics on first intuition. However, the overall contribution to system stiffness of the upper support is insignificant compared to the reduction in mass, making this change a fruitful choice, driving up the fundamental eigenvalue to 128 Hz.

With the need to increase the fundamental eigenvalue further, the choice of pillar dimensions was analysed. The contribution of stiffness to the test structure is dominated by the four pillars. The stiffness of a structure is typically related to material properties and geometric quantities by,

$$k \propto \lambda \frac{EI}{l^3} \tag{5.2}$$

where λ is a constant dictated by the boundary conditions, E is the material Young's modulus, I is the second moment of area of the cross-sectional shape, and l is the axial length of the structure.

For a pillar with a circular cross-section, the second moment of area, I is given by,

$$I = \frac{\pi}{4} r^4 \tag{5.3}$$

where π is a mathematical constant, and r is the radius of the circular cross-section.

According to Equations 5.2 and 5.3, there are two adjustable parameters that can help increase the structural stiffness, and hence the eigenvalues. These are the axial lengths, and the radii of the pillars. The first preference would be to increase the radius of the pillars, given that it has a fourth power, as opposed to the negative cubic power of the axial length. As an example, if the radius is doubled, the stiffness would increase by a factor of 16 (i.e. 2^4), and if the axial length is halved, it would increase by a factor of 8 (i.e. 0.5^{-3}).

The pillar size was increased from its original diameter of 10 mm to 35 mm. This increased the fundamental eigenvalue to 972 Hz. Whilst further increase in the diameter would yield more favourable results, there were limitations in terms of both structure base size and practicality. In terms of size, the maximum diameter of the pillars is limited to the dimensions of the ring surface, whereas for practicality reasons, very thick pillars will cause restrictions when samples are loaded and unloaded. Once a satisfactory pillar diameter was concluded upon, the pillar axial lengths were halved, finally giving a fundamental eigenvalue of 2537 Hz. The pillar lengths were not reduced further to allow flexibility for other material samples to be tested in the future.

Table 5.3 summarises the final dimensions of the test structure.

Part	**Dimension**	**Value, mm**
Structure base	Height	20
	Outer diameter	150
	Inner diameter	80
Upper support	Height	20
	Outer diameter	140
	Inner diameter	80
Pillars	Height	75
	Diameter	35

Table 5.3: Final dimensions of test structure designed using FE

The resonant frequency for any system is not necessarily the same as the natural frequency of the system. It instead occurs at a frequency close to the natural frequency, depending on the amount of structural damping present. For an SDOF system with steady state forced vibration, the resonant frequency can be calculated as,

$$\omega_r = \omega_n \sqrt{1 - 2\zeta^2} \tag{5.4}$$

where ω_r is the resonant frequency, ω_n is the natural frequency, calculated using Equation 5.1, and ζ is the damping ratio, calculated by,

$$\zeta = \frac{c}{c_c} = \frac{c}{2\sqrt{mk}} \tag{5.5}$$

where c is the modal coefficient of damping (in Ns/m) and c_c is the critical damping coefficient. Typically for metallic structures, the metallic damping ratio is of the order of 0.001, hence the difference between the resonant and natural frequencies can be insignificant.

For any structure undergoing vibrational loading, the frequency response does not simply amplify only at the resonant frequency. The amplitudes around the resonant frequency are also much higher than the static amplitude (i.e. at 0 Hz). The final consideration made with the finalised design, therefore, was the dynamic magnification occurring on the structure at the frequencies of interest. This was calculated as a dynamic magnification factor (DMF),

$$DMF = \frac{X}{X_{stat}} = \frac{Xk}{F} = \frac{1}{1 - r^2 + j2\zeta r} \tag{5.6}$$

where X is the amplitude at a particular frequency, X_{stat} is the amplitude at 0 Hz, F is the forcing amplitude, and r is the frequency ratio,

$$r = \frac{\omega}{\omega_n} \tag{5.7}$$

where ω is the frequency of the steady state forcing.

While Equation 5.6 is straightforward to solve, in practice, the modal parameters are almost always unknown. They can be calculated using modal fitting algorithms, but require data from real structures. For design purposes, the DMFs are commonly evaluated using FE models.

The final model created for the modal analysis task was used to study its harmonic behaviour. Under harmonic analysis, after the boundary conditions were set, a stepped sine analysis was performed, where the starting frequency (0 Hz), ending frequency (4000 Hz), and the spatial resolution (4 Hz) were set. A 155 N axial force (the force limit of the V20 shaker) was applied to the bottom face of the loading bolt - the actual value does not matter because the analysis being performed was a linear one, and the final result being sought out was a linear ratio.

The frequency response obtained from the harmonic analysis is shown in Figure 5.3.

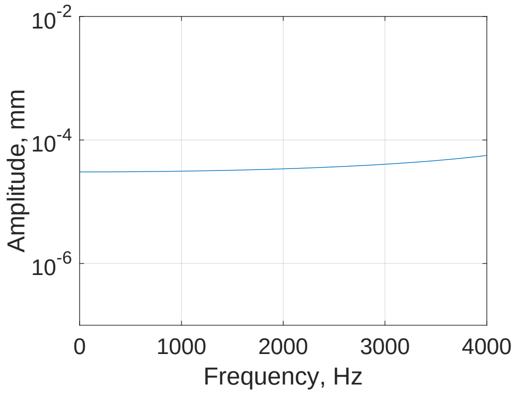

Figure 5.3: Frequency responses obtained from the FE model of the test structure for up-to-down motion

The frequency response in Figure 5.3 does not contain any peak in the frequency range shown because the first mode in the up-to-down direction occurs above the frequency range studied.

From the frequency response in Figure 5.3, the DMF was calculated simply as the ratio of amplitude at the frequency of interest to the amplitude at 0 Hz. The DMF estimated from Figure 5.3, at 500 Hz, which was the upper frequency limit for the testing range, was 1.006. At the quoted maximum forcing capacity of the shaker (155 N), the DMF was estimated to be equivalent to a displacement of 30.6 μm in the axial direction (up-to-down motion of upper support) at 500 Hz. As this displacement was considered minuscule, it was concluded that the test structure was appropriate for high frequency testing, and it was moved onto the manufacturing stage. Figure 5.4 shows the manufactured test structure.

Figure 5.4: Test structure manufactured following FE analysis

5.2.3 Sensors

Sensors are essential in any test system, as they provide the necessary data for analysis. There were a total of four sensors associated with this test structure, namely:

- Static load cell
- Dynamic load cell
- Laser displacement probe
- Accelerometer

Static load cell

The static load cell, as the name suggests, is a static force transducer that was used to measure specimen loads when the shaker and moving plate were driven upwards. The type used in the high frequency test structure was the CLS-500NB-T, a resistive load cell.

In load cells, a number of strain gauges (typically four, arranged to replicate a Wheatstone Bridge circuit) are placed on an electrically conductive, load bearing member within the cell. When there is no load applied, the system is in equilibrium, no current flows through the circuit and the output voltage is null. As the cell is stressed with a force, the strain gauges deform, modifying the resistance of the circuit, and allowing current to flow through the network. This changes the output voltage, which can then be converted into a static force using a calibration coefficient.

Table 5.4 summarises some important characteristics of the CLS-500NB-T load cell.

Type	**Value**
Measurement range	500 N
Rated output	1.5 mV/V
Natural frequency	50 kHz

Table 5.4: Technical specifications of the CLS-500NB-T static load cell

The static load cell used was button shaped. One face of the load cell was flat, while the other surface of the cell consisted of a small protrusion - the load carrying member. Because the tangled metal wire (TMW) devices under consideration are ring shaped that have uneven surfaces, there were two options for incorporating the static load cells with the test structure.

- Housing mechanism: With this method, this mechanism would hold the static load cell in its place. One such mechanism was built that consisted of a plate, hollowed out at the centre to accommodate the load cell. The plate had 8 slots to house shouldered screws that connected it to the main loading bolt. The screws allowed axial movement along the length of the shoulders.
- Gauge blocks: This method was simple and more practical. The static load cell was placed onto the moving plate, and the main loading bolt was tightened to increase the load to a desired level, as indicated by the load cell. A number of gauge blocks were slipped into the gap between the base of the test structure and the moving plate, and used as a reference when the test specimens were loaded.

Dynamic load cell

A dynamic load cell was used in the test structure to measure oscillating forces. The load cell consists of a slender piezoelectric material, typically quartz, that is sandwiched by pairs of electrodes. As the piezoelectric material is subjected to axial loads, an electrostatic charge is emitted from it, proportional to the load applied. The electrodes collect the charge, which are of high impedance, and feed it to a constant current signal conditioner to produce a low impedance voltage signal. These load cells were not applicable for measuring static loads because the charge emitted by the piezoelectric material would simply leak away. In dynamic loads, the forces continuously vary in magnitude, the charge therefore continuously changes, and the resulting voltage is constantly sampled by a data acquisition system.

The dynamic load cell used with the test structure was the PCB 208C02. Its properties are summarised in Table 5.5.

Type	**Value**
Measurement range	444.8 N
Sensitivity	88.96 N/V
Upper frequency limit	36 kHz

Table 5.5: Technical specifications of the PCB 208C02 dynamic force transducer

Laser displacement probe

Laser displacement probes simply emit a laser signal from a sender to a target and measure the reflection coming back from the target to a receiver. The reflection falls onto the receiver at a characteristic angle, depending on the distance travelled by the laser. Using the known distance between the laser emitter and laser sensor, and simple trigonometric calculations, the displacement of a target can be measured. This process is known as triangulation.

The laser displacement probe used with the test structure was the LD1630-50. Its properties are summarised in Table 5.6.

Type	**Value**
Measurement range	50 mm
Start of measurement range	115 mm
Sensitivity	2.5 mm/V
Resolution at 230 Hz	7.5 μm

Table 5.6: Technical specifications of the LD1630-50 laser displacement probe

From Table 5.6, it is clear that the "Start of measurement range" was greater than the design height of the test structure. For this reason, the moving plate, which was connected directly to the pushrod/electrodynamic shaker system, was machined at an angle of 45°. Additionally, the laser displacement probe was inclined to an angle of 45°, and directed towards the inclined plate.

As the shaker provided axial displacements in the vertical direction, and the laser displacement probe measured angular displacements when inclined, some trigonometric manipulation of the acquired data was required. Figure 5.5 illustrates a schematic of the orientation angles of the laser displacement probe and the moving plate, as well as the measured displacement by the displacement probe and the required displacement measurement.

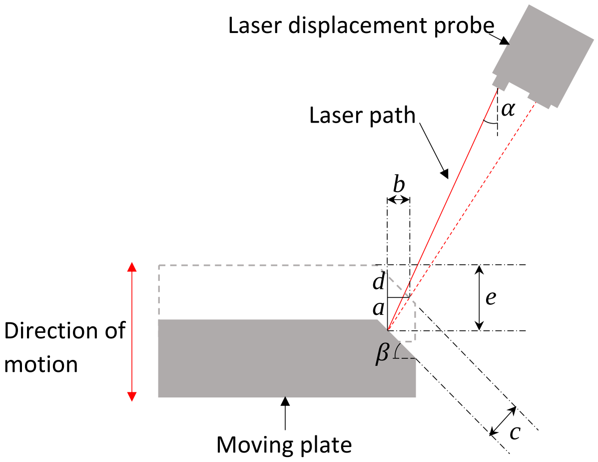

Figure 5.5: Schematic of laser displacement probe and moving plate arrangement

In the instance shown in Figure 5.5, the laser displacement probe measures a displacement of length c, whereas the required measurement is length e. e is calculated as the summation of lengths a and d. For a laser displacement probe angular orientation of α, and a moving plate orientation of β, displacement e can be calculated, accordingly, through Equations 5.8 to 5.11 .

$$a = c.\cos(\alpha) \tag{5.8}$$

$$b = c.\sin(\alpha) \tag{5.9}$$

$$d = b.\tan(\beta) \tag{5.10}$$

$$e = a + d = c.\cos(\alpha) + c.\sin(\alpha).\tan(\beta) \tag{5.11}$$

Equation 5.11 was then used in the postprocessing of the data.

Accelerometer

Accelerometers are one of the most widely used data acquisition sensors in practice. Depending on the application, they can have a wide range of sizes, sensitivities and usable frequency ranges [85]. Accelerometers, like force transducers, contain a piezoelectric crystal, as well as a moving plate. The device converts the kinetic energy from mechanical movements to proportional electrical energy, in the form of charge, courtesy of the piezoelectric crystal embedded in it. Like the dynamic force transducer, the charges are converted to voltages using electrical circuits that are either embedded within the device, or more commonly found in signal conditioners.

The accelerometer used with the high frequency test structure was the Dytran 3035B2G, and its properties are summarised in Table 5.7.

Type	**Value**
Measurement range	±100 g
Sensitivity	20 g/V (196.2 $m/s^2/V$)
Resonant frequency	> 45 kHz

Table 5.7: Technical specifications of the Dytran 3035B2G accelerometer

5.2.4 Initial setup

While the outer configuration of the test structure has been discussed in detail so far, little has been said about the compression mechanism - the main purpose of the test structure. The initial setup of the test structure is shown in the following schematic, Figure 5.6.

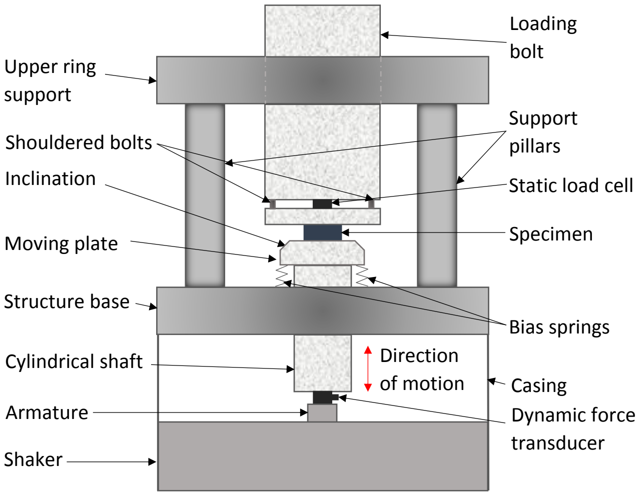

Figure 5.6: Schematic showing the initial setup for the high frequency test structure

As per Figure 5.6, the bottom face of the dynamic force transducer was connected directly to the armature of the electrodynamic shaker. The top face was connected to a cylindrical aluminium shaft whose other end was attached to the aluminium moving plate, which was inclined to accommodate the inclined laser displacement probe. The specimen came next, followed by the static load cell and its housing. This in turn was connected to the main loading bolt, used for the pre-compression of the specimens. The bias springs, placed in between the moving plate and the test structure casing, complemented the loading bolt. That is, compressive displacements, provided by the loading bolt, caused the bias springs to produce a restoring force, which was transmitted to the specimen via the moving plate. During the initial setup, three sets of stacked natural rubber blocks, uniformly distributed along the circumference of the moving plate, were used as the bias springs.

The high frequency test structure was essentially a prototype. As with all other prototypes found in engineering, the design phase was only one aspect of the entire process. The other, and more important, aspect is the functionality of the final manufactured component, and how it satisfies its purpose. In order to understand its dynamic characteristics, a number of trial runs were attempted on the test structure. These are discussed next.

Practical implications

Before discussing the practical implications of the sensors with the test structure, it is important to understand limitations of the laser displacement probe and the accelerometer sensors that were available for these high frequency experiments. Laser displacement probes require a minimum amount of displacement amplitude to acquire any meaningful data. At very low displacements, noise tends to dominate acquired signals, i.e. the signal to noise ratio becomes low. Generally, at high frequencies, vibration amplitudes drop due to power limitations of the amplifier and electrodynamic shaker. This makes laser displacement probes inappropriate for high frequency vibrations. Conversely, at the lower frequencies, acceleration signals are lower for a given displacement amplitude, which result in low signal to noise ratios in accelerometers. Noting that the maximum dynamic displacement applied to the TMW device is ± 0.15 mm, as discussed in Chapter 4, at 20 Hz, for example, the acceleration for this amplitude is approximately 4.74 m/s^2. For the accelerometer used, this corresponded to an amplitude of ± 11.5 mV. With noise levels of ± 5 mV, the acceleration signal for this amplitude was quite "hidden". Whilst it could be possible to use higher sensitivity velocity probes, or accelerometers, it was decided to use the available sensors to reduce time costs. Therefore, the initial plan was to use the laser displacement probe for frequencies below 100 Hz, and the accelerometer for higher frequencies.

A trial test run was performed on the structure, without any specimens loaded, in order to assess the PI controller with the angled laser displacement probe, LD1630-50. The electrodynamic shaker was set to provide an axial displacement of 1 mm at a frequency of 1 Hz. A time trace of the signal recorded by the laser displacement probe was acquired, and it was noticed that the signal measured from the angled sensor was distorted. This can be seen in Figure 5.7, where the signal amplitude was corrected using Equation 5.11. Figure 5.8 illustrates a measured force time trace from the force transducer at 80 Hz with no specimen loaded to the test structure. It does not correspond to the displacement time trace seen in Figure 5.7, since forces were not measured at the time, but it provides a representative force signal provided by the force transducer.

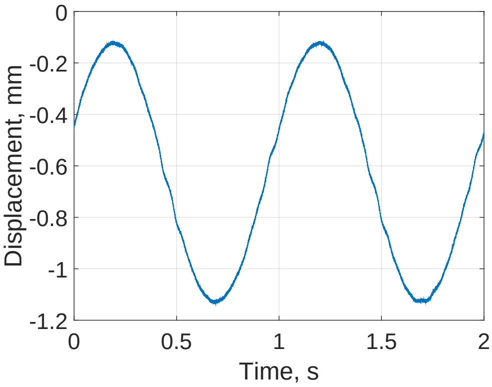

Figure 5.7: Time trace of displacement signal measured from the angled probe

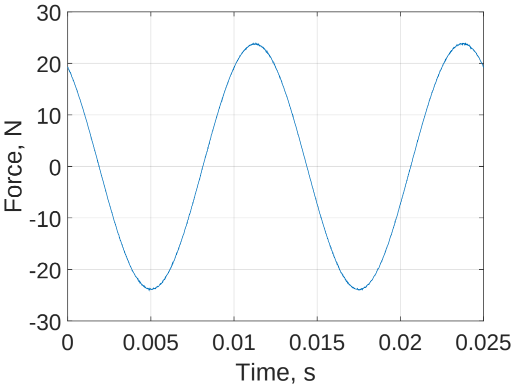

Figure 5.8: Time trace of force signal measured from the force transducer

This distortion arose due to misalignments of the angled sensor and inclined plate. As the plate vibrated, the laser signal reflected on it was seen to be moving vertically, as well as slightly horizontally. With perfect alignment, the signal should have only been moving in the vertical direction. After a number of adjustments were made to the test structure and sensor positions, it was concluded that the use of angled laser displacement sensors was not viable. As a result, it was decided to only use an accelerometer for the experiments. An unfortunate consequence of this was that no tests were allowed at the lower frequencies (< 20 Hz).

Further trial test runs were then performed, this time with a specimen of natural rubber, of known properties, loaded to the structure. The time traces of the acceleration and dynamic force were observed for a number of frequencies and amplitudes. It was noted that the amplitude of the force dropped quite significantly within a small frequency band around 100 Hz. This was attributed to the resonance of the moving plate and spring system, which acted as an SDOF system. The equations of motion of this system, Equation 5.12, can be used to explain why this occurred.

$$m_{mp}\ddot{x} + k_{nr}x + k_s x = f_{ft} \tag{5.12}$$

where x and $\ddot{x}$ are the displacement and acceleration, respectively, m_{mp} is the mass of the moving plate, k_{nr} and k_s are the stiffness coefficients of the natural rubber specimen and springs, respectively, and f_{ft} is the force signal acquired by the force transducer.

Substituting the acceleration term in Equation 5.12 with an equivalent displacement term gives,

$$-m_{mp}\omega^2 x + k_{nr}x + k_s x = f_{ft} \tag{5.13}$$

where ω is the frequency of vibration.

From Equation 5.13, it can be seen that the inertial term, which increases significantly at resonance, reduced the force being acquired by the dynamic force transducer. This needed to be corrected for during the post-processing phase of the analysis, i.e. by adding the inertial force of the moving plate to the force signal acquired by the transducer. To increase the amplitude of the force being detected by the transducer, and hence reduce uncertainty, the transducer needed to be moved closer to the test specimen. This would help reduce the inertial term since the mass above the transducer would be lower. Hence, the amplitude of the dynamic force signal recorded by the transducer would be higher.

Another practical implication of the initial set of tests was, once again, related to the position of the force transducer. The force transducer used for these experiments had a protrusion that allowed data acquisition cables to be attached to it. The clearance between the protrusion and the test structure casing was approximately 4 mm. In one instance during the tests, the shaker went out of control due to incorrect gains applied in the PI controller. When this occurred, there was a substantial impact between the protrusion and the test structure casing, which broke and caused irreparable damage to the force transducer.

The final practical implication of the initial setup was related to the housing mechanism of the static load cell. When subjected to oscillatory motion, the shouldered screws kept loosening, introducing rattling motion of the housing mechanism over time, and hence increased structural damping. Therefore, it was decided to abandon its use in the test structure, and use the other option considered earlier: gauge blocks.

Hence, a final modification of the test system was required, as detailed in the following section.

5.2.5 Final setup

From the lessons learned from the initial runs on the prototype test structure, a modification was planned, with the following objectives.

- Improve force transducer signal measurement.
- Accommodate accelerometer.
- Increase clearance between test structure casing and dynamic force transducer protrusion.
- Limit increase in moving mass.

The final design can be seen in Figure 5.9.

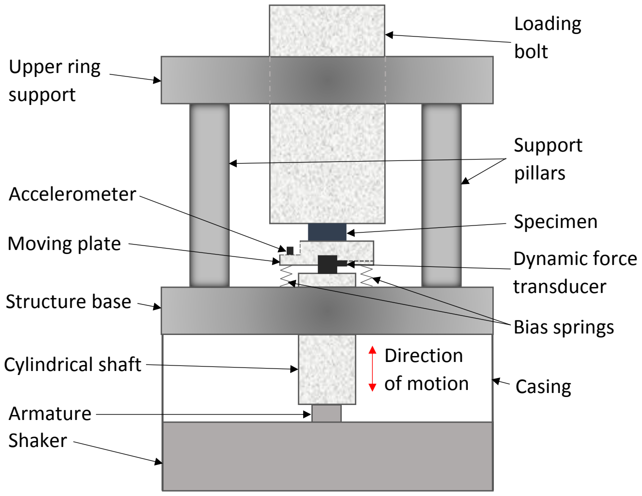

Figure 5.9: Schematic showing the final setup for the high frequency test structure

Comparing Figures 5.6 and 5.9, there is one distinct difference: the dynamic force transducer had been moved further upstream, closer to the location of the test specimens.

In accordance to Figure 5.9, the moving plate was partially hollowed out to accommodate the dynamic force transducer and its protrusion, and reduce the mass that it supported. Since the mass it supported was lower, the amplitude of force read by the dynamic force transducer was higher than before, especially at resonance. With this configuration, it was also possible to protect the integrity of the protrusion on the force transducer. A spacer was placed between the moving plate and structure base to ensure that the force transducer did not break in case the PI controller went out of control.

In order to balance out the mass that was removed on one side of the moving plate, material was removed on the opposite side to accommodate the accelerometer. The calculated mass removal took into account the mass removed for the dynamic force transducer protrusion, as well as the mass added by the accelerometer itself.

To keep the overall height of the moving mass the same, the height of the cylindrical shaft (see Figure 5.9) had to be increased. This was because the moving plate was hollowed out to allow the force transducer to fit inside it partially, whereas in the previous design, the total height of the force transducer added to the overall height of the structure. Therefore, a compromise was made based on the reduced mass that the force transducer supports, and the increase in overall mass due to the increase in height of the cylindrical shaft.

To conclude this section, the choice of a bias spring, used to apply static compressions, as well as apply balance to the vibrating plate, is discussed.

The initial intention was the use of wave springs, shown in Figure 5.10.

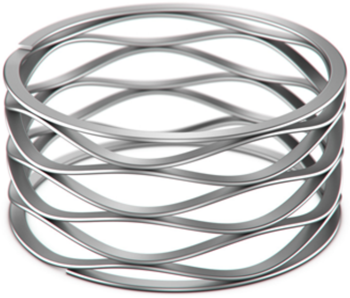

Figure 5.10: Exemplar wave spring (Source: [86])

Wave springs are capable of providing a significant amount of stiffness over a limited height. A range of wave springs were chosen with variable stiffness coefficients to match the range of stiffness coefficients of the TMW devices tested in Chapter 4. They were then assessed for suitability by performing low frequency dynamic tests on the MTS Test System, and analysing the results. The hysteresis curves of these springs showed that they not only behaved nonlinearly, as illustrated by Figure 5.11, but they also possessed a moderately high loss factor (> 0.2). These arose due to a combination of the increase in contact area between the interfaces of the wave springs and the friction that resulted when loading was increased. As reducing uncertainty in results was of paramount importance, the option of using wave springs was ruled out.

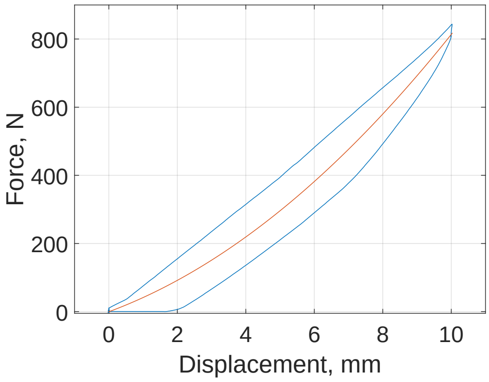

Figure 5.11: Hysteresis curve of a wave spring device

The next consideration for the bias springs was the use of natural rubbers. Depending on the variant of natural rubber used, bias springs made of this material can be very linear, and produce relatively low loss. There were some linear, low loss natural rubber specimens (grade 45 IRHD[1]) available and they were used in the initial set of tests. Unfortunately, the size of these specimens were not compatible with the sizing requirements for the test structure. It is widely accepted that sizing down natural rubber and other elastomers is quite difficult. Therefore, natural rubber specimens in the form of bobbin mounts (example in Figure 5.12) were acquired and tested on the MTS Test System to observe their dynamic behaviour and check for compatibility with the test structure. These mounts were also found to be nonlinear, as depicted in Figure 5.13, with a moderate amount of loss (between 0.1 and 0.2). Because time was a critical constraint when this stage was reached, and identifying a supplier of linear, low loss natural rubber was difficult, it was decided to abandon the idea, and move on to the next (and final) option.

Figure 5.12: Exemplar bobbin mount (Source: [87])

---

[1] International Rubber Hardness Degree

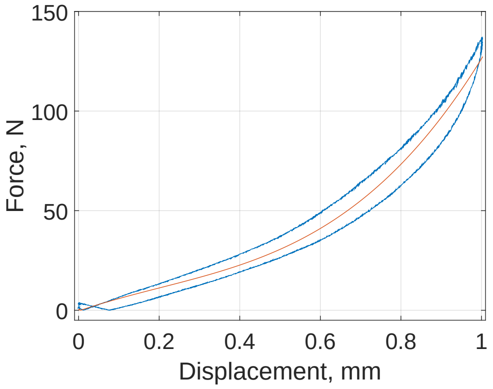

Figure 5.13: Hysteresis curve of a bobbin mount made from natural rubber

The final choice for the bias spring was the use of helical springs. While helical springs can be inherently nonlinear due to their shape, the loss they produce is significantly lower than the wave springs (because no sliding takes place). Similar to the wave springs, a range of helical springs of appropriate stiffness coefficients were selected. The benefit of the helical springs option was that they were loaded in parallel form. This allowed a variable number of helical springs to be added/removed from the system, allowing the overall stiffness coefficient of the system to be altered for given test specimen types. In order to restrict the movement of the helical springs, 8 recesses were incorporated to the bottom face of the moving plate. The validation of the helical bias springs will be discussed in more detail in the following section.

5.3 Experimental methodology

5.3.1 Data acquisition

The following line diagram, Figure 5.14, illustrates the full experimental setup. Data from the accelerometer was fed into a low pass Butterworth filter. The filter output was then passed to the CompactRIO input, which was used in the PI controller. There were two outputs of the CompactRIO system. The first was the PI controller output, which was sent into the input channel of a Data Physics PA300E 300 W power amplifier. The other output fed the generated ideal sine waveform into the data acquisition system, in the form of a PicoScope 4423 device. The two other signals which were fed into the PicoScope device were the unfiltered signals from the accelerometer and force transducer, respectively. The ideal sine wave and unfiltered accelerometer signal were used to tune the PI controller. The data was acquired at a rate of 50 kS/s.

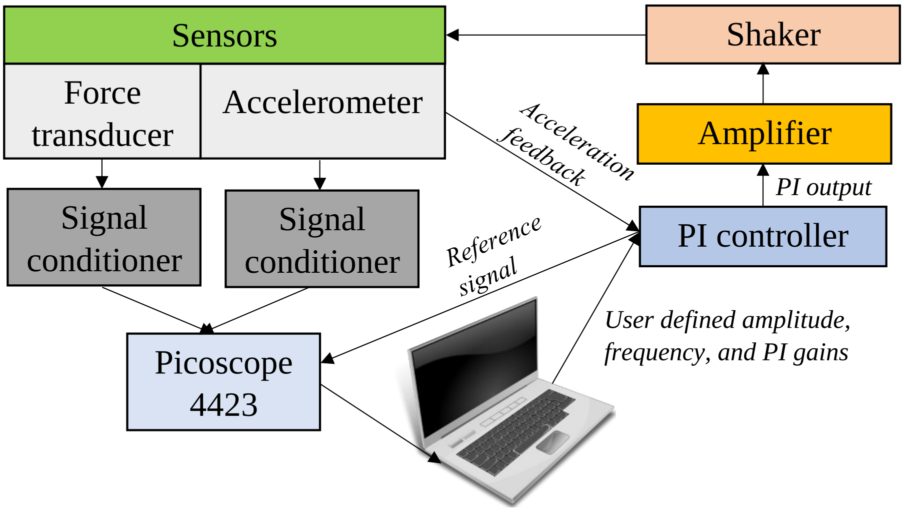

Figure 5.14: Line diagram of controller and data acquisition system

5.3.2 Testing protocol

In addition to the study of high frequency behaviour, other characteristics that were further investigated included the behaviour at different static compressions, and dynamic amplitudes, similar to those discussed in Chapter 4.

The TMW specimens were tested at six frequencies, between 50 Hz and 400 Hz. Table 5.8 summarise the static amplitudes, frequencies, and dynamic amplitudes tested at the corresponding frequencies.

Static Strain	**Frequency, Hz**	**Dynamic Strain**
1%	50	1%, 2%
	80	1%, 2%
	100	1%, 2%
	200	0.5%, 1%, 2%
	300	0.25%, 0.5%, 1%
	400	0.1%, 0.25%, 0.5%
5%	50	1%, 2%, 5%
	80	1%, 2%, 5%
	100	1%, 2%, 5%
	200	0.5%, 1%, 2%
	300	0.25%, 0.5%, 1%
	400	0.1%, 0.25%, 0.5%

Table 5.8: Range of static and dynamic strains examined for the respective frequencies tested

There are some important justifications to be made from Table 5.8:

- There were two static amplitudes tested. These amplitudes were chosen in terms of the approximate average force resulting from a strain of 1% and 5% from the quasi-static experimental results in Chapter 4. For the lower relative density TMW devices ($\tilde{\rho} = 0.18$), these corresponded to forces equivalent to approximately 12 N and 35 N, respectively. For the higher relative density TMW devices($\tilde{\rho} = 0.23$), these corresponded to forces equivalent to approximately 20 N and 60 N, respectively.
  - Although the force corresponding to the 1% static strain of the lower relative density specimens was 12 N, the forcing was increased to 20 N. It was noted that the applied dynamic strains caused a loss of contact between the loading bolt and the specimens being tested when the pre-compression was 12 N.
- At a static strain of 1%, dynamic amplitudes of up to 2% were tested between 50 Hz and 100 Hz. This ensured that there was no loss of contact between the TMW specimens and the loading bolt holding them in place.
- The dynamic amplitude were decreased as the frequencies increased because of shaker limitations, although there were overlaps of two dynamic amplitudes for successive frequencies tested.

- The highest frequency tested was 400 Hz. This limitation was imposed by poor quality reference signals produced by the CompactRIO industrial controller for the higher frequencies.

The materials that were tested are listed as follows:

- Helical bias springs
- Natural rubber
- TMW devices

The helical bias springs, as previously mentioned, are inherently nonlinear. Therefore, they were tested on their own to obtain their mechanical properties. These results were then used to apply corrections to the mechanical properties calculated for the other materials tested.

The mechanical properties for the natural rubber material tested were known beforehand. A natural rubber specimen was therefore tested with the aim of validating the test structure.

The TMW devices chosen for these set of experiments were the same as those in Chapter 4, allowing direct comparisons to be made between the experiments. The TMW devices had to be carefully monitored between the experiments to ensure that the properties would not be influenced by external effects such as shock loading.

The results from Chapter 4 indicated that the TMW devices were significantly stiff, especially at lower dynamic amplitudes. The choice of the bias spring stiffness coefficient was considered very important in the experimental setup. If a spring with a very low stiffness coefficient was chosen, the specimen would not have been able to be pre-compressed, whereas if the stiffness coefficient was too high, the system response would have been dominated by the springs. A total of 8 bias springs were used for all the experiments. Each spring had a nominal stiffness of approximately 22 N/mm, making the total bias spring stiffness 176 N/mm.

The testing protocol can be summarised in the following steps:

1. The static load cell was first inserted between the loading bolt and moving plate. This was followed by tightening the bolt to increase the load to a desired level, as indicated by the static load cell signal captured on PicoScope. Gauge blocks were inserted between the structure base and the moving plate to measure the displacement of the helical bias springs. The static load cell was then finally removed.

2. The test specimen was inserted between the loading bolt and moving plate. The loading bolt was tightened until the moving plate came in contact with the gauge blocks. The gauge blocks were then removed.

3. Once the testing of the specimen at the various prescribed frequencies and dynamic amplitudes was completed, the specimen was removed from the test structure.

4. Steps 1, 2, and 3 were repeated for the next static compression level. If testing was complete on a particular test specimen, it was replaced, and the procedure was repeated for the next test specimen.

5.4 Results and discussion

The core analysis of these high frequency results followed the same procedure as that of the low frequency results in Chapter 4. However, because it was an acceleration signal that was recorded, it needed to be numerically integrated twice with respect to time in postprocessing to obtain the displacement signal. The integrated signals were low-pass filtered to remove the constants of integration. Furthermore, the captured force signal had to be modified to remove the inertial effects of the moving plate, and the force from the springs. That is, the equation of motion can be described as:

$$m_{mp}a + k_{spr}x + k_{spec}x = f_{ft} \tag{5.14}$$

where a is the acceleration signal captured by the accelerometer, x is the calculated displacement signal from double integration of the acceleration signal, m_{mp} is the mass of the moving plate (measured to be 99.93 g using an electronic weighing scale with resolution 0.01 g), k_{spr} and k_{spec} are the stiffness coefficients of the helical springs and specimen being tested, respectively, and f is the force trace recorded by the force transducer.

The properties of the specimen were extracted from Equation 5.14 following some rearrangement:

$$k_{spec}x = f_{ft} - m_{mp}a - k_{spr}x \tag{5.15}$$

It should be noted that there was some uncertainty in the exact mass, m_{mp} that participated when the test structure was subjected to dynamic loading. It was assumed that the entire mass of the moving plate (reported earlier) contributed to the dynamic response recorded. It should also be noted that in Equations 5.14 and 5.15, the inertial term of the specimen mass has been omitted (i.e. $\frac{1}{3}m_{spec}a$). This omission is justified by the fact that the specimen mass is significantly smaller than the mass of the test structure above it. Now that Equation 5.15 has been defined, the results may be discussed.

5.4.1 Helical bias springs

Three additional springs were added to the test structure, in between the moving plate and the loading bolt. When evaluating the mechanical properties of the helical bias springs, k_{spr} from Equation 5.15 was set to 0. In doing so, it was possible to obtain the stiffness coefficients and loss factors for the 11 springs combined. It was then assumed that all 11 springs contributed an equal amount of stiffness and damping to the test structure. These were then divided by 11 and then multiplied by 8 to obtain the total stiffness coefficient and loss factor for the 8 springs installed in between the structure base and the moving plate.

The tests were performed at the same frequencies (ranging between 50 Hz to 400 Hz), static pre-compressions (20 N, 35 N and 60 N) and dynamic amplitudes (dynamic strains ranging between 0.1% and 5%) as those performed on the natural rubber and TMW devices.

The results are summarised in Table 5.9.

Frequency, Hz	Dynamic Strain	Stiffness coefficient, N/mm			Loss factor, η		
		20N	35N	60N	20N	35N	60N
50	1%	191.54	192.45	197.33	0.018	0.024	0.015
	2%	189.38	189.58	198.74	0.017	0.016	0.010
	5%	-	184.53	197.52	-	0.016	0.015
80	1%	188.05	188.74	194.15	0.014	0.016	0.002
	2%	186.50	187.05	193.28	0.012	0.008	0.009
	5%	-	183.26	192.55	-	0.014	0.004
100	1%	186.84	187.57	191.93	0.012	0.007	0.009
	2%	183.92	185.05	191.12	0.006	0.014	0.010
	5%	-	178.85	191.21	-	0.014	0.013
200	0.5%	177.87	179.81	179.97	0.0001	0.011	0.018
	1%	176.84	177.28	180.48	0.0001	0.011	0.020
	2%	177.58	173.14	179.67	0.011	0.003	0.007
300	0.25%	167.97	155.85	167.94	0.0001	0.0001	0.0001
	0.5%	165.60	161.05	168.16	0.0001	0.0001	0.0001
	1%	162.33	160.40	165.22	0.0001	0.0001	0.0001
400	0.1%	153.43	152.00	155.45	0.0001	0.0001	0.0001
	0.25%	151.86	144.20	151.66	0.0001	0.0001	0.0001
	0.5%	152.72	141.21	146.22	0.0001	0.0001	0.0001

Table 5.9: Mechanical properties of 8 helical springs for range of frequencies, dynamic strains and static pre-compression forces

It is appreciated that the stiffness coefficient of the helical springs reduces as the frequency increases, which should not be the case. This could have happened due to the wrong mass of the moving plate being used, or even due to slipping occurring between the surfaces of the helical springs and moving plate. However, when compared to the stiffness of the TMW devices, the change in magnitude of the helical spring stiffness coefficient was considered to be tolerable.

Because the springs and specimens being tested were setup in a parallel configuration, it was possible to subtract the mechanical properties shown in Table 5.9 from the calculated mechanical properties of the specimens.

5.4.2 Experimental validation with natural rubber

The test rig was validated using a cylindrical natural rubber specimen of known mechanical properties (grade 45 IRHD). It was tested as part of a larger project that tested other natural rubber variants, provided by Trelleborg. The specimen was tested on a Metravib VA2000 Viscoanalyser, as well as on the MTS test system. Master curves were used to predict the mechanical properties of the natural rubber specimen for a range of frequencies and temperatures. According to the ASTM D1415 and BS 903 (standard test certifications for rubber), 45 IRHD natural rubber specimens have Young's moduli of 1.86 MPa and 1.76 MPa, respectively. Based on experimental tests carried out during the investigations mentioned above, the 45 IRHD natural rubber specimen had a Young's modulus of 2 MPa (tests were carried out at strains up to 0.02). The Viscoanalyser test revealed that the specimen has a Young's modulus of 2.61 MPa (tests were carried out at a very small strain of 0.001). The effect of frequency is to make the Young's modulus higher, but typically the increase in magnitude is less than 10%.

Table 5.10 shows the results obtained for the natural rubber specimen.

Frequency, Hz	**Dynamic Strain**	**Stiffness coefficient, N/mm**		**Loss factor, η**	
		20N	**60N**	**20N**	**60N**
50	1%	156.33	179.31	0.109	0.099
	2%	157.86	179.82	0.099	0.118
	5%	-	167.40	-	0.135
80	1%	163.95	192.75	0.076	0.096
	2%	161.35	186.65	0.092	0.085
	5%	-	183.26	-	0.188
100	1%	169.99	189.71	0.085	0.059
	2%	168.04	182.65	0.090	0.109
	5%	-	169.56	-	0.134
200	0.5%	178.14	199.99	0.070	0.049
	1%	172.29	200.04	0.066	0.098
	2%	151.52	194.11	0.075	0.124
300	0.25%	173.19	179.19	0.139	0.100
	0.5%	174.53	179.68	0.044	0.154
	1%	165.51	180.86	0.058	0.150
400	0.1%	164.13	194.14	0.104	0.128
	0.25%	184.76	163.88	0.002	0.066
	0.5%	180.48	166.88	0.112	0.069

Table 5.10: Mechanical properties of natural rubber specimen for a range of frequencies, dynamic strains and static pre-compression forces

The stiffness coefficient of viscoelastic materials is typically calculated from the complex modulus, using Equation 5.16.

$$k = \frac{E^*A}{L} \tag{5.16}$$

where A is the cross-sectional area, L is the axial length, and E^* is the complex modulus, which is defined according to Equation 5.17:

$$E^* = E(1 + \beta S^2) \tag{5.17}$$

where E is the material Young's modulus, β is a dimensionless constant (reported as a value of 2 for unfilled elastomers and 1.5 for filled elastomers [88]), and S is the shape factor, which is defined as:

$$S = \frac{Area_{loaded}}{Area_{force-free}} = \frac{\pi r^2}{2\pi r L} = \frac{r}{2L} \tag{5.18}$$

Rearranging Equation 5.16, and substituting in the terms from Equations 5.17 and 5.18 gives the theoretical equation for E.

$$E = \frac{kL}{A(1 + \beta S^2)} = \frac{kL}{\pi r^2(1 + 2(\frac{r}{2L})^2)} = \frac{2kL^3}{\pi r^2(2L^2 + r^2)} \tag{5.19}$$

Substituting the calculated stiffness values from Table 5.10 into Equation 5.19 gave a range of Young's moduli. Figures 5.15 and 5.16 graphically illustrate these results.

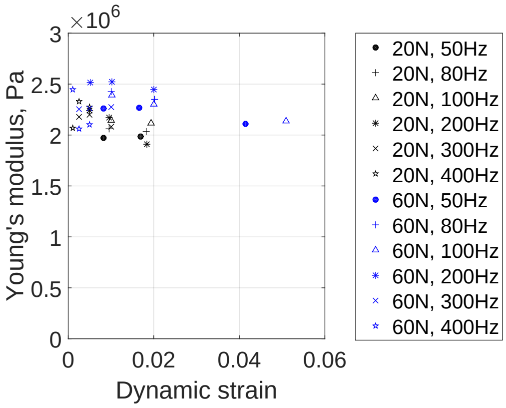

Figure 5.15: Natural rubber Young's modulus variation with dynamic strain over range of static strains and frequencies

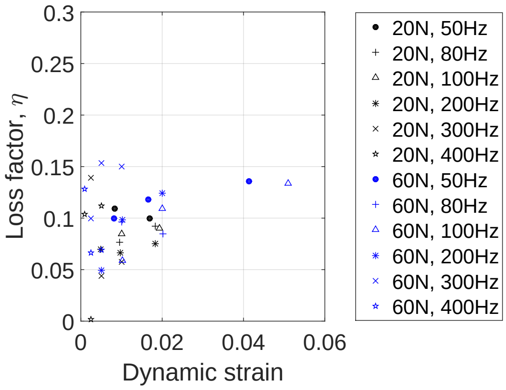

Figure 5.16: Natural rubber loss factor variation with dynamic strain over range of static strains and frequencies

The results shown in Figures 5.15 and 5.16 were reasonably comparable to the results previously reported. The Young's modulus of the material was shown to vary between 1.9 MPa and 2.53 MPa, compared to the previously reported results, which showed a Young's modulus of between 1.7 MPa and 2.6 MPa. The measured loss factor was slightly higher than expected. This was possibly attributed to friction between the interfaces of the natural rubber and the test structure. However, the results were still within a reasonable range. The loss factor ranges between 0.04 and 0.15 (with the exception of an anomaly for the 20 N, 400 Hz test), whereas the Viscoanalyser tests indicated loss factors between 0.07 and 0.13 at 0°, and 0.04 and 0.08 at 20°. With reasonable agreements made between the sets of results, the test rig was considered to be validated.

5.4.3 Tangled metal wire devices

With the high frequency test structure validated, the behaviour of the TMW devices were then analysed. The displacement time history for a test performed at 200 Hz is seen in Figure 5.17, and the corresponding force time history is seen in Figure 5.18

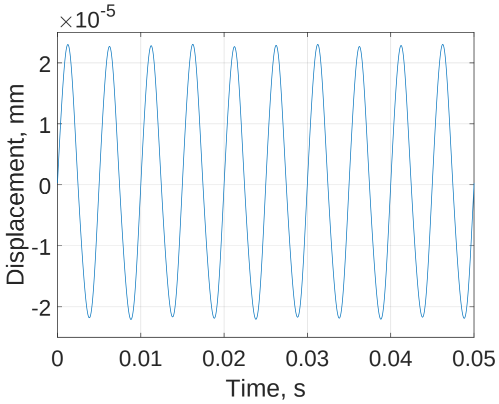

Figure 5.17: Displacement time history for an experiment carried out at 200 Hz

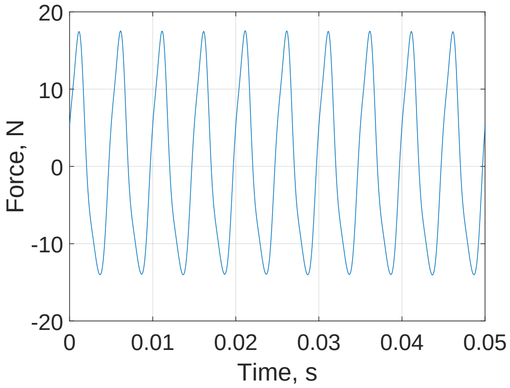

Figure 5.18: Force time history for an experiment carried out at 200 Hz

The force-displacement hysteresis curve obtained from the data shown above is seen in Figure 5.19.

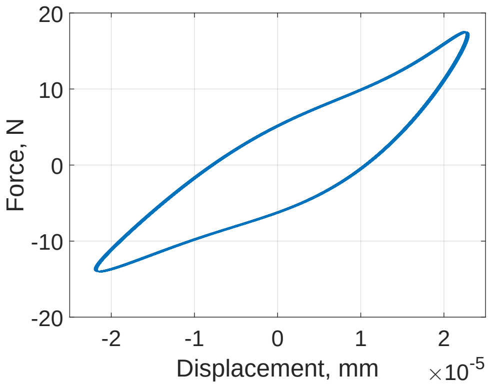

Figure 5.19: Force-displacement hysteresis curve obtained from for the experimental results shown in Figure 5.17 and 5.18

The hysteresis curve in Figure 5.19 appears aesthetically similar to the low frequency hysteresis curves reported in Chapter 4. This observation helps as an indicator that TMW devices exhibit frequency independence. If they were frequency dependent, the shape of the hysteresis curves would have changed, and the sharp ends of the hysteresis curves would tend to become more rounded. Whilst the hysteresis curve in Figure 5.19 does not have as sharp edges as those reported in the low frequency results (e.g. see Figure 4.11), this was attributed to the uncertainty over the exact mass that participated in the inertial term in Equation 5.15. If the mass is taken into account incorrectly, frequency dependency may be artificially applied to the results because inertia is a frequency dependent phenomenon. However, since the moving plate was assumed to act as an SDOF system, the use of the full measured mass of the moving plate was justified.

The results for the average dynamic stiffness and loss factor were once again analysed against the applied dynamic strain. They were scrutinised with respect to the hypotheses proposed in Chapter 4. The frequency dependency, in particular, was an important hypothesis to analyse because it did not particularly have a distinct effect on the reported results in Chapter 4. As the frequency was extended to a much larger range in this chapter, the results reported here have a much higher weighting because inertial effects were more significant at the higher frequencies.

Average dynamic stiffness

Figure 5.20 (a) - (e) show the high frequency average stiffness results obtained for a range of dynamic amplitudes and frequencies. It is interesting to note that the lower density TMW devices ($\tilde{\rho} = 0.18$) in Figure 5.20 (a) - (c) all behaved very similarly, in that the increase in pre-compression from 20 N to 35 N did not affect the average stiffness significantly. This was most likely due to the higher amount of empty space within the microstructure. As the pre-compression was increased, the rate of change of contacts between 20 N and 35 N was not as high as that of the higher relative density specimens, between 20 N and 60 N.

The frequency dependency hypothesis was, once again, not illustrated in the results. In general, average stiffness was shown only to depend on the static pre-compression and dynamic amplitudes of vibration, a characteristic of classical Coulomb friction.

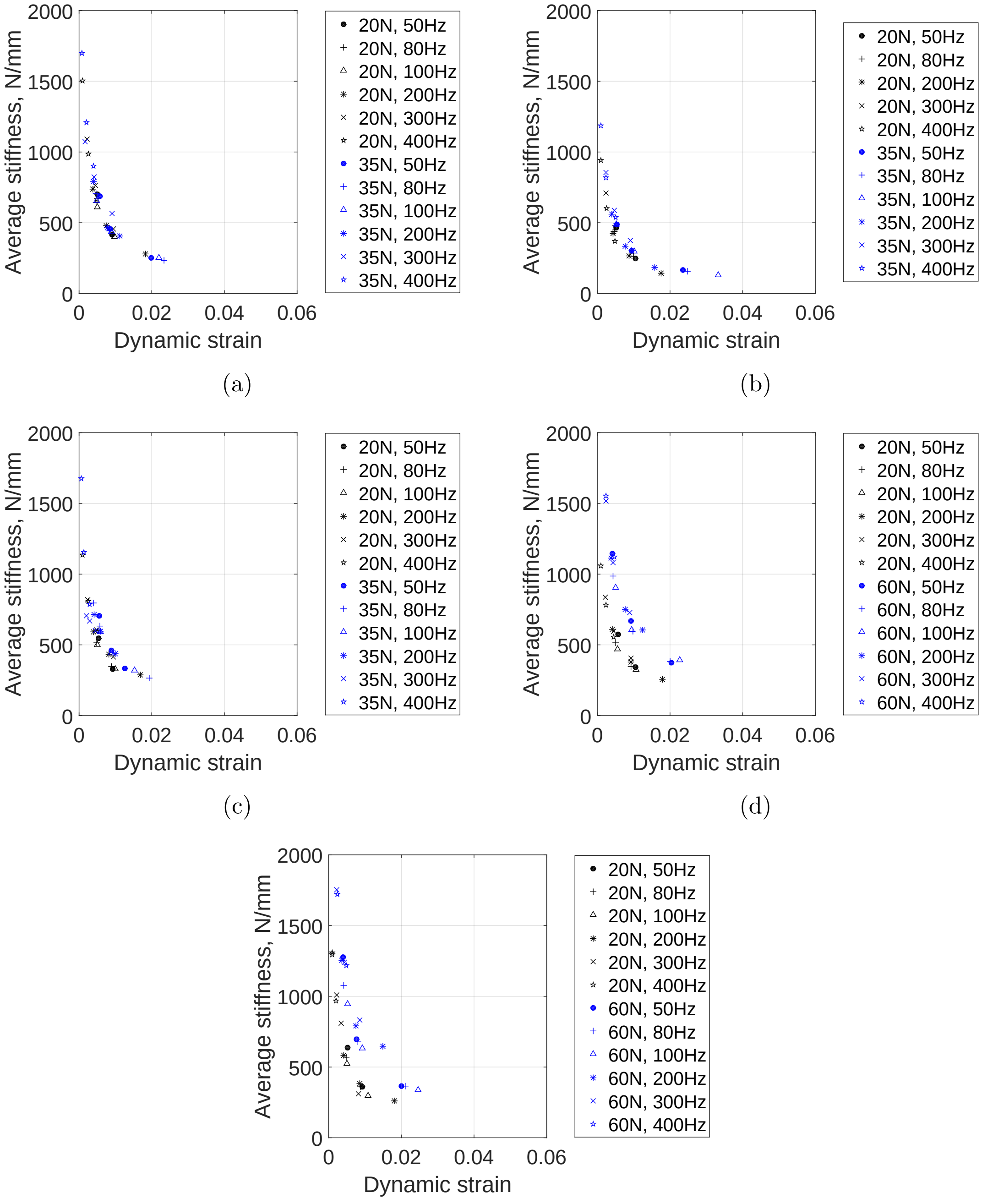

(a) (b) (c) (d) (e)

Figure 5.20: Average stiffness variation with dynamic strain over range of static strains and frequencies for: (a) $\tilde{\rho} = 0.18$, Specimen 1, (b) $\tilde{\rho} = 0.18$, Specimen 2, (c) $\tilde{\rho} = 0.18$, Specimen 3, (d) $\tilde{\rho} = 0.23$, Specimen 1, and (e) $\tilde{\rho} = 0.23$, Specimen 2

Loss factor

Figure 5.21 (a) - (e) show the high frequency loss factor results obtained for a range of dynamic amplitudes and frequencies. There was one distinct set of results in Figure 5.21 (c) that was different from the trends shown for the other specimens. The results for the 300 Hz and 400 Hz frequencies, which had relatively low dynamic amplitudes, showed relatively high loss factors. This was assumed to be caused due to anomalies in the data collection, and can thus be ignored from the results. It could have been caused due to resonance of the mass/spring system (i.e. the combination of the moving plate, and helical springs and TMW specimen stiffness).

The increase of static pre-compression levels, in general, caused higher levels of damping for the respective dynamic amplitudes. It was also seen that another important effect on loss factor was that of the dynamic amplitudes of vibration. As the dynamic amplitude increased, the level of damping also was shown to increase to a maximum plateau, in a logarithmic manner. The frequency dependency hypothesis was not shown to a significant extent for these loss factor results, and therefore, it can conclusively be stated that the specimens are independent of frequency.

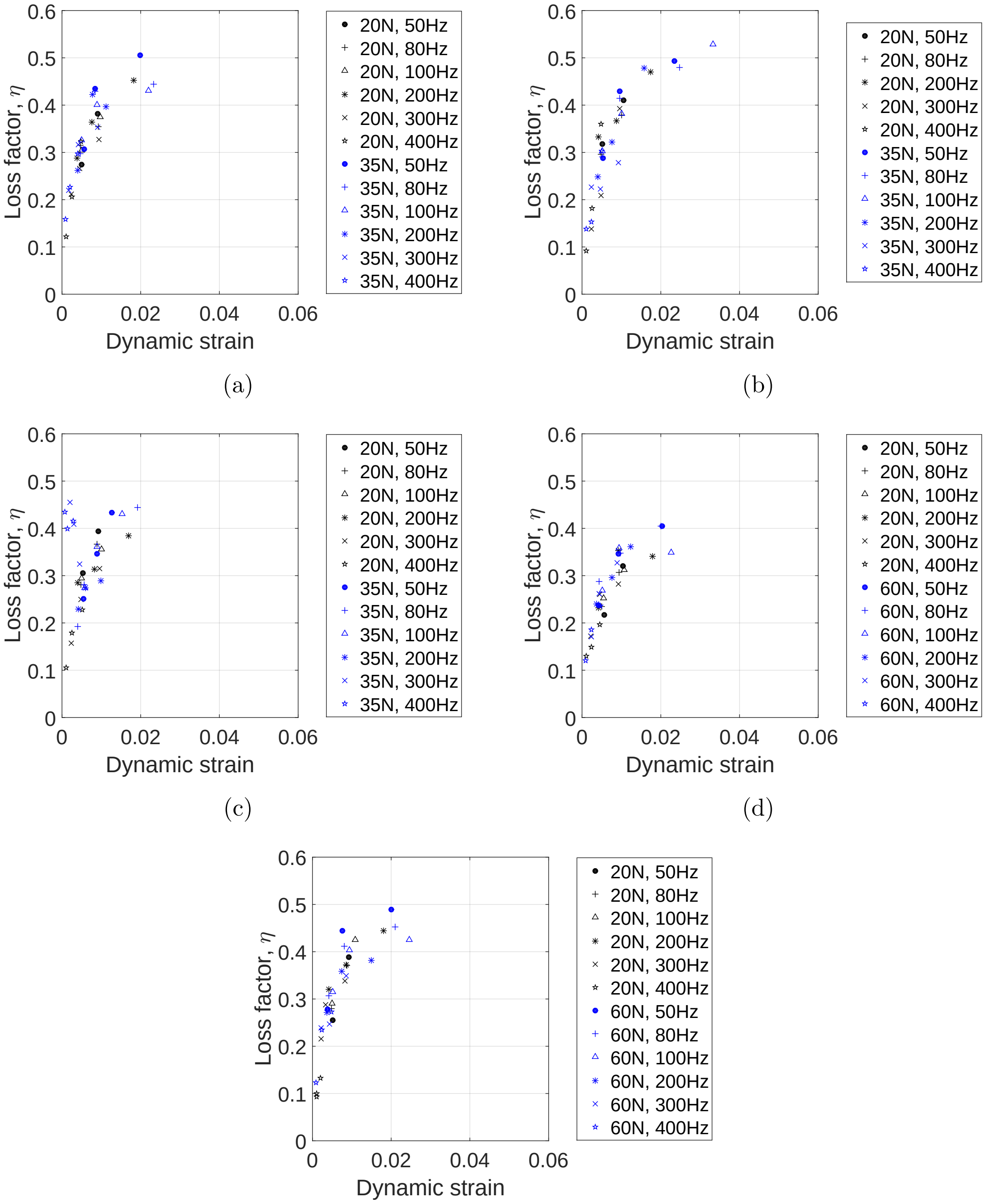

(a) (b) (c) (d) (e)

Figure 5.21: Loss factor variation with dynamic strain over range of static strains and frequencies for: (a) $\tilde{\rho} = 0.18$, Specimen 1, (b) $\tilde{\rho} = 0.18$, Specimen 2, (c) $\tilde{\rho} = 0.18$, Specimen 3, (d) $\tilde{\rho} = 0.23$, Specimen 1, and (e) $\tilde{\rho} = 0.23$, Specimen 2

Comparison with literature

Table 5.11 provides an indication of the approximate range of TMW device coefficients of stiffness and loss factors, as reported by other researchers in literature, as well as the results reported in this thesis. In the reported results shown below, the TMW devices studied were made from stainless steel, apart from the study made by Ertas, et al., where the TMW device was made of copper. "N. R." stands for "not reported" in the table.

Author	**Frequency range**	**Coefficients of stiffness**	**Loss factors**
Wang, et al. [23]	80 & 125 Hz	170 - 780 N/mm	0.03 - 0.18
Ma, et al. [34]	1 - 2000 Hz [2]	N. R.	0.35 - 0.45 [3]
Ma, et al. [36]	10 - 240 Hz	500 - 3000 N/mm	0.3 - 0.75
Ertas, et al. [37]	20 - 300 Hz	3000 - 15000 N/mm	N.R. [4]
Chandrasekhar, K. [present work]	50 - 400 Hz	130 - 1750 N/mm	0.09 - 0.53

Table 5.11: Range of TMW coefficients of stiffness and loss factors reported in literature for high frequency testing, as well as those reported in this thesis

Similar to the comparisons with literature shown in Chapter 4, the mechanical properties of TMW devices vary significantly from one researcher to another. Once again, the main reason for these variations is due to the different designs and dimensions of the TMW devices tested. Frequency dependence has been repeatedly reported by other researchers in their respective results. These could be introduced into the results due to the following reasons:

- In some of the above work, the mechanical properties were studied as a function of frequency rather than dynamic amplitude. If the dynamic amplitudes reduce at higher frequencies, frequency dependence may have been perceived.
- In high frequency testing, it is important to take the inertial mass into account. The need for this is emphasised especially in the work carried out by Ma, et

---

[3] Random excitation.

[4] Loss factor range estimated from reported damping ratios (by doubling the damping ratios, which were found from frequency response functions using the half power method).

[5] Damping reported in terms of damping coefficient, rather than loss factor - 1000 - 31000 Ns/m.

al. [36], where the slope of the hysteresis curves reduced significantly as the frequency was increased, and even becoming negative at 240 Hz. The frequency dependence may have therefore been artificially induced in the results of their work, as well as in the results reported by other researchers.

- Finally, the filtering techniques applied in the analysis of acquired data could have led to frequency dependence being illustrated. In some of the hysteresis curves reported in literature, the ends of the curves (i.e. where stick/slip is prominent) were rounded, rather than the characteristic sharp ends of TMW devices. As the stick/slip regions consist of high frequency content, and if these frequency content were low pass filtered, frequency dependence would be artificially introduced in the analysed results.

5.5 Conclusion

This chapter has included a wide aspect of discussions, ranging from the design of the high frequency test structure, to the choice of sensors, and results and discussion stemming from the test structure.

A high frequency test structure was designed and manufactured with the aim of testing frequencies above 20 Hz, the limiting frequency in Chapter 4. However, due to the choice of sensor in the form of an accelerometer, it was noted that the lowest frequency that could have been applied for the amplitudes of vibration tested was 50 Hz.

A number of materials were tested, in the form of helical springs, natural rubber, and the TMW devices. Helical springs were tested independently due to their inherent nonlinear behaviour. The results yielded from these experiments were used to apply corrections to the mechanical properties obtained for the natural rubber and TMW devices. A natural rubber specimen was tested with the aim of validating the test rig. The properties of the specimen were known beforehand, allowing direct comparisons to be made with the results obtained in this chapter.

The TMW devices were tested once the test structure was validated. Once again, the mechanical properties, in the form of average stiffness and loss factor, were tested as a function of dynamic strain. The results were studied according to the respective hypotheses proposed in Chapter 4. The trends observed in the high frequency results matched those seen in the low frequency results. The static and dynamic amplitudes were reported to be the fundamental phenomena driving the performance of the TMW devices. The TMW devices were also shown to be frequency independent, as was the case with the low frequency results. The results in this chapter have a more significant bearing since the inertial effects at higher frequencies are much more significant.

The results reported in Chapter 4 and in this chapter can hence conclusively state that the TMW devices can be modelled using classical Coulomb friction. The most important effects that need to be modelled are the influence of the number of contacts (due to static pre-compression), and travel of wires (due to dynamic amplitude) on the specimen behaviour. Chapter 6 will now discuss the analytical modelling aspects carried out in this thesis.

Chapter 6

Analytical Modelling

6.1 Introduction

During the course of this thesis, it has been established that researchers have generally concentrated on the physical behaviour of tangled metal wire (TMW) devices. Some aspects of the analytical modelling of TMW devices have also been attempted. Chapter 2 reported these models, and noted that the most successful attempt was a "black-box" model [13]. The reason that other, more physical models, have failed to work thus far is that the microstructural and mechanical characteristics of TMW devices have not been fully understood or appreciated. Chapter 3 explored the use of micro-computed tomography (μ)-CT and proposed a new technique for obtaining microstructural information through processing of scan images. Other researchers [54] have also looked at μ-CT technology to aid in the understanding of the microstructural characteristics, but have only observed rendered three-dimensional images, which do not give advanced microstructural information. Therefore, the associations of experimental behaviour to microstructure physics are only made in a qualitative matter.

This chapter introduces the thought process involved in proposing analytical models that are based on the mechanics of the TMW microstructure. Before the work carried out in this thesis, the general consensus in literature was that the primary energy dissipation mechanism of TMW devices was friction. Previous researchers also had reasons to believe that this was not the only type of damping coming from the

TMW microstructure, with some reports showing frequency dependency - a characteristic of viscous damping. There are a number of reasons why this might have been reported by researchers, including inertial terms not being taken into account, or experiments being performed using acceleration control, rather than displacement control (since for the same acceleration, displacements reduce significantly at higher frequencies). Chapters 4 and 5 showed that frequency dependency of stiffness and damping is non-existent for TMW devices, and hence indicated that energy dissipation in TMW devices is instead purely frictional. This paves the way to eliminate some of the complexities associated with modelling frequency dependency, and in particular, nonlinear frequency dependency.

This chapter starts off by discussing some of the experimental characteristics of frictional systems. Frictional models, some simple, others more complex, are also briefly introduced. The more detailed discussion focuses on various different types of analytical models, such as the well known Kelvin-Voigt and Maxwell models. These models form the basis of the analytical modelling proposed for TMW devices. The primary goal is to capture trends observed in the experimental hysteresis curves. Once this is exhibited, a more precise model is attempted by means of parameter identification for the proposed model using the Metropolis-Hastings algorithm.

An attempt is also made to justify the use of such a physical model through the use of the image processing results. It must be appreciated that, while the approach proposed in Chapter 3 is novel, it is still in its infancy, with some level of uncertainty still existing. This is especially true in the way the results should be analysed. Therefore, there is significant room for improvement. With this being noted, it should also be appreciated that previous analytical models that have been proposed in literature have made several assumptions regarding the microstructural state of TMW devices. This thesis has made a significant stride in the understanding of TMW microstructure through the processing of $\mu - CT$ images, hence reducing the uncertainties introduced by the assumptions made, and hence allowing for more accurate and justified modelling techniques to be employed.

6.2 Friction

Friction is a phenomenon that occurs in any set of contacts where relative motion occurs. The contacts may be macroscopic or even microscopic (e.g. grain boundaries within materials). Due to this, friction occurs in all mechanical systems. Examples can be found in bearings, brakes, wheels [89], air flow over wings on an aircraft, etc. These can be divided into several categories that include dry friction, fluid friction, lubricated friction, skin friction, and internal friction.

Methods of modelling friction have long been a source of interest for researchers. There are several phenomena that occur in systems with friction, and these have to be considered in applications, such as friction compensation required for accurate motion of robots. It is noteworthy that not all friction phenomena can be characterised in a single model, and there are several models available, each tackling a single or several of the phenomena presented by friction. To add to the complexity, friction is easily influenced by several factors such as the physical properties of a material, geometry of contacts, roughness, wear, surface temperature [90], [91].

Leonardo da Vinci was reportedly the first to study friction in a scientific manner [92]. He noted that the friction force was proportional to the weight of the body in frictional contact, that the force was independent of apparent area of contact for different bodies, and that the force produced depended on the surface of the bodies in frictional contact (bodies with a smoother surfaces produced lower friction). Although these studies were never published, another physicist, Guillaume Amontons, also reported the first two findings of da Vinci. These are now known as “Amontons' First and Second Laws of Friction”. The third law proposed by Charles Augustin Coulomb states that the dynamic friction is independent of the sliding velocity. These three laws only exist in the case of dry friction, and can provide only a rough approximation of actual system behaviour.

Amontons' Second Law suggests that the friction contacts deform elastically, which is why friction is independent of apparent area of contact. This is however not the case in experimentally observed phenomena, and researchers sometimes study friction in terms of real area of contact, which is contradictory to Amontons' Second Law. The real area of contact is actually made up of small asperities on the surfaces of frictional contacts, and when they interact, atomic scale contacts also occur. These asperities deform elastically or plastically depending on the force application, and therefore influence the friction force.

6.2.1 Experimentally observed frictional phenomena

The major friction phenomena that occur in experimental studies are now briefly discussed.

Static friction, break-away force and dynamic friction

Static friction is defined as the friction force when the velocity between the friction surfaces is zero. Static friction is related to the shear strains experienced by the bodies of contacts and increases with displacement up to the break-away force. Break-away force, which is seen as the peak in the friction force-displacement graph, is the force required to initiate sliding. Dynamic friction is the friction force in sliding. The break-away force is generally unique to a pair of contacts under static loading, and inversely proportional to the rate of application of force under dynamic conditions [93]. Both static and dynamic friction forces are generally non-unique i.e. have a range of infinite values.

Pre-sliding displacement

This phenomenon can only be seen if the tangential force remains below the break-away force. In this regime, microscopic motion occurs between the asperities of the two contact surfaces. The friction force is dependent on the displacement, rather than velocity [94]. The regime is extremely sensitive to plastic deformation. When a load is removed, and reapplied, it can be observed that the load path follows a different route. This indicates that there may be some permanent plastic deformation of contact area (more specifically, asperity junctions). Note that with the applied tangential forces, the asperities first deform elastically, before plastic deformation occurs. Due to this behaviour, the asperities act as nonlinear hysteretic springs [94]. Pure sliding motion only occurs when the break-away force is exceeded, which is enough to break the asperities.

Stribeck effect

In the low relative velocity regime, the friction force tends to drop with increasing velocity, before increasing again. This phenomenon has been named after Richard

Stribeck, as the Stribeck effect. In dry friction, the effect is dependent on normal creep of asperities, the surface topography, and tangential stiffness and inertia of the asperities [94].

Hysteretic effects

Hysteretic effects are categorised into two different classes: hysteresis caused by contact compliance, and that caused by frictional memory.

Deformation of asperities creates contact compliance - the asperities act like springs, therefore with tangential forcing, the asperities undergo minuscule deformation. Courtney-Pratt and Eisner observed that the changes in the process were mostly irreversible, with only some displacement being reversible with a reduction in tangential forcing of two metals in contact [95]. They could not identify a finite range of values of the tangential forces to produce reversible displacements. This causes a narrow hysteresis around zero relative velocity, as seen in Figure 6.1 (a).

Frictional memory, shown in Figure 6.1 (b), is defined as the lag between the change in relative velocity and frictional force [91]. Hysteresis arises in oscillating conditions of macroscopic magnitude. Under the Stribeck effect, the friction force lags behind the relative velocity by a phase of 90° in steady conditions. The friction characteristics will follow the same hysteresis curve in both acceleration and deceleration. However, under unsteady conditions e.g. periodic variations in forcing, frictional memory arises, where there is a time lag between the maximum relative velocity and minimum friction force (or vice versa). Due to this lag, the friction force can have more than one value for a particular velocity, depending on whether the contacts are accelerating or decelerating. For example, if stick is considered in the model, the friction force is at maximum during stick, and reduces to an asymptotic value with increase in relative velocity. However, when the velocity is reversed, the path followed by the friction force is different. The friction force increases until stick is reached, and the path is not the same as the initial one, thereby generating a hysteresis curve. In the case of velocity being restricted to pure sliding, Hess and Soom [96] correlated the time lag between friction force and relative velocity to the multiple valued friction values in lubricated contacts. This time lag was attributed to the film thickness of the lubrication changing with velocity. In dry friction, the time lag can be explained by the reconfiguration of the asperity junctions as they are being sheared.

When sign changes of the velocity are taken into account, hysteresis curves are created on either side of the stick zone (relative velocity is zero) in the gross sliding velocities. There is no hysteresis curve observed where relative velocity is zero. However, it can be seen if the pre-sliding displacement is taken into account. The friction forces are higher in the accelerating phase. This is because as the system accelerates, the coefficient of friction switches from static to dynamic, and so the friction force drops. If the system is subjected to a steady state oscillatory motion, the system then decelerates (accelerates in the negative direction), and so the friction force drops further [97]. These hysteresis curves are non-reversible in nature, and the models generally describe the friction force as a function of both relative velocity and acceleration, the latter allowing for the memory effect to be taken into account.

Hysteretic models are described by internal state variables, which are essentially differential equations, to define the friction force, and can be considered as dynamic models.

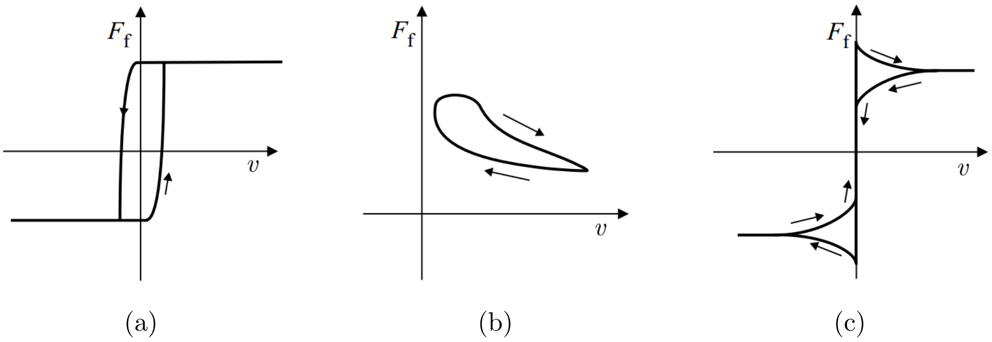

Figure 6.1: (a) Contact compliance, (b) Frictional memory, and (c) Non-reversibility of dry friction (Source: [90])

Dwell time and rising break-away force

Break-away force is known to rise with dwell time. Dwell time is the time in which a friction surfaces spend in the zero relative velocity regime. The break-away force initially increases rapidly, followed by a slow rise with dwell time and then plateaus at a large dwell time. A compilation of some of the time-dependent static friction models that take into account the dwell time can be found in [91].

Stick-slip motion

Stick-slip motion arises because static friction is characteristically higher than dynamic friction. The friction surfaces may stick or slip alternatively in this phenomenon. The initial practice, from Coulomb's work, was to use a higher static coefficient of friction and a lower dynamic coefficient of friction to explain stick-slip motion. However, this is not universally accepted, and there are several models that attempt to represent this behaviour.

6.2.2 Friction models

Friction models can be characterised into two categories: static and dynamic friction models. The biggest difference between the two types of models is the exclusion of frictional memory in the static models. Static models usually consist of a direct relationship between frictional force and the relative velocity [90]. Static models are described with the non-reversibility of friction force. Frictional memory, or hysteresis, is introduced into dynamic models in terms of state variables to describe friction. The changes in the state variables over time are described by differential equations. As mentioned previously, there are several models proposed by several researchers, for both static and dynamic friction. Only some of the models will therefore be discussed in order to maintain conciseness.

Static models

In these models, friction is solely dependent only on the relative velocity between the friction surfaces [91]. The most commonly found static friction models are the Coulomb model, Coulomb with viscous friction model, Coulomb with viscous and stiction (friction during stick) model, and Coulomb with viscous and Stribeck friction model.

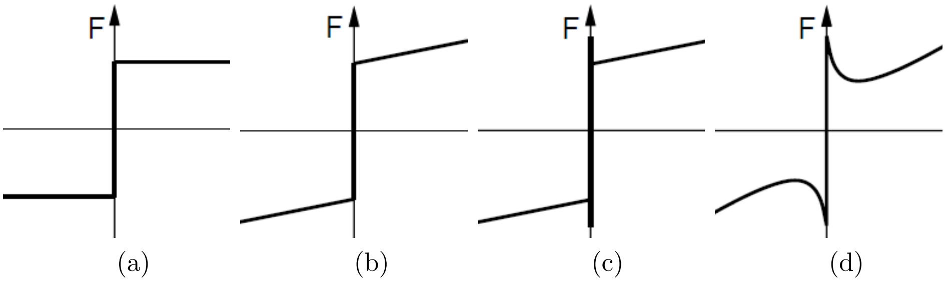

Figure 6.2: Friction characteristics of static models: (a) Coulomb friction model, (b) Coulomb + viscous model, (c) Coulomb + viscous + stiction model, and (d) Coulomb + viscous + Stribeck effect model (Source: [98])

Coulomb friction: In Coulomb friction damping, the friction forces oppose the motion of vibration [99]. The forces are also independent of frequency [100]. Under this model, friction is assumed to be independent of apparent area of contact. The force is only dependent on the relative velocity between the contacts, but not the magnitude of the velocity [101].

$$F = F_c \operatorname{sgn}(V_r) \tag{6.1}$$

where V_r is the relative velocity between the friction contacts, F_c is the Coulomb friction (or break-away force) and

$$F_c = \mu |f_n| \tag{6.2}$$

where μ is the coefficient of friction and f_n is the normal force acting on the contact. The force-velocity behaviour is seen in Figure 6.2 (a). Coulomb friction can also be regarded as kinetic friction because it holds for non-zero velocities. The signum function, $\operatorname{sgn}(V_r)$ is defined as,

$$\operatorname{sgn}(V_r) = \begin{cases} +1 & \text{for } V_r > 0 \\ 0 & \text{for } V_r = 0 \\ -1 & \text{for } V_r < 0 \end{cases} \tag{6.3}$$

The following question arises: what is the friction force at zero velocity? This is one of the major setbacks of the Coulomb friction model, or in fact any other static friction model for that matter: there is a discontinuity at zero velocity, where the friction force can take up an infinite number of values. This is not justifiable in a physical sense, because in reality, the force must be non-singular. This can introduce instabilities in computational codes that attempt to model Coulomb friction.

Viscous and Coulomb friction: The fluid layer between two friction contacts may lead to viscous losses. This is represented as a linear function of velocity [101].

$$F = cV_r \tag{6.4}$$

where c is the viscous loss, which is proportional to the viscosity of the fluid. At zero velocity, viscous friction is zero since the fluid is stationary. The force-velocity relationship, along with Coulomb friction can be seen in Figure 6.2 (b).

Stiction: It is widely accepted that the friction force at rest is greater than kinetic friction. Stick-slip motion occurs because of this. A break-away force is the force required that is greater than or equal to the stiction force, and initiates slipping. This can be represented by:

$$F(V_r) = \begin{cases} F_c\,\mathrm{sgn}(V_r) & \text{if } V_r \neq 0 \\ F_e & \text{if } V_r = 0 \& |F_e| \leq |F_s| \\ F_s & \text{if } V_r = 0 \& |F_e| > |F_s| \end{cases} \tag{6.5}$$

where F_e is the externally applied force, and F_s is the static friction force. Equation 6.5 is also known as the Morin model. Slipping only occurs if the external force exceeds the stiction force. Again, at zero velocity, the friction force can take up any value between the interval $-F_s$ to F_s, and so, it is discontinuous. Stiction is seen in Figure 6.2 (c), which includes the Coulomb and viscous terms as well. It is seen as the peak at zero relative velocity on the force-velocity diagram.

Haessig and Friedland [102] replaced the discontinuity in the friction force-relative velocity diagram with a steep slope in order to avoid it. The choice of slope is very important. If the slope has a very high gradient, the solution becomes numerically stiff and so can take a lot of time to compute. Having a lower gradient reduces this time. In any case, the presence of the slope indicates that the body is accelerating even if the external force is less than the stiction force, which is not justifiable in a physical sense because if the external force is less than the stiction force, no motion can happen [91]. The Karnopp model is another model that aims to avoid the discontinuity at zero velocity by defining a narrow band, inside which the body is assumed to be in the stick mode, and outside which the body is slipping.

Complexity with such models increases with complexities in the system due to the switching between the functions, and using the external force to detect whether the body is sticking or not [91].

Stribeck effect: The Stribeck effect is considered static because it is a function of velocity. There are several models available to replicate this phenomenon. The general form of the friction forces are:

$$F(V_r) = N\mu(V_r)\,\mathrm{sgn}(V_r) \tag{6.6}$$

when viscous effects are ignored, and

$$F(V_r) = N\mu(V_r)\,\mathrm{sgn}(V_r) + cV_r \tag{6.7}$$

when viscous effects are taken into account. N is the normal load applied, c is the viscous friction coefficient (viscosity of fluid) and $\mu(V_r)$ is the relative velocity dependent coefficient of friction, which is also a representation of the Stribeck effect, which has a number of forms throughout literature. Examples of these forms that have been developed are the Gaussian (Equation 6.8) and the Laurentzian (Equation 6.9) models:

$$\mu(V_r) = \mu_k + \Delta\mu \mathrm{exp}\left(-\left(\frac{V_r}{V_s}\right)^2\right) \tag{6.8}$$

$$\mu(V_r) = \mu_k + \frac{\Delta\mu}{1+\frac{V_r}{V_s}} \tag{6.9}$$

where μ_k is the minimum coefficient of kinetic friction, $\Delta\mu = \mu_s - \mu_k$, μ_s is the coefficient of static friction, V_r is the relative velocity between the contacts and V_s is the Stribeck velocity (the relative velocity at which the contacts switch from microslip to macroslip). Note that some Stribeck functions already contain viscous effect terms. This effect is seen in Figure 6.2 (d).

Dynamic models

The primary objective of these models is to capture the hysteretic behaviour that characterise systems with friction. This is made possible by making the friction force dependent on internal states of the system in addition to the relative velocity. The internal states generally refer to average asperity displacements in the frictional contacts.

Dahl model: Dahl introduced the first dynamic model in friction, while working on modelling of dynamic systems with sliding or rolling friction [91]. The fundamental assumption in this model is that the microscopic asperities continually form and break throughout the loading process. The Dahl model is a basic representation of the Coulomb model with a lag in friction with changes in displacement direction [103]. The steady-state representation of the Dahl model leads to the basic Coulomb model. The Dahl model requires the Coulomb friction force, current applied force, the magnitude and sign of the relative velocity and the stiffness at zero displacement to be known. The time variation of the forces can be represented by:

$$\frac{dF(x)}{dt} = \frac{dF(x)}{dx} \cdot \frac{dx}{dt} \tag{6.10}$$

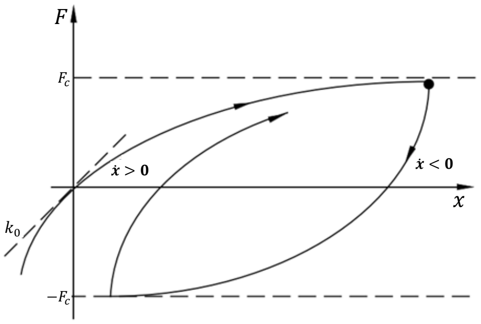

Figure 6.3: Frictional force-displacement relationship in the Dahl model (Source: [89])

Figure 6.3 illustrates the friction force $F(x)$ (denoted simply as F on the diagram) as a function of relative displacement, x in the pre-sliding regime. $\frac{dF(x)}{dx}$ is the friction slope function, and is always positive. Depending on the sign of the relative displacement, $F(x)$ can be seen to reach the Coulomb friction limits $\pm F_c$ in an asymptotic manner. The general form for the friction slope function is described as:

$$\frac{dF(x)}{dx} = k_0 \left| 1 - \frac{F}{F_c}\,\mathrm{sgn}(\dot{x}) \right|^n \mathrm{sgn}\left(1 - \frac{F}{F_c}\,\mathrm{sgn}(\dot{x})\right) = k_0 \left| 1 - \frac{F}{F_c}\,\mathrm{sgn}(\dot{x}) \right|^n \cdot S \quad (6.11)$$

where k_0 is the gradient of the curve at zero displacement, and n is an exponent that determines the shape of the curve. The signum function, S in Equation 6.11 is essentially a stabilising factor in numerical solutions [91]. If the exponent, n is used as one in a model, then this stabilising factor can be set to unity. Note that $\dot{x}$ is the same as V_r that was used previously. Incorporating Equation 6.10 with Equation 6.11 leads to:

$$\frac{dF(x)}{dt} = k_0 V_r \left| 1 - \frac{F}{F_c}\,\mathrm{sgn}(V_r) \right|^n \mathrm{sgn}\left(1 - \frac{F}{F_c}\,\mathrm{sgn}(V_r)\right) \quad (6.12)$$

Taking $n = 1$, Equation 6.12 simplifies to:

$$\frac{dF}{dt} = k_0 V_r \left(1 - \frac{F}{F_c}\,\mathrm{sgn}(V_r)\right) \quad (6.13)$$

Introducing an internal state - the average microscopic contact asperity displacement, $\hat{Z}$, where $F = k_0\hat{Z}$, we get:

$$\frac{d\hat{Z}}{dt} = V_r \left(1 - \frac{k_0\hat{Z}}{F_c}\,\mathrm{sgn}(V_r)\right) \quad (6.14)$$

To show that the Dahl model is the Coulomb model under steady-state conditions, the time evolution of the internal state is set to zero.

$$\frac{d\hat{Z}}{dt} = 0 \quad (6.15)$$

which means that,

$$\hat{Z} = \frac{F_c}{k_0}\,\mathrm{sgn}(V_r) = \frac{F}{k_0} \quad (6.16)$$

and therefore,

$$F = F_c\,\mathrm{sgn}(V_r) \quad (6.17)$$

which is the Coulomb friction model stated earlier. The Dahl model, however, is not capable of modelling the Stribeck effect [103].

Bristle model: This model was introduced by Haessig and Friedland [102]. The randomness posed by friction is tackled in this model, primarily due to the random distribution of asperities (or bristles). The bristles deform both elastically and plastically when an external force is applied. The friction force between two contacts is assumed to be caused by the compliance by a large number of bristles, that are bonded at contact points [89]. If the force is sufficiently large, the bristles deflect and can produce slip rather than yielding [103].

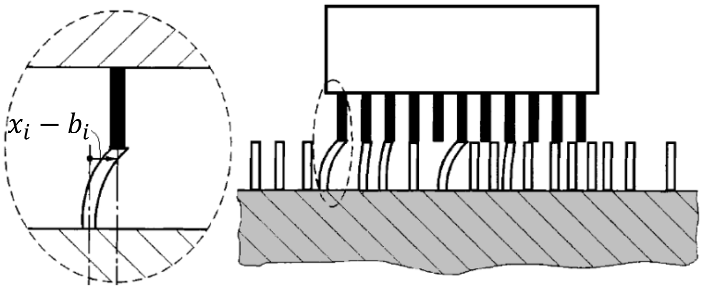

Figure 6.4: Bristle interaction (Source: [101])

As the surfaces move relative to each other, the bristles face a strain. Figure 6.4 illustrates the deflection that the bristles undergo $x_i - b_i$. The bristles essentially act as springs. A new connection between bristles is established after the strain exceeds a critical amount. The new connection will possess a new strain, which is randomly created. The friction force is then calculated as the sum of the spring forces experienced by the bristles. The friction-velocity relation is created by assuming that the number of bristles also depends on the relative velocity between the contacts.

$$F = \sum_{i=1}^{N} k_0(x_i - b_i) \tag{6.18}$$

where N is the total number of bristles, k_0 is the stiffness of the bristles (which can be made velocity dependent), x_i is the relative position of the bristles, and b_i is the contact location of two opposing bristles. This model represents the random nature of friction, and fundamentally seems correct in considering that the asperities that lead to friction essentially behave as springs. However, as the number of bristles increases, so does the complexity of the model. Due to this, the computational efficiency of this model is extremely poor [101]. Acceptable results have been produced when 20-25 bristles have been employed in the model [89]. Oscillatory motion may also be produced, even when the surfaces are stationary (sticking), because no damping of bristles is introduced in the model [89].

LuGre model: In the LuGre model, proposed by de Wit, et al. [103], friction is modelled similar to the Bristle model. The applied force allow the bristles to deflect as springs, which slip if the force surpasses a critical threshold. The steady state deflection of the bristles is dependent on the velocity, which decreases with increasing velocity [89]. This model has the inclusion of the Stribeck effect, and can be shown to be reduced to the simplified Dahl model (Equation 6.12) under certain conditions. The bristle time evolution can be defined as:

$$\frac{dz}{dt} = V_r - k_0 \frac{|V_r|}{g(V_r)} z \tag{6.19}$$

and

$$F = k_0 z + c(V_r)\frac{dz}{dt} + f(V_r) \tag{6.20}$$

where z is the average bristle deflection, k_0 is the stiffness, $c(V_r)$ is a velocity dependent damping coefficient, $f(V_r)$ is a function that includes the viscous effects, and $g(V_r)$ is a function of the Stribeck effect, which can take the form of the Gaussian and Laurentzian functions stated earlier. An advantage of this model is that the damping is taken into account, when the damping coefficient takes the form:

$$c(V_r) = c\exp\Big(-\Big(\frac{V_r}{V_s}\Big)^2\Big) \tag{6.21}$$

There are other dynamic models available in literature, such as the Leuven model [104], which is a modification of the LuGre model that includes several friction phenomena that includes hysteresis behaviour in pre-sliding, Stribeck effects in sliding, stick-slip motion, varying breakaway force and frictional lag. The hysteresis behaviour in pre-sliding is modelled with a hysteretic model with nonlocal memory [104]. A modification of the Leuven model was also created by the same authors in [105], as it was found that when the hysteresis curve approaches its ends, there was a discontinuity of the force. This was overcome by using the nonlinear state function as a continuous friction force at all times.

6.3 Microelement modelling

Microelement models have extensively been used historically to simplify and analytically explain the behaviour of mechanical structures. They are typically found in single and multiple degrees of freedom (SDOF/MDOF) free body diagrams. Some examples of these can be seen in Figure 6.5.

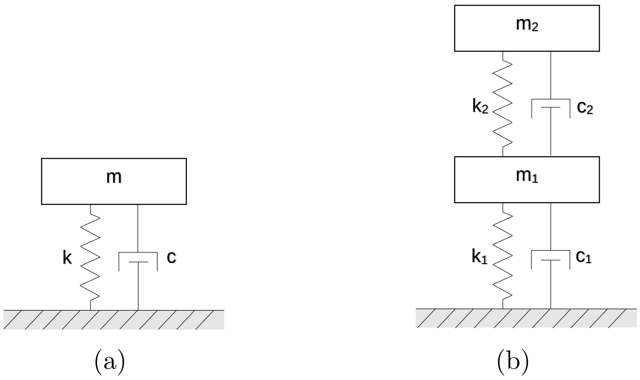

(a) (b)

Figure 6.5: Example of: (a) SDOF, and (b) MDOF models used to analytically explain structural behaviour

In Figure 6.5, m is the mass, k is the stiffness coefficient, and c is the damping coefficient. In the following sections, the components of microelement models are discussed. They are then applied in various configuration to describe the mechanical characteristics in the contexts of stiffness and energy dissipation. The lessons learnt from the analyses will then be applied to the proposed analytical modelling of TMW devices, discussed in Section 6.4.

6.3.1 Component description

The primary microelement components used in analytical modelling can be listed as follows:

- Linear spring: A linear spring is one that obeys Hooke's law. A linear spring that is compressed/extended by a displacement, x, produces a force, F_k, which is directly proportional to the deformation. The constant of proportionality is the stiffness coefficient, k of the spring, and is proportional to the Young's modulus of the material. Equation 6.22 shows the mathematical equation, and Figure 6.6 (a) illustrates a linear spring microelement.

$$F_k = kx \tag{6.22}$$

- Viscous dashpot: A viscous dashpot is used to describe damping that results from viscous friction. A viscous dashpot element produces a force, F_d, which is directly proportional to the velocity, $\dot{x}$, applied to it. The constant of proportionality in this case is the coefficient of damping, c. Equation 6.23 shows this mathematically, and Figure 6.6 (b) illustrates a viscous dashpot microelement.

$$F_d = c\dot{x} \tag{6.23}$$

- Frictional slider: The frictional slider is used to describe characteristics of frictional contacts. Various characteristics and models of friction have already been described in Section 6.2. The most common model used as the frictional slider is the classic Coulomb friction model, which was mathematically defined in Equations 6.1 - 6.3. Figure 6.6 (c) illustrates a frictional slider microelement.

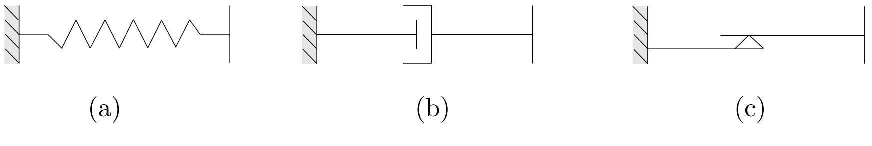
(a) (b) (c)

Figure 6.6: Microelement components: (a) linear spring, (b) viscous dashpot, and (c) frictional slider

These microelements are applied in various configurations, which are used to describe a wide variety of physical phenomena. The most commonly used models are described next.

Prior to beginning the discussion of the individual models, some assumptions need to be stated. The applied displacement to these models takes the form:

$$x = X\exp(j\omega t) \tag{6.24}$$

where X and ω are the amplitude and frequency of the cyclic loading, respectively, t is the time, and j is the imaginary unit - square root of negative one.

The time derivative of displacement, $\dot{x}$ (i.e. velocity) is given as:

$$\dot{x} = j\omega X\exp(j\omega t) = j\omega x \tag{6.25}$$

The resultant force takes the form of:

$$F = f_0\exp(j\omega t) \tag{6.26}$$

where f_0 is the amplitude of the resultant force.

6.3.2 Kelvin-Voigt

The Kelvin-Voigt model consists of a linear spring microelement that in parallel with a viscous dashpot microelement. It is typically used to describe materials that are viscoelastic in nature (i.e. they portray both viscous and elastic characteristics), and can be used to study creep. Figure 6.7 illustrates the model.

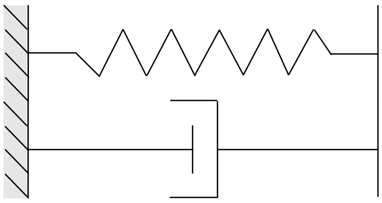

Figure 6.7: Kelvin-Voigt model

Because both microelements are in a parallel configuration, the displacement in each is the same:

$$x_{tot} = x_k = x_d \tag{6.27}$$

where x_{tot} is the total displacement applied, x_k, and x_d are the displacements of the linear spring and viscous dashpot microelements, respectively. The total force produced by this configuration can then be calculated as the sum of the individual microelements:

$$F_{tot} = F_k + F_d \tag{6.28}$$

where F_{tot} is the total resulting force, F_k, and F_d are the forces produced by the linear spring and viscous dashpot microelements, respectively. Substituting Equations 6.22 and 6.23 into Equation 6.28 yields:

$$F_{tot} = kx + c\dot{x} \tag{6.29}$$

Substituting in the displacement, velocity, and force forms in Equations 6.24, 6.25, and 6.26 into Equation 6.29 gives:

$$f_0 \exp(j\omega t) = kX \exp(j\omega t) + j\omega cX \exp(j\omega t) = X \exp(j\omega t)(k + j\omega c) \tag{6.30}$$

which simplifies to:

$$f_0 = X(k + j\omega c) \tag{6.31}$$

The magnitude and phase of Equation 6.31 can then be calculated:

$$|f_0| = \sqrt{X^2(k^2 + (\omega c)^2)} \tag{6.32}$$

$$\angle f_0 = \phi = \arctan\left(\frac{\omega c}{k}\right) \tag{6.33}$$

The total force in Equation 6.29, can now be rewritten:

$$F_{tot} = f_0 \exp(j\omega t) = X\sqrt{k^2 + \omega^2 c^2}\exp(j\phi)\exp(j\omega t) \tag{6.34}$$

where

$$f_0 = |f_0| \exp(j\underline{/f_0}) \tag{6.35}$$

which simplifies to,

$$F_{tot} = X\sqrt{k^2 + \omega^2 c^2}\exp(j(\omega t + \phi)) \tag{6.36}$$

Equation 6.36 shows that the response is a function of three components: the stiffness coefficient, the damping coefficient, and the frequency. Figure 6.8 shows the force-displacement behaviour for: (a) a constant damping coefficient and a number of different stiffness coefficients, (b) a constant stiffness coefficient and a number of different damping coefficients, and (c) various frequencies.

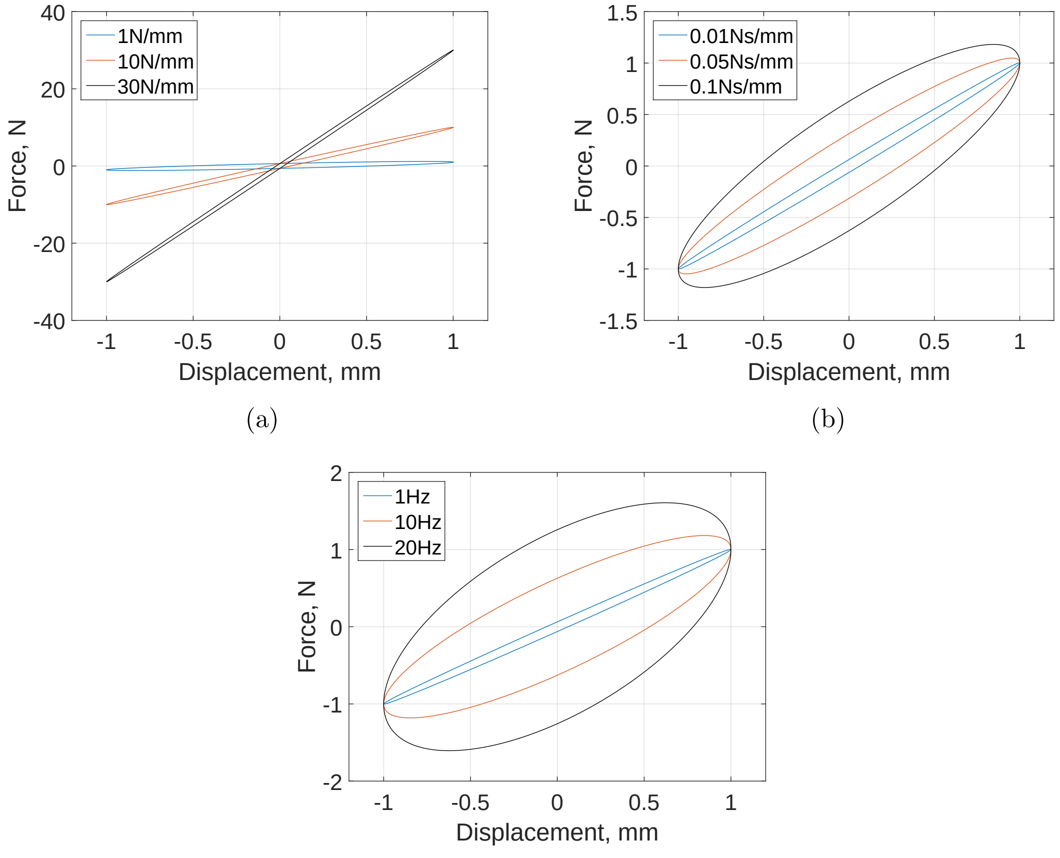

(a) (b)

(c)

Figure 6.8: Kelvin-Voigt force-displacement behaviour for (a) various linear spring stiffness coefficients, (b) various viscous dashpot damping coefficients, and (c) various frequencies

Figure 6.8 (a) shows that stiffness coefficient increases the slope of the curve, and (b) and (c) show that the damping coefficient and frequency have an equivalent effect in that they increase the size of the hysteresis.

6.3.3 Maxwell

The Maxwell model consists of linear spring and viscous dashpot microelements in series with each other, and is also used to alternatively describe viscoelastic materials, especially when studying stress relaxation. Figure 6.9 illustrates the model.

Figure 6.9: Maxwell model

In this series configuration, the total force produced by this model is the equal to the forces produced by each microelement.

$$F_{tot} = F_k = F_d \tag{6.37}$$

where F_{tot} is the total resultant force, F_k, and F_d are the forces produced by the linear spring and viscous dashpot microelements, respectively. The displacements within each microelement in this configuration can then be calculated as the sum of the individual microelements:

$$x_{tot} = x_k + x_d \tag{6.38}$$

where x_{tot} is the total displacement of the model, x_k, and x_d are the displacements in the linear spring and viscous dashpot microelements, respectively.

The steps for the final force-displacement relationship for the Maxwell model are skipped to maintain conciseness. Including the forms of displacement, velocity and force, the simplified equation for the force-displacement relationship is then given as:

$$f_0 = \left(\frac{j\omega c}{1 + j\omega \frac{c}{k}}\right) X \tag{6.39}$$

$$F_{tot} = f_0 \exp(j\omega t) \tag{6.40}$$

Equation 6.39 shows that the response is a function of: the stiffness coefficient, the damping coefficient, and the frequency, similar to the Kelvin-Voigt model. Figure 6.10 shows the force-displacement behaviour for: (a) various stiffness coefficients, (b) various damping coefficients, and (c) various frequencies.

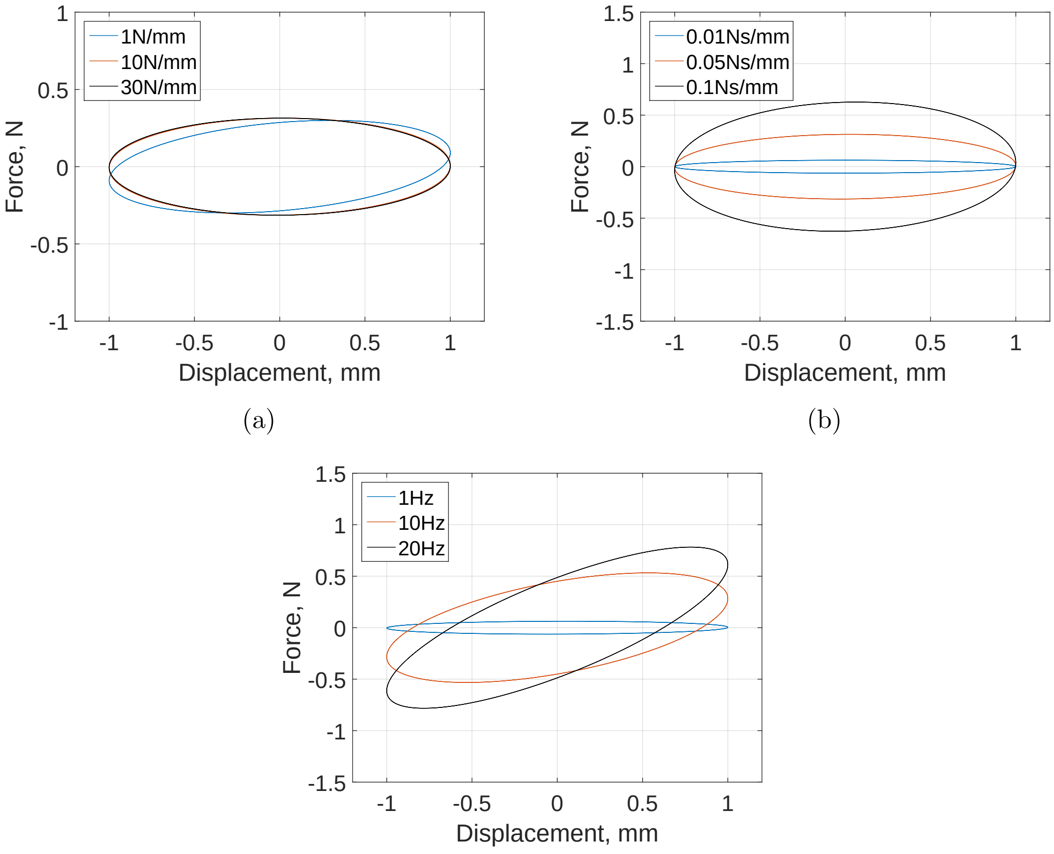

(a)

(b)

(c)

Figure 6.10: Maxwell force-displacement behaviour for (a) various linear spring stiffness coefficients, (b) various viscous dashpot damping coefficients, and (c) various frequencies

The stiffness coefficient in the Maxwell model has an effect of making the hysteresis curve more symmetrical about the zero axis. Increasing the damping coefficient or frequency increases the size of the hysteresis. Frequency has an additional effect of stiffening the response.

6.3.4 Zener

The Zener model, more commonly known as the standard linear solid (SLS) model, is the combination of the Kelvin-Voigt and Maxwell models. Figure 6.11 illustrates the model, which consists of a linear spring microelement in parallel with a linear spring microelement, which is in series with a viscous dashpot microelement.

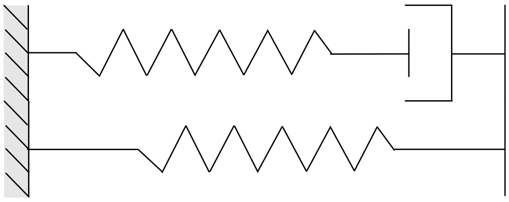

Figure 6.11: Zener model

The Kelvin-Voigt and Maxwell models are much simpler than the Zener model, and are more widely found in practice. However, the Kelvin-Voigt model does not exhibit material relaxation, which is the tendency of a material to have a reduction in stress when the strain in the material is kept constant. The Maxwell model, on the other hand, does not exhibit material creep, in a realistic manner for materials typically associated with damping. Creep is the tendency of a material to deform permanently when the applied stress is maintained. When these two characteristics need to be analysed together, then the Zener model is an important model choice.

The magnitude of the force produced by the Zener model is given by:

$$f_0 = \left(k_p + \frac{j\omega c_s}{1 + j\omega \frac{c_s}{k_s}} \right) X \tag{6.41}$$

$$F_{tot} = f_0 \exp(j\omega t) \tag{6.42}$$

where k_p is the stiffness coefficient of the parallel linear spring microelement, and c_s and k_s are the coefficients of the series viscous dashpot and linear spring microelements.

Figure 6.12 shows the force-displacement behaviour for: (a) various parallel linear spring stiffness coefficients, (b) various series linear spring stiffness coefficients, (c) various series viscous dashpot damping coefficients, and (d) various frequencies.

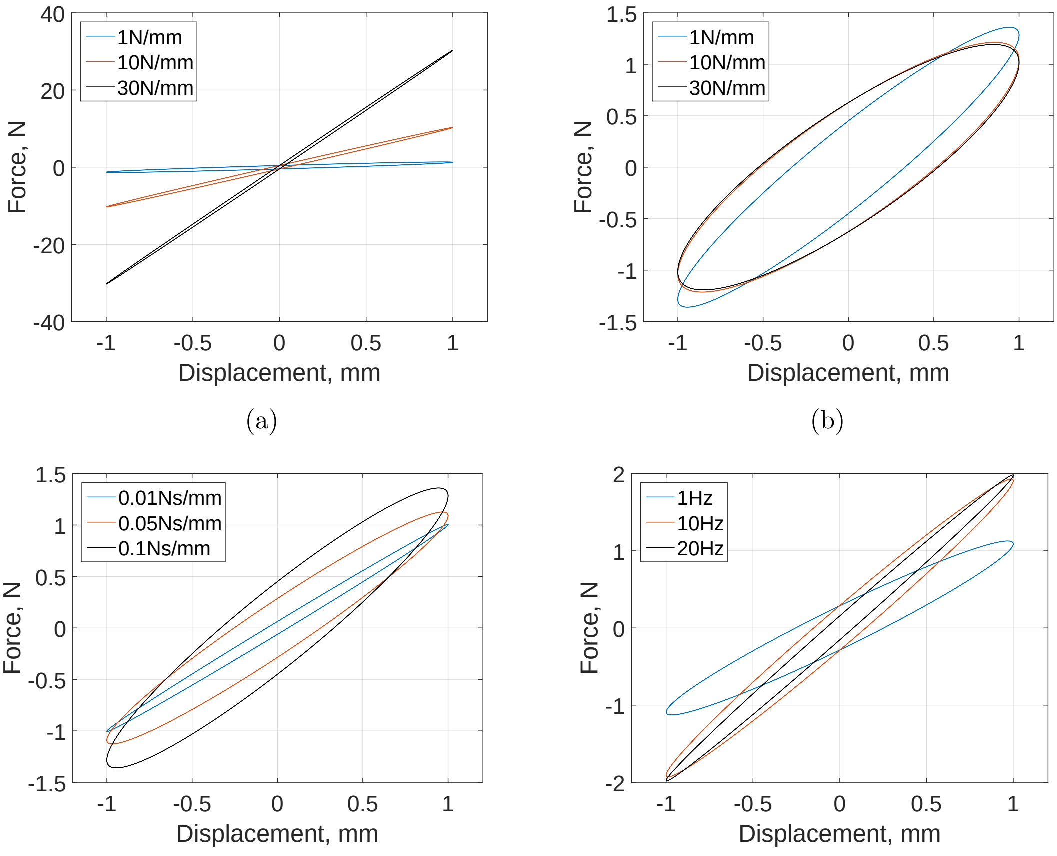

(a) (b) (c) (d)

Figure 6.12: Zener model force-displacement behaviour for (a) various parallel linear spring stiffness coefficients, (b) various series linear spring stiffness coefficients, (c) various series viscous dashpot damping coefficients, and (d) various frequencies

In the Zener model, increasing the parallel spring stiffness coefficient increases the slope of the hysteresis. Increasing the series spring stiffness coefficient initially reduces the slope of the hysteresis, before having very negligible effects on the response. The damping coefficient has a more elaborate effect on the slope, whilst also increasing the size of the hysteresis. Finally, the frequency increases the slope, whilst reducing the size of the hysteresis.

6.3.5 Coulomb friction

The Coulomb friction model has already been discussed in this chapter, and so it will not be discussed here. This model will be implemented with the slider microelement. In the following discussions, the damping type is swapped from viscous damping, to dry frictional Coulomb damping. In doing so, the following variants are obtained:

- Frictional Kelvin-Voigt
- Frictional Maxwell
- Frictional Zener

Since there is no velocity dependent viscous dashpot microelements in the frictional variants, the response is no longer a function of frequency. Instead, the response depends on the sign of the velocity.

6.3.6 Frictional Kelvin-Voigt

The frictional Kelvin-Voigt model is shown in Figure 6.13.

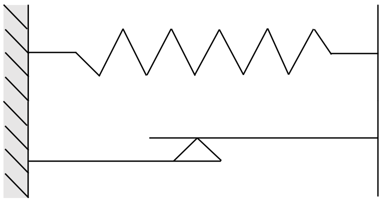

Figure 6.13: Frictional Kelvin-Voigt model

The force-displacement relationship can be defined as:

$$F_{tot} = kx + f_c \operatorname{sgn}(\dot{x}) \tag{6.43}$$

where f_c is the Coulomb friction force (μN). The graphical representation of Equation 6.43 is seen in Figure 6.14, where in (a) the linear spring stiffness coefficient is varied and the Coulomb friction force is maintained, and (b) the Coulomb friction force is varied and the linear spring coefficient is maintained.

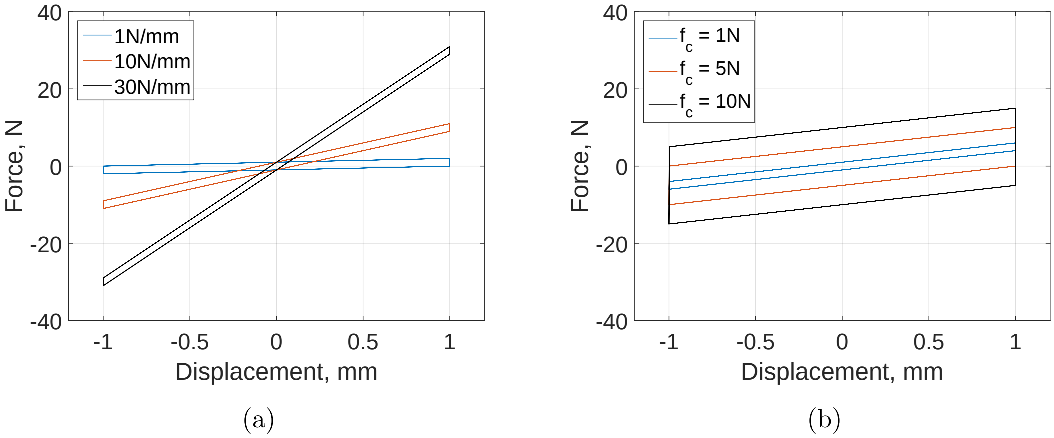

(a) (b)

Figure 6.14: Frictional Kelvin-Voigt force-displacement relationship for: (a) various linear spring stiffness coefficients, (b) various Coulomb friction forces

In the frictional Kelvin-Voigt model, the stiffness coefficient of the linear spring microelement controls the gradient of the hysteresis, whereas the Coulomb friction force dictates the size of the hysteresis. It is evident here that the Coulomb friction force has an effect only at the extreme ends of the curves, where the velocity is zero. The change in the direction of velocity causes a stick-slip region, where the force-displacement relationship is the most difficult to define.

6.3.7 Frictional Maxwell

The frictional Maxwell model is shown in Figure 6.15.

Figure 6.15: Frictional Maxwell model

The force-displacement relationship of the frictional Maxwell model can be stated as:

$$F_{tot} = \begin{cases} kx & \text{if } |kx| < f_c \\ f_c \operatorname{sgn}(\dot{x}) & \text{if } |kx| \geq f_c \end{cases} \tag{6.44}$$

Physically, this means that sliding only occurs if the stored force in the linear spring microelement exceeds the Coulomb friction force. Until then, the force is provided by the linear spring microelement. When sliding occurs, the linear spring microelement is inactive.

Figure 6.16 shows the force-displacement relationship for: (a) various linear spring stiffness coefficients and Coulomb friction force maintained, and (b) for various Coulomb friction forces, with the linear spring stiffness coefficient maintained.

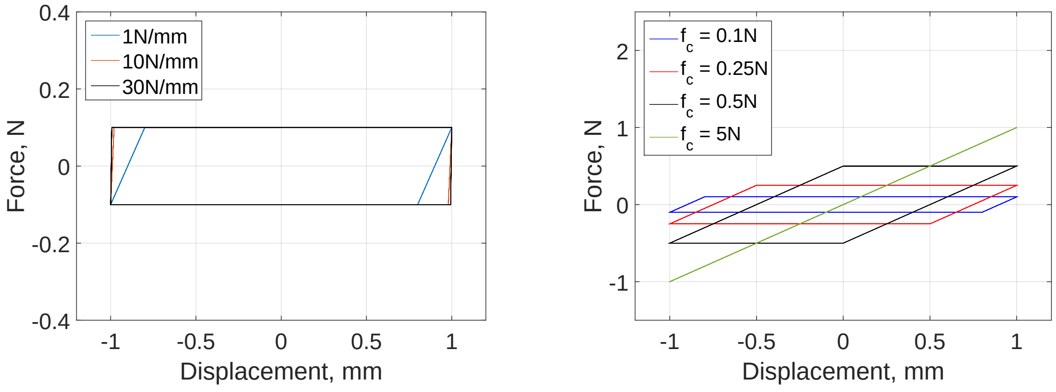

(a) (b)

Figure 6.16: Frictional Maxwell force-displacement relationship for: (a) various linear spring stiffness coefficients, (b) various Coulomb friction forces

In the frictional Maxwell model, increasing the stiffness coefficient of the linear spring causes the spring force to increase above the Coulomb friction force at a lower amplitude, causing an increase in the gradient of the hysteresis curve. Increasing the Coulomb friction force, on the other hand, allows the spring microelement to operate over a longer distance, increasing the hysteresis, maintaining the same force-displacement gradient. After a critical Coulomb friction force, however, the size of the hysteresis curve diminishes, with the model operating as a stand alone linear spring microelement.

6.3.8 Frictional Zener

Like the normal Zener model, the frictional Zener model is a combination of both the frictional variants of the Kelvin-Voigt and Maxwell models. The model is shown in Figure 6.17

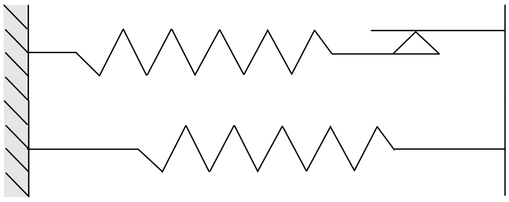

Figure 6.17: Frictional Zener model

The force-displacement relationship can be described as:

$$F_{tot} = \begin{cases} k_p x + k_s x & \text{if } |k_s x| < f_c \\ k_p x + f_c \,\mathrm{sgn}(\dot{x}) & \text{if } |k_s x| \geq f_c \end{cases} \tag{6.45}$$

Figure 6.17 shows a typical force-displacement response for a Zener model. Given that the characteristics seen in this figure correspond to the observed hysteresis behaviour of the TMW devices, the frictional Zener model was chosen as the base model for further analysis, which is explored in further detail in the next section.

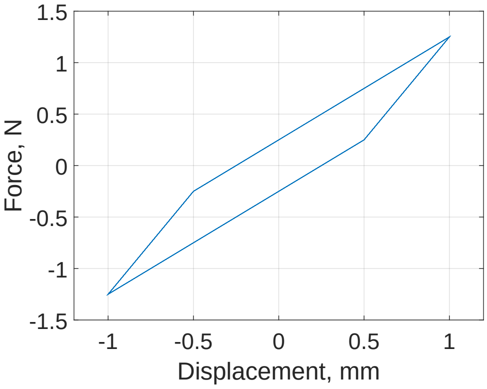

Figure 6.18: Frictional Zener force-displacement relationship

6.4 Proposed analytical modelling of TMW devices

In this section, the TMW devices are examined from an analytical point of view. The primary aim is to reflect the overall trends in terms of the shape of the experimental hysteresis curves through the use of a microelement model. Once the trends are successfully captured, more accurate parameters of the proposed microelement model are identified using the Metropolis-Hastings algorithm. Finally, the results of the proposed model, with the newly identified parameters, are compared to different experimental hysteresis curves. The choice of parameters are also compared with the image processing results from Chapter 3 to conclude the work carried out in this thesis in a holistic manner.

6.4.1 Basic model and effect of model parameters

The basic model (the frictional Zener model) and its governing equations were introduced in the preceding section. This model was chosen as the base model due to its stark likeness to the experimentally observed TMW device hysteresis characteristics when compared to the other models. The characteristics of the frictional Zener model will now be analysed in further detail.

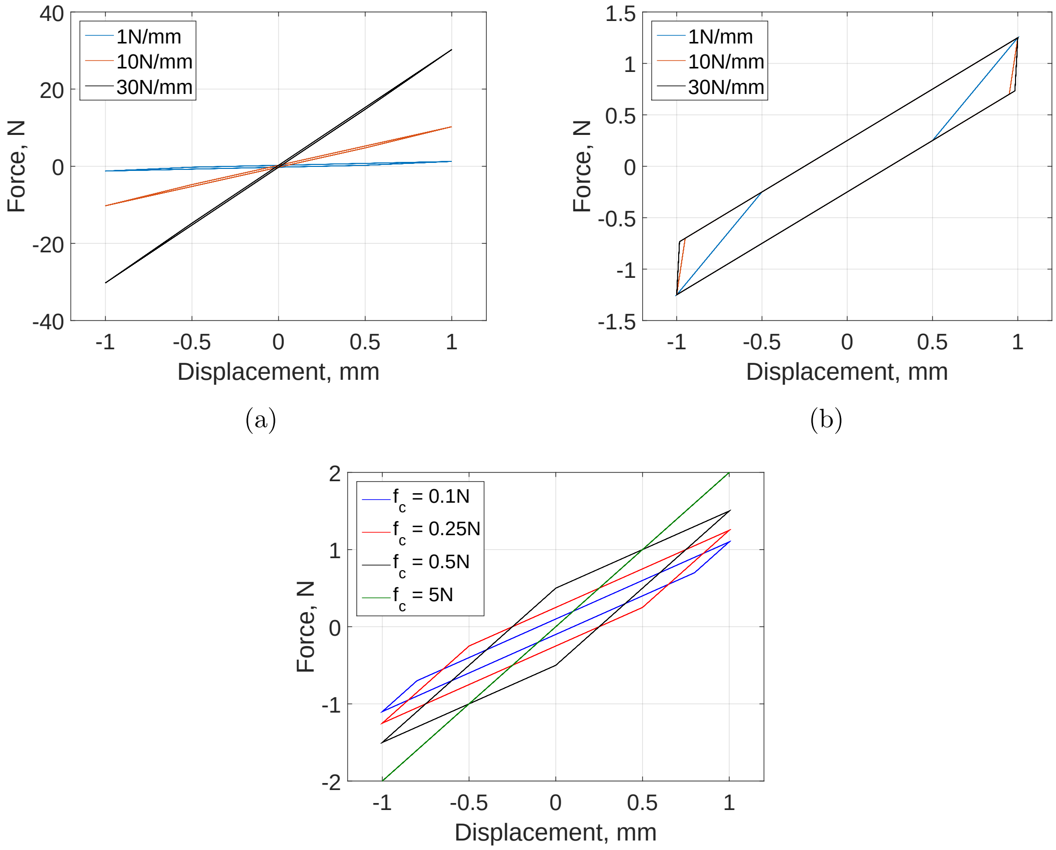

(a)

(b)

(c)

Figure 6.19: Frictional Zener model force-displacement behaviour for: (a) various parallel linear spring stiffness coefficients, (b) various series linear spring stiffness coefficients, and (c) various Coulomb friction forces acting on the frictional slider

From the results in Figure 6.19 (a), (b), and (c) , it can be seen that:

- As the parallel spring stiffness coefficient increases, the overall gradient of the hysteresis increases. This is true with all the analytical models that contain a parallel linear spring microelement discussed thus far.
- As the stiffness coefficient of the series linear spring microelement increases, the shape of the hysteresis curves becomes more akin to the frictional Kelvin-Voigt model. This is because the spring force exceeds the Coulomb friction force earlier, allowing sliding to take place. The frictional slider hence becomes the dominant microelement in the series section of the model.

- As the Coulomb friction force increases, the size of the hysteresis curve increases. If this force is increased further, the frictional slider plays no further part in the dynamics, and the frictional Zener effectively becomes two parallel linear springs.

Based upon the above analysis, the parallel spring microelement can be used to define the stiffness characteristics of the bulk TMW devices' material. That is, this term defines the “backbone” of the hysteresis curve, which experimentally, is seen as the centreline of the force-displacement curves.

The combination of the series spring and frictional slider microelements can be used to define the contact characteristics:

- Based on the experimental hysteresis observed, the initial force-displacement slope at low quasi-static or dynamic displacement levels is small in comparison to the slope at higher displacement levels. Therefore, the series spring microelement can be used to define the opposing “stick-slip” regions at the extreme ends of the hysteresis curves.
- The experimental results showed that the loss factor seemingly approached a plateau in a logarithmical fashion over the range of dynamic strains tested. It could be predicted that the loss factor would eventually drop at higher dynamic strains because the level of normal forces acting on the contacts in the microstructure would continue to rise to a level where sliding will be completely restricted. This is akin to the effect of the frictional slider microelement, which also showed a drop in the size of the hysteresis (and hence loss factor).

This effectively means that the parallel spring microelement can be used to control the global elastic characteristics of the TMW devices, whereas the series spring and frictional slider microelements can control the local effects of the contacts, which contribute to the hysteretic aspect of the global characteristics.

6.4.2 Development of basic model

Thus far, the discussion of the frictional Zener model has been based on a single chain of the series microelements. The fact that the TMW devices have numerous contacts within the microstructure means that more of these chains are required to capture the hysteresis trends observed experimentally in a realistic manner. Intuitively, the following question emerges: how many of these chains would be required to represent the state of the contacts within the microstructure successfully?

To achieve complete accuracy, it would be fair to assume that each contact should have an associated chain comprising its own linear spring and frictional slider microelements. This would however lead to unnecessary computational costs, with little or no additional benefit in terms of accuracy. Additionally, when the microstructure is loaded, the state of contacts changes immediately, with several new contacts being formed. Consequently, more microelements would need to be added to the model to capture the new microstructural state. Hence, it is important to have a relatively simple model without compromising its accuracy in representing the properties of the entire microstructure.

The development of the basic frictional Zener model led to the multi-chain frictional Zener model. The effect of the number of series chains were studied first. The multi-chain frictional Zener model was then tested with randomly chosen model parameters to gauge its response in comparison with TMW devices, assuming that the contacts had random properties. Judging from the observed results, the Coulomb friction term was modified, and the proposed form was justified.

Figure 6.20 illustrates the multi-chain frictional Zener model, where there are n chains of the linear spring and frictional slider microelements.

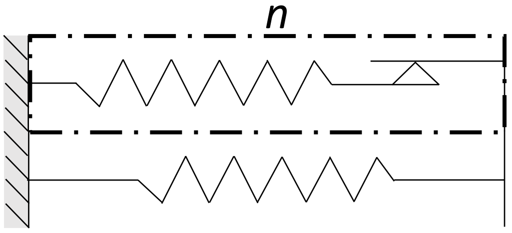

Figure 6.20: Multi-chain frictional Zener model with n microelement chains

Randomly chosen model parameters

The analysis carried out here was based on randomly chosen parameters (for the series microelements) obtained from a uniform distribution over the range 0 to 100

N/mm for the spring microelements, and 0 to 10 N for the forces on the frictional sliders. This was done for two interlinked reasons:

- The model parameters were unknown. As there was still some uncertainty from the image processing results, the simplest choice was to choose random parameters.
- There are numerous contacts within the microstructure, and different regions have different stiffness and friction characteristics, depending on neighbouring contacts, as well as relative angles of orientation.

In order to keep the analysis consistent, once the parameters were randomly generated, they were saved and used for all the analysis carried out.

Effect of number of microelement chains - the multi-chain frictional Zener model

The effect of number of elements is shown in 6.21. Note that the forces have been normalised for comparison purposes.

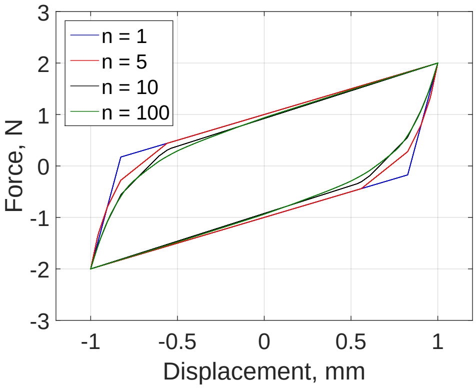

Figure 6.21: Effect of increasing the number of microelement chains

When more microelement chains were introduced to the multi-chain frictional Zener model, the edges of the hysteresis curves smoothed in the stick-slip regions. This occurred because the overall force was a superposition of all the individual microelement chains. Since all the parameters for the respective chains were randomly chosen from a uniform distribution, different chains contributed a different amount of force, some small, some large. As there was only one single microelement dominating the overall stiffness of the hysteresis, the slope remained unchanged.

The experimental hysteresis curves observed for the TMW devices were smooth as seen in the preceding chapters. Accordingly, having more microelement chains would have improved the ability of the model to replicate the experimentally observed phenomena. While accuracy is important, the overall computation cost and ease of adaptability is also highly regarded. Besides, having many parameters leads to reduced control over their magnitudes, and also reduced understanding of the resulting analysis. Additionally, it can be seen in Figure 6.21, the improvement in the "roundedness" of the curves reduces, so there is nothing valuable to be achieved in having, say 100 chains when 10, or even 5 would suffice.

Modification of Coulomb friction form

Judging from the shape of the hysteresis curves seen in Figure 6.21, it is apparent that there is symmetry present about the elastic zone. The TMW devices' experimentally observed hysteresis curves, on the other hand, portrayed a distinct asymmetry. The symmetry in the model was observed because the Coulomb friction coefficients chosen for all the frictional slider microelements were constants. In reality, as mentioned in previous chapters, as the devices are loaded, there is a combination of many new contacts being formed, and an increase in the loads that each set of contacts carry. These loads are essentially normal forces acting on the frictional sliders, and hence modify the Coulomb friction forces. While unloading occurs, the number of contacts reduces, and hence so do the Coulomb friction forces. In a nutshell, this made having a constant Coulomb friction force inappropriate for modelling.

In an effort to increase asymmetry on the hysteresis curves, the constant Coulomb friction force term was changed to a sinusoidal form. In this way, as the compression displacement increased, the Coulomb friction forces acting on the sliders increased, and during unloading, the opposite was true. This is mathematically defined as:

$$f_c = f \sin(2\pi\omega t) + C \tag{6.46}$$

where f is the magnitude of the sinusoidal Coulomb friction force, and C is a constant that ensures that the Coulomb friction force does not possess a negative value, and is never zero.

The effect of the sinusoidal Coulomb friction force on the hysteresis curves can be seen in Figure 6.22.

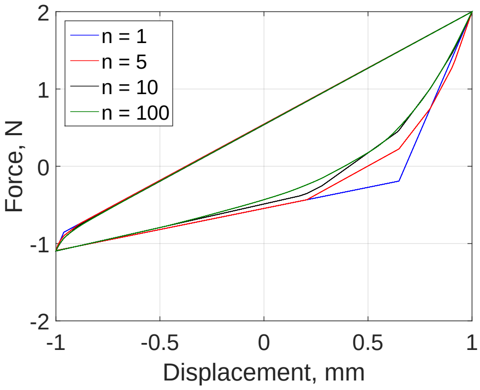

Figure 6.22: Effect of including sinusoidal Coulomb friction term

As it is seen on Figure 6.22, the inclusion of a sinusoidal Coulomb friction force in the multi-chain frictional Zener model introduced asymmetry similar to the experimentally observed hysteresis curves. However, there was one further improvement possible. The slope of the hysteresis curve at the extreme end, where unloading occurs, still does not reflect the slope seen experimentally, especially when the number of microelement chains were increased. This can be seen as a trade-off between using more microelement chains and model accuracy. In order to reduce the trade-off and improve the model further, an exponent was included to the multi-chain frictional Zener model, akin to the Dahl dynamic friction model discussed in this chapter. This exponent helped control the slope of the hysteresis curves, especially at the extreme ends. The Coulomb friction force can now be defined as:

$$f_c = f[\sin(2\pi\omega t)]^e + C \tag{6.47}$$

where e is an exponent constant. From a physical point of view, it can be used to define the change in the number of contacts, and the accompanying changes to the forces acting on them.

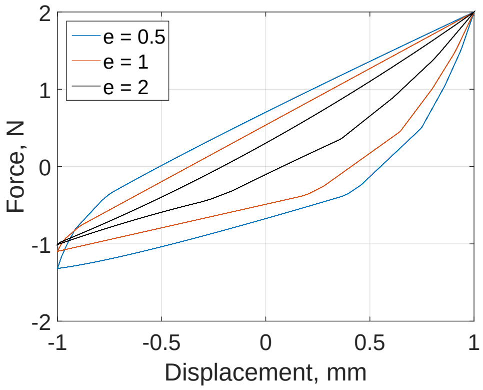

Figure 6.23: Effect of including sinusoidal Coulomb friction term with an exponent

Figure 6.23 shows the behaviour of the hysteresis curves with three different exponent values in a multi-chain frictional Zener model which consists of 10 microelement chains. It can be said that having an exponent lower than 1 made the slope characteristics closer to those seen experimentally. However, it must be noted that the figure is used just for illustrative purposes. In each case, the exponent term was considered as a constant term across all microelement chains. In reality, however, if incorporated into the model, each chain would consist of its own exponent, similar to how each chain consists of a different coefficient for the linear spring and frictional slider. Therefore, the exponent need not necessarily be a value less than 1.

Justification of exponential, sinusoidal Coulomb slider form

With the aim of justifying the selection of a sinusoidal form for the Coulomb friction force, which includes an exponent factor, the results from the image processing performed in this thesis are revisited. In the analysis presented here, the total free and total contact lengths of the wires are considered.

Earlier, in Chapter 3, histograms were shown for the different applied static displacements for the different specimens. These histograms showed the distributions of the free and contact wire lengths within the microstructure. Interestingly, there were results shown for lengths less than 150 μm, which is the diameter of the wires. In reality, it is physically unlikely for a wire to either be free or in contact for a length less than the diameter of the wire. It can occur when a wire is in contact with two other wires either side of it, but cannot occur when a wire is in contact with two other wires on the same side. The reason why lengths less than the wire diameter appeared in the histograms can be explained by two reasons:

- There were several breaks in the *centroidTracker* algorithm that stopped the wire detection from continuing. While the same wire could have been detected later on in sequential images, there was no merging taking place between these two sets of identified wires. This had a direct impact on the calculated free and contact lengths.
- Since the images contained discretised pixels, the identified wire centroid locations were seen to oscillate slightly about the true centroid locations. Smoothing of these identified wire segments was not performed following the initial wire centroid identification. Due to this, when whether a wire segment was free or in contact was determined, uncertainty was introduced. For example, a wire that may have been free over a long distance could have potentially been broken down into two or more smaller free wires, due to the misidentification of a contact over its length.

While these are areas that could be improved upon in the future, the analysis presented henceforth ignores any wire lengths that are less than the wire diameter. Furthermore, since the number of total free and total contact wire lengths varied between different specimens and loading conditions, the total free and total contact lengths were normalised by the respective total lengths, which are the total sums of the total free and total contact lengths. Figure 6.24 shows the results of the free and contact length ratios.

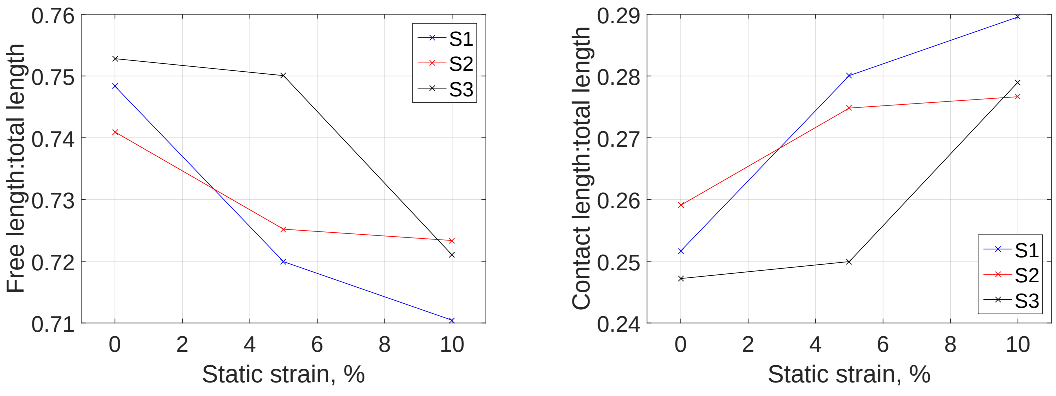

(a)

(b)

Figure 6.24: (a) Free length:total length ratio vs. applied static strain, and (b) Contact length:total length ratio vs. applied static strain

As expected, it can be seen that as the static strain increases, the amount of free wires within the microstructure reduces, whereas the amount of wires in contact increases. This helps justify the use of a sinusoidal Coulomb friction force, since the change in free/contact wires would continuously change as the specimen is loaded sinusoidally. This changes the normal forces acting in the microstructure, causing the frictional force within the contacts to change. The manner in which free and contact ratios change between the loading states is nonlinear. This can defined mathematically by an exponent since the change between the free and contact states as a specimen is statically loaded is shown to vary in a logarithmic/exponential manner, as seen in Figure 6.24.

From these results, it is also seen that the different specimens have different total free and total contact length ratios. As a result, if these specimens are modelled, they would consist of different coefficients, even though the model structure would be similar.

6.4.3 Parameter identification with Metropolis Hastings

The proposed models in the previous section were shown to portray force-displacement hysteresis behaviour similar to those exhibited by the TMW devices. In order to show the proof of concept, and hence choose and validate a proposed model, it was decided to identify parameters for the models. There are several algorithms available to identify parameters, such as the Rejection Sampling Method, the Differential Evolution algorithm, and the Nelder Mead algorithm [106]. For the purposes of this thesis however, the chosen strategy to identify parameters was the Metropolis Hastings (MH) algorithm. Since the algorithm in itself was not the primary focus of the modelling, only a brief introduction is given, and detailed equations are skipped. Further literature may be found in [107]. The MH algorithm used here was developed by Tiboaca, D. et al. at the University of Sheffield [108], [109].

Brief Introduction

The Metropolis-Hastings (MH) algorithm is a method that uses Markov Chain Monte Carlo (MCMC) sampling, which can estimate the probability density of a system using samples obtained statistically. MCMC sampling is especially useful for a system that consists of a large number of parameters (or dimensions) that cannot easily be solved simply because of the large range of values that the parameters can take up. Therefore, the method identifies an estimated value for each parameter that would result in a distribution that is similar to a target (typically Gaussian) distribution of parameter values.

In the MH algorithm, parameter values are first initiated using a value within a predefined range, which cannot be exceeded. The algorithm then randomly picks another value within this range, and evaluates the Metropolis acceptance ratio, a, given by:

$$a = \frac{P^*(x')}{P^*(x^{(t)})} \tag{6.48}$$

where P^* is a cost function, x' is the randomly picked proposed value, and $x^{(t)}$ is the current value at iteration t. Then the Metropolis acceptance rule is evaluated, which is given by:

$$x^{(t+1)} = \begin{cases} x' & \text{if } a \geq 1 \\ x^{(t)} & \text{otherwise} \end{cases} \tag{6.49}$$

The cost function, P^* used in the work carried out here is given by,

$$P^* = \sum \left(F_e - F_m\right)^2 \tag{6.50}$$

where F_e is the experimental force signal, and F_m is the force signal generated by the model. The MH algorithm explores all the parameter spaces for the respective parameters in parallel, and each time, evaluates the Metropolis acceptance rule [107]. Once this is done over several iterations, Markov Chains are created and a density function is built up for each parameter. The histograms of the individual parameters can be used to estimate the respective probability density functions. If one chooses the expected (or mean) values of each distribution, there is a high likelihood that the result will describe the properties of the entire system.

Comparison with experimental results

This chapter introduced three models that were variants of the basic frictional Zener model. These included the:

- Model 1: multi-chain frictional Zener model with n microelement chains.
- Model 2: multi-chain frictional Zener model with n microelement chains, and a sinusoidal Coulomb friction force.
- Model 3: multi-chain frictional Zener model with n microelement chains, and a sinusoidal Coulomb friction force with an exponent term.

The results from each of these models were evaluated in relation to experimental observations of TMW device behaviour. The input to the MH algorithm was the displacement time history of the experiment. The force time history was utilised in the cost function (Equation 6.50), which was used to evaluate whether a randomly chosen parameter passed the Metropolis acceptance rule. The specimen for which parameters were identified using the MH algorithm was $\tilde{\rho} = 0.18$, Specimen 2. The experimental data selected was for a static strain of 5%, dynamic strain of 1%, and frequency of 1 Hz.

To reduce the number of parameters in the MH algorithm, the friction forms from Equations 6.46 and 6.47 were modified to vary simply with the sinusoidal input displacement for Models 2 and 3. That is, Equation 6.46 became:

$$f_c^{(i)} = f^{(i)}x \tag{6.51}$$

where i denotes the microelement chain number, and x is the experimental sinusoidal displacement. Equation 6.47 became:

$$f_c^{(i)} = f^{(i)}x^{e(i)} \tag{6.52}$$

For the simulations, a multi-chain frictional Zener model with 5 microelement chains was initially used because these gave a compromise between having a small number of parameters, whilst still being able to provide the relatively smooth hysteresis curves seen experimentally. The identified parameters for each of the models discussed is shown in Table 6.1.

Parameter	**Model 1**	**Model 2**		**Model 3**
	5 chains	**5 chains**	**10 chains**	**10 chains**
k_p, **N/mm**	85	81	82	80
$k_s^{(1)}$, **N/mm**	136	140	137	137
$k_s^{(2)}$, **N/mm**	140	151	150	150
$k_s^{(3)}$, **N/mm**	137	138	140	136
$k_s^{(4)}$, **N/mm**	155	148	149	149
$k_s^{(5)}$, **N/mm**	148	130	129	130
$k_s^{(6)}$, **N/mm**	-	-	135	136
$k_s^{(7)}$, **N/mm**	-	-	150	150
$k_s^{(8)}$, **N/mm**	-	-	136	137
$k_s^{(9)}$, **N/mm**	-	-	149	150
$k_s^{(10)}$, **N/mm**	-	-	130	129
$f_c^{(1)}$, **N**	1.0	6.2	2.7	10.1
$f_c^{(2)}$, **N**	0.4	3.6	2.1	10.1
$f_c^{(3)}$, **N**	3.5	5.9	0.7	10.3
$f_c^{(4)}$, **N**	0.8	3.3	2.7	9.6
$f_c^{(5)}$, **N**	1.8	5.6	3.0	8.5
$f_c^{(6)}$, **N**	-	-	4.4	10.0
$f_c^{(7)}$, **N**	-	-	1.9	8.6
$f_c^{(8)}$, **N**	-	-	3.7	8.9
$f_c^{(9)}$, **N**	-	-	1.5	9.7
$f_c^{(10)}$, **N**	-	-	2.7	9.4
$e^{(1)}$	-	-	-	4.1
$e^{(2)}$	-	-	-	4.4
$e^{(3)}$	-	-	-	4.2
$e^{(4)}$	-	-	-	3.6
$e^{(5)}$	-	-	-	0.5
$e^{(6)}$	-	-	-	3.7
$e^{(7)}$	-	-	-	2.6
$e^{(8)}$	-	-	-	3.9
$e^{(9)}$	-	-	-	3.2
$e^{(10)}$	-	-	-	1.4

Table 6.1: Parameters identified by the Metropolis-Hastings algorithm for the discussed multi-chain frictional Zener models

Model 1 (Multi-chain frictional Zener model with 5 microelement chains): Figure 6.25 shows a comparison between the experimental hysteresis curves and the hysteresis curve produced by the model employing parameters identified by the MH algorithm.

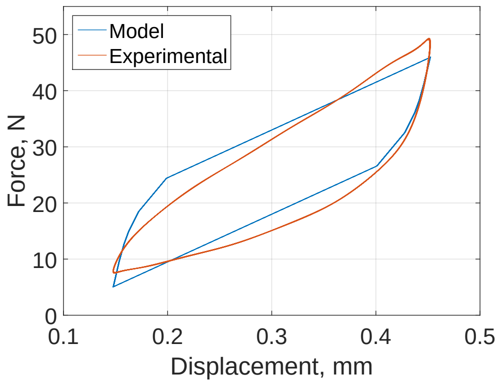

Figure 6.25: Hysteresis curve comparison between experimental observations and those produced by a multi-chain frictional Zener model with 5 microelement chains

As expected, the hysteresis curve produced by the model was symmetric about the neutral axis. The shape of the hysteresis was also quite different from the experimental hysteresis curves, largely attributed to the wrong model being chosen. The MH algorithm identified parameters that produced the closest fit to the model. **Model 2 (Multi-chain frictional Zener model with 5 and 10 microelement chains)**: Figure 6.26 shows the comparison between the experiment and the model.

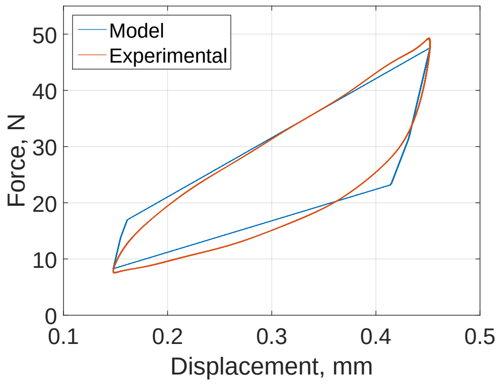

Figure 6.26: Hysteresis curve comparison between experimental observations and those produced by a multi-chain frictional Zener model with 5 microelements, and a sinusoidally varying Coulomb friction force

Figure 6.26 shows this model improved the asymmetric characteristics in the hysteresis curves. However, the stick-slip regions had a sharp transition, whereas it was much smoother in the experimentally observed hysteresis curves. Therefore, a multi-chain frictional Zener model with 10 microelements was also studied to see if this could be improved. This is shown in Figure 6.27.

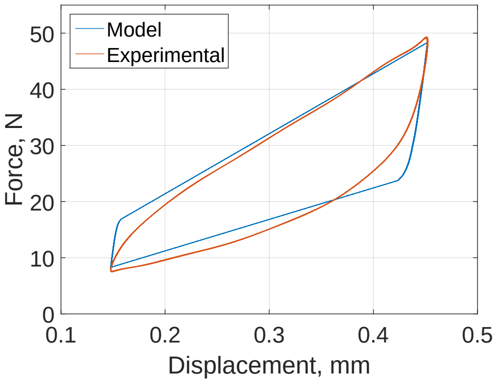

Figure 6.27: Hysteresis curve comparison between experimental observations and those produced by a multi-chain frictional Zener model with 10 microelements, and a sinusoidally varying Coulomb friction force

The stick-slip regions with this model configuration had a smoother transition, but the slope of this region was increased slightly. This was most likely due to an artefact of the MH parameter identification. Hence, it was concluded that having a larger number of microelement chains in the multi-chain frictional Zener model was better. However, as discussed earlier, having too many microelements meant longer computation times of the MH algorithm, less intuition in the understanding of the models, and limited further accuracy improvements. Therefore, the number of microelements in the multi-chain frictional Zener model was set at, and limited to, 10 in the next model.

Model 3 (Multi-chain frictional Zener model with 10 microelement chains): The effect of the inclusion of the exponent term is shown in Figure 6.28

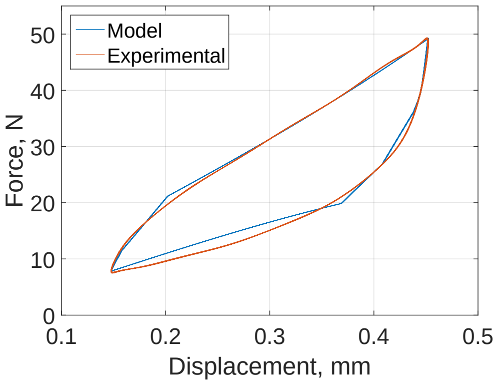

Figure 6.28: Hysteresis curve comparison between experimental observations and those produced by a multi-chain frictional Zener model with 10 microelements, a sinusoidally varying Coulomb friction force, and an exponent term

According to Figure 6.28, it is clear that this model was much better at predicting the hysteresis curves displayed by the TMW devices, when compared to the other variants of the multi-chain frictional Zener models analysed.

The comparison of the average dynamic stiffness and loss factors of the experiment and model is shown in Table 6.2. The parameter identification was performed for an experimental test (obtained from the work carried out in Chapter 4) performed at 1 Hz for a selected static pre-compression (5% static strain), and dynamic amplitude (1% dynamic strain). The table also shows comparisons for the tests performed at 3 Hz, 10 Hz, and 20 Hz, for the same specimen, pre-compression and dynamic amplitude.

	Average stiffness, (N/mm)	**Loss factor, (η)**
Experiment, 1Hz	83.1	0.551
Model, 1Hz	69.9	0.555
Error, 1Hz	15.8%	-0.726%
Experiment, 3Hz	85.3	0.540
Model, 3Hz	69.6	0.544
Error, 3Hz	18.4%	-0.741%
Experiment, 10Hz	89.1	0.537
Model, 10Hz	70.2	0.565
Error, 10Hz	21.1%	-5.21%
Experiment, 20Hz	100.5	0.498
Model, 20Hz	75.9	0.591
Error, 1Hz	24.5%	-18.7%

Table 6.2: Comparison between experimental and modelled average stiffness and loss factor at different frequencies

There was a noticeable difference between the average stiffness coefficients calculated for the experiments and the model. This mainly occurred due to the uncertainty of the force-displacement behaviour when the direction of loading/unloading changed, both in the experiments and in the models.

On the other hand, the correlation between loss factors was much better, especially at 1 Hz and 3 Hz. The dynamic amplitudes were almost the same at both these frequencies. The experimental dynamic amplitudes at 10 Hz and 20 Hz reduced because of the limitations of the test system, as discussed in Chapter 4. As established in Chapters 4 and 5, the TMW devices exhibit only amplitude dependency, and no frequency dependency. Therefore, in order to improve accuracy of the model, parameters will need to be re-identified for the higher frequency results since the dynamic strains reduced in amplitude.

Thus, it can be concluded that the multi-chain frictional Zener model with 10 microelement chains, and sinusoidally varying Coulomb friction forces, with an exponent term, is a valid model, and therefore appropriate for analytical modelling of TMW device behaviour.

6.5 Conclusion

This chapter discussed the modelling aspects of the analytical work carried out in this thesis. Initially, various experimentally observed frictional phenomena were discussed. This was followed by a discussion of various friction models proposed in literature. It was noted that there was no universal frictional model, but instead, different models were created to tackle different friction problems.

Microelement modelling was then introduced as a means to analytically model the hysteretic behaviour of tangled metal wire (TMW) devices. Following an introduction to various microelement components, several pre-existing analytical models were exhibited, and their behaviour explained. The models discussed were the Kelvin-Voigt model, the Maxwell model, the Zener model, and their respective frictional variants. Since the TMW devices displayed only amplitude dependency as discussed in Chapters 4 and 5, the primary friction model chosen was the classic Coulomb friction model.

The frictional Zener model was chosen as the base model for further development since the shape of the hysteresis curves resembled those observed experimentally for TMW devices. The model consisted of one parallel spring that was used to model the overall stiffness characteristics of the bulk TMW device structure. The model was explored by introducing a number of microelement chains that consisted of a linear helical spring in series with a frictional slider having a constant Coulomb friction force, hence yielding the “multi-chain frictional Zener model”. These chains were used to model the elastic and inelastic (i.e. frictional) characteristics of the contacts in the TMW microstructure. The model was further developed by introducing a sinusoidally varying Coulomb frictional force, and then introducing an exponent as well, and the respective effects of these additions were discussed. The choice of both the sinusoidal frictional forces, and the exponent terms were justified by the changes in the physical contact conditions within the TMW device microstructure.

The Metropolis-Hastings (MH) algorithm was then used to identify parameters for the three discussed models and hence reject/accept and validate them. Once the parameters were identified, the results were compared to the experimentally observed hysteresis curves. The results reported in this chapter were for a single pre-compression and dynamic amplitude. If the pre-compression were to increase, or the dynamic amplitude were to reduce, the stiffness coefficient parameters identified by the MH algorithm would tend to increase.

It was found that the multi-chain frictional Zener model that included 10 microelement chains, and a sinusoidally varying Coulomb friction force with an exponent term successfully modelled the TMW hysteresis to a highly accurate level. The parameters identified for the proposed model can be used to model behaviour for various frequencies, as long as the applied static and dynamic strains are similar. This is because the proposed model possesses frequency independency like the physical TMW devices.

The proposed model is akin to the Dahl model, in that the exponent provides better control over the shape of the hysteresis curves.

Chapter 7

CONCLUSIONS AND FURTHER WORK

During the course of this thesis, several aspects of tangled metal wire (TMW) device behaviour were explored. These ranged from the physical state of the microstructure, the quasi-static, low and high frequency response, and finally the analytical modelling aspects. In each chapter, the final section provided a list of important conclusions that respectively stemmed from the work carried out. The purpose of this chapter is to summarise the key findings from each chapter, and provide a direction for how future research on TMW devices and other entangled, fibrous materials, should be headed.

7.1 Overall conclusions

In Chapter 2, the state of the art, prior to the work carried out in this thesis, was reported and discussed. It was shown that majority of the focus was placed on experimental work. It was made clear that there were very few analytical models reported. This was primarily due to the lack of in-depth understanding of the TMW microstructure. The successful models have tended towards being "black-box" models, whereby parameters and functions were fitted to experimental data.

Chapter 3 set about to fill in the gaps with respect to the understanding of the TMW device microstructure. Micro-computed tomography scans were conducted on the TMW devices subjected to different levels of compression for a number of pre-conditioned specimens. A novel image processing algorithm was developed to identify the skeletal structure of the TMW devices. The algorithm was able to identify a large proportion of wires that were in contact, which would have otherwise not been detected using standard image processing tools. It was importantly shown that the microstructures of the TMW devices do not change for the same applied compressions, in between load cycles, largely attributed to the pre-conditioning exercises that were carried out. This was particularly useful because it predicted repeatable behaviour seen for the quasi-static, low, and high frequencies experiments that followed. The results also allowed preliminary analysis of the microstructure evolution between successive load cycles. The results showed that the free wire lengths changed the most between successive loads, indicating that these lengths and the number of contacts within the microstructure were the most important microstructural parameters dictating the hysteretic behaviour of TMW devices.

Chapters 4 and 5 presented the experimental work carried out on TMW devices. In Chapter 4, the quasi-static and low frequency experimental results were analysed, and explained based on the state of the microstructure. Interestingly, it was shown that the TMW devices were frequency independent (hence disproving one of the hypotheses proposed before the work was carried out), and only amplitude dependent (confirming the other two hypotheses proposed). In Chapter 5, a new test rig was designed and manufactured for the sole purpose of observing TMW device behaviour at higher frequencies. The results were in agreement with the low frequency dynamic response presented in Chapter 4, in that the results were shown only to be amplitude dependent, and frequency independent.

Finally, Chapter 6 presented the analytical modelling aspects of TMW devices. The unanimous conclusion in Chapters 4 and 5 was that energy dissipation in TMW devices arises from interface friction at the contact points. Among the models studied was the frictional Zener model, which portrayed similar force-displacement hysteretic behaviour as the physical TMW devices. The model was chosen for further development, and some multi-chain frictional Zener models were identified. The Metropolis-Hastings algorithm was used to identify parameters for these models after they showed satisfactory trends in the shapes of the hysteresis curves. The final model studied was the multi-chain frictional Zener model, which consisted of 10 microelement chains, a sinusoidally varying Coulomb friction force, and an exponent factor. It was seen that the model replicated the experimental behaviour to within a 1% margin when comparing results of equivalent static and dynamic amplitudes.

Hence, the model was considered valid.

7.2 Contributions to the state of the art

The main aims and objectives of the thesis, outlined in Chapter 1, were successfully met. The following summarises the key contributions to the state of the art:

- For the first time, quasi-static, low, and high frequency behaviour of TMW devices were studied together for the same specimens. The results were explained using the effects of loading on the microstructure.
    - The explanation for the experimental observations from each of the sets of results were consistent with each other, and also consistent with the microstructural changes occurring within the TMW devices.
- Previous researchers stated the need to incorporate viscous damping models due to perceived frequency dependency in TMW behaviour. In this work, it was shown that the TMW devices showed only amplitude dependency, whereas there were no indications of any frequency dependency. This conclusively proved that friction was the dominant energy dissipation mechanism.
    - The amplitude dependency and frequency independency indicated that the simple classic Coulomb friction model may be adopted for analytical modelling purposes.
    - Analytical modelling of TMW devices was successfully carried out using a derivative of the frictional Zener model, the multi-chain frictional Zener model. The proposed model was shown to successfully model the hysteretic trends observed experimentally.
    - Parameters were identified for the proposed analytical models using the Metropolis-Hastings algorithm. The results from the model and experiments showed an agreement within 1% when the static and dynamic amplitudes were of similar orders of magnitude.
- A novel image processing algorithm has been proposed to study and understand the complex evolution of the microstructural state of TMW devices due to loading. Preliminary results from the algorithm were used to explain the microstructure.

  - Attempts were made to link the characteristics of the proposed model to the results from the image processing. Since the analysis techniques of the image processing results are still quite basic, further work can be done to improve analysis.

7.3 Further work

The novel *centroidTracker* algorithm proposed in this work can be considered to be in its alpha stage. Whilst it was shown that the algorithm was able to identify over 70% of the wires in the microstructure, there are several areas where the algorithm can be further improved upon. Some of these can be summarised as follows:

- Currently, there is no protocol in place to merge identified wire centroid locations that have a gap in between them. The algorithm stops detecting a wire when it cannot separate a group of wire segments that are in contact. If the same wire is re-identified a few images later, when it is free from other contacts again, it is counted as a new wire altogether. Having a post-processing merging algorithm can allow improvements in the histogram distributions, where currently, there are several short wires being detected.
- When an identified wire is examined carefully, it can be observed that successive centroid positions do not lie along smooth, continuous curves, since the algorithm is working with discretised images. Therefore, smoothing should be performed on the tracked wires in three-dimensional space to further improve the analysis carried out. The physical size of the wire limits the degree of curvature, and therefore the smoothing algorithm should take this into account.
- The algorithm currently focuses on only out-of-plane wires, and the algorithm stops working when a wire turns in-plane. Therefore, in addition to the previous two improvements, wire centroid locations obtained by analysing image slices in the coronal plane (X-Z) and the sagittal plane (Z-Y) should be combined in order to minimise the number of unidentified image objects. Therefore, these suggestions can complete the representation of the full TMW device microstructure.

As a result of some of the inconsistencies in the *centroidTracker* stated above, the current analysis techniques are somewhat limited as there are still some sources of uncertainty. If the above mentioned areas of improvements are completed, further improvements in the analysis techniques should be made to obtain:

- More representative histograms of microstructural states.
- Accurate calculations of stiffness coefficients between contact points.
- Estimation of forces acting on the contacts.
- Wire orientation, as these influence the amount of normal forces acting on contacts.

If the complete representation of the microstructure is achieved, new methods such as digital volume correlation (DVC) could also be used to analyse strain and deformation measurements following the application of loads. Once fully developed, the *centroidTracker* algorithm can also be used to understand the microstructure of other materials that consist of fibrous, or entangled structures. These can range from identifying the microstructure of carbon fibre composite materials, fibre optic networks, or more innovative dampers, such as the coconut husk (coir) dampers.

For the experimental aspects of this thesis, it would be beneficial to reduce the height of the base of the high frequency test rig, and hence move the specimens closer to the armature of the shaker. Since the magnitude of the moving mass can be reduced, testing can take place for an extended range of frequencies.

Some TMW devices have different core volumes than others. Typically, the microstructure in the core of a given device is different to the microstructure present in the outer edges. It should be noted that specimens studied in research elsewhere often have higher core volumes. In the case of the TMW devices studied in this thesis, discontinuities present at the hollow section at the centres of the TMW devices affect the microstructure at the core. Since the surface area-to-bulk volume ratio is an important parameter, further research should be conducted with the aim of understanding this parameter in more detail.

It would be important to test TMW device performance on real structures, e.g. where nominal strain in the specimen is inconsistent such as in rocking modes, in order to get further insight on their capabilities, and also learn their limitations. The analytical model proposed in this thesis can also be incorporated with these experiments to see if the model can predict the dynamic response of the TMW devices with the real structures.

Finally, the identified parameters by the Metropolis-Hastings algorithm should be investigated further in relation to the image processing results. This should be feasible if the above mentioned improvements to the *centroidTracker* algorithm are made.

BIBLIOGRAPHY

[1] S.S. Rao. *Mechanical Vibrations.* Addison-Wesley Longman, Incorporated, 1986.

[2] B. Bona and M. Indri. Friction compensation in robotics: an overview. In *Proceedings of the 44th IEEE Conference on Decision and Control*, pages 4360–4367, Dec 2005.

[3] K.Y. Sanliturk, D.J. Ewins, R. Elliott, and J.S. Green. Friction damper optimization: Simulation of rainbow tests. *Journal of Engineering for Gas Turbines and Power*, 123(4):930–939, 2001.

[4] D.J. Mead. *Passive vibration control.* Wiley, 1999.

[5] C.-H. Menq, J.H. Griffin, and J. Bielak. The influence of microslip on vibratory response, part ii: A comparison with experimental results. *Journal of Sound and Vibration*, 107(2):295–307, 1986.

[6] M.L. Tinker. Modeling of nonlinear vibration isolators using the advanced continuous simulation language (acsl). *SE Simulation Conference Proceedings.*

[7] D.W. Childs. Space shuttle main engine high-pressure fuel turbopump rotordynamic instability problem. *J Eng Power Trans ASME*, 100(1):48–57, 1978.

[8] Randy L Dickerman and Wayne R Melchior. High temperature metal rubber gasket, July 18 1989. US Patent 4,849,295.

[9] Jennifer H Lalli, William Harrison, Theodore Distler, Michael Bortner, Keith Hill, Jacob Dennis, Bradley Davis, Richard O Claus, Jeffery W Baur, and

Ryan S Justice. Shape memory-metal rubber morphing aircraft skins. In *ASME 2009 conference on smart materials, adaptive structures and intelligent systems*, pages 161–168. American Society of Mechanical Engineers, 2009.

[10] J. Hong, L. Chen, Y. Ma, G.R. Tomlinson, and J.A. Rongong. Hysteretic properties of metal rubber particles. *Proceedings of the Institution of Mechanical Engineers, Part C: Journal of Mechanical Engineering Science*, 227(4):693–702, 2013.

[11] Jones, A.M. Experimental Examination of Wire Mesh Dampers Subjected to Large Amplitude Displacements. Master's thesis, Texas A&M University, 2007.

[12] J. Hong, B. Zhu, and Y. Ma. Theoretical and experimental investigation on nonlinear characterization of metal rubber. volume 6, pages 877–886, 2011.

[13] B. Zhang, Z.Q. Lang, S.A. Billings, G.R. Tomlinson, and J.A. Rongong. System identification methods for metal rubber devices. *Mechanical Systems and Signal Processing*, 39(1-2):207–226, 2013.

[14] Zarzour, M.J. Experimental evaluation of a metal-mesh bearing damper in a high speed test rig. Master's thesis, Texas A&M University, 1999.

[15] M.J. Zarzour and J. Vance. Experimental evaluation of a metal mesh bearing damper. *Journal of Engineering for Gas Turbines and Power*, 122(2):326–329, 2000.

[16] B.H. Ertas, E. Al-Khateeb, and J.M. Vance. Rotordynamic bearing dampers for cryogenic rocket engine turbopumps. *Journal of Propulsion and Power*, 19(4):674–682, 2003.

[17] E. Al-Khateeb and J. Vance. Experimental evaluation of a metal mesh bearing damper in parallel with a structural support. *Proceedings of the ASME Turbo Expo*, 4, 2001.

[18] A.B. Barnes. Improvements in machinery for woven wire mesh. *Wire Industry*, 51(605):403–404, 1984.

[19] Burshid, S.M. Experimental Evaluation of Rotordynamic Coefficients for Hybrid Metal Mesh Pocket Damper Seals in Turbomachinery. Master's thesis, Texas A&M University, 1999.

[20] A. Okayasu, T. Ohta, T. Azuma, T. Fujita, and H. Aoki. Vibration problem in the le-7 lh2 turbopump. *26th Joint Propulsion Conference*, 1990.

[21] Al-Khateeb, E. *Design, modeling and experimental investigation of wire mesh vibration dampers*. PhD thesis, Texas A&M University, 2002.

[22] H. Zuo, Y.H. Chen, H.B. Bai, and H. Sun. The compression deformation mechanism of a metallic rubber. *International Journal of Mechanics and Materials in Design*, 2(3-4):269–277, 2005.

[23] H. Wang, J.A. Rongong, G.R. Tomlinson, and J. Hong. Nonlinear static and dynamic properties of metal rubber dampers. pages 1301–1315, 2010.

[24] J.X. Yan and L.H. Nie. Sma pseudo-rubber metal and its application in vibration control [j]. *Journal of Beijing University of Aeronautics and Astronautics*, 1:018, 2003.

[25] Ma, Y. *Theoretical and Experimental Investigation of a Novel Adaptive Squeeze Film Damper*. PhD thesis, Beijing : School of Jet Propulsion, Beijing University of Aeronautics and Astronautics, 2005.

[26] J.P. Den Hartog. *Mechanical Vibrations*. Civil, Mechanical and Other Engineering Series. Dover Publications, 1985.

[27] Q. Tan, P. Liu, C. Du, L. Wu, and G. He. Mechanical behaviors of quasi-ordered entangled aluminum alloy wire material. *Materials Science and Engineering: A*, 527(1):38–44, 2009.

[28] L.J. Gibson and M.F. Ashby. *Cellular Solids: Structure and Properties*. Cambridge Solid State Science Series. Cambridge University Press, 1999.

[29] H. Ao, H. Jiang, and A.M. Ulanov. Dry friction damping characteristics of a metallic rubber isolator under two-dimensional loading processes. *Modelling and Simulation in Materials Science and Engineering*, 13(4):609–620, 2005.

[30] D. Zhang, F. Scarpa, Y. Ma, K. Boba, J. Hong, and H. Lu. Compression mechanics of nickel-based superalloy metal rubber. *Materials Science and Engineering A*, 580:305–312, 2013.

[31] Y. Ma, D. Gao, and J. Hong. Investigation on the effect of dimension on the compression mechanics of metal rubber. In *ASME Turbo Expo 2014: Turbine Technical Conference and Exposition*, pages V07AT34A003–V07AT34A003. American Society of Mechanical Engineers, 2014.

[32] Y. Ma, D. Gao, D. Zhang, and J. Hong. Compressive and dissipative behavior of metal rubber under constraints. *physica status solidi (b)*, 252(7):1675–1681, 2015.

[33] J.F. Hou, H.B. Bai, and D.W. Li. Damping capacity measurement of elastic porous wire-mesh material in wide temperature range. *Journal of Materials Processing Technology*, 206(1-3):412–418, 2008.

[34] Y. Ma, H. Wang, H. Li, and J. Hong. Study on metal rubber materials characteristics of damping and sound absorption. In *ASME Turbo Expo 2008: Power for Land, Sea, and Air*, pages 477–486. American Society of Mechanical Engineers, 2008.

[35] T. Pritz. Unbounded complex modulus of viscoelastic materials and the kramers-kronig relations. *Journal of Sound and Vibration*, 279(3-5):687–697, 2005.

[36] Y. Ma, H. Zhu, D. Zhang, and J. Hong. Experimental investigation on dynamic mechanical behavior of the elastic ring support with metal rubber. In *ASME 2013 International Mechanical Engineering Congress and Exposition*, pages V04BT04A053–V04BT04A053. American Society of Mechanical Engineers, 2013.

[37] B.H. Ertas and H. Luo. Nonlinear dynamic characterization of oil-free wire mesh dampers. *Journal of Engineering for Gas Turbines and Power*, 130(3):032503, 2008.

[38] K. Zhang, Y. Zhou, and J. Jiang. Experimental study and dynamic modeling of metal rubber isolating bearing. In *IOP Conference Series: Materials Science and Engineering*, volume 103, page 012048. IOP Publishing, 2015.

[39] Choudhry, V. V. Experimental Evaluation of Wire Mesh for Design as a Bearing Damper . Master's thesis, Texas A&M University, 2004.

[40] G. He, P. Liu, and Q. Tan. Porous titanium materials with entangled wire structure for load-bearing biomedical applications. *Journal of the mechanical behavior of biomedical materials*, 5(1):16–31, 2012.

[41] G. He, P. Liu, Q. Tan, and G. Jiang. Flexural and compressive mechanical behaviors of the porous titanium materials with entangled wire structure at different sintering conditions for load-bearing biomedical applications. *Journal of the mechanical behavior of biomedical materials*, 28:309–319, 2013.

[42] Q. Tan and G. He. Stretching behaviors of entangled materials with spiral wire structure. *Materials & Design*, 46:61–65, 2013.

[43] P. Liu, G. He, and L.H. Wu. Impact behavior of entangled steel wire material. *Materials Characterization*, 60(8):900–906, 2009.

[44] P. Liu, Q. Tan, L. Wu, and G He. Compressive and pseudo-elastic hysteresis behavior of entangled titanium wire materials. *Materials Science and Engineering: A*, 527(15):3301–3309, 2010.

[45] P. Liu, G. He, and L. Wu. Uniaxial tensile stress–strain behavior of entangled steel wire material. *Materials Science and Engineering: A*, 509(1):69–75, 2009.

[46] M. Huang, X. Dong, and G. Liu. 3d modeling of the preparation process of metal rubber material. *International Journal of Minerals, Metallurgy, and Materials*, 17(1):75–79, 2010.

[47] A.I. Safin, A.A. Igolkin, and A.B. Prokofev. A mathematical model of acoustic properties of gas turbine engine sound absorbing elements made from elastic porous metal rubber. *Russian Aeronautics (Iz VUZ)*, 57(4):430–434, 2014.

[48] Y. Ma, Z. Liang, H. Wang, D. Zhang, and J. Hong. Theoretical and experimental steady-state rotordynamics of an adaptive air film damper with metal rubber. *Journal of Sound and Vibration*, 332(22):5710–5726, 2013.

[49] Y.-H. Ma, H.-W. Lu, Z.-D. Ma, B. Zhu, and J. Hong. Theoretical research of thermal conductivity model of metal rubber based on the wire helix. In

ASME 2012 International Mechanical Engineering Congress and Exposition, pages 1179–1185. American Society of Mechanical Engineers, 2012.

[50] Y. Ma, W. Hu, D. Zhang, Q. Zhang, and J. Hong. Tunable mechanical characteristics of a novel soft magnetic entangled metallic wire material. *Smart Materials and Structures*, 25(9):095015, 2016.

[51] Y. Ma, Q. Zhang, D. Zhang, F. Scarpa, B. Liu, and J. Hong. A novel smart rotor support with shape memory alloy metal rubber for high temperatures and variable amplitude vibrations. *Smart Materials and Structures*, 23(12):125016, 2014.

[52] Y. Ma, F. Scarpa, D. Zhang, B Zhu, L. Chen, and J. Hong. A nonlinear auxetic structural vibration damper with metal rubber particles. *Smart Materials and Structures*, 22(8):084012, 2013.

[53] Y. Ma, Q. Zhang, D. Zhang, F. Scarpa, B. Liu, and J. Hong. Tuning the vibration of a rotor with shape memory alloy metal rubber supports. *Journal of Sound and Vibration*, 351:1–16, 2015.

[54] Y. Ma, Q. Zhang, D. Zhang, F. Scarpa, B. Liu, and J. Hong. The mechanics of shape memory alloy metal rubber. *Acta Materialia*, 96:89–100, 2015.

[55] Qingbiao Tan and Guo He. 3d entangled wire reinforced metallic composites. *Materials Science and Engineering: A*, 546:233–238, 2012.

[56] Q. Li, J. Li, and G. He. Compressive properties and damping capacities of magnesium reinforced with continuous steel wire. *Materials Science and Engineering: A*, 680:92–96, 2017.

[57] A.M. Ulanov and G.V. Lazutkin. Description of an arbitrary multi-axial loading process for non-linear vibration isolators. *Journal of Sound and Vibration*, 203(5):903–907, 1997.

[58] S. Chen and S.A. Billings. Representations of non-linear systems: The narmax model. *International Journal of Control*, 49(3):1013–1032, 1989.

[59] M.L. Tinker and M.A. Cutchins. Damping phenomena in a wire rope vibration isolation system. *Journal of Sound and Vibration*, 157(1):7–18, 1992.

[60] SR Dahl and RB Rice. A derivation of equivalent linear viscous and elastic constants for viscoelastic materials. Technical report, DTIC Document, 1984.

[61] J Kerley. Concepts and effects of damping in isolators. Technical report, DTIC Document, 1984.

[62] I. Pivovarov and O. Vinogradov. The phenomenon of damping in stranded cables. *26th Structures, Structural Dynamics, and Materials Conference*, 1985.

[63] Shin, H. -C. *The Static and Dynamic Structural Properties of Fibrous Media.* PhD thesis, University of Hull, 2004.

[64] K.L. Johnson. *Contact Mechanics.* Cambridge University Press, 1987.

[65] Baudequin, M., Ryschenkow, G., Roux, S. Non-linear elastic behavior of light fibrous materials. *The European Physical Journal B - Condensed Matter and Complex Systems*, 12(1):157–162, 1999.

[66] J.H. Hubbell. Photon mass attenuation and energy-absorption coefficients. *The International Journal of Applied Radiation and Isotopes*, 33(11):1269–1290, 1982.

[67] A.H. Compton. A quantum theory of the scattering of x-rays by light elements. *Physical review*, 21(5):483, 1923.

[68] G. W. Grodstein. X-ray attenuation coefficients from 10 kev to 100 mev. Technical report, DTIC Document, 1957.

[69] X. Pan, E.Y. Sidky, and M. Vannier. Why do commercial ct scanners still employ traditional, filtered back-projection for image reconstruction? *Inverse problems*, 25(12):123009, 2009.

[70] MATLAB. *version 8.4.0 (R2014b).* The MathWorks Inc., 2014.

[71] J. Kittler and J. Illingworth. Minimum error thresholding. *Pattern Recognition*, 19(1):41 – 47, 1986.

[72] Y. She et al. Thresholding-based iterative selection procedures for model selection and shrinkage. *Electronic Journal of statistics*, 3:384–415, 2009.

[73] J.N. Kapur, P.K. Sahoo, and A.K.C. Wong. A new method for gray-level picture thresholding using the entropy of the histogram. *Computer Vision, Graphics, and Image Processing*, 29(3):273 – 285, 1985.

[74] Prasanna K Sahoo, SAKC Soltani, and Andrew KC Wong. A survey of thresholding techniques. *Computer vision, graphics, and image processing*, 41(2):233–260, 1988.

[75] Chandrasekhar, K., Rongong, J.A., Cross, E.J. Frequency and amplitude dependent behaviour of tangled metal wire dampers. *Proceedings of International Conference on Noise and Vibration Engineering and International Conference on Uncertainty in Structural Dynamics*, pages 559–572, 2014.

[76] J.A. Meganck, K.M. Kozloff, M.M. Thornton, S.M. Broski, and S.A. Goldstein. Beam hardening artifacts in micro-computed tomography scanning can be reduced by x-ray beam filtration and the resulting images can be used to accurately measure bmd. *Bone*, 45(6):1104–1116, 2009.

[77] SkyScan NV. SkyScan NRecon User Manual. *User Manual*, 2011.

[78] Boas, F.E., Fleischmann, D. CT artifacts: Causes and reduction techniques. *Imaging in Medicine*, 4(2):229–240, 2012.

[79] M. Shibano, H. Kakuma, and H. Yasuyama. Hydraulic vibration tester, September 1983. US Patent 4,403,511.

[80] J.H. Weatherby. Actuator having a drive screw and a selectively rotatable nut, February 1981. US Patent 4,250,762.

[81] B. Darabi and J.A. Rongong. Polymeric particle dampers under steady-state vertical vibrations. *Journal of Sound and Vibration*, 331(14):3304–3316, 2012.

[82] Babak Darabi. Dissipation of vibration energy using viscoelastic granular materials. 2013.

[83] K.H. Huebner, D.L. Dewhirst, D.E. Smith, and T.G. Byrom. *The finite element method for engineers.* John Wiley & Sons, 2008.

[84] S.S. Rao. *The finite element method in engineering.* Elsevier, 2010.

[85] Kenneth G McConnell. *Vibration testing: theory and practice.* John Wiley & Sons, 1995.

[86] Smalley Steel Ring Company. Crest-to-crest wave springs, 2016. `http://www.smalley.com/wave-springs/crest-crest`, [Accessed: 18-09-16].

[87] Anti-Vibration Methods (Rubber) Co. Bobbin mounts, 2013. `http://www.antivibrationmethods.com/product/bobbin-mounts`, [Accessed: 18-09-16].

[88] A.D. Nashif, D.I.G. Jones, and J.P. Henderson. *Vibration Damping.* Wiley-Interscience publication. Wiley, 1985.

[89] H. Olsson, K.J. Astrom, C. de Wit, M. Gafvert, and P. Lischinsky. Friction Models and Friction Compensation. *European Journal of Control*, 4(3):176–195, 1998.

[90] J. Wojewoda, A. Stefanski, M. Wiercigroch, and T. Kapitaniak. Hysteretic effects of dry friction: modelling and experimental studies. *Philosophical Transactions of the Royal Society A-Mathematical Physical and Engineering Sciences*, 366(1866):747–765, MAR 13 2008.

[91] Saha, A. *Analysis and control of friction-induced vibrations by time-delayed position feedback.* PhD thesis, Department of Mechanical Engineering, Indian Institute of Technology, 2012.

[92] B. Feeny, A. Guran, N. Hinrichs, and K. Popp. A historical review on dry friction and stick-slip phenomena. *Applied Mechanics Reviews*, 51(5):321–341, 1998.

[93] V.I. Johannes, M.A. Green, and C.A. Brockley. The role of the rate of application of the tangential force in determining the static friction coefficient. *Wear*, 24(3):381–385, 1973.

[94] F. Al-Bender. Fundamentals of friction modeling. In *Proceedings, ASPE Spring Topical Meeting on Control of Precision Systems, MIT, April 11-13, 2010*, pages 117–122. ASPE-The American Society of precision Engineering, 2010.

[95] J. S. Courtney-Pratt and E. Eisner. The effect of a tangential force on the contact of metallic bodies. *Proceedings of the Royal Society of London A: Mathematical, Physical and Engineering Sciences*, 238(1215):529–550, 1957.

[96] D.P. Hess and A. Soom. Friction at a lubricated line contact operating at oscillating sliding velocities. *Journal OF Tribology-Transactions of the ASME*, 112(1):147–152, Jan 1990.

[97] M. Wiercigroch, V.W.T. Sin, and Z.F.K. Liew. Non-reversible dry friction oscillator: design and measurements. *Proceedings of the Institution of Mechanical Engineers, Part C: Journal of Mechanical Engineering Science*, 213(5):527–534, 1999.

[98] I. Virgala and M. Kelemen. Experimental friction identification of a dc motor. *International Journal of Mechanics and Applications*, 3(1):26–30, 2013.

[99] W. Thomson. *Theory of Vibration with Applications.* Taylor & Francis, 1996.

[100] R.D. Peters. Toward a universal model of damping–modified coulomb friction. *Macon, Georgia : Mercer University*, 2002.

[101] C. Iurian, F. Ikhouane, J. Benede, J. Rodellar, and R. Grino. Identification of a system with dry fiction. *Reports de recerca de l'Institut d'Organitzacio i Control de Sistemes Industrials*, (20):1, 2005.

[102] D.A. Haessig and B. Friedland. On the modeling and simulation of friction. *Journal of Dynamic Systems, Measurement, and Control*, 113(3):354–362, 1991.

[103] C. De Wit, H. Olsson, K.J. Astrom, and P. Lischinsky. A new model for control of systems with friction. *IEEE Transactions on automatic control*, 40(3):419–425, 1995.

[104] J. Swevers, F. Al-Bender, C.G. Ganseman, and T. Projogo. An integrated friction model structure with improved presliding behavior for accurate friction compensation. *IEEE Transactions on automatic control*, 45(4):675–686, 2000.

[105] V. Lampaert, J. Swevers, and F. Al-Bender. Modification of the leuven integrated friction model structure. *IEEE transactions on Automatic Control*, 47(4):683–687, 2002.

[106] Kenneth Price, Rainer M Storn, and Jouni A Lampinen. *Differential evolution: a practical approach to global optimization*. Springer Science & Business Media, 2006.

[107] D.J.C. MacKay. *Information theory, inference and learning algorithms*. Cambridge university press, 2003.

[108] D. Tiboaca, P.L. Green, R.J. Barthorpe, and K. Worden. Bayesian parameter estimation and model selection of a nonlinear dynamical system using reversible jump markov chain monte carlo. In *Proceedings of ISMA 2014, International Conference on Noise and Vibration Engineering*. Sheffield, 2014.

[109] D. Tiboaca, P.L. Green, R.J. Barthorpe, I. Antoniadou, and K. Worden. Bayesian inference and rjmcmc in structural dynamics: On experimental data. In *Model Validation and Uncertainty Quantification, Volume 3*, pages 23–36. Springer, 2016.

[110] Desborough, L., Miller, R. Increasing customer value of industrial control performance monitoring-honeywell's experience. *AIChE symposium series*, pages 169–189, 2002.

[111] K. J. Astrom and T. Hagglund. Pid controllers: theory, design and tuning, 1995.

[112] National Instruments. Compactrio application areas, 2016. `http://www.ni.com/compactrio/applications/`, [Accessed: 03-06-16].

[113] National Instruments Corporation. *Reconfigurable Chassis for CompactRIO: cRIO-911x*. National Instruments, 2015. `http://www.ni.com/datasheet/pdf/en/ds-227`, [Accessed: 03-06-16].

[114] National Instruments Corporation. *NI 9234 Datasheet*. National Instruments, 2015. `http://www.ni.com/pdf/manuals/376926a_02.pdf`, [Accessed: 03-06-16].

[115] National Instruments Corporation. *NI 9260 Datasheet*. National Instruments, 2015. `http://www.ni.com/pdf/manuals/374238a_02.pdf`, [Accessed: 03-06-16].

[116] National Instruments Corporation. *LabVIEW: FPGA Module User Manual.* National Instruments Corporation, 2015. `http://www.ni.com/pdf/manuals/370690b.pdf`, [Accessed: 03-06-16].

Appendix A

PID Control

What is, and why use PID control?

A PID controller is a type of feedback controller that can be used to regulate a variety of process conditions, such as positions, temperatures, and speeds, in quite a robust manner. It is one of the most commonly used controllers for industrial applications. Desborough, L. and Miller, R. [110] performed a survey in 2002, and found that of the 11000 controllers employed in the refining, chemical, pulp and paper industries, 97% were PID feedback controllers.

The acronym PID stands for proportional, integral, and derivative, respectively. The individual components can be arranged either in series, parallel, or a combination of both, with the most common one being the parallel arrangement, which was used for the work carried out here, shown in Figure A.1.

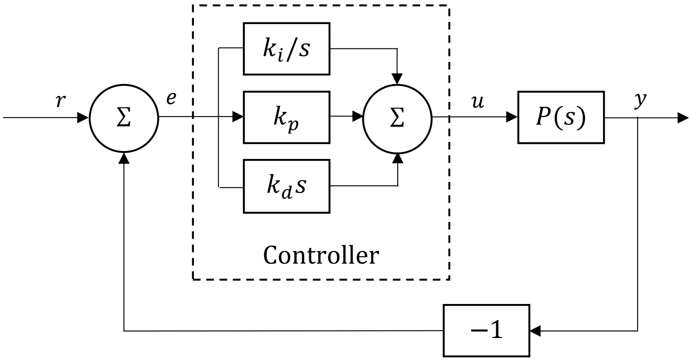

Figure A.1: Block diagram of a PID feedback controller in parallel configuration

PID control works on the basis of finding the difference, e (known as the error) between a setpoint, r (an ideal, reference signal) and the actual signal level, y. The error is fed into the proportional, k_p, integral, k_i/s, and derivative, $k_d s$, terminals. These determine the control gain that is sent to a regulator (in this case, a power amplifier) that alters the signal going into a process, $P(s)$, as per Figure A.1.

The general equation for a PID system output in this form may be written as,

$$u(t) = k_p \left(e(t) + \frac{1}{T_i} \int_0^t e(\tau) d\tau + T_d \frac{de}{dt} \right) \tag{A.1}$$

where u is the control signal, e is the error in the signal (i.e. the difference between the setpoint, r and the current value, y), k_p is the proportional gain parameter, T_i is the integral time, and T_d is the derivative time. Equation A.1 can be rewritten to separate and treat each gain parameter separately as,

$$u(t) = k_p e(t) + k_i \int_0^t e(\tau) d\tau + k_d \frac{de}{dt} \tag{A.2}$$

where k_i and k_d are the integral and derivative gains, respectively.

Each term handles a defined task in the control process using a prescribed gain value. These gains can be calculated accurately using existing control equations, and requires complete knowledge of the system transfer function, which in most cases are unknown. Therefore, the gains are typically determined by "tuning" the PID controller for specific tasks. As TMW devices are nonlinear, the system transfer function is different for each device, as well as at different amplitudes. Hence, tuning was required for each experiment performed.

The performances of each of these gains are briefly summarised in the following text for a PID controller applied to a simple single degree of freedom system. Without going into detailed control theory, which is not the focus of this work, the performances of each term are illustrated instead for a unit step input. The performance indicators are:

- Rise time, defined as the time taken for the signal to achieve 90% of the target (ideal) value, measured from when the signal is 10% of the target value.
- Overshoot, defined as the amount (typically as a percentage) that the signal goes over the intended target value.
- Settling time, defined as the time taken for the signal to stabilise around the target value, with most literature quoting that this occurs when the signal attains a value within 5% of the target value [111].
- Steady state error, defined (as before) as the difference between the final signal value and the target value.

Proportional gain

The main aim of proportional action is to reduce the steady state error, while making the system responsively quicker [111]. For a step input, a controller with purely proportional gain, the output level, y increases with increasing gains, without reaching the required setpoint, r, meaning that there is always a steady state error. While increasing levels of k_p reduces the rise time, it also increases the overshoot, and can lead to oscillatory motion about the final output value. These characteristics are illustrated in Figure A.2.

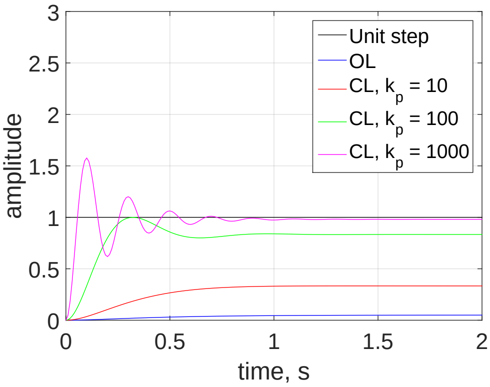

Figure A.2: Effects of proportional action on system response

The curve "OL" in Figure A.2 represents open loop behaviour, i.e. there is no controller implemented. Closed loop behaviour is denoted by "CL", which indicates that there is a controller active in the form of a feedback controller. In the closed loop curves, only the proportional term is active, with the integral and derivative gains being set to zero.

Integral gain

The main purpose of integral action is to eliminate the steady state error [111]. Increasing the integral gain gradually reduces the steady state error before eliminating it. It also makes the controller more responsive by reducing the rise time, however the settling time can potentially increase due to the increasing overshoot, as well as the oscillatory motion about the chosen setpoint. Figure A.3 graphically exhibits these behaviours, where the proportional gain is set to a constant value of 100, and derivative gain is set to zero.

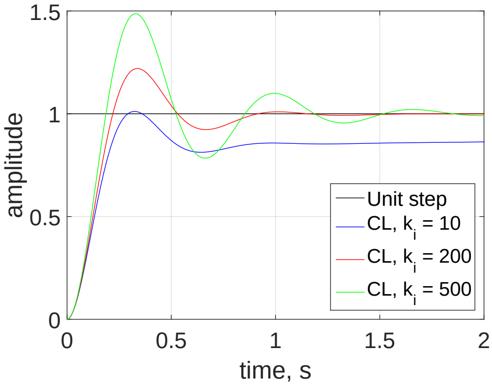

Figure A.3: Effects of integral action on system response

Derivative gain

Derivative action is generally used to damp the oscillatory motion that arise due to the introduction of proportional and integral action [111]. Increasing gains helps in reducing overshoots adequately. It has a negligible effect on rise time, and reduces the settling time when the derivative gain is set to a reasonable value. However, after a certain gain level, derivative action may cause the system to be overdamped, leading to sluggish response from the system. Hence, the rise and settling times may increase. Figure A.4 shows the mentioned behaviour, where the proportional and integral gains are maintained constant at 100 and 500, respectively.

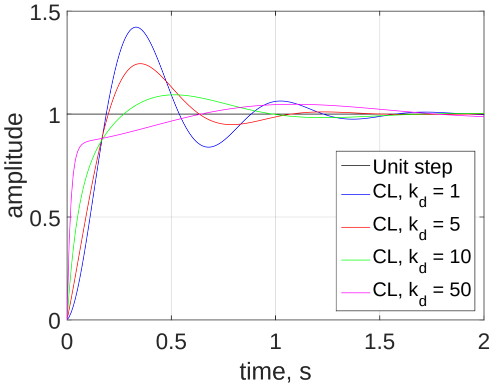

Figure A.4: Effects of derivative action on system response

In practice, most controllers employ only PI action because the derivative action can potentially destabilise systems due to the inherent presence of high frequency noise from sensors. Low pass filters may be used to mitigate noise, but adding a filter can introduce a time-lag in the system, which is undesired in most control applications.

Table A.1 summarises the effects of increasing the proportional, integral, and derivative action on system response.

Closed loop response	**Rise time**	**Overshoot**	**Settling time**	**Steady state error**
k_p	Reduce	Increase	Negligible	Reduce
k_i	Reduce	Increase	Increase	Eliminate
k_d	Negligible	Reduce	Reduce/Increase	None

Table A.1: Summary of system effects of increasing proportional, integral, and derivative gains

While these discussions have been based on a step input, the same principles may be extended to other kinds of inputs.

National Instruments CompactRIO Industrial Controller

A CompactRIO 9024 (cRIO-9024) Industrial Controller, manufactured by National Instruments, was used to implement a PID controller to the test structure. The acronym "RIO" stands for reconfigurable input and output. CompactRIO controllers, which are real-time controllers, have been used across several industries, and the systems can be robustly configured to cater for a wide range of applications, such as in condition monitoring, robotics, and hydraulic control [112].

The cRIO-9024 consisted of a reconfigurable chassis with eight input/output slots (cRIO-9114) [113], a module that contained four simultaneous BNC[1] input channels (NI-9234) [114], and a module that contained two simultaneous BNC output channels (NI-9260) [115]. The chosen input and output modules both allowed a maximum sampling rate of 51.2 kS/s/ch (kilo samples per second per channel), hence adequate resolutions for moderately high frequencies were acquired.

These controllers generally consist of two separate options for processing and controlling signals:

---

[1] Bayonet Neill-Concelman

- A real-time processor and controller, used as an interface between the controller and systems running LabVIEW software, and as a signal processor.
- A field-programmable gate array (FPGA), which allows robust control at significantly higher speeds.

Codes developed for any application must first be compiled. Compilation converts the code from the LabVIEW block diagrams to a hardware description language (HDL) that the FPGA can read. This was performed by a compilation software prepared by Xilinx, the inventors of FPGAs. The HDL was deployed to the controller via an ethernet cable, which was also used for user communication between the computer and controller.

The cRIO-9024 is self-sufficient due to the embedded real-time processor, and connection to a computer to perform its tasks is not required. It only requires a computer when a user needs to change certain parameters, although these parameter changes can also be pre-programmed to satisfy known conditions.

PI control on LabVIEW

The main characteristic that sets apart LabVIEW from other programming software is its visualisation aspect. The “codes” developed contain two related entities, the front panel and the block diagram. The front panel indicates inputs and outputs of the program, whereas the block diagram contains internal functions that link the inputs to the outputs contained in the front panel. As the PID theory has already been introduced earlier, this subsection briefly discusses the PI algorithm developed on LabVIEW.

The PI controller was implemented on the FPGA target because it dealt with data at much higher speeds than the CompactRIO (cRIO-9024) real-time processor and controller. Due to its implementation directly to hardware, the code developed was considered as low-level programming. A low-level program is one that is independent from the restrictions imposed by the processor instructions architecture of the operating system it is created in [116]. This meant that initialisation of all hardware, data processing, and termination of all hardware were clearly defined in the process, and the processes were ordered in the correct sequence. This included starting all modules, setting the data transfer rates, and stopping all modules. If this was not performed, startup errors could have arose when the system was used next. This was because some of the hardware may have assumed that their tasks were not complete yet and hence may have remained in a state of “limbo”.

The front panel of the PI controller is shown in Figure A.5. The front panel contained inputs for the initialisation of the input and output modules data sampling rates, and the input module configuration. These inputs provided a standard drop-down list that users could choose from. The input and output module data rates were set at the maximum levels to allow for better control at high frequencies. The input module that could be configured as an AC or a DC channel, depending on the type of sensor used, were set to the AC configuration. The front panel also contained inputs for the pre-compression level, the amplitude and frequency of vibration for the testing that were performed. Finally, there were two clusters of inputs for the parameters of the PI controller. The “Sine Wave Gains” cluster had inputs for the proportional, and integral gains. The “Sine Wave Output Range” cluster included the limits that the PI saturated at. This ensured that the PI controller remained within the safety limits of the hardware and equipment.

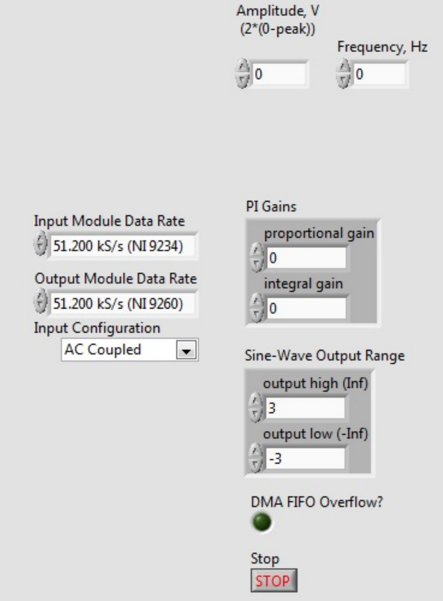

Amplitude, V (2*(0-peak)): 0
Frequency, Hz: 0

Input Module Data Rate: 51.200 kS/s (NI 9234)
Output Module Data Rate: 51.200 kS/s (NI 9260)
Input Configuration: AC Coupled

PI Gains
proportional gain: 0
integral gain: 0

Sine-Wave Output Range
output high (Inf): 3
output low (-Inf): -3

Figure A.5: Front panel of the PID algorithm developed on LabVIEW

The block diagram of the PID controller, shown in Figure A.6, was designed in a flat sequence structure. Each section within this type of structure must first be processed and completed before moving on to the next stage of the sequence.

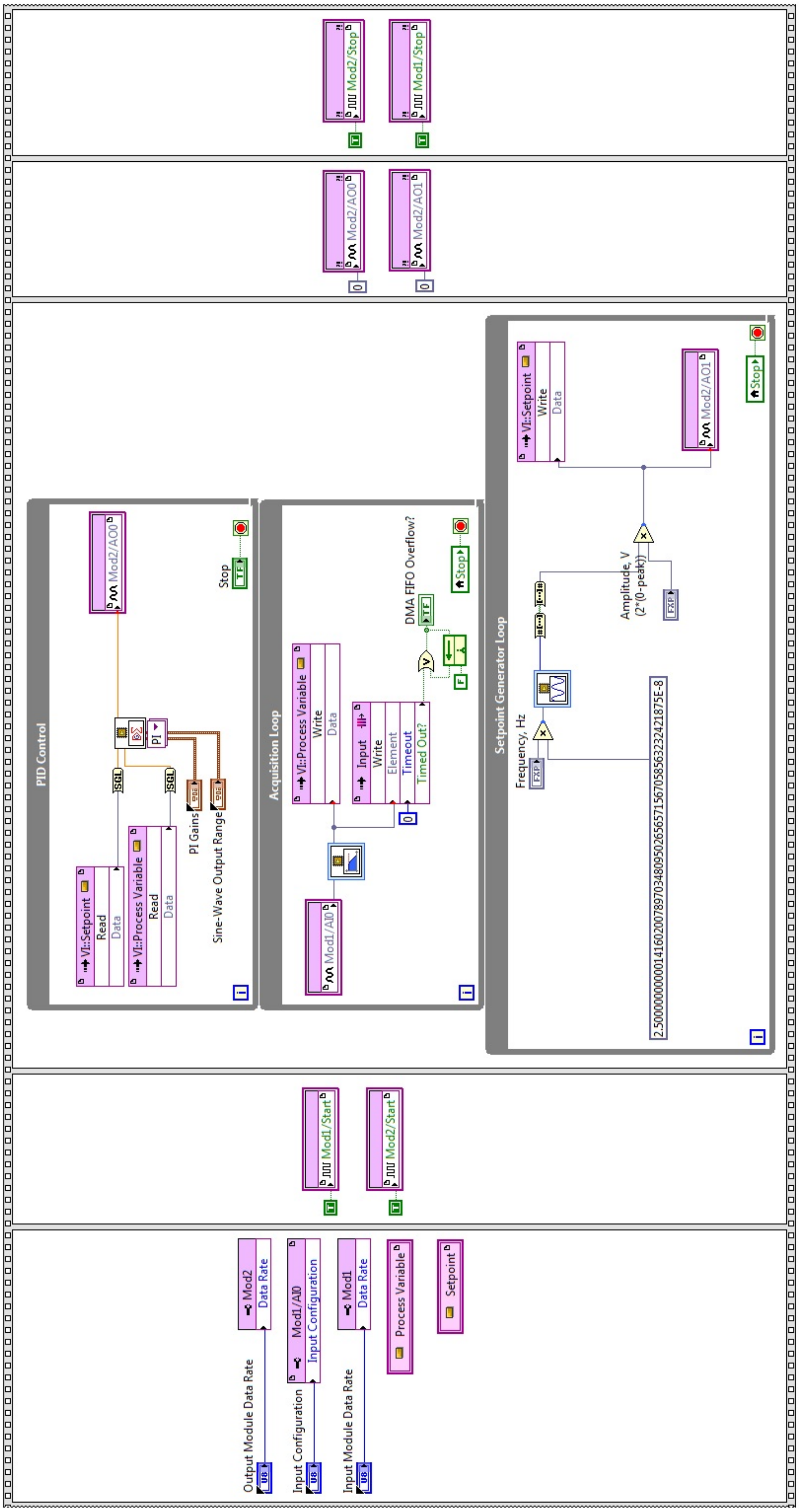

Figure A.6: Front panel of the PID algorithm developed on LabVIEW

There were a total of five sequences, which are explained as follows:

- The first section contained the configurations of the inputs - the input configuration, and the input and output data sampling rates were defined. There were also two “registers” that were initialised. These registers, the “Process Variable” and “Setpoint” were used in the third section in the sequence, and were used to transfer collected data between three parallel processes.
- The second section sent messages to the CompactRIO and FPGA systems for the input and output modules to commence acquiring data.
- The third section in the sequence was the PID control section. It contained three parallel processes in the form of parallel loops. These were the “Acquisition”, “Setpoint Generator”, and “PID Control” loops.
  - The Acquisition Loop collected data from the input module, filtered it, and wrote it into the Process Variable register.
  - The Setpoint Generator Loop used the user defined frequency input and fed it into a predefined sine wave generator. The input for this generator required the frequency to be defined in terms of periods/tick, and so the user defined frequency was multiplied by a constant. Since the clock rate of the FPGA was set to 40MHz, each tick was the inverse of this rate. Note that since FPGA systems work on the basis of integers, some data conversion was required, depending on the number of bits that the input and output modules processed. The sine wave generated, which had a unit amplitude, was then multiplied to the user defined amplitude. Finally, the data was sent to the Setpoint register, as well as to one of the two channels of the output module - this allowed the controlled signal to be directly compared to the ideal signal.
  - The PID Control Loop used the data from the Setpoint and Process Variable registers, as well as the user inputs for the PI parameters to perform the control. The output from the predefined PI control block was sent directly to the remaining channel of the output module, which was sent to the amplifier.

- The PI control was terminated using a “Stop” button. This allowed the program to move to the fourth section of the sequence, where the output modules were set to produce an output of zero.
- The final part of the sequence terminated the use of the input and output modules, which means that they would be ready to be initiated in the next run of the controller.